



**University of
Nottingham**
UK | CHINA | MALAYSIA

**T-cell and Macrophage exhaustion in the colorectal cancer
microenvironment and impact on survival**

**Thesis submitted to the University of Nottingham
for the degree of Master of Research
March 2025**

Tahereh Hojjatipour

**Supervised by
Dr. Judith Ramage
Dr. Andrew Jackson**

**University of Nottingham
Faculty of Medicine and Health Sciences
School of Medicine
Tumour immunology group**

Contents:

Abstract

Acknowledgement

Table of contents

List of figures

List of tables

Abbreviations

Abstract:

Colorectal cancer (CRC) is one of the most common cancers worldwide. In recent years, attention has turned to the role of immune cells within the tumour microenvironment (TME). Immunoscore is one development that histopathologically classifies CRC based on the differences in the immune architecture of CD3+ and CD8+ T-cells. However, the colorectal TME is complex than this and more comprehensive approaches are required to map and interpret its composition. T cells and macrophages are abundant in the CRC TME, and their composition and functionality can significantly impact patient prognosis and survival. In particular, T cell exhaustion, characterized by non-functional bystander T cells expressing immune checkpoint molecules, plays a critical role in fostering malignant TME to promote cancer growth. Macrophages are also manipulated to favor tumour growth; however, there is limited data on their expression of checkpoint molecules.

The CRC TME is well-established as one of the most diverse tumour microenvironments among solid cancers. Many studies have described the prognostic impact of macrophages and T cells, and the impact of factors such as tumour sidedness (right vs. left), mismatch repair (MMR) status (MSI vs. MSS), sample location (invasive margin, luminal side, tumour center, and adjacent normal tissue), and tumour grade/stage. With the advent of improved immune spatial platforms, we conducted a comprehensive exploration of the distribution and prognostic impact of T cells and macrophages that expressed PD1, LAG3, and TIM3 checkpoint molecules.

Multiplex immunohistochemistry was applied to a tissue microarray representing 1,000 CRC patients each described by four cores from different pathological locations. Spatial analysis identified five distinct regions within the CRC TME and using Cytomaps identified a region characterized by a high density of macrophages and T cells. We found that the density of all studied checkpoint molecules was greater on macrophages and T cells in the stromal compartment compared to those in the intraepithelial regions. Notably, PD1 was expressed significantly more in T cells than in macrophages, while macrophages predominantly expressed TIM3. Intraepithelial infiltration of T cells associated with improved survival, regardless of the exhaustion markers or other variables analyzed in this study. In contrast, CD68 did not demonstrate prognostic value on its own; however, it may indicate a favorable prognosis at the invasive margins of MSS-CRC, particularly on the right side, during both early and advanced stages. Additionally, PD1 expression on T cells correlated with better survival outcomes, whereas the expression of TIM3 on both macrophages and T cells associated with reduced survival. LAG3 was not expressed in macrophages, and its expression on T cells did not provide prognostic value.

Our findings underscore the need to consider the location and interactions of immune cells with and without checkpoint molecules within the CRC tumour microenvironment, not just their overall expression levels. Future research in this area is vital for creating effective, personalized immunotherapy treatments.

Acknowledgement:

I wish to extend my sincere gratitude to Dr. Judith Ramge, my first supervisor on this course. Her guidance was invaluable, and I deeply appreciate her role not only as an exceptional mentor throughout this journey but also as a sympathetic individual who listened and offered support beyond the academic realm. It was a distinct privilege and honor to learn from her during the different stages of this work, drawing inspiration from her wisdom in both academic and personal spheres.

I am also deeply thankful to my second supervisor, Dr. Andrew Jackson, who graciously stepped in to guide the project following unexpected circumstances. His willingness to take on full supervision and his steadfast support were instrumental in bringing this work to fruition. Having the guidance of two such supportive and dedicated supervisors during this past year has been an extraordinary privilege, one I value immensely from my academic life thus far.

My gratitude extends further to the members of the tumour immunology group. The insightful advice and thoughtful comments from Dr. Ian Spendlove, Dr. Hester Franks, and Dr. Anna Malecka significantly helped shape and enrich this project. I must also express my thanks to Dr. Mohammad Ilyas and Dr. Abhik Mukherjee for generously providing the CRC TME slides, and for responding to our pathological enquiries. Their input was essential for this research. Additionally, I wish to express my gratitude to members of the Akoya Bioscience technical Support Team, particularly Adam Dickinson, for his thorough response and invaluable assistance in optimizing the mIHC panel and addressing troubleshooting.

I would also like to acknowledge my PhD friends and colleagues: Zhyuian Cheng, Shakhnoza Jumaniyazova, and Qianya Xu. Their help during the initial training, alongside the shared experiences and delightful moments we enjoyed, truly made this journey smoother and brighter. A special note of heartfelt thanks goes to my dear friend, Gaye Pisiren, for the shared laughter and unwavering personal support that meant so much.

To my love, Farzan Falahat, my heartfelt thanks. His sincere partnership throughout this journey—encompassing both emotional and personal support, and patient troubleshooting of R codes—was invaluable. His support was truly indispensable throughout this journey. Moreover, my deepest appreciation goes to my parents. Their constant love and solid support, sent across the distance, have been my bedrock and have made all this possible. This accomplishment is built upon the foundation they provided.

Finally, I thank myself for not giving up and for continuing to pursue my dreams.

Contents

Contents.....	v
List of Figures.....	vii
List of tables	xiii
1 Chapter 1: Introduction	1
1.1. Colorectal cancer	1
1.1.1 Epidemiology	1
1.1.2 Origin and Etiology	1
1.2 Tumour Microenvironment.....	5
1.2.1 Tumour Immune Microenvironment:.....	6
1.2.2 Immunoscore	9
1.2.3 Macrophage.....	12
1.2.4 T cell	18
1.2.5 Exhaustion.....	20
1.3 Hypotheses and Aims.....	28
1.3.1 Hypothesis	28
1.3.2 Aims.....	29
2 Chapter 2: Materials and Methods.....	30
2.1 Patients.....	30
2.2 TMA slide preparation.....	34
2.3 Chromogenic IHC	35
2.4 Multiplex IHC (mIHC).....	37
2.5 Library slides preparation	39
2.6 Image acquisition, Scanning, and InForm training.....	40
2.7 Drop-out and stripping efficiency test.....	40
2.8 Statistical analysis	41
3 Chapter 3: Result	44
3.1 Optimizing mIHC panel.....	44

3.1.1	TIM3 Ab optimization	44
3.1.2	LAG3 Ab Optimization	51
3.1.3	PD1 Ab Optimization	58
	Multiplex panel Optimization	60
3.2	Library slides	77
3.3	Staining and Scanning	79
3.4	Initial InForm training output	80
3.5	Analysis of the result of multiplex panel	82
3.5.1	Cell density analysis within tumour related cores, including IM, CT, and LS	82
3.5.2	Correlation analysis	90
3.5.3	Comparison of cell density between adjacent normal and tumour regions .	95
3.5.4	Neighborhood analysis with Cytomap.....	128
3.5.5	Survival analysis regarding the cell density.....	130
3.5.6	Prognostic impact of T cell and macrophage density across different tumour regions	143
3.5.7	On the relationship between TNM stage and infiltration by T-cells and macrophage	151
3.5.8	Tumour sidedness impact on CD3+ and CD68+ cell densities and prognosis	160
3.5.9	MMR status and immune infiltration	166
4	Chapter5: Discussion.....	173
4.1	Intraepithelial CD3 is a strong prognostic factor regarding all variables in CRC tumour microenvironment.	177
4.2	CD68 marker in the right sided CRC of all stages can be prognostic factor	179
4.3	Impact of the location:	180
4.4	Impact of the sidedness:	182
4.5	Impact of MMR status:.....	184
4.6	Impact of TNM stage:.....	185
5	Chapter6: Reference	191

List of Figures

Figure 1. CRC Progression from Polyp to Adenocarcinoma.	3
Figure 2. CRC Classifications.	4
Figure 3. Mismatch Repair (MMR) System Function and Assessment.	8
Figure 4. Immune Landscape of CRC and its Association with Prognosis.	11
Figure 5. CD68 Expression, Ligands, and Function.	13
Figure 6. Macrophage Polarization Pathways.	14
Figure 7. Macrophage Development and TAM Main Functions.	17
Figure 8. T Cell Development, Maturation, and Activation within the Hematopoietic Niche.	19
Figure 9. Exhaustion Markers: Structure, Ligands, and Function in Immune and Tumour Cells.	23
Figure 10. Schematic illustration of CRC sidedness and staging (Stages 0-IV), based on the TNM classification.	31
Figure 11. Tissue Cores from Four Patients with Colorectal Cancer.	32
Figure 12. Workflow and Principles of Chromogenic Immunohistochemistry (IHC) and mIHC for Tissue Analysis.	36
Figure 13. Schematic diagram of a final optimised six-cycle mIHC protocol for staining of FFPE human CRC tissue sections.	38
Figure 14. Schematic diagram of single-plex staining procedures for generating a spectral library.	39
Figure 15. High background staining observed with overnight incubation of TIM3 antibody in a mIHC panel on human CRC tissue from two cores (patients).	45
Figure 16. Comparison of TIM3 IHC staining in human CRC tissue (one patient) using antigen retrieval buffers at pH 6 and pH 9, showed PH9 as the optimized PH.	47
Figure 17. High background observed with overnight incubation of TIM3 antibody on human CRC tissue (one core).	47
Figure 18. TIM3 IHC staining on CRC human tissue sections using a 1-hour incubation at room temperature and pH 9 antigen retrieval in different cores (patients).	48
Figure 19. Dropout test demonstrated signal carry-over in a two-cycle mIHC experiment targeting TIM3 on CRC tissue sections.	49
Figure 20. Evaluation of microwave-based antibody stripping efficiency in a mIHC panel using a TIM3 antibody on CRC tissue sections in different patient samples (Cores).	50
Figure 21. High background staining observed with overnight incubation of LAG3 antibody in a mIHC panel on human CRC tissue in one core (patient).	51
Figure 22. Optimization of pH for LAG3 IHC Staining in Colorectal Cancer in two different cores (patients) showed PH9 as the optimized PH.	52
Figure 23. Overnight Incubation for LAG3 IHC in a CRC core (patient).	53
Figure 24. Subcellular Localization of LAG3 (1:100. PH:9, 1h incubation) in CRC Tissue as Demonstrated by Chromogenic IHC in different cores (patients).	54

Figure 25. Dropout test demonstrated signal carry-over in a two-cycle IHC experiment targeting LAG3 on FFPE human CRC cores.	55
Figure 26. Optimization of Opal 480 concentration for LAG3 detection in a mIHC panel on human CRC tissue sections in different cores (patients).....	56
Figure 27. mIHC optimization of human CRC tissue showing high background of PD1, LAG3, and TIM3 in initial panels in one core.....	58
Figure 28. Optimization of PD1 (1:200, PH:9, 1h incubation) immunohistochemical staining in human CRC tissue sections in different cores (patients) reveals cytoplasmic/membrane staining in immune cells and possible nuclear staining in tumour cells.	59
Figure 29. Optimization of a six-plex immunofluorescence panel for human CRC tissue sections.	62
Figure 30. Representative images of TIM3 (Opal 690) expressions in human CRC tissue sections in different cores (patients) stained with the optimized mIHC panel (Table 4).	63
Figure 31. Representative images of PD1 (Opal 570) expression in human CRC tissue sections in different cores (patients) stained with the optimized mIHC panel (Table 4).	64
Figure 32. Representative images of LAG3 (Opal 480) expression in human CRC tissue sections in different cores (patients) stained with the optimized mIHC panel (Table 4).	65
Figure 33. Representative images of CD3 (Opal 620) expression in human CRC tissue sections in different cores (patients) stained with the optimized mIHC panel (Table 4).	66
Figure 34 . Representative images of CD68 (Opal 520) expression in human CRC tissue sections in different cores (patients) stained with the optimized mIHC panel (Table 4).	67
Figure 35. Representative images of CK (Opal 780) expression in human CRC tissue sections in different cores (patients) stained with the optimized mIHC panel (Table 4).	68
Figure 36. Nuclear expression of TIM3 and PD1 in Cytokeratin-positive (CK+) epithelial cells in human CRC tissue sections in different cores (patients) stained with the optimized multiplex panel (Table 4).....	69
Figure 37. Co-expression of TIM3 and CD68 on macrophages in human CRC tissue sections in two different cores as demonstrated by the optimized mIHC panel (Table 4).	70
Figure 38. Co-expression of TIM3 and LAG3 on a CD3 cell in human CRC tissue section in one core (patient) stained with the optimized mIHC panel (Table 4).	71
Figure 39. Co-expression of TIM3 and CD68 on macrophages in human CRC tissue section in one core (patient) stained with mIHC panel (table 4).	72
Figure 40. Spatial distribution and co-localization of multiple immune markers in human CRC tissue section in one core (patient) stained with the optimized mIHC panel (Table 4).....	73
Figure 41. Co-expression of immune markers CD3, LAG3 and TIM3 on lymphocyte and CD68 expressing macrophages in human CRC tissue section in one core (patient) stained with the optimized mIHC panel (Table 4).....	74
Figure 42. Co-expression of immune checkpoint markers PD1 and TIM3 on lymphocytes within human CRC tissue section in one core (patient) stained with the optimized mIHC panel (Table 4).	75
Figure 43. Co-localization of T-cells and macrophages with PD1-expressing cells in human CRC tissue section in one core (patient) stained with the optimized mIHC panel (Table 4).	76
Figure 44. Co-expression of PD1 with T-cell and macrophage markers in a region of high immune infiltration in human CRC tissue section in one core (patient) stained with the optimized mIHC panel (Table 4).....	77
Figure 45. Single-channel images of a spectral library slide prepared for mIHC with an anti-CD8 antibody (each core belongs to a sperate slide).	78

Figure 46. Overview of the Workflow for Multiplex Immunohistochemical Analysis of CRC Tissue Microarrays.	79
Figure 47. Schematic diagram illustrating the cell phenotypes identified and quantified using InForm software, categorized into Macrophages, T cells, Epithelial cells, and Other cell types, based on marker expression.	80
Figure 48. InForm image analysis workflow for adaptive tissue segmentation, cell segmentation, and phenotyping of mIHC images of human CRC tissue sections in three different cores (patients) stained with the optimized mIHC panel (Table 4).	81
Figure 49. Differential densities of immune cell subsets and epithelial cells between stromal and intraepithelial regions in human CRC tissue sections showing higher density of cells in stromal compartment compared to intraepithelial compartments.	82
Figure 50. Significantly higher densities of both exhausted and non-exhausted CD3+ cells in the stromal compartment compared to the intraepithelial regions of human CRC tissue sections.	84
Figure 51. Densities of CD3+ cell phenotypes expressing exhaustion markers in stromal and intraepithelial regions of human CRC tissue sections.	85
Figure 52. Higher Density of macrophages in stromal compartment compared to Intraepithelial compartments.	86
Figure 53. Densities of macrophage expressing immune checkpoint inhibitors (IR) in stromal and Intraepithelial regions of human CRC tissue sections.	87
Figure 54. Comparison of exhaustion marker cell densities between CD3+ and CD68+ cells showed higher Tim3 on macrophages compared to T cells.	88
Figure 55. The percentage of different phenotypes of macrophage according to the Inform training.	89
Figure 56. The percentage of different phenotypes of CD3 cells according to the Inform training.	90
Figure 57. Spearman rank correlation matrix of cell densities showing the correlation between exhausted T cells and IR+ macrophages.	92
Figure 58. There is a positive correlation between CD3.ex and Total CD3 cells.	93
Figure 59. There is weak positive correlation between stromal CD68.IR+ and total CD68 in the stromal compartment.	94
Figure 60. Comparison of non-exhausted CD3 cell densities in stroma and intraepithelial regions of adjacent normal and tumour-related cores showed a higher density of T cells in intraepithelial compartment of adjacent normal compared to tumor related cores.	96
Figure 61. Heatmap of non-exhausted CD3+ cell density in colorectal cancer.	97
Figure 62. Spearman correlation analysis of CD3.non.ex densities within the tumour microenvironment of colorectal cancer, performed on the entire patient cohort.	98
Figure 63. Higher density of CD3.ex in the stromal compartment of tumor related cores compared to adjacent normal.	99
Figure 64. Heatmap of exhausted CD3+ cell density in colorectal cancer.	100
Figure 65. Spearman correlation analysis of CD3.ex densities within the tumour microenvironment of colorectal cancer, performed on the entire patient cohort.	101
Figure 66. Comparison of PD1+ CD3 cell densities in Stroma and intraepithelial Regions of Adjacent Normal and Tumour-Related Cores.	102
Figure 67. Heatmap of PD1+ CD3+ cell density in colorectal cancer.	103
Figure 68. Spearman correlation analysis of PD1+CD3 densities within the tumour microenvironment of colorectal cancer, performed on the entire patient cohort.	104

Figure 69. Higher density of stromal Tim3+ CD3 cells in tumor related cores compared to adjacent normal.....	105
Figure 70. Heatmap of TIM3+ CD3+ cell density in colorectal cancer.....	106
Figure 71. Spearman correlation analysis of TIM3+CD3 densities within the tumour microenvironment of colorectal cancer, performed on the entire patient cohort.	107
Figure 72. Comparison of LAG3+ CD3 cell densities in stroma and intraepithelial regions of adjacent normal and tumour-related cores.	108
Figure 73. Heatmap of LAG3+ CD3+ cell density in colorectal cancer.	109
Figure 74. Spearman correlation analysis of LAG3+CD3 densities within the tumour microenvironment of colorectal cancer, performed on the entire patient cohort.	110
Figure 75. Higher density of TIM3+PD1+ CD3 cell densities in stromal compartment of tumor related cores compared to adjacent normal.	111
Figure 76. Heatmap of TIM3+PD1+ CD3+ cell density in colorectal cancer.....	112
Figure 77. Spearman correlation analysis of TIM3+PD1+ CD3 densities within the tumour microenvironment of colorectal cancer, performed on the entire patient cohort.....	113
Figure 78. Higher density of macrophages (Excluding IR+ cells) in stromal and intraepithelial regions of tumour-related cores compared to adjacent normal.....	114
Figure 79. Heatmap of IR- macrophage cell density in colorectal cancer.....	115
Figure 80. Spearman correlation analysis of CD68.IR negative densities within the tumour microenvironment of colorectal cancer, performed on the entire patient cohort.....	116
Figure 81. Comparison of macrophage densities (IR+ cells) in stromal and intraepithelial regions of adjacent normal and tumour-related cores of human CRC tissue sections.	117
Figure 82. Heatmap of macrophage (IR+) cell density in colorectal cancer.	118
Figure 83. Spearman correlation analysis of IR+CD68 macrophage densities within the tumour microenvironment of colorectal cancer, performed on the entire patient cohort.....	119
Figure 84. Comparison of PD1+ macrophage cell densities in stromal and intraepithelial regions of adjacent normal and tumour-related cores.	120
Figure 85. Heatmap of PD1+ macrophage cell density in colorectal cancer.	121
Figure 86. Spearman correlation analysis of PD1+ CD68. densities within the tumour microenvironment of colorectal cancer, performed on the entire patient cohort.	122
Figure 87. Comparison of CD68 expressing TIM3 cell densities in Stroma and Tumour Regions of Adjacent Normal and Tumour-Related Cores.....	123
Figure 88. Heatmap of macrophage expressing TIM3 density in colorectal cancer.....	124
Figure 89. Spearman correlation analysis of TIM3+ macrophage densities within the tumour microenvironment of colorectal cancer, performed on the entire patient cohort.....	125
Figure 90. Higher density of TIM3+ PD1+ macrophages densities in stromal and intraepithelial compartments of adjacent normal compared to tumour related cores.	126
Figure 91. Heatmap of macrophage expressing TIM3/ PD1 density in colorectal cancer.	127
Figure 92. Spearman correlation analysis of TIM3+/PD1 macrophage densities within the tumour microenvironment of colorectal cancer, performed on the entire patient cohort.....	128
Figure 93. Cytomap analysis of spatial heterogeneity in human CRC tissue sections. (A) Determination of optimal cluster number identified 5 clusters.	129
Figure 94. Fold-change in cell population densities across five distinct regions in human CRC tissue sections showing 5 different regions.	130
Figure 95. Total CD3 cells correlated with improved survival.	131

Figure 96. Kaplan-Meier survival curves for overall survival stratified by stromal CD3+ cell density showed intraepithelial CD3 cells correlated with improved survival.	132
Figure 97. Kaplan-Meier survival curves for overall survival stratified by intraepithelial CD3+ subpopulation showed PD+ CD3 cells correlated with improved survival, although stromal Tim3+ T cells correlated with reduced survival.	133
Figure 98. Kaplan-Meier survival curves for overall survival stratified by intraepithelial CD3+ subpopulation cell density showed PD1+Tim3+ T cells correlated with reduced survival.	134
Figure 99. Kaplan-Meier survival curves for overall survival stratified by CD68+ cell density in stromal and intraepithelial compartments showed that total CD68 does not correlate with survival.	136
Figure 100. Kaplan-Meier survival curves for overall survival stratified by CD68+ IR+ macrophage subsets in stromal and intraepithelial compartments showed that Tim3 macrophages correlated with reduced survival.	138
Figure 101. Multivariable cox proportional hazards regression analysis of overall survival in CRC patients showed that total intraepithelial CD3 acts as an independent prognostic factor.	140
Figure 102. Multivariable cox proportional hazards regression analysis of overall survival in CRC patients showed that Tim3+ T cells and Tim3+PD1+ T cells acts as an independent prognostic factor.	141
Figure 103. Multivariable cox proportional hazards regression analysis of overall survival in CRC patients showed no independent prognostic impact for total macrophages.	142
Figure 104. Multivariable cox proportional hazards regression analysis of overall survival showed that Tim3+ macrophages and Tim3+ PD1+ macrophages act as an independent prognostic factor. ...	143
Figure 105. Kaplan-Meier survival curves for CRC patients stratified by stromal CD3+ cell densities in different tumour regions showed that Invasive margin has the most prognostic impact.	144
Figure 106. Kaplan-Meier survival curves for CRC patients stratified by intraepithelial CD3+ cell densities in different tumour regions showed that luminal side has the lowest prognostic impact.	145
Figure 107. Kaplan-Meier survival curves for CRC patients stratified by stromal CD3+ subpopulation densities in different tumour regions showed that location has an impact on the survival impact.	146
Figure 108. Kaplan-Meier survival curves for CRC patients stratified by intraepithelial CD3+ subpopulation densities in different tumour regions showed that location has an impact on the survival impact.	148
Figure 109. Kaplan-Meier survival curves for CRC patients stratified by stromal CD68+ subpopulation densities in different tumour regions showed that location has an impact on the survival impact.	149
Figure 110. Kaplan-Meier survival curves for CRC patients stratified by intraepithelial CD68+ subpopulation densities in different tumour regions showed that location has an impact on the survival impact.	151
Figure 111. distribution of stromal CD3+ T Cell subset densities across TNM Stages in colorectal cancer showed higher density of CD3 cells in early stages compared to advanced stages.	152
Figure 112. Distribution of intraepithelial CD3+ T Cell subset densities across TNM stages in colorectal cancer showed higher density of CD3 cells in early stages compared to advanced stages.	153
Figure 113. Distribution of stromal CD68+ cell subset densities across TNM stages in colorectal cancer showed there is almost no difference in the density of macrophages between early and advanced stages.	154

Figure 114. Distribution of intraepithelial CD68+ cell subset densities across TNM Stages in colorectal cancer showed there is almost no difference in the density of macrophages between early and advanced stages.	155
Figure 115. Kaplan-Meier survival curves for overall survival stratified by CD3+ cell density in stromal and intraepithelial compartments of patients with low stage (I, II) and high stage (III, IV) CRC showing there is no impact of tumour stage on CD3 prognostic impact between early and advanced stages.	156
Figure 116. Kaplan-Meier survival curves for overall survival stratified by CD3+ subpopulation cell density in stromal and intraepithelial compartments of patients with low stage (I, II) and high stage (III, IV) CRC showing PD1 CD3 cells in early stage not in the advanced stage of CRC correlated with reduced survival.	157
Figure 117. Kaplan-Meier survival curves for overall survival stratified by CD68+ cell density in stromal and intraepithelial compartments of patients with low stage (I, II), stage (III, IV) CRC showing that Tim3 macrophages in the advanced stages, but not early stages correlated with reduced survival.	159
Figure 118. Comparison of CD3 cell densities in Stroma and intraepithelial Regions of Right and left sided CRC showing there is higher density of exhausted CD3 cells on the right sided compared to left sided.	161
Figure 119. Comparison of macrophage cell densities in stromal and intraepithelial regions of right and left sided CRC showing there is no difference in macrophage density between right and left CRC.	162
Figure 120. Kaplan-Meier survival curves for overall survival stratified by CD3+ cell density in stromal and intraepithelial compartments of patients with right and left-sided colorectal CRC showing right-CRC provides more prognostic information compared to left-CRC.	163
Figure 121. Kaplan-Meier survival curves for overall survival stratified by CD3.ex sub population density in stromal and intraepithelial compartments of patients with Right and Left -sided CRC showing right-CRC provides more prognostic information compared to left-CRC.	164
Figure 122. Kaplan-Meier survival curves for overall survival stratified by CD68+ cell density in stromal and intraepithelial compartments of patients with Right and Left-sided CRC showing right-CRC provides more prognostic information compared to left-CRC.....	165
Figure 123. Comparison of CD3 cell densities in stromal and intraepithelial regions of MSS/MSI CRC showing MSI-CRC has significant higher CD3 density compared to MSS-CRC	167
Figure 124. Comparison of macrophage densities in stromal and intraepithelial regions of MSS/MSI CRC showing there is almost no difference in the density of macrophages between MSS and MSI-CRC.	168
Figure 125. Kaplan-Meier survival curves for overall survival stratified by CD3+ cell density in stromal and intraepithelial compartments of patients with MSS and MSI CRC showing exhausted CD3 cells in MSS -CRC but not MSI-CRC correlated with reduced survival.	169
Figure 126. Kaplan-Meier survival curves for overall survival stratified by CD3+ subpopulation cell density in stromal and intraepithelial compartments of patients with MSS and MSI CRC showing Tim3+ T cells in MSS-CRC, but not in MSI-CRC correlated with reduced survival.	171
Figure 127. Kaplan-Meier survival curves for overall survival stratified by CD68+ cell density in stromal and intraepithelial compartments of patients with MSS and MSI-CRC showing MSS-CRC provide more prognostic impact compared to MSI-CRC.	172

Figure 128. Summary of associations between CD3+ subset densities and survival in colorectal cancer, stratified by location, TNM stage, MMR status, sidedness, and compartment. 174

Figure 129. Summary of associations between macrophage subset densities and survival in colorectal cancer, stratified by location, TNM stage, MMR status, sidedness, and compartment. 175

Figure 130. Significant Differences in Cell Density of CD3+ Cells and Macrophages in Colorectal Cancer. 176

List of tables

Table 1. Summary of Hereditary Syndromes Linked to CRC Risk.2

Table 2. Frequently Mutated Genes in CRC.7

Table 3. Summary of the clinicopathological characteristics of the patient cohort. 33

Table 4. Antibody and Opal Reagent Incubation Details for the Optimized mIHC Panel in Human CRC Tissue Sections. 62

Table 5. Signal and background statistics for the optimized mIHC panel in human CRC tissue sections. 62

Abbreviation:

A

Ab: Antibody

AD: Autosomal Dominant

ADAM: A Disintegrin And Metalloprotease

Ag: Antigen

AKT: Ak Strain Transforming (protein kinase B)

AR: Autosomal Recessive

a-Syn: Alpha-Synuclein

B

BAT3: B-Associated Transcript 3

BM: Bone Marrow

BMPRI1A: Bone Morphogenetic Protein Receptor Type 1A

BRRS: Bannayan-Riley-Ruvalcaba Syndrome

C

CEACAM1: Carcinoembryonic Antigen- Related Cell Adhesion Molecule 1

CCL: CC-Chemokine Ligands

CD: Cluster Of Differentiation

CIMP: CPG Island Methylator Phenotype

CIN: Chromosomal Instability

CHRPE: Congenital Hypertrophy of The Retinal Pigment Epithelium

CK: Cytokeratin

CLL: Chronic Lymphocytic Leukemia

CMMRD: Constitutional Mismatch Repair Deficiency

CRC: Colorectal Cancer

CS: Cowden Syndrome

CSF: Colony Stimulating Factor 1

CT: Core Of the Tumour

CTLA: Cytotoxic T-Lymphocyte Antigen 4

CXCL: C-X-C Motif Chemokine Ligand

CXCR: Chemokine Receptor

D

DAPI: 4',6-Diamidino-2-Phenylindole

DC: Dendritic Cell

DLBCL: Diffuse Large B-cell lymphoma

DNA: Deoxyribonucleic Acid

DPX: Dibutylphthalate Polystyrene Xylene

E

EALS: EPCAM-Associated Lynch Syndrome

EDTA: Ethylene Deaminate Tra Acetic Acid

EGFR: Epidermal Growth Factor Receptor

EMT: Epithelial-Mesenchymal Transition

EPCAM: Epithelial Cell Adhesion Molecule

F

FAP: Familial Adenomatosis Polyposis

FFPE: Formalin-Fixed Paraffin-Embedded

FGL-1: Fibrinogen-Like Protein 1

Fyn: Fyn Tyrosine Kinase

G

Gal-3: Galectin-3

GI: Gastrointestinal

GM-CSF: Granulocyte-Macrophage Colony-Stimulating Factor

GS: Gorlin Syndrome

GVHD: Graft Versus Host Disease

H

HCT-8: Human Ileocecal Colorectal Adenocarcinoma Cells

HIV: Human Immunodeficiency Virus

HLA: Human Leukocyte Antigen

HMGB1: High Mobility Group Box 1

HMPS: Hereditary Mixed Polyposis Syndrome

HNPCC: Hereditary Nonpolyposis Colorectal Cancer

HSC: Hematopoietic Stem Cell

I

IDO: Indoleamine 2,3-Dioxygenase

IFN: Interferon

IHC: Immunohistochemistry

IL: Interleukin

IM: Invasive Margin

ITIM: Immunoreceptor Tyrosine-Based Inhibitory Motif

ITSM: Immunoreceptor Tyrosine-Based Switch Motif

J

JAK: Janus Kinase

JP: Juvenile Polyposis

K

L

LAG3: Lymphocyte Activation Gene 3

LAMP4: Lysosome-Associated Membrane Protein 4

LCMV: Chronic Lymphocytic Choriomeningitis Virus

LIF: Leukemia Inhibitory Factor

LKB1/STK11: Liver Kinase B1/ Serine-Threonine Kinase 11

LPS: Lipopolysaccharide

LS: Lynch Syndrome

LSEctin: Liver and Lymph Node Sinusoidal Endothelial Cell C-type Lectin

M

mAb: Monoclonal Antibody

MAC: Macrophage

MAP: MUTYH-Associated Polyposis

MCP-1: Monocyte Chemoattractant Protein-1

MDSC: Myeloid Derived Suppressor Cells

mIHC: Multiplex Immunohistochemistry

MHC: Major Histocompatibility Complex

MIP: Macrophage Inflammatory Protein

Mir: MicroRNA

MMR: Mismatch Repair

MPS: Mononuclear Phagocytic System

MSI: Microsatellite Instability

MSH2: MutS Homolog 2

MSH6: MutS Homolog 6

MSS: Microsatellite Stable

mTOR: Mammalian Target Of Rapamycin

MUTYH: MutY DNA Glycosylase

N

NADPH: Nicotinamide Adenine Dinucleotide Phosphate

NK: Natural Killer Cell

NKT: Natural Killer T Cells

NOS: Nitric Oxide Synthase

O

Ox-LDL: Oxidized Low-Density Lipoprotein

P

PD-1: Programmed Cell Death Protein 1

PD-L1/2: Programmed Cell Death Ligand 1/2

PGE2 : Prostaglandin E2

PI3K: Phosphoinositide-3 Kinase

PMN: Polymorphonuclear Leukocyte

POLD1: Polymerase Delta 1, Catalytic Subunit

POLE: Polymerase Epsilon, Catalytic Subunit

PPAP: Polymerase Proofreading-Associated Polyposis

PS: Peutz-Jeghers Syndrome,

PS: Phosphatidylserine

PTEN: Phosphatase and Tensin Homolog,

PtSer: Phosphatidylserine

R

RNF43: Ring Finger Protein 43

ROS: Reactive Oxygen Species

S

SCAD1: Scavenger Receptor Class D-Member 1

SMAD4: SMAD Family Member 4

STAT: Signal Transducer And Activator Of Transcription

T

TAM: Tumour Associated Macrophages

TBST: Tris-Buffered Saline With Tween 20

TCR: T Cell Receptor

TFH: Follicular Helper T cell

TGF: Transforming Growth Factor

Th: T Helper

THP-1: Tohoku Hospital Pediatrics-1(macrophage cell line)

TIM3: T-cell Immunoglobulin and Mucin-domain containing-3

TLR: Toll-Like Receptor

TMA: Tissue Microarray

TME: Tumour Microenvironment

TNF: Tumour Necrosis Factor

TNM: Tumour, Node, Metastasis

TSG: Tumour Suppressor Genes

Treg: T regulatory cells

V

VEGF: Vascular Endothelial Growth Factor.

W

WNT: Wiggless-Related Integration Site

Chapter 1: Introduction

1.1. Colorectal cancer

1.1.1 Epidemiology

Colorectal cancer (CRC) is the third most common cancer and the second leading cause of cancer-related death worldwide [1]. The incidence of CRC is significantly higher in developed countries compared to less developed regions [2]. While individuals over 50 face a greater risk, with over 90% of cases occurring in this age group, there has been an alarming increase in CRC incidence in recent years, particularly among younger populations [3].

1.1.2 Origin and Etiology

Based on the presence of adenomatous polyps (sessile lesions found in the luminal part of the colorectum), there are two main classes of hereditary CRC, including the category of hereditary nonpolyposis colorectal cancer or Lynch syndrome (HNPCC), and the category of familial adenomatous polyposis (FAP). In the category of FAP, one or more polyps in the absence of surgery develop into adenocarcinoma [4]. However, in HNPCC, previously known as Lynch syndrome, no polyps grow into adenocarcinoma, and they account for about 3 per cent of CRC [5]. This category usually involves the right cecum and colon.

Polyps' development into CRC adenocarcinoma takes several years via the accumulation of different genetic and epigenetic modifications [6]. Accumulated mutational burden (Table 1) contributes to significant inter-polyp heterogeneity within individuals, with only a limited subset of polyps progressing to CRC adenocarcinoma, Figure 1 [7].

Table 1. Summary of Hereditary Syndromes Linked to CRC Risk.

This table details the syndrome name, affected gene(s), inheritance pattern (AD: Autosomal Dominant, AR: Autosomal Recessive), and key clinical manifestations. BMPR1A; Bone Morphogenetic Protein Receptor Type 1A, BRRS; Bannayan-Riley-Ruvalcaba Syndrome, CS; Cowden syndrome, GS; Gorlin syndrome, PS; Proteus-like syndromes, CHRPE: Congenital Hypertrophy of the Retinal Pigment Epithelium, CMMRD; Constitutional Mismatch Repair Deficiency, CRC; Colorectal Cancer, EALS; EPCAM-associated Lynch Syndrome, EPCAM; Epithelial Cell Adhesion Molecule, FAP; Familial Adenomatous Polyposis, GI; Gastrointestinal, HMPS; Hereditary Mixed Polyposis Syndrome, JP; Juvenile Polyposis, LKB1/STK11; Liver Kinase B1/ Serine-Threonine Kinase 11, LS: Lynch Syndrome MAP; MUTYH-Associated Polyposis, MLH1; MutL Homolog 1, MMR; Mismatch Repair, MSH2; MutS Homolog 2, MSH6; MutS Homolog 6, MUTYH; MutY DNA Glycosylase, PMS2; PMS1 Homolog 2, Mismatch Repair System Component, POLD1; Polymerase Delta 1, Catalytic Subunit, POLE; Polymerase Epsilon, Catalytic Subunit, PPAP; Polymerase Proofreading-Associated Polyposis, PS; Peutz-Jeghers Syndrome, PTCH, Patched 1, PTEN: Phosphatase and Tensin Homolog, RNF43; Ring Finger Protein 43, SMAD4: SMAD Family Member 4.

	Name	Affected gene	Inheritance	Clinical manifestation
Inherited polyposis syndrome and associated spectra	FAP	APC	AD	Benign soft tissue tumour, CHRPE
	MAP, MUTYH-associated polyposis;	MUTYH	AD	CRC-proximal colon, mucin, lymphocyte infiltration
	PPAP, polymerase-proofreading-associated polyposis	POLE, POLD1	AD	Lynch syndrome-like phenotype in a minority
	Sessile polyposis	RNF43	AD	≥5, >rectum (≥2, ≥10 mm), ≥20 (≥5, >rectum)
	PS	LKB1/ STK11	AD	Mucocutaneous pigmented macules
	JP, Juvenile polyposis	SMAD4, BMPR1A	AD	≥5, extra bowel JP, family history
	PHTS, PTEN hamartoma tumour syndrome	PTEN, PTCH	AD	Several syndromes including BRRS, CS, GS, PS.
	HMPS, hereditary mixed polyposis.	SCG5/GREM1	AD	Adenoma, serrated/inflammatory polyp
Lynch syndrome and associated spectra	LS	MMR genes: MLH1, MSH2, MSH6, PMS2	AD	
	Muir-Torre	<i>MMR</i> genes and <i>MUTYH</i>	65% AD (35%, AR)	
	CMMRD, constitutional MMR deficiency	PMS2, MSH6	AD	
	EALS, EPCAM-associated LS	<i>EPCAM</i> , <i>MSH2</i> silencing		congenital tufting enteropathy
	familial colorectal cancer type X.	Unidentified genes		site-specific distal CRC
	Tucket syndrome	MLH1/ PMS2/APC	AR	

"Adenocarcinoma" and "Cancer"

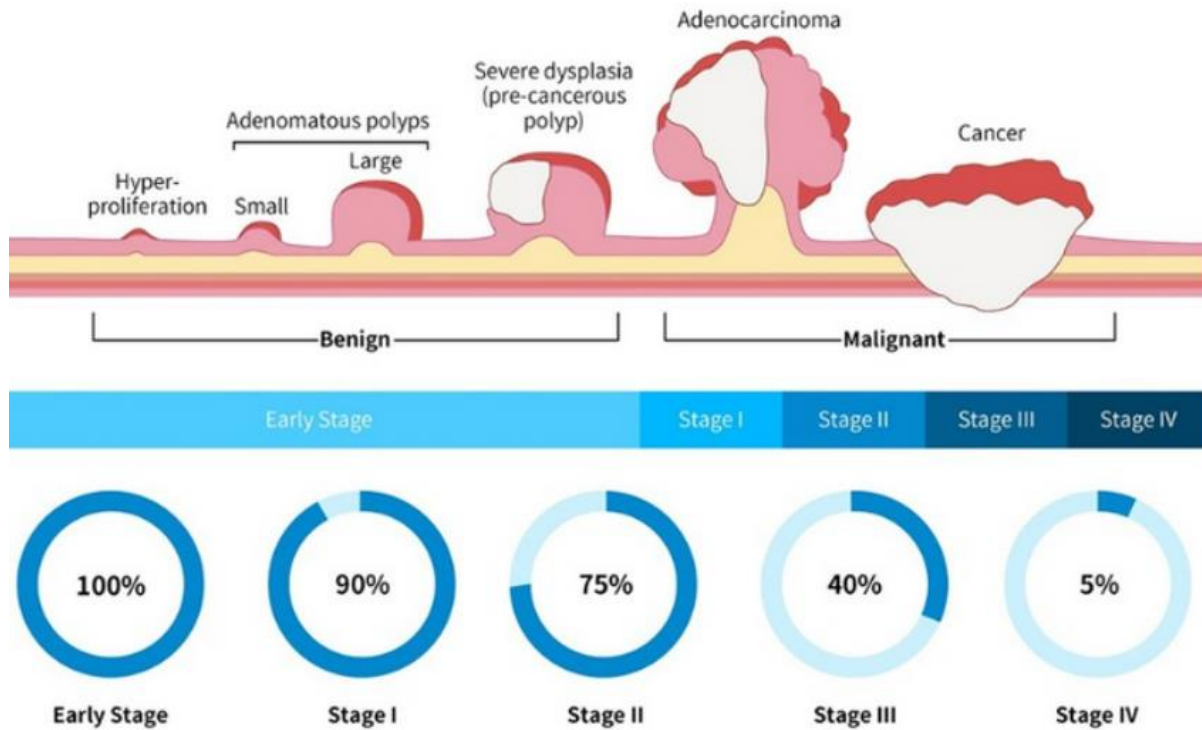


Figure 1. CRC Progression from Polyp to Adenocarcinoma.

This diagram illustrates the stages of CRC development, beginning with small, benign polyps that can progress to larger adenomatous polyps (less than 1cm) and then to advanced adenomas (greater than 1cm). These advanced adenomas may develop into malignant adenocarcinoma (cancer). The percentages (from left to right: 100%, 90%, 75%, 40%, and 5%) represent the approximate proportion of individuals who will develop each respective stage in the absence of screening. [8]. The stages displayed in the image are Early Stage, Stage I, Stage II, Stage III and Stage IV. These are split into two categories: Benign (Early Stage) and Malignant (Stage I, Stage II, Stage III and Stage IV) [8].

1.1.2.1 CRC Classifications and survival

The TNM (tumour, node, metastasis) system is the most common system for determining the survival of cancer. The information at the time of tumour resection helps predict the tumour stage and the likely outcome of the tumour. The TNM system is based on the pathology of tumour at the time of resection, in which T showing the tumour size, N showing the involvement of lymph nodes and M showing the presence of metastasis. The higher degrees correlate with unfavorable outcomes. TNM system does not use other

techniques, such as molecular signatures and immunohistochemistry for classification, which can provide valuable information regarding tumour growth.

Several ways can be used to classify CRC's dynamic disease, which helps to provide a comprehensive understanding of its development and allows for personalized treatment approaches. Figure 2 shows different ways of CRC classifications. Histopathology-based classification provides a modest prognosis information [9]. Tumour location can provide different prognostic values, as left and right sides of colon have different embryonic origin and histology [8].

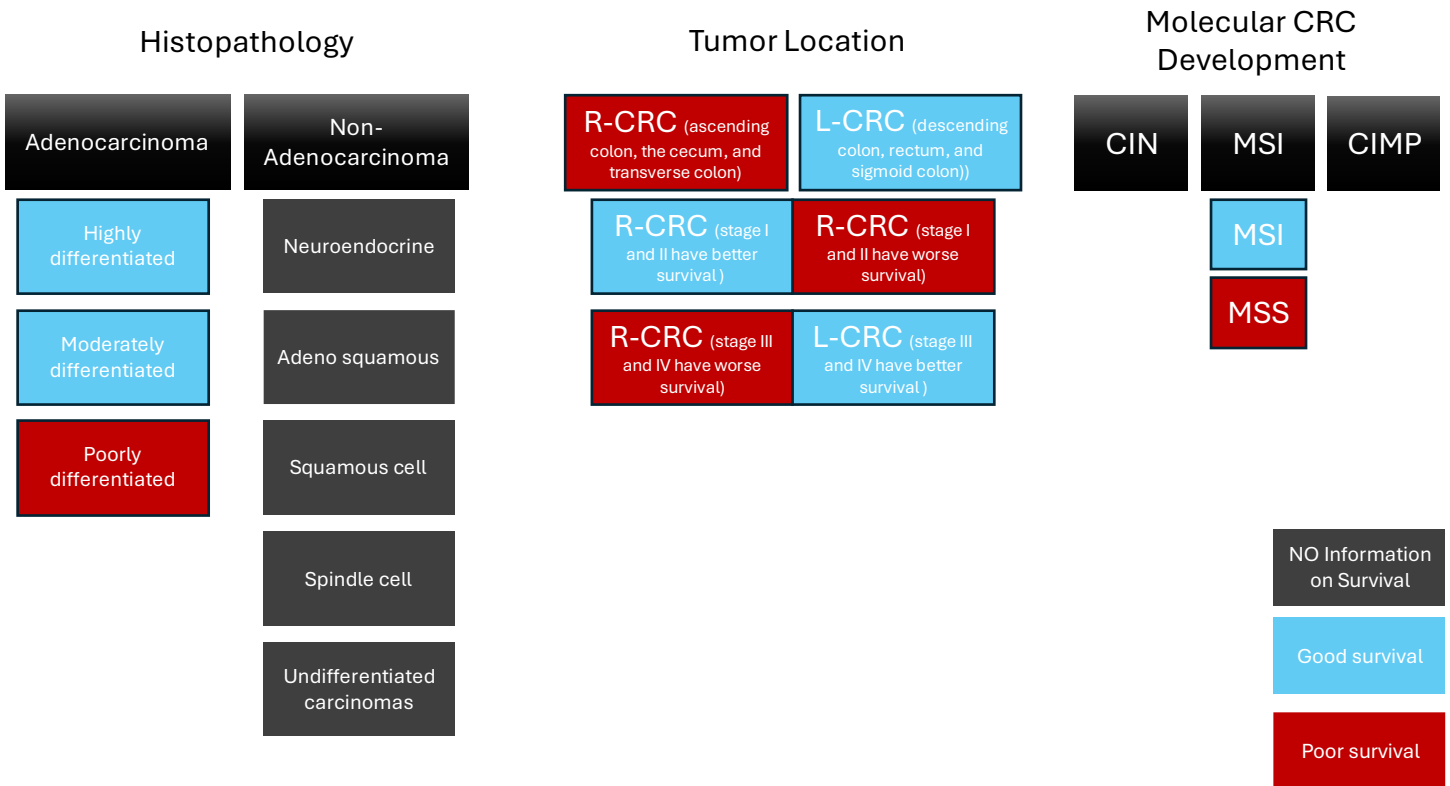


Figure 2. CRC Classifications.

This diagram illustrates three different ways to classify CRC: by histopathology (microscopic appearance of tumour cells), tumour location within the colon, and molecular subtype. Red boxes indicate a poorer prognosis, Blue boxes indicate a better prognosis, and Gray boxes indicate no information available. Histopathological classifications include adenocarcinoma (and its differentiation grades), neuroendocrine, adenosquamous, squamous cell, spindle cell, and undifferentiated carcinomas. Tumour location is divided into right-sided (R-CRC) and left-sided (L-CRC), with further prognostic distinctions based on disease stage. Molecular subtypes include chromosomal instability (CIN), microsatellite instability (MSI), CpG island methylator phenotype (CIMP), and microsatellite stable (MSS). Adapted from [8-10].

Molecular classification provides three different categories of CRC, including **Chromosomal instability (CIN)**, **Microsatellite instability (MSI)**, and CpG Island methylator phenotype (CIMP). **CIN** occurs due to a loss of function mutation in tumour suppressor genes (TSG) like AFP and P53 or gaining a function for an oncogene like KRAS genes [11]. As a result, newly formed tumour cells exhibit frequent genetic abnormalities. [12, 13]. FAP tumours and 80 per cent of sporadic CRC fall into CIN category [10]. **MSI** leads to the formation of tumour cells and results from mutations in mismatch repair (MMR) genes, including MLH1, MSH2, MSH6, and PMS2. The products of these genes participate in DNA repair and loss of their functionality results in a hypermutable phenotype in which there is a failure to fix errors in the repetitive elements of the genome [14]. About 15 per cent of sporadic tumours and Lynch syndrome tumours have MSI [15]. MSI provides valuable information regarding CRC prognosis in which MSI-positive adenocarcinoma has a more favorable response to immunotherapy, a poor response to 5-fluorouracil, and a better overall prognosis [16], **Figure 3**.

The third way of CRC formation is related to the **aberrant epigenetic modifications** which is called CpG Island methylator phenotype (CIMP). Although there is no mutation, the expression of TSGs, oncogenes, and MMR genes were changed due to aberrant methylation and acetylation [17]. Right-originated CRC are usually MSI and CIMP positive, while the left-originated CRC are mainly microsatellite stable (MSS) and CIMP negative [18-20].

None of these classifications match the statistical strength of TNM classifications. Nevertheless, the TNM system has faced challenges to its predictive accuracy as multiple patients with the same histological tumour stage showed opposing outcomes [21, 22]. This indicates the reliance of the TNM system on the tumour cells which ignores the fact that tumour progression is a dynamic process of tumour cell interaction with tumour microenvironment elements, including mesenchymal elements and the immune system which is a critical contributor in the patient survival.

1.2 Tumour Microenvironment

Tumour milieu, also known as TME, is a major contributing factor in developing CRC prognosis and survival and consists of tumour cells surrounded by stroma. The stroma is composed of connective tissue and cells other than tumour epithelial cells. The composition of the stroma has a huge impact on the thriving or evading of tumours in

which the interaction of different elements from immune cells, extracellular matrix and stromal cells, including fibroblasts, platelet, leukocytes, and endothelial cells can determine the fate of the disease [23, 24]. In other words, tumour cells not only influence the recruitment of cells present to the TME by releasing soluble messengers but can also be affected by the present cells and components in the TME through specific receptors and ligands [25]. The '**seed and soil**' hypothesis proposed by Paget in 1889, presented the concept of molecularly modified susceptible tumour cells as a seed that can only grow in a tumour-supporting TME. It has been documented that many reasons for treatment failure are rooted in overlooking the TME components and its development alongside tumour progression that brings further opportunities in disease-personalized treatment [26, 27].

1.2.1 Tumour Immune Microenvironment:

Modern classification of CRC in recent years has seen a considerable shift in the focus from cancer cells to the interplay between immune cells and cancer cells in the TME [28].

The complex bidirectional interaction between tumour cells and immune cells have established the concept of **cancer immunoediting** in which tumour cells can be suppressed, especially in initial phases of growth or paradoxically well survived and developed by immune cells [29]. Cancer immunoediting consisted of three phases, including elimination, equilibrium, and escape.

Elimination or immune surveillance is the first step of cancer immunoediting in which both innate and adaptive immunity try to kill tumour cells. If there is a failure in both recognition or killing the tumour cells, the long-lasting second step initiates and there is an equilibrium between anti-tumour functions and tumour growth. At this stage the tumour does not grow as the tumour cells are killed by immune cells, but immune cells can not destroy all the tumour cells [30]. During this step, new mutations gradually armor tumour cells to find immune escape strategies and even recruit immune cells to protect their growth through sculpting an immune suppressive tumour microenvironment [31]. Table 2 showing the frequent genes that are mutated in CRC [31, 32].

Table 2. Frequently Mutated Genes in CRC.

This table summarizes genes commonly mutated in CRC, categorized as either Tumour Suppressor Genes (TSGs) or Oncogenes. For each gene, the table provides its primary biological function, the type of mutation typically observed in CRC, and the approximate frequency of that mutation.

TSG				Oncogene			
Gene	Function	Type of mutation	Frequency	Gene	Function	Type of mutation	Frequency
APC	Wnt signaling inhibition	Frameshift, point mutation, deletion, allele loss	70-80%	KRAS	Cell proliferation and survival	Point mutation in codons 12,13,61	50-60%
TP53	Cell cycle arrest and apoptosis	Point mutation, allelic loss	50-60%	NRAS	Cell proliferation and survival	Point mutations in codons 12, 13, 61	<5%
FBXW3	Degrading target proteins	Nonsense, missense, deletion	20%	PIK3CA	Cell proliferation and survival	Point mutations in exon 9 and 20	15-25%
SMAD2	TGF-B intracellular signaling	Nonsense, missense, allele loss	5-10%	CTNNB1	Tumour growth and invasion	Point mutation, in frame deletions in N terminal	<5%
SMAD4	TGF-B intracellular signaling	Nonsense, missense, allele loss	10-15%	SOX9	Cell proliferation and stemness	Point mutations	4%
TCF7L2	Wnt signaling regulation	Frameshift, nonsense	5%	BRAF	Cell proliferation and survival	Point mutations in codon 600	46%
FAM123B	ECM transition	Nonsense mutation	7%				
ARID1A	Chromatin remodeling	Point mutation, deletion	5%				
ATM	Cell cycle arrest	Point mutation, deletion	7%				

Escape can occur in three main ways: Tumour cells decrease their immunogenicity. Secondly, recruit mechanisms to avoid immune response, or promote inflammation. Tumour cells evolve to become less visible to the immune system over time in two main ways. The immune system's natural ability to eliminate highly immunogenic tumour cells creates a selective pressure, allowing tumour cells with lower immunogenicity to thrive. These less conspicuous cells, which are better at evading immune detection, gain a growth advantage as their more recognizable counterparts are destroyed. In addition, tumour cells can actively develop mechanisms to suppress or tolerate the immune response, further enhancing their survival and contributing to the overall decrease in tumour immunogenicity [33]. In the second way, tumour cells downregulate the expression of high immunogenic antigen through different mechanisms, including hypermethylation of immunogenic antigens, or acquire gene mutations coding low immunogenic antigens [34]. For instance, longitudinal study in metastatic CRC showed that the end stage of diseases

is accompanied with mutations of low immunogenic antigens even in high infiltrating tumours showing the advantages of these antigens in tumour outgrowth [35]. Furthermore, there is lower antigen presentation in TME which is basically a result of downregulation of MHC molecules due to gene mutation or epigenetic modifications in CRC tumour cells [36, 37]. Tumour cells can also suppress dendritic cells via activation of WNT- β -catenin pathway leading to lower antigen presentation, as well [38]. In this stage, mutations in the MMR system also are expected.

The MMR system plays a crucial role in maintaining the stability of repeated elements of DNA like microsatellite which are prone to be mis replicated by DNA polymerase. (Figure.2). In the absence of a functional DNA MMR system, errors that occur during DNA replication, such as base-pair mismatches or small insertions and deletions will remain. Consequently, these uncorrected errors can result in different types of mutations, especially frameshift mutations [16]. Subsequent transcription leads to the formation of new antigen and epitopes in the MSI positive tumour cells. The higher neo-antigen load in MSI-CRC enhances their immunogenicity, leading to increased infiltration of T cells and other immune cells into TME. This increased immune response is associated with improved patient outcomes, including increased survival rates, better prognosis, and a lower likelihood of metastasis [39].

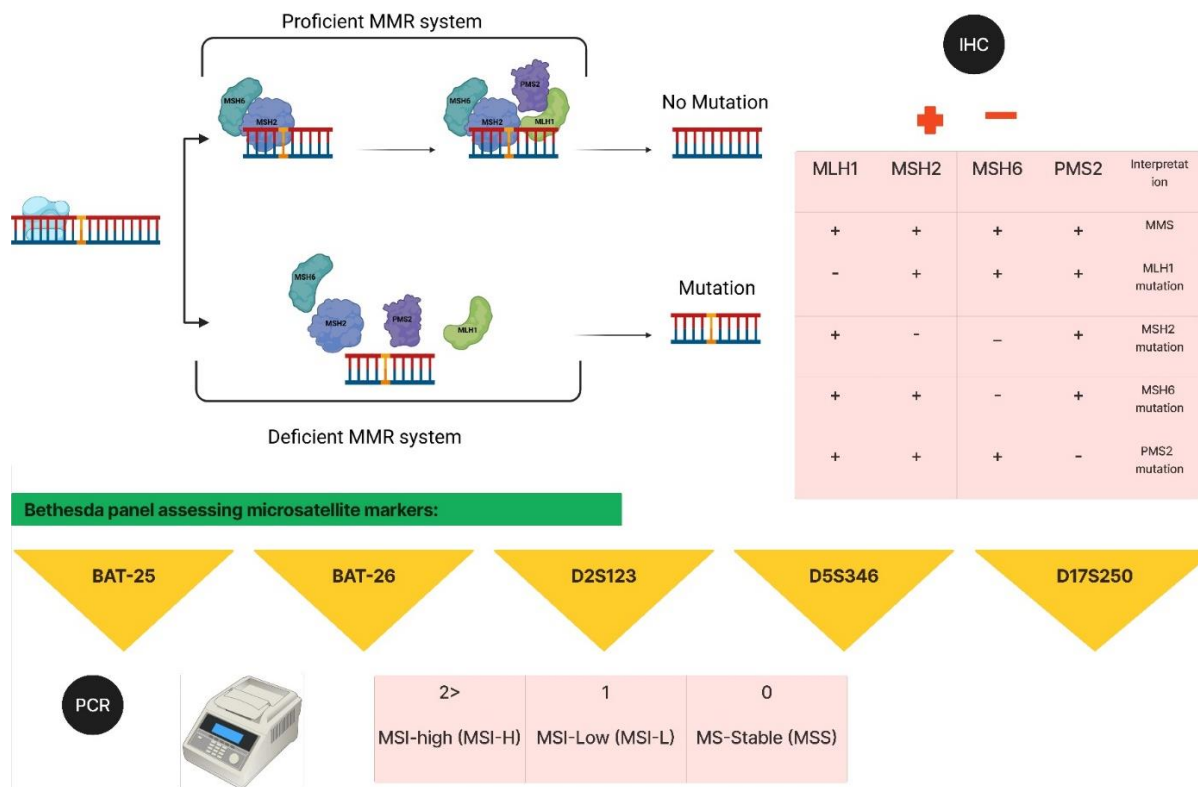


Figure 3. Mismatch Repair (MMR) System Function and Assessment.

This figure illustrates the role of the MMR system in preventing mutations and two methods for evaluating its function: the **Bethesda panel** and **Immunohistochemistry (IHC)**. The Bethesda panel uses PCR to analyze the length of five microsatellite markers (short, repetitive DNA sequences: BAT-25, BAT-26, D2S123, D5S346, and D17S250). Results are categorized as microsatellite instability-high (MSI-H), MSI-low (MSI-L), or microsatellite stable (MSS). The clinical significance of MSI-L versus MSS is still under investigation [40]. IHC detects the presence or absence of MMR proteins (MLH1, MSH2, MSH6, and PMS2). A "+" indicates protein presence (normal function), while a "-" indicates protein absence (suggesting a potential gene mutation). A proficient MMR system has no mutations and all proteins are functional, whereas a deficient system will have a mutation in one or more proteins [41].

Tumour cells can avoid immune destruction through production of immunosuppressive cytokines, recruitment of immunosuppressive cells like T regulatory cells (Tregs), M2-like macrophages, Myeloid derived suppressor cells (MDSC), and upregulation of checkpoint molecules to create bystander, dysfunctional exhausted immune cells. Studies showed that most T cells present in CRC TME that are specific to tumour cell are dysfunctional because of frequent interaction with tumour antigen leading to an increase the expression of checkpoint molecules [42, 43]. This will be discussed later. Furthermore, it has been demonstrated that some T cells present in the TME are bystander T cells that are not specific to tumour cells, and they are not exhausted [44].

1.2.2 Immunoscore

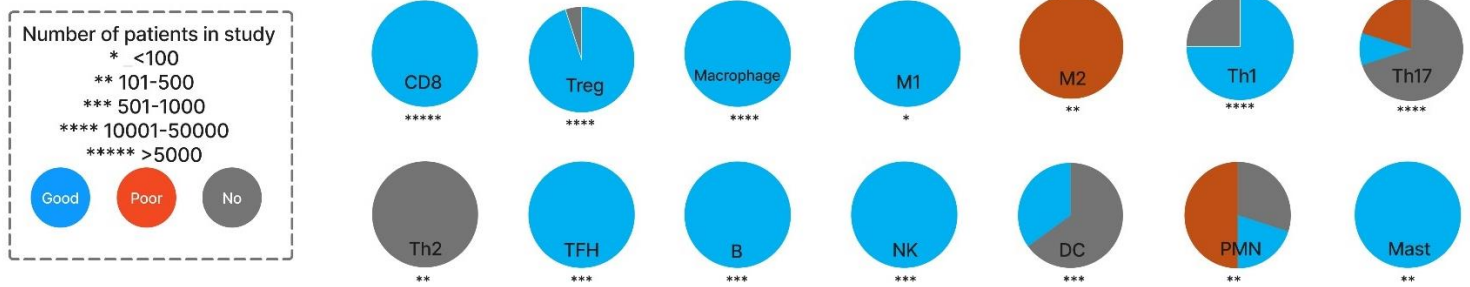
The ongoing interactions between tumour and immune cells creates a unique immune cell topography which can be clinically translated as **Immunoscore** [45]. Immunoscore has emerged as a key predictor of outcome and responsiveness to therapy, demonstrating greater predictive reliability than TNM staging in some studies [46]. Type, density, and location are critical in classifying patients into subgroups and predicting disease-free survival and overall survival [47]. Immunoscore needs a proper technique to differentiate various immune cells based on unique T-cell markers. Furthermore, different regions of TME, including the core of the tumour (CT), the invasive margin (IM) (1mm region of tumour parenchyma which is the border between CT and stroma), and stroma may have different distribution for immune cells [48]. The density of immune cells (Cells/mm²) is another crucial factor highlighting the importance of trustworthy digital tools in counting cells. In this regard, it has been demonstrated that effector CD8 T-positive cells in CRC TME are a significant predictor of all stages of CRC correlating with favourable ultimate survival for patients [49, 50]. On the contrary, the poorest outcome was associated with the low density of CD3 and CD8 positive cells in CT and IM [51], **Figure 4**.

1.2.2.1 Hot, Cold, and Excluded TME

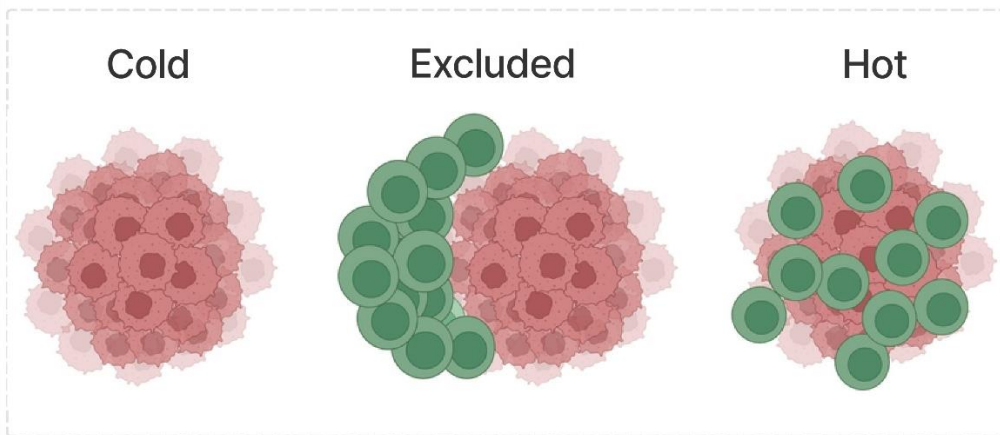
The TME acquires a diverse spatial heterogeneity with different composition of immune cells in tumour and stroma. Inflamed, active, or hot tumours have a high number of CD8 cells and associates with improved survival [52]. In contrast, immune-desert or cold tumours have a low CD8 infiltration and increased T-reg and MDSC associating with poor prognosis [53, 54]. Inherent immunologic status can impact on the infiltration of immune cells in TME. For instance, having genes related to the IFN- γ signaling pathways correlate with hot tumours [55]. There is another recent term as excluded TME which is defined as TME with a lot of lymphocytes in stroma without penetration into parenchyma. [56].

Based on the density of CD3, and CD8 cells there is an Immunoscore from 0 to 4. Zero means there is a low density of both cell types in both IM, CT, and four means there are a high density of both cells in both regions. Immunoscore is considered such a powerful prognostic factor that in a large study of CRC patients (602 patients), about 5% of patients with Immunoscore 4 relapsed after 5 years in contrast to 72% of recurrence in patients with low immunoscore (I. II) [57]. Furthermore, patients with a high density of CD8 cells expressing PD1 in the IM responded better to anti-PD1 therapy, while Immune-excluded TME are resistant to checkpoint inhibitor therapy [56, 58].

A. Immune Cell Types



B. Immune Cell Location



C. Cell Density

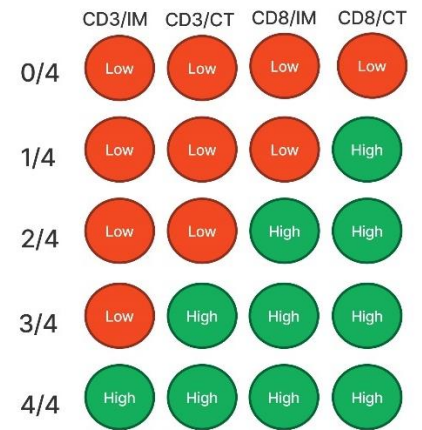


Figure 4. Immune Landscape of CRC and its Association with Prognosis.

This figure summarizes the role of immune cells in CRC, their spatial organization within the tumour microenvironment (TME), and their association with patient outcomes. **A. Immune Cell Types and Prognosis:** This panel depicts various immune cell types and their association with prognosis. The number of stars represents the number of patients in the study that researched that cell type, as indicated by the key. Blue indicates a positive association with prognosis (good), Red indicates a negative association (poor), and Gray indicates an unknown association. CD8; Cytotoxic T cell, Treg; Regulatory T cell, M1; M1 Macrophage, M2; M2 Macrophage, Th1; T Helper 1 cell, Th17; T Helper 17 cell, Th2; T Helper 2 cell, TFH; Follicular Helper T cell, B; B cell, NK; Natural Killer cell, DC; Dendritic Cell, PMN; Polymorphonuclear Leukocyte, Mast; Mast Cell.[59]. **B. Spatial Organization of Immune Cells in the TME:** This panel illustrates three distinct TME patterns based on immune cell infiltration. Cold: Absence of immune cells within the tumour. Excluded: Immune cells are present but confined to the periphery, unable to penetrate the tumour. Hot: Immune cells have successfully infiltrated the tumour core. **C. Immunoscore Based on CD3+ and CD8+ Cell Density:** This panel outlines the immunoscore classification, which quantifies the density of CD3+ (pan T cell marker) and CD8+ (cytotoxic T cell) cells in the tumour core (CT) and invasive margin (IM). The immunoscore ranges from 0/4 (low infiltration in both regions) to 4/4 (high infiltration in both regions) and is associated with patient survival.

It has been suggested that innate cells are key contributors to the formation of hot and cold tumours. Innate cells facilitate the trafficking of T cells and create hot tumours through soluble factors [60]. CXCL9 and CXCL10 released by APC promote the infiltration of CXCR3 expressing T cells [61, 62]. On the other hand, cold tumours often have elevated

numbers of myeloid cells (e.g. macrophage) whose experimental depletion from breast TME leads in the higher infiltration of CD8 cells [63]. Tumour associated macrophages can induce tumour growth through excluding T cells in TME. For instance, it is shown that myeloid cells secrete RNS which induce post translational modifications in T cell chemo attractants and prevent their migration into TME [64]. They also can activate TGF- β signaling which is potent T cell suppressor [65].

1.2.3 Macrophage

Macrophages are one of the most abundant immune cells in the CRC TME as the colon tissue possesses the highest number of macrophages in the body. Macrophages as a member of mononuclear phagocytic system (MPS) participate in both innate and adaptive immunity to initiate inflammation and keep homeostasis [66]. They rapidly clear the lumen of pathogens [67] and are considered a coordinator of leukocyte infiltration [68]. They have key roles in all steps of adaptive immunity where they can trigger adaptive responses through antigen presentation to adaptive cells and through multiple degradation of apoptotic cells, they can affect the type of Ag that presented. Their release of soluble mediators influences the nature of adaptive response and by producing anti-inflammatory cytokines they contribute to homeostasis [69, 70].

Macrophage differentiation and maturation starts from Hematopoietic stem cell (HSC) in the Bone marrow (BM) which develops into monocytes. Circulating monocytes can penetrate tissues during immune response through CC-chemokine ligands 2(CCL2), CCL5, and cytokines colony stimulating factor 1(CSF1) [71, 72]. A second source of tissue macrophages that originated from stem cells in the yolk sac during embryogenesis, however, after birth the major source of tissue macrophages are HSC-derived macrophages [73], **Figure 6.A**. Macrophages in the tumour microenvironment are called tumour associated macrophages (TAMs) and arise from both sources, but the percentage can be different according to the tissue type [74-76]. For example, in colon tissue the majority of embryonic macrophages were substituted with HSC-derived macrophages after birth [72]. In addition, there is evidence that under the stimulation of specific chemokines, myeloid-derived suppressor cells (MDSC) can differentiate into TAM [77]. MDSC are mainly CD68 positive cells differentiated from circulating monocytes and show the ability to suppress immune cell proliferation and function in tissues and TME [78].

Macrophages are highly plastic, and their phenotypes reflect both the local tissue and their origin. In general, the naïve macrophages (M0) can further differentiate into two states which are known as macrophage polarization, including pro inflammatory or classically

activated M1 and anti-inflammatory or activated M2 macrophages [79]. CD68, CD16, and CD14 are some examples of pan macrophages markers. **Figure 5** showing basic information about CD68.

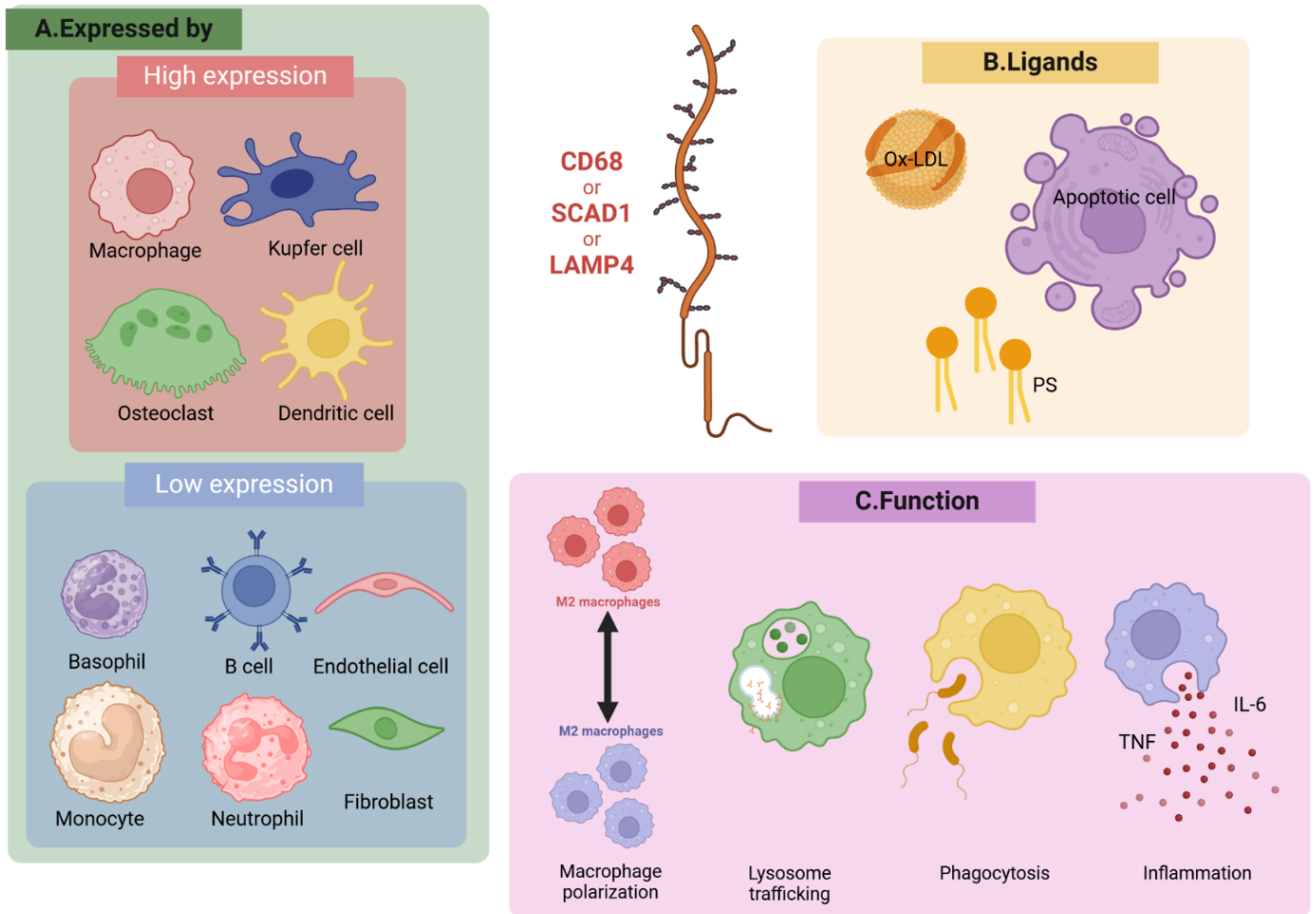


Figure 5. CD68 Expression, Ligands, and Function.

A. CD68 is a transmembrane glycoprotein expressed in macrophages, with lower expression in other cell types. **B.** As a scavenger receptor, CD68 binds to various ligands, including oxidized low-density lipoprotein (Ox-LDL) and phosphatidylserine (PS) on apoptotic cells. **C.** CD68 plays a role in macrophage polarization, lysosome trafficking, phagocytosis, and inflammation, including the release of pro-inflammatory cytokines like Tumour Necrosis Factor (TNF) and Interleukin-6 (IL-6) [80, 81]. IL-6: Interleukin-6 LAMP4; Lysosome-Associated Membrane Protein 4, Ox-LDL; Oxidized Low-Density Lipoprotein, PS; Phosphatidylserine, SCAD1; Scavenger Receptor Class D-Member 1, TNF; Tumour Necrosis Factor.

Macrophage Polarization

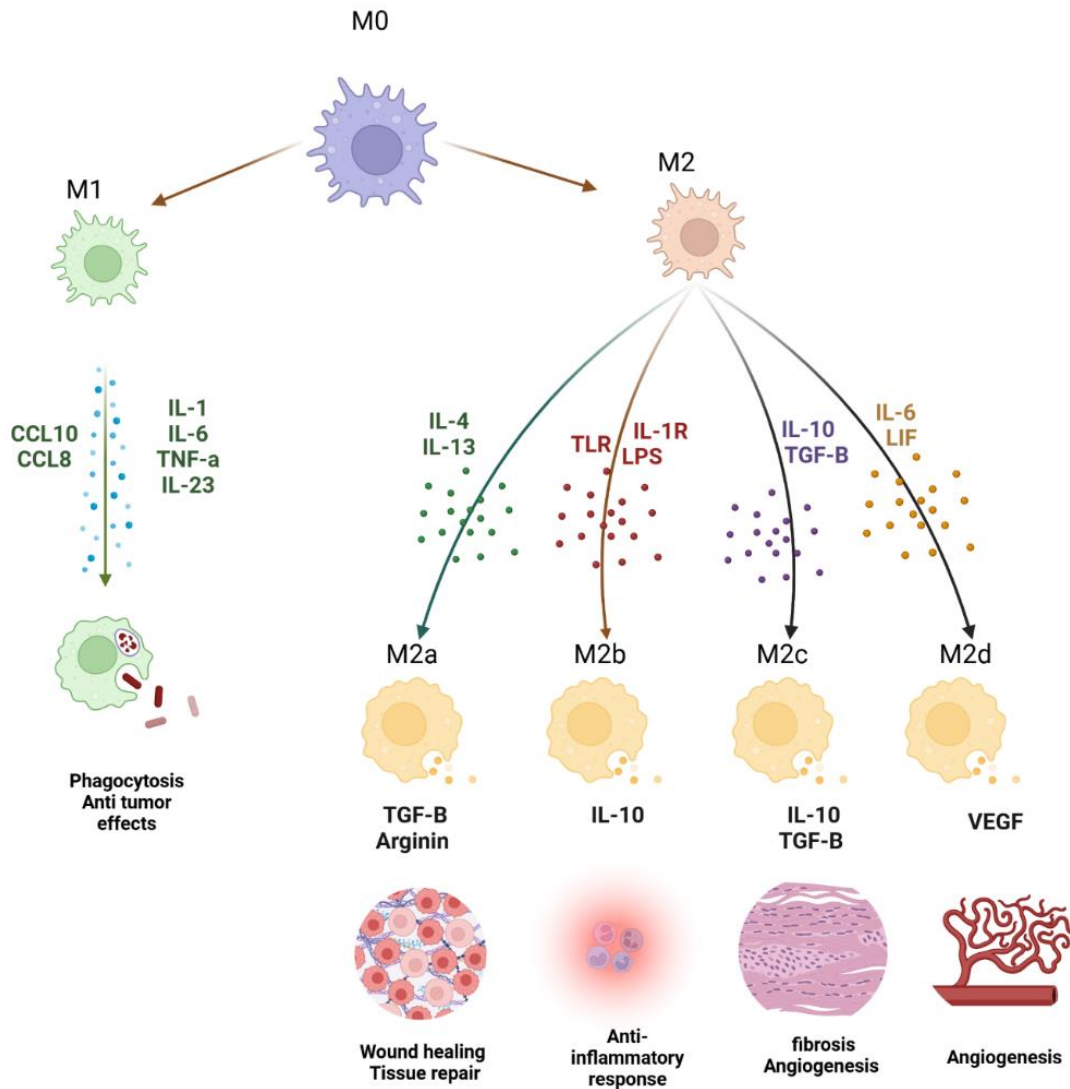


Figure 6. Macrophage Polarization Pathways.

Macrophages can differentiate into distinct functional subtypes, broadly categorized as M1 and M2. M1 macrophages are activated by factors such as Lipopolysaccharide (LPS) and are characterized by the release of pro-inflammatory cytokines (e.g., IL-1, IL-6, TNF- α) and the promotion of anti-tumour responses. M2 macrophages, associated with anti-inflammatory responses, tissue repair, and angiogenesis, are further divided into four subtypes (M2a, M2b, M2c, M2d) based on their activation stimuli and cytokine profiles. The figure depicts the stimuli (e.g., IL-4, IL-13, TLR ligands, IL-10, TGF- β , IL-6, LIF) that drive M2 polarization, and the main functions associated with each subtype. CCL8; Chemokine (C-C motif) Ligand 8, CCL10; Chemokine (C-C motif) Ligand 10, IFN- γ ; Interferon-gamma, IL-1 β ; Interleukin-1 beta, IL-1R; Interleukin-1 Receptor, IL-4; Interleukin-4, IL-6; Interleukin-6, IL-10; Interleukin-10, IL-13; Interleukin-13, IL-23; Interleukin 23, LIF; Leukemia Inhibitory Factor, LPS; Lipopolysaccharide, TGF- β ; Transforming Growth Factor-beta, TLR; Toll-Like Receptor, TNF- α ; Tumour Necrosis Factor-alpha, VEGF; Vascular Endothelial Growth Factor.

M1 and M2 Macrophages can switch to each other's states. For instance, during tissue repair M1 macrophage switch to M2 phenotype [82]. M1 macrophages are induced by interferon γ (IFN- γ), GM-CSF, lipopolysaccharide (LPS), or tumour necrosis factor- α (TNF- α) and promote Th1 functions and show anti-tumour responses through release of IL-6, IL23, ROS and IL-1 β [83, 84]. In contrast, M2 macrophages are triggered by Th2 cytokines (eg IL-4, IL-10, IL-13) and produce IL-10, TGF- β , and pro-angiogenic mediators, driving tissue remodeling, tumour progression and immune evasion [85]. CD80, CD86, and TLR4 are usually defined as M1 markers, whilst CD204, CD163, and CD206 are employed as M2 markers [86]. M2 macrophages are further divided into four classifications according to the source of stimulation and the function, **Figure 6** [87, 88].

In the early stages of CRC, M1 macrophages are abundant and produce ROS and NOS which further trigger gene mutations and oncogene gain of functionality [89]. However, in solid tumours, the majority of TAM have a phenotype similar to M2-like macrophages [90]. The number of macrophages can be a prognostic factor in the TME. For example, high numbers of M2-like macrophages in gastric cancer are associated with decreased survival, while the high number of M1-like macrophages relates to improved survival [91]. High number of macrophages expressing CD163 (marker of M2 cells) correlated with poor prognosis in many cancers, including CRC [92].

TAMs interact with tumour cells through releasing cytokines and vesicles and induce their proliferation, invasion, and progression **Figure 7.B**. Coculture of colon cancer cell line (HCT-8 and HCT-116) with the macrophage cell line (THP-1) revealed that tumour cells, through releasing EGF, trigger the EGFR/PI3K/AKT/mTOR pathway and switch the polarization into M2-like macrophages [93]. Tumour cells produce exosomal miR-1246 which increases the polarization of M2-like macrophages [94]. Another study showed that tumour cells produce several chemokines such as CXCL1, CXCL2, CXCL5, CCL3, CCL4, and the cytokines such as IL-1- β , IL-3 which participate in M2 polarization [95].

It seems that TAM and tumour cells have a two-sided relationship with each other in cancer growth in TME. Tumour cells secrete TGF β to increase RGC-32 expression in macrophages to increase the migration of macrophages into TME [96]. In addition, they produce IL-10 which help to further differentiation of monocyte into M2-like macrophages [97]. Through regulating the NADPH oxidase activity, TAM provides an oxidation-reduction state with low ROS in which tumour cell proliferation can be promoted [98].

TAM also can provide a further opportunity for tumour metastasis and invasion. TAM secretes MCP1, MIP-1- α and MIP-2- α to increase tumour invasion [99]. TAM increases the expression of S100A8/A9 in tumour cells which help to tumour migration [100]. Through

secreting IL-6 and jak2/stat pathway they increase the EMT transition and CRC migration, as well [101].

TAM release immune suppressive cytokines like IL-10, TGF-beta, and immunosuppressive metabolites like IDO and PGE2. They produce VEGF and platelet-derived endothelial cell growth factor to increase the angiogenesis in the TME via triggering the STAT pathway in endothelial cells [102, 103]. They suppress the cytotoxic ability of CD8 positive cells in the TME[104]. They also can recruit T-reg cells through releasing CCL2 chemokine and create a suppressive TME which can suppress immune response against tumour cells [105].

Hence, macrophages play a crucial, dichotomous role in the tumour microenvironment (TME), influencing both the initial and terminal stages of cancer. In the early phases, a higher proportion of M1 macrophages actively participate in tumour eradication. Conversely, during the advanced stages of cancer development and progression, M2 macrophages become dominant, effectively aiding the tumour by promoting its growth, migration, and metastasis.

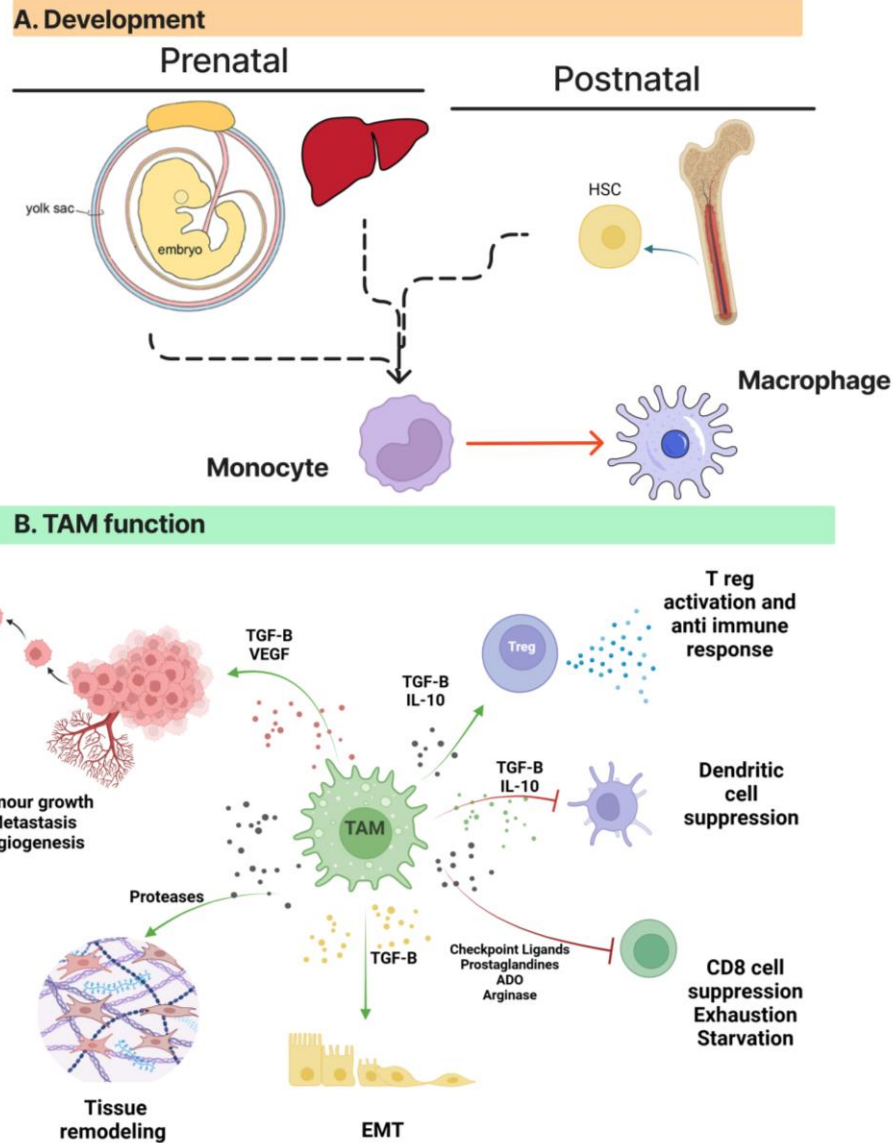


Figure 7. Macrophage Development and TAM Main Functions.

A. Macrophage Development: Macrophages originate from the yolk sac and fetal liver prenatally and from bone marrow hematopoietic stem cells (HSCs) postnatally. HSCs differentiate into monocytes and then into mature macrophages. **B.** Tumour-Associated Macrophage (TAM) Functions: TAMs promote tumour progression by contributing to tumour growth, metastasis, angiogenesis (via TGF- β , VEGF), immune suppression (via Treg activation, dendritic cell and CD8+ T cell inhibition - mediated by TGF- β , IL-10, checkpoint ligands, prostaglandins, ADO, and arginase), tissue remodeling (via proteases), and epithelial-mesenchymal transition (EMT). IL, Interleukin; TAM, tumour associated macrophages, EMT; Epithelial-mesenchymal transition, TGF; Tumour growth factor, VEGF; Vascular Endothelial Growth Factor, ADO; Adenosine, T reg; T regulatory, TNF; Tumour necrosis factor, LPS; lipopolysaccharide, TLR; Toll-like receptor, LIF; Leukemia inhibitory factor, CCL; Chemokine (C-C motif) ligand 1, HSC; hematopoietic stem cell.

1.2.4 T cell

T cells, a critical compartment of the adaptive immune system, play a fundamental role in cell-mediated immunity. As depicted in Figure 8, T cell development initiates from hematopoietic stem cells (HSCs) within the bone marrow in which they committed to differentiate into T-cells. These progenitor cells, following Notch signaling, migrate to the thymus. Within the thymus, they undergo stringent positive and negative selection, ultimately differentiating into mature single-positive T cells expressing either CD4 or CD8 [106]. TCR interaction with the peptide-MHC complex constitutes the initial step in T cell activation. Similar to immunoglobulins (Igs), both the alpha and beta chains of the TCR consist of constant and variable regions, with the variable regions being unique to each lymphocyte clone [107]. However, the short cytoplasmic domain of both α and β chains lacks the ITAM (Immunoreceptor Tyrosine-based Activation Motif) domain, preventing them from independently initiating T cell activation or transferring signals [108, 109]. Consequently, TCR signaling exclusively relies on the CD3 protein complex to transduce signals to second messengers. This function is analogous to that of the CD79 protein complex in the B cell receptor (BCR) [110]. CD3 is a complex multimeric protein composed of three subunits, forming three distinct multimer arrangements: CD3 $\zeta\zeta$ homodimer, CD3 $\gamma\epsilon$ heterodimer, and CD3 $\delta\epsilon$ heterodimer. The CD3 $\gamma\epsilon$ and CD3 $\delta\epsilon$ heterodimers interact with the β and α chains of the TCR, respectively, and possess relatively short cytoplasmic domains. In contrast, the CD3 $\zeta\zeta$ homodimer associates with the α chain and, due to its long cytoplasmic domain, plays a significant role in TCR signal transduction [111, 112]. Therefore, the TCR recognizes the peptide-MHC complex, while the CD3 complex is responsible for signal transduction, together forming a functional unit [108]. Any mutation within any component of this complex can lead to a very low or undetectable amount of the TCR complex on the cell surface [113].

CD4 T cells represent a heterogeneous group of immune cells, classically categorized into Th1, Th2, and Th17 subsets. However, other T helper cell populations, such as follicular helper T cells, T regulatory cells, Th9, and Th22, have also been identified based on specific transcription factors and unique expression patterns of surface molecules and cytokines [114]. Among these, Th1 and Th9 cells are recognized as major participants in eliminating malignant cells. Conversely, T regulatory (Treg) cells and Th2 cells are predominantly identified by their immune suppressive behavior [106]. CD8 T cells, also known as cytotoxic T lymphocytes (CTLs), eliminate malignant cells primarily through two main mechanisms. Firstly, apoptosis is induced in target cells via caspase pathways following the interaction of Fas Ligand (FasL) and TNF-Related Apoptosis-Inducing Ligand (TRAIL), expressed on T cells, with their respective receptors, FAS and TRAILR, on the surface of

target cells. Secondly, CTLs possess cytolytic granules containing granzyme B and perforin, which are released to directly kill target cells [115].

In the current project, CD3 is utilized as a pan-T cell marker, as it is expressed on T cells from the pro-T stage within the thymus.

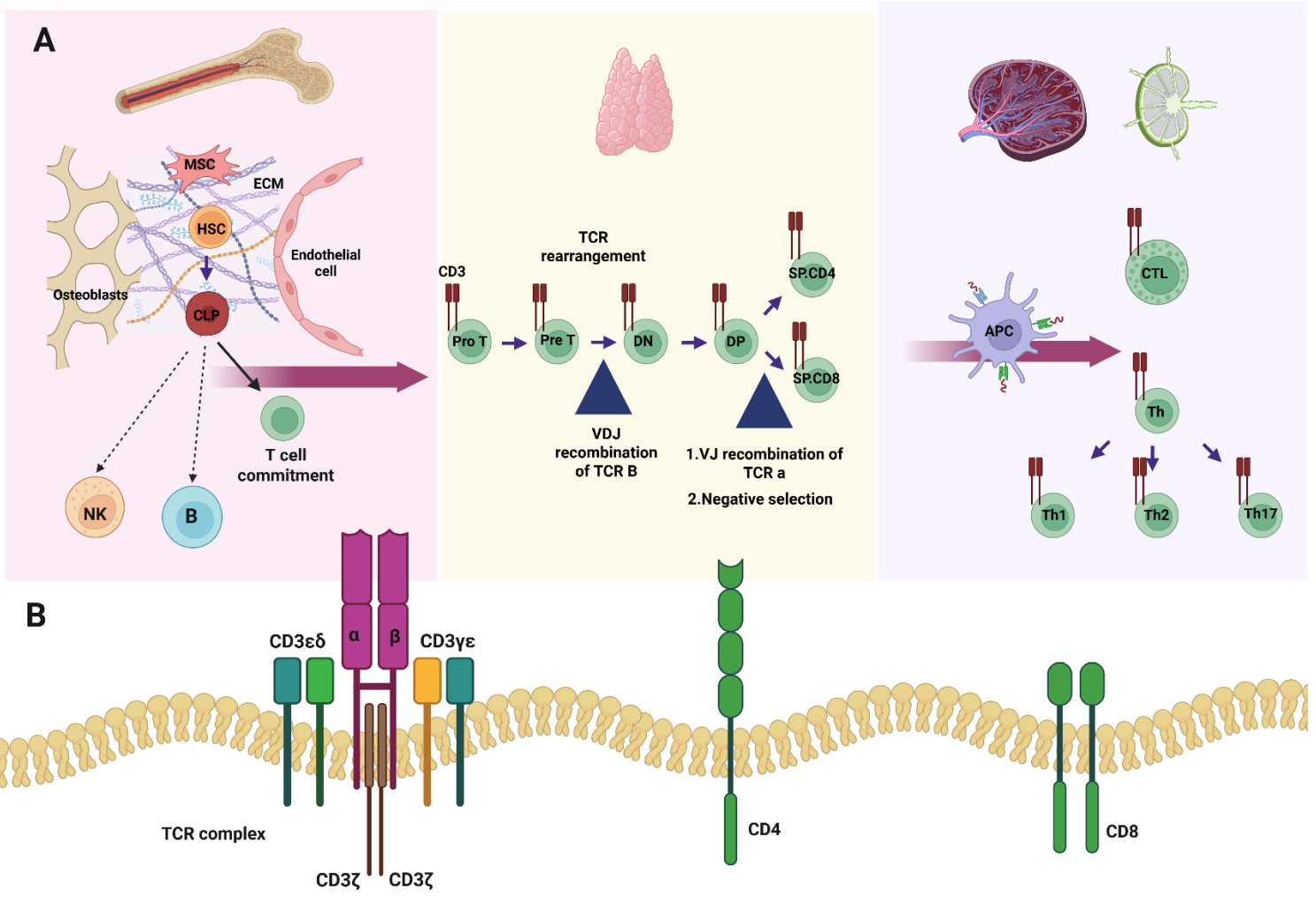


Figure 8. T Cell Development, Maturation, and Activation within the Hematopoietic Niche.

(A) T Cell Lineage Development and Thymic Maturation from the HSC Niche. Hematopoietic stem cells (HSCs) reside in specialized niches within the bone marrow, crucial for their maintenance and differentiation. This HSC niche is comprised of key components including Mesenchymal Stromal Cells (MSCs), which provide essential growth factors and cytokines. The Extracellular Matrix (ECM) offers vital structural support and biochemical cues to HSCs, aiding their anchorage and modulating cellular interactions. Endothelial cells, lining the bone marrow's blood vessels, regulate HSC trafficking and quiescence, forming a critical vascular niche. Osteoblasts, responsible for bone formation, also play a

significant role in maintaining HSC quiescence by secreting specific factors. From this niche, common lymphoid progenitors (CLPs) are generated, which then commit to the T cell lineage. T cell precursors subsequently migrate to the thymus, where they undergo TCR rearrangement, progressing through Pro-T, Pre-T, Double-Negative (DN) for CD4 and CD8, and Double-Positive (DP) stages. This maturation involves VDJ recombination of the TCR beta chain, followed by VJ recombination of the TCR alpha chain, and crucial negative selection processes, leading to the development of mature, self-tolerant T cells. In secondary lymphoid organs like spleen and lymph nodes, upon encountering an antigen presented by an APC, T cells become activated. This leads to clonal expansion and differentiation into various effector T cell subsets, including Cytotoxic T Lymphocytes (CTLs), T helper 1 (Th1), T helper 2 (Th2), and T helper 17 (Th17) cells, each with distinct immune functions. CD3 is the pan T cell marker which is expressed from pro T stage. **(B) T Cell Receptor (TCR) Complex and Co-receptors.** The mature TCR complex is shown on the cell surface, consisting of alpha and beta chains associated with CD3 ϵ , CD3 γ , CD3 δ , and CD3 ζ chains, which are essential for signal transduction. Nearby, co-receptors CD4 and CD8 are depicted, which bind to MHC Class II and MHC Class I molecules, respectively, on antigen-presenting cells (APCs).

1.2.5 Exhaustion

Exhaustion is a step of immune homeostasis in which chronic Ag stimulation leads to depressed leukocyte proliferation and function due to elevated expression of checkpoint molecules that serve as exhaustion markers [116]. Exhaustion was first described in chronic lymphocytic choriomeningitis virus (LCMV) infection, in which T cells had a dysfunctional state because of long-lasting exposure to Antigen and repetitive TCR stimulation [117, 118]. It is a process to protect T cell- clones from activation-induced cell death which gradually results in the loss of specific clone by repetitive activation and death [117]. For example, in elderly patients, loss of CMV-specific T cell clone relates to higher patient mortality [119]. Furthermore, exhaustion can protect the tissue from necrosis and expanding autoimmune diseases [120, 121].

It is worth knowing that there are other types of dysfunctionality states that different stimuli and pathways are involved, and they have different manifestations that should be differentiated from exhaustion.

Senescent immune cells usually are seen in elderly patients who have shortened telomere and damaged DNA should be distinguished from exhausted immune cells. Senescent immune cells secrete a high amount of proinflammatory cytokines and destructive substances like ROS [122]. This phenomenon is an evolutionary irreversible process[123]. The other phenotype that must be distinguished is **suppressed phenotype** of immune cells which can be resulted by external signaling of suppressive cells like T-reg, MDSC, Macrophages, or hypoxic condition and adenosine pathway [124]. Suppression is reversible when the suppressive signaling is abandoned. On the other hand, exhaustion is

a lower functionality of immune cells because of overexpression of checkpoint molecules, it is reversible and usually indicates that resources are used and there is a need for regeneration [125].

1.2.5.1 Immune checkpoint molecules

Immune checkpoint molecules are essential receptors in regulating immune cells functionality and acting as immune gatekeepers. They evolved with stimulatory molecules simultaneously and possess immunoreceptor tyrosine-based inhibitory motif (ITIM) and immunoreceptor tyrosine-based switch motif (ITSM) to transfer immunosuppressive signaling [126]. Checkpoint molecules functionality recruitment is frequently seen in chronic inflammation or cancer as a mechanism for immune escape [127], in which one of the critical characteristics of TME is high expression of checkpoint molecules. Hence, understanding the molecular biology of checkpoint molecules expression in different immune cells and in different textures is critical to have a more comprehensive view on the TME. Most of our understanding about checkpoint molecules comes from T cell studies which means that there is almost limited data of their functionality in other immune cells.

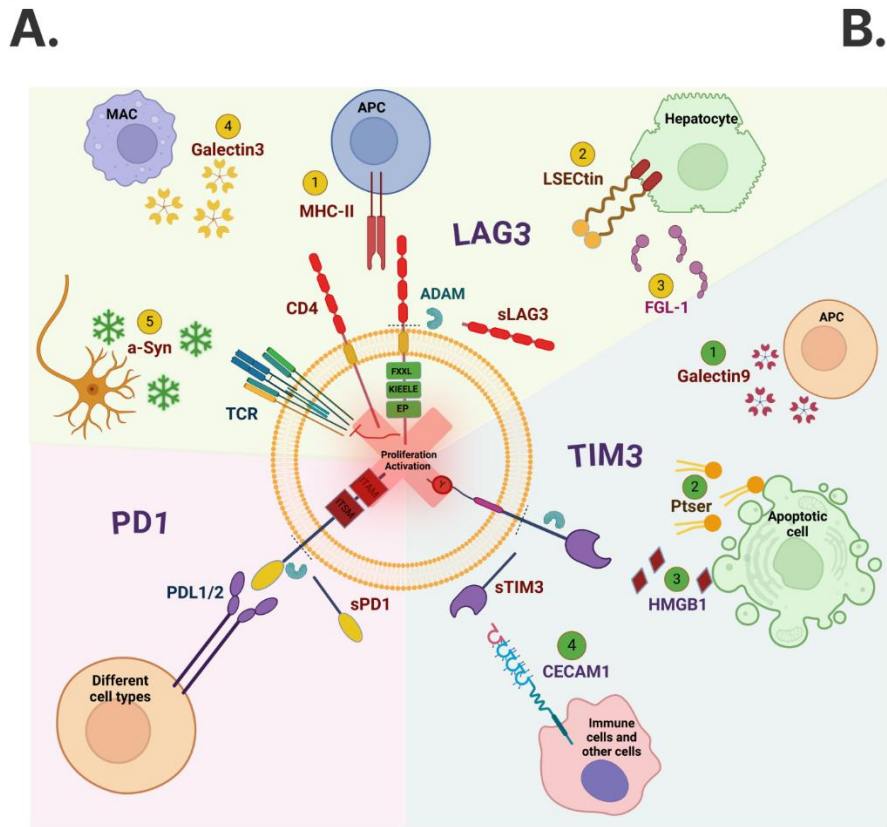
The use of antibodies to checkpoint molecules which is also known as Checkpoint inhibitor therapy has revolutionized cancer immunotherapy as first demonstrated in melanoma [127]. The most successful checkpoint inhibitor therapy was anti-PD1 and anti-PD-L1 therapy which has been approved for a wide range of cancers. However, the response rate to checkpoint blockade therapy was between 10-30 percent and accounted as the major drawback of checkpoint-blockade therapy [128]. For instance, in MMR sufficient CRC patient there was nearly zero percent response rate to anti-PD1 and anti-PD-L1[129]. Apart from specific molecular profile of the tumours in these patients, other factors can be involved in non-responsiveness of patients to checkpoint inhibitor therapy, including the variation in checkpoint expression levels and also expression in different types of cells apart from T cells which seems to have different functions compared to initial well-recognized inhibitory function in T cells [130, 131].

1.2.5.1.1 LAG3

LAG3 is an inhibitory receptor that negatively regulates host cell proliferation and effector function in which LAG3 over expression is usually associated with cell exhaustion [132, 133]. LAG3 is expressed on a variety of immune cells, such as activated T cells (CD4, CD8,

and T reg), plasmacytoid dendritic cells, NKT cells, and NK cells [134]. Malignant B cells also expressed LAG3 in Diffuse large B-cell lymphoma (DLBCL) [135].

LAG3 is an ancestral homolog of CD4, and the extracellular domain is very similar to CD4 structure consisting of four immunoglobulin superfamily like domain [136]. The intracellular domain of LAG3 is different from the rest of checkpoint molecules as it does not have ITIM or ITSM domains to transfer suppressor signaling and also it is not similar to the intracellular domain of CD4. Instead, it is constituted of three motifs that are highly conserved in human and mice. The KIEELE motif has a critical function in LAG3-mediated suppression in which its deletion disrupts LAG3 functions although its exact functionality is not clear yet [137].



B.

	LAG3	PD1	TIM3
T cell	Exhaustion	Exhaustion, High in highly activated T cell	Exhaustion
Macrophage	There is evidence of expression but the role is unclear [128]	M2 types has higher expression compared to M1 [129]	Quiescent state: high (tolerance) Active state: low (activation) Higher expression in M2 than M1 [130]
Tumor	Expression: Some tumours in RNA levels and cell lines. Function: Unknown [130,131]	Some tumours: Oncogene Some tumours: TSG [132]	Tumour oncogene in many tumours [133]

Figure 9. Exhaustion Markers: Structure, Ligands, and Function in Immune and Tumour Cells.

This figure illustrates the structure and interactions of three key immune checkpoint molecules associated with exhaustion (LAG3, PD1, and TIM3) and summarizes their functions in different cell types. **A. Structure and Ligands:** This panel depicts the interactions of three immune checkpoint molecules associated with exhaustion: LAG3, PD1, and TIM3 with their respective ligands. LAG3 binds to MHC class II, LSECtin, and potentially a-Syn. PD1 binds to PD-L1 and PD-L2. TIM3 binds to Galectin-9, phosphatidylserine (PtSer), and HMGB1. These interactions play roles in regulating immune cell activation and proliferation. The extracellular domain of exhaustion markers can be shed by ADAM, generating a soluble form that may play a regulatory role. **B. Functional Summary:** This table summarizes the roles of LAG3, PD1, and TIM3 in T cell exhaustion and their expression patterns in various cell types, including T cells, macrophages, and tumour cells. "Exhaustion" refers to a state of T cell dysfunction. Notably, TIM3 expression is higher in M2 (anti-inflammatory) compared to M1 (pro-inflammatory) macrophages. And there is vague image on the role of exhaustion markers in macrophages. [135, 138-143] a-Syn; alpha-Synuclein, ADAM; A Disintegrin and Metalloprotease, APC; Antigen-Presenting Cell, FGL-1; Fibrinogen-Like Protein 1, HMGB1; High Mobility Group Box 1, LAG3; Lymphocyte-Activation Gene 3, LSECtin; Liver and Lymph Node Sinusoidal Endothelial Cell C-type Lectin, MAC; Macrophage, MHC-II; Major Histocompatibility Complex Class II, PD1; Programmed Cell Death Protein 1, PD-L1/2; Programmed Cell Death Ligand 1/2., PtSer; Phosphatidylserine, TCR; T-cell Receptor, TIM3; T-cell Immunoglobulin and Mucin-domain containing-3, TSG; Tumour Suppressor Gene.

A range of ligands for LAG3 have been identified. MHCII is LAG3 ligand which binds to the D1 extracellular domain of LAG3 with higher affinity than CD4 [144]. Dimerization of LAG3 facilitates the binding of LAG3 to MHCII [136]. Furthermore, there is no difference in the

type of MHCII, and LAG3 can recognize the complex of MHCII and peptide regardless of MHC type and the protein [145]. However, a higher affinity of peptide binding to MHCII and a more stable expression of peptide- MHCII leads to higher binding of LAG3 to MHCII [145].

Galectin-3 (Gal-3), expressed by epithelial cells, endothelial cells, fibroblasts, cancer cells, and macrophages, is a lectin ligand of LAG3. Suppression of CTL following the interaction of LAG3-Gal3 has been reported[146]. In a study investigating the interaction between LAG3 and its ligands, blocking Gal-3 but not MHC-II significantly increased proliferation of CD8 cells indicating that Galectin-3 plays a more significant role than classical MHC class II molecules (HLA-DR, HLA-DP, and HLA-DQ) in regulating CD8+ T cell function in multiple myeloma [147].

Another Lectin, LSEctin, suggested as a novel ligand for LAG3. It is expressed by hepatocytes and melanoma tumour cells and its further interaction with LAG3 transfer suppressing signaling in immune cells through the immunosuppressor cytoplasmic domain of LAG3 [148]. Hepatocytes also express Fibrinogen-like protein 1 (FGL1) which can bind to LAG3 and transmit inhibitory signals in LAG3 expressing cells. Expression of FGL1 in tumour cells correlates with immunotherapy resistance and poor prognosis [149]. α -syn is another ligand recognized for LAG3 which is bound to D1 domain like MHCII, but its role in the function of LAG3 is unknown [150].

The expression of LAG3 is tightly regulated. LAG3 is stored in late endosome after translation which is a facilitator for quick transition to the surface of the host cell following TCR activation or upon stimulation by certain cytokines, including IL-12, IL-27, IL-15, IL-2, and IL-7. Following binding to its ligands it can transmit inhibitory signals into the cell. [134]

The second level of LAG3 regulation is controlled at the surface of the cell in which certain metalloproteinases, ADAMTS10 and ADAMTS17, cleave LAG3 and produces soluble LAG3 which have no functionality without cytoplasmic domain [151]. Mice studies showed that non-cleavable LAG3 or inhibitors of ADAMTS resulted in impaired functionality of T-cells, it means that producing soluble LAG3 is a way to regulate LAG3 inhibitory function [152]. In addition, there is another way for regulation of membranous LAG3 expression in which cells endocytosis LAG3 after binding to α -syn and keep them in the endosome for further expression [153]. In fact, it has been shown that LAG3 can be stored in recycling endosome and secretory lysosomes, especially in CD4 positive cells [154]. Much of understanding on LAG3 function comes from T cells studies, representing the functions of LAG3 in different T cells.

However, studies also show that there is a spatial association between LAG3 and CD68 expressing macrophages in TME [135]. In Lymphoproliferative disorders like DLBCL and

CLL, leukemic B cells express LAG3 and possess a high number of macrophages. It has been suggested that malignant B cells polarized macrophages into immunosuppressive M2 macrophages [155, 156]. The study also showed that M2 macrophages are spatially close to B malignant cells expressing LAG3 in DLBCL [135]. In addition, some studies showed the expression of LAG3 in macrophages. One study in gastric cancer showed LAG3 expressing macrophages but in a significant lower level compared to CD3 positive cells in gastric cancer TME [138].

There is some limited evidence that LAG3 is expressed on the surface of solid tumour cells in lung, colon, and breast cell line [141, 157]. In addition, leukemic cells like DLBCL, Hodgkin lymphoma and CLL cells have been reported as LAG3 expressing cells [155, 158].

1.2.5.1.2 TIM3

T cell immunoglobulin and mucin domain- containing protein 3 (TIM3) is a member of immunoregulatory proteins of TIM. TIM3 can be expressed on different immune cells, including T cells, mast cells, monocyte, macrophages, and NK cells [159-161]. The main feature of TIM3 like LAG3 and compared to other checkpoint molecules is the lack of an inhibitory motif in the intracellular domain. Instead TIM3 has five conserved tyrosine in its intracellular domain that are bound to HLA- B-associated transcript 3 (BAT3) in normal situations [162]. There are different ligands recognized by different regions of TIM3: Galectin-9, phosphatidylserine (PtdSer), high mobility group protein B1 (HMGB1), and carcinoembryonic antigen- related cell adhesion molecule 1 (CEACAM1). Following their interaction with TIM3 and subsequent Tyrosine phosphorylation, BAT3 disconnect and FYN, a tyrosine Kinase, is recruited to mediate subsequent TIM3 inhibitory signaling, including, disrupting immunologic synapsis, TCR signaling suppression, and apoptosis[163]. Like soluble LAG3, soluble TIM3 results from metalloproteinase activity, however its function remains to be clarified [164]. It is interesting that increased plasma levels of TIM3 correlated with increased load of HIV infection, worse outcome of osteosarcoma, and GVHD [165-167].

The ultimate outcome of TIM3 activation can be different and highly depends on the cell type that expresses it [168, 169]. For instance, the interaction of galectin-9 with TIM3 expressed by T cells, suppress them and induce apoptosis [170]. On the other hand, it has been demonstrated that monocyte and macrophages in their quiescent state express high amount of TIM3 which is associated with immune tolerance, low cytokine production, and reducing TLR activation. However, when macrophage activates into M1 like macrophages,

the TIM3 expression decreases, and cytokine production, including IL-6, IL-12 increase favors T-lymphocyte activation [171]. It is interesting to know that macrophage Cis activation of TIM3 resulted from interaction between TIM3 and galctin3 on the same macrophage activate TLR and enhance cytokine production, while the trans activation of TIM3 decrease cytokine production and TLR activation which is assumed as macrophage suppression [172]. In addition, it has been reported that TAM like M2 macrophages also expressed high amount of TIM3 which is unlike M1 macrophages [173].

There is ample data r3egarding the TIM3 expression on the surface of tumour cells, including melanoma, prostate cancer, renal carcinoma, and hepatocellular carcinoma [173-176]. There is also some evidence of its expression in CRC cell lines in which knocking down the expression of Tim3 can suppress the proliferation of tumour cells, their migration and invasion [143]. In this regard, an study showed that Tim3 acts as a tumour oncogene in CRC cell lines and anti-Tim3 therapy can show antineoplastic effects [143].

1.2.5.1.3 PD1

PD1 belongs to the CD28-CTLA subfamily of Ig superfamily [177], and its ligand are B7 family members, including PDL1 (B7-H1; CD274) and PDL2 (B7-DC; CD273) [178] which are expressed by different types of cells and APC, including macrophages [179]. The cytoplasmic domain of PD1 processes both ITIM and ITSM domain [180]. Subsequent PD1 activation after binding to its ligand promotes an inhibiting signaling and a phenotype in which there are suppression of differentiation, proliferation, and survival of T cells [181]. Hence, the initial functionality of PD1 is the regulation of immune response. Tumour cells can wildly exploit this interaction to avoid immune recognition.

PD1 is one of the well-studied exhaustion receptors in T and B cells that can be induced following TCR activation and upregulated by cytokines stimulation [182]. PD1 suppresses lymphocytes to prevent autoimmunity and tissue damage and induces fetal-maternal immunity [183, 184]. Hence, it is not surprising that tumour infiltrating T cells express high amount of PD1 on their surface due to over stimulation and the tumour suppressing nature of the tumour microenvironment and show lower functional activity against cancer cells [185]. Exhausted T cells have increased expression of inhibitory molecules, and decreased secretion of effector molecules [186]. In this regard, PDL1 expression on the surface of tumour cells, seems to have a pivotal role in tumour evasion. In fact, many cancer cells and myeloid cells express PDL1 in their surface and can upregulate its expression

following different cytokine stimulation [187]. This is the reason behind successful immune checkpoint inhibitors therapies against PD1 and PDL1[187].

There is some evidence of the expression of both PD1 and PDL1 on the surface of macrophages. PDL1 expression on M2 macrophages is higher than M1 macrophages. PDL-1 interaction on macrophages with PD1 on T cells, transmit inhibitory signals to T cells, and suppress the proliferation and activation of macrophages [188]. However, it has been demonstrated that PD1 can be expressed on TAM, but not on circulatory macrophages or on macrophages in the spleen. One study on TAM, showed that there are two populations of TAM in TME regarding PD1 expression. PD1 expressing TAM tends to polarize into M2 macrophages, while PD1 negative macrophages polarize into M1 macrophages. Furthermore, cancer progression is accompanied by an accumulation of tumour-associated macrophages (TAMs) expressing high levels of PD-1 and CD206, coupled with a reduction in MHC-II expression [139]. PD1 expressing macrophages express high number of anti-inflammatory cytokines like IL-10 which is assumed as a mechanism to slow down the immune response. PD1 blockade increased M1 polarization, phagocytosis and the tumour killing of macrophages [139].

1.3 Hypotheses and Aims

Macrophages and T cells are two main immune cells in the CRC immune microenvironment to illuminate cancer. In this regard, especially in recent years, many efforts have been made to augment and boost patient immune system against tumour cells. Immune checkpoint inhibitor therapy is one of the most successful types of cancer immunotherapy, however, despite recent progress with anti-PD1/PD-L1 therapies in cancers like Melanoma, CRC has not seen the same level of success. Ampel studies and trials are assessing the effect of combination therapy with other conventional therapies and also other checkpoint inhibitors [189]. Nevertheless, there is a gap in our understanding of the co-expression of these exhaustion markers, especially on innate cells like macrophages. The effect of expression of these receptors on macrophages results have different outcomes compared to lymphocytes. Furthermore, conventional therapies like chemotherapy, besides their primary anti-tumour role, can trigger immune responses against tumour cells[190], which means therapies other than immunotherapy also have the potential to change the TME context such as the expression level of checkpoint molecules. Hence, a comprehensive study is crucial to map the unique distribution and organization of exhaustion markers within the CRC tumour microenvironment and uncover potential therapeutic targets.

In this study, we are using multiplex immunohistochemistry (mIHC) to analyze the spatial distribution of immune exhaustion markers LAG3, TIM3, and PD1 on CD3+ cells and macrophages within the tumour microenvironment of a large cohort (N=1000) of CRC patients. By examining three distinct tumour regions (invasive margin, tumour center, and luminal side), we will also assess intertumoral heterogeneity of these markers.

Furthermore, we will explore the association between exhaustion marker expression and clinicopathological features, including patient survival, to explore the potential of incorporating this spatial data into the Immunoscore for enhanced prognostic accuracy and personalized treatment guidance in CRC.

1.3.1 Hypothesis

1. We hypothesise that the expression of check point molecules on T cells and macrophages associated with poor survival in CRC patients.
2. The immune active microenvironment of MSI-CRC displays increased check point molecule density and with greater prognostic relevance than in MSS-CRC.

3. Expression of immune checkpoints by the different immune architecture of right and left sided CRC have different prognostic value.
4. Advanced stages of CRC have higher expression of check point molecules and corresponding worse survival.
5. The prognostic value of T cells and macrophages vary according to their location within the tumour mass.

1.3.2 Aims

1. Optimizing a multiplex panel for assessing the exhaustion markers (TIM3, PD1, and LAG3) expression on macrophages (CD68) and CD3 positive cells.
 - Finding the optimum temperature, incubation time, and Ag retrieval buffer for each Ab (LAG3, PD1, TIM3, CD68, CD3, CK) via chromogenic IHC.
 - Finding the optimum position for each Ab with chromogenic IHC and then in mIHC.
 - Finding the optimum pair of opal (480, 520, 570, 620, 690, 780) with each Ab
 - Generating library slides as a guide for Inform software to unmix components properly.
2. Staining four different samples (Adjacent normal, Invasive margins, center of tumour, Luminal side) per patient from a cohort of 1000 CRC patients according to the optimized panel, scanning, training with Inform software, and analyzing the Inform output according to the hypothesis.

Chapter 2: Materials and Methods

2.1 Patients

This study was conducted on tissue microarrays (TMAs) constructed from tumour samples of 1000 CRC patients who were treated at Nottingham University Hospitals NHS Trust between 2008 and 2012. The average follow-up period for these patients was 53.6 months. Cancer specific survival was tracked from the date of the primary surgical treatment to time of death due to cancer. This study involved human participants and had the approval of East Midlands- Leicester Centre Research Ethics committee (REC reference 23/EM/0079). The written informed consent of the patients was collected. 56.85% (568) patients were biologically male and 43.2% (432) were biologically female. The median age was 69 (range 16-94) with clinical stages: 16% stage I, 40% stage II, 32% stage III and 12% stage IV. Further details on tumours characteristics have been published previously [191] (**Table 3**). Four cores (sections) were taken from distinct regions within each tumour: Adjacent Normal (AN), Invasive Margin (IM), Center of Tumour (CT), and Luminal Side (LS) as shown in **Figure 10**, **Figure 11**.

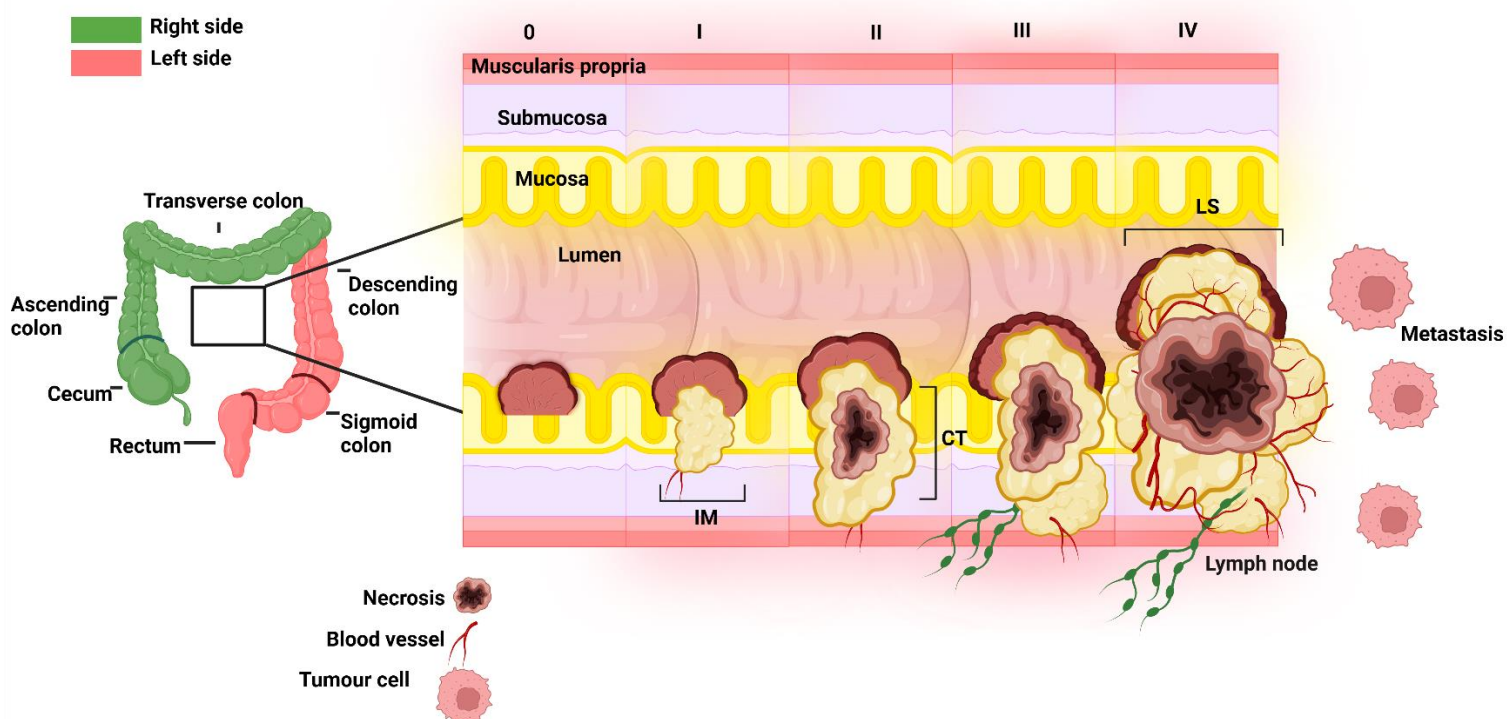


Figure 10. Schematic illustration of CRC sidedness and staging (Stages 0-IV), based on the TNM classification.

The diagram shows the colorectal sidedness in the left which is divided into two colors, right: green and left: red. Right side shows the tumour growth from the luminal side (LS) through the layers of the colon wall, including mucosa, submucosa, and muscularis propria. Three main compartments of tumour tissue is depicted as invasive margin (IM), where angiogenesis occur and the tumour is actively invading into the surrounding normal tissue; the tumour center (CT) with areas of necrosis in later stages is hypoxic and nutrient-deprived, leading to cell death. LS is the area where tumour contacts with the lumen. Lymph node involvement is the main feature of Stage III; and distant metastasis is the prominent feature of Stage IV which is shown through massive access to the blood supply . The inset indicates the anatomical location within the right and left colon.

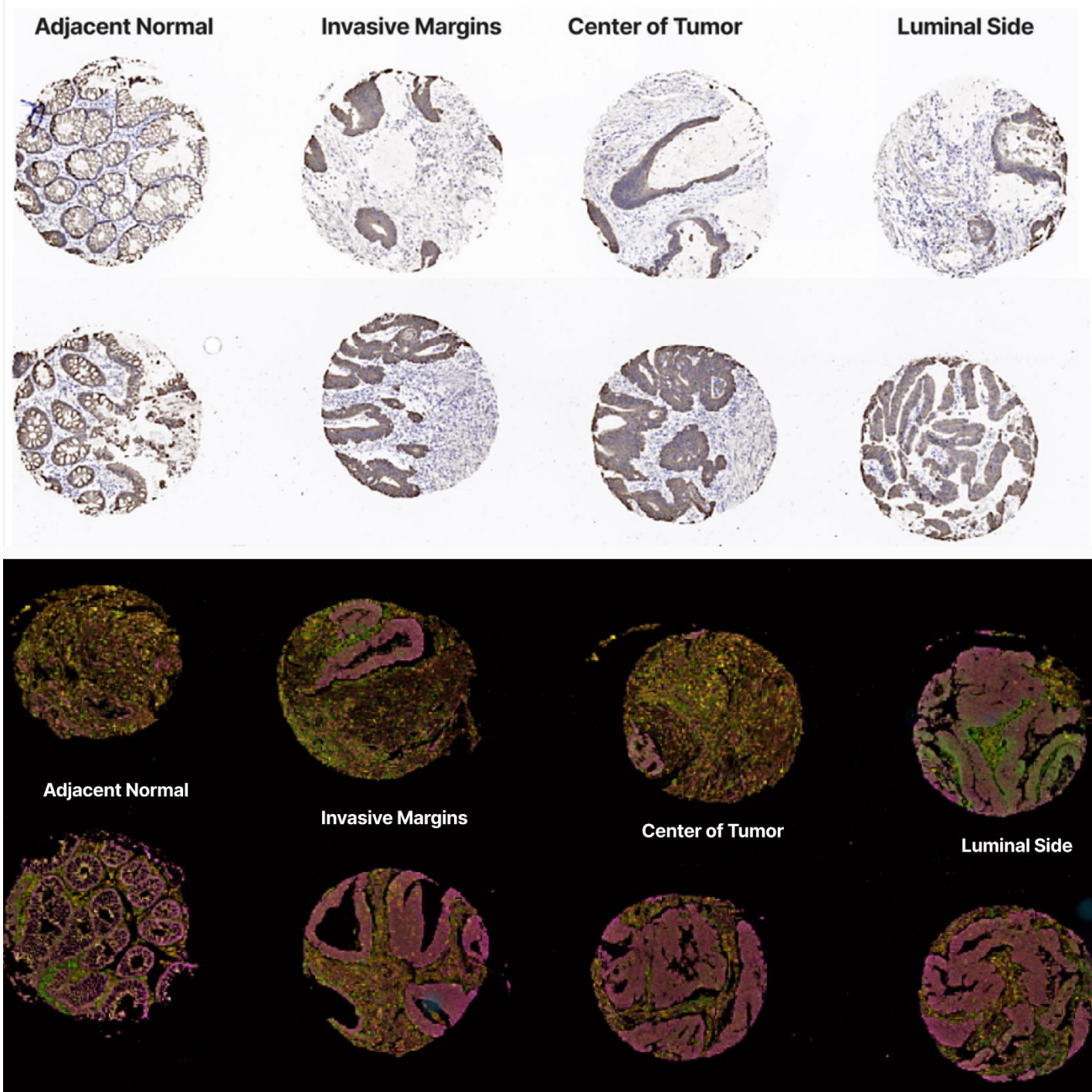


Figure 11. Tissue Cores from Four Patients with Colorectal Cancer.

This upper figure displays pseudo-colored images of tissue cores obtained from two different CRC patients, the lower showing tissue cores from two other patients with fluorescent m-IHC staining. Four cores were taken from distinct regions within each tumour: Adjacent Normal tissue, Invasive Margin, Center of Tumour, and Luminal Side. The images

were obtained from pseudopathological view of Phenochart software for cytokeratin. Brown is Cytokeratin and blue is DAPI.

Table 3. Summary of the clinicopathological characteristics of the patient cohort.

[191]N; number, DSS; disease free survival, SE; standard error.

Clinic-pathological parameters		N (%)	mean (DSS) months	SE	95 %Confidence interval		Survival distribution (Log rank-mantel cox) of overall colorectal patients	
					lower	Upper	Z (or Chi-square)	P-value
Gender	Male	568 (56.8%)	99.9	1.861	92.9	100.2	1.51	0.219
	Female	432 (43.2%)	96.6	1.853	96.3	103.6		
	Overall	1000	101.2	1.39	98.51	104		
Age	(<69)	489	101.2	1.91	97.48	104.9	0.004	0.95
	(>69)	511	96.65	1.88	92.98	100.32		
	Overall	1000	101.2	1.39	98.51	103.9		
N-Regional lymph node	N0 (No lymph node metastasis)	570 (58.5%)	106.82	1.23	104.41	109.23	103.35	0
	N1 (Regional lymph node metastasis)	405(41.5%)	78.79	2.36	74.18	83.42		
	overall	975 (100%)	96.26	1.313	93.69	98.83		
Metastases (M)	M0 (no distant metastasis)	881 (88.1%)	107.6	1.28	105	110	272.73	0
	M1 (Distant metastasis)	119 (11.9%)	45.3	4.037	37.4	53.22		
	Overall	1000	101.2	1.39	98.51	103.97		
Site of Primary Tumour	Right colon	461 (46.1%)	93.07	1.87	89.41	96.74	3.995	0.262
	Left colon	363 (36.3%)	99.53	2.33	94.95	104.17		
	Rectal	147 (14.7%)	98.02	2.76	92.61	103.4		

	Unknown	29 (2.9%)	103.8	5.08	93.85	113.84		
	Overall	1000	101.24	1.39	98.51	103.97		
TNM stage	I	161 (16.1%)	119.2	1.28	116.7	121.7	307.78	0
	II	402 (40.2%)	103.7	1.41	100.9	106.5		
	III	319 (31.9%)	88.8	2.36	84.15	93.43		
	IV	118 (11.8%)	45.4	4.08	37.43	53.45		
	Overall	1000	101.2	1.39	98.51	103.97		
Extramural vascular invasion	Absence	502 (50.9%)	110.9	1.48	108	113.8	56.655	0
	Present	483 (49%)	84.1	2.07	80.13	88.3		
	Overall	985	101	1.404	98.32	103.8		
Microsatellite status	Microsatellite stable (MSS)	818	100.6	1.54	97.59	103.6	2.082	0.149
	Microsatellite instable (MSI)	160	95.07	2.66	89.85	100.2		
	Overall	978	101.5	1.398	98.75	104.2		

2.2 TMA slide preparation

Tissue microarray (TMA) slides utilized for official staining procedures were obtained from pathologists. Slides for optimization purposes were prepared from formalin-fixed, paraffin-embedded (FFPE) tissue blocks previously obtained. Sections were cut at 5 µm thickness using a Leica RM2235 microtome after chilling the blocks in an ice box. Resulting tissue ribbons were floated on a 40°C distilled water bath and individual sections were carefully mounted onto Superfrost™ Plus Adhesion Microscope Slides (Epredia, Cat# J1800AMNZ). Slides were then air-dried vertically for 30 minutes, labeled with the corresponding tissue block ID, and incubated overnight at 37°C to enhance tissue adhesion. Prepared slides were stored at 4°C until required.

2.3 Chromogenic IHC

Chromogenic IHC is vital for optimizing individual antibody parameters and their optimal order in multiplex panels. This method is more affordable for initial testing compared to using expensive Opal fluorophores. The fundamental distinction from fluorescent mIHC resides solely in the final detection step, ensuring robust parameter validation for subsequent complex multi-cycle fluorescent experiments.

TMA slides were heated at 60°C for 1 hour, deparaffinized, and rehydrated using xylene and 100% ethanol, 95% ethanol and 85% ethanol. Slides were soaked in EDTA-based buffer (pH9.0) or citrate-based buffer (pH6.0) and microwaved for 1-minute 1000W and then 14 minutes 200W. Commercially available protein blocking (RE7102, Leica) and peroxidase blocking (RE7101, Leica) agents were used to block the protein and endogenous peroxidase for 5 minutes each. Tris-buffered saline with 0.1% Tween® 20 (TBST) was used for an additional block to decrease the intensity of the background after adding each reagent. Following blocking, the primary antibody was incubated for an appropriate incubation temperature and time as shown in **Table 4**. Next, the post primary (RE7111, Leica) was incubated for 30 minutes, and Novolink polymer (RE7112, Leica) was incubated for 30 minutes. After DAB-Haematoxylin stain, the section was dehydrated following the sequence: 85%, 95%, 100% ethanol, xylene(2x). slides were mounted using DPX mountant (Sigma-Aldrich) and whole-slide images were acquired at 40x magnification using the Phenomager HT system (Akoya Biosciences).

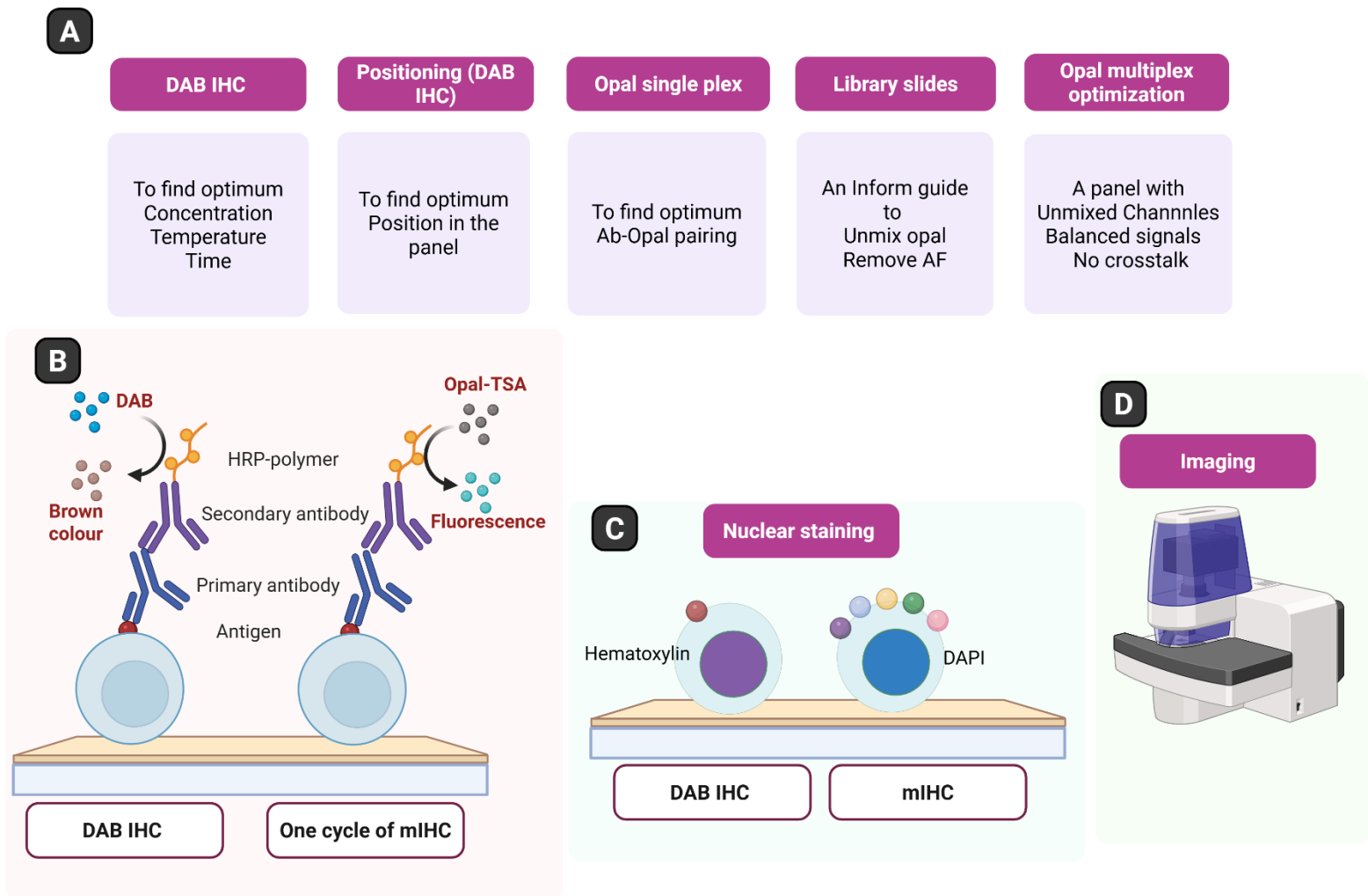


Figure 12. Workflow and Principles of Chromogenic Immunohistochemistry (IHC) and mIHC for Tissue Analysis.

(A) Step-by-step Workflow for Optimizing IHC and mIHC Panels. This diagram, largely based on Akoya guidelines, illustrates the sequential steps involved in developing and optimizing multiplex immunohistochemistry panels initiated with chromogenic IHC. The initial **DAB IHC** step focuses on finding the optimum concentration, temperature, and incubation time for individual antibodies. Following this, **Positioning (DAB IHC)** is crucial to determine the ideal order for each antibody within a multiplex panel. Due to the sequential nature of staining and stripping, positions 1 and 2 behave similarly, as do positions 3 and 4, and positions 5 and 6. Therefore, for each antibody, it is necessary to run three distinct tests, focusing on positions 1, 3, and 5, to identify its best placement in a 6-color panel. Next, **Opal single-plex** aims to find the optimum antibody-Opal fluorophore pairing. **Library slides** refer to an Inform guide used to unmix Opal signals and remove autofluorescence, preparing for complex multiplex analysis. Finally, **Opal multiplex optimization** ensures that the developed panel has three key features: unmixed channels, balanced signals across all fluorophores, and minimal or no crosstalk between colors. **(B) Comparison of Chromogenic IHC and Multiplex IHC Principles.** This section illustrates the fundamental difference between traditional chromogenic IHC (left) and one cycle of mIHC (right). In **DAB IHC**, a primary antibody binds to the antigen, followed by a secondary antibody conjugated to a Horseradish Peroxidase (HRP) polymer. The HRP then catalyzes a reaction with DAB, producing a brown color precipitate at the antigen site. In contrast, **One cycle of mIHC** utilizes an HRP-polymer conjugated secondary antibody that, upon binding, activates an Opal-TSA (Tyramide Signal Amplification) reagent. This results in the covalent deposition of an Opal fluorophore (fluorescence) at the antigen site, which remain intact in subsequent cycles. **(C) Nuclear Staining.**

After the antibody staining process, nuclear staining is performed using materials like Hematoxylin or DAPI to visualize cell nuclei in DAB-IHC and mIHC respectively, providing critical morphological context for subsequent analysis. **(D) Imaging.** Both chromogenically and fluorescently stained slides are then imaged using the same specialized device, such as the Akoya Phenolmager, to capture high-resolution images for quantitative analysis.

2.4 Multiplex IHC (mIHC)

Following optimization of antibody concentration, antigen retrieval pH, incubation time, and panel order based on chromogenic IHC results, a six-plex IHC panel was designed to assess macrophage and CD3+ cell immune checkpoint molecule expression in FFPE CRC sections. The final optimized panel demonstrated balanced signal intensity across all fluorophores with minimal bleed-through. Immunostaining was done with the Opal kit (Akoya Bioscience) for the panel in the following order: TIM3 (1:100 dilution, Cell Signaling technology Cat# 45208S), LAG3 (1:100 dilution, Cell Signaling technology Cat# 15372S), PD1 (1:200 dilution, Abcam Cat# ab52587), CD68 (1:300 dilution, Abcam Cat# ab213363), CD3 (1:300 dilution, Abcam Cat# ab16669) and CK(1:250 dilution, BioLegend Cat# 905901) on TMA sections. Slides were deparaffinized and rehydrated in xylene and 100%, 95%, and 85% ethanol, respectively. Antigen retrieval was performed by microwave treatment for 15 minutes with pH6 or pH9 Antigen retrieval (AR) buffer (Akoya Bioscience). Peroxidase and protein block was done for 5 minutes (Akoya Bioscience). TMA sections were subsequently incubated with primary Antibody for 1 hour at room temperature, post primary Antibody (Leica Biosystems, RE7260-K) for 30 minutes, and polymer (Leica Biosystems, RE7260-K) for 30 minutes. After each incubation, slides were washed twice with TBST. Finally, Opal reagent were added in the order prescribed (**Table 4, Figure 13**). Following each cycle, slides were placed in a pH-optimized AR buffer and subjected to microwave treatment to remove previous cycle antibodies. After the final staining cycle, slides were counterstained with Spectral DAPI (Akoya Biosciences) and mounted with ProLong® Diamond Antifade Mountant (Thermo Fisher Scientific).

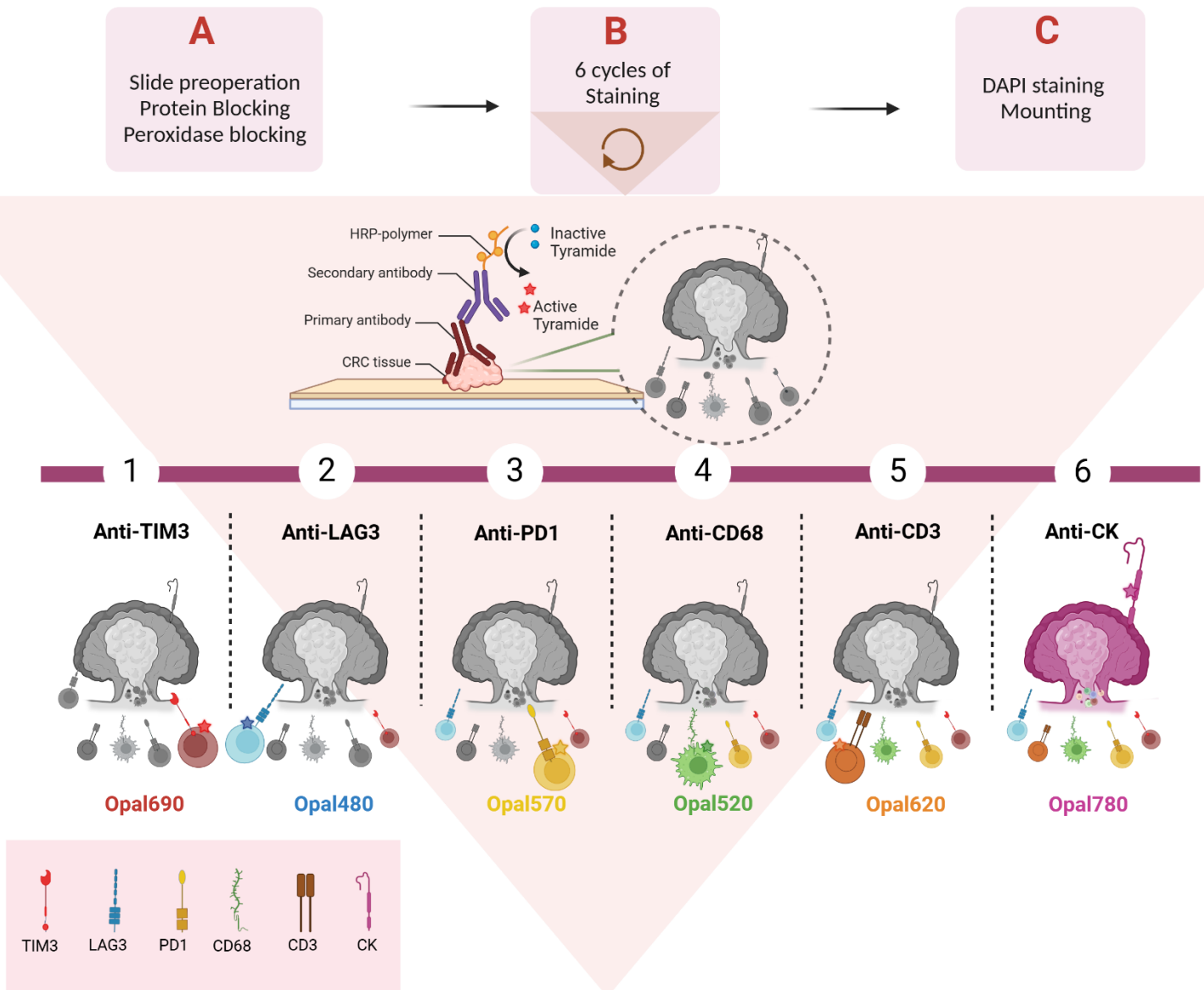


Figure 13. Schematic diagram of a final optimised six-cycle mIHC protocol for staining of FFPE human CRC tissue sections.

The process is divided into three main stages: (A) Slide Preparation: This involves initial steps to prepare the tissue section for antibody staining, including deparaffinization, rehydration, protein blocking (to minimize non-specific antibody binding), and peroxidase blocking (to quench endogenous peroxidase activity). (B) Cyclic Immunofluorescence Staining: The core of the mIHC process, consisting of six iterative cycles of antibody staining, signal amplification, and antibody stripping. Each cycle targets a different antigen. The magnified image in B shows a simplified representation of a single staining cycle, highlighting the interaction between the primary antibody, secondary antibody-HRP conjugate, and the activated tyramide. Step 1: Anti-TIM3/ Opal 690 (red). Step 2: Anti-LAG3/ Opal 480 (cyan). Step 3: anti-PD1/ Opal 570 (yellow). Step 4: Anti-CD68/ Opal 520 (green). Step 5: Anti-CD3/ Opal 620 (orange). Step 6: Anti-CK/ Opal 780 (purple). To visualize the cumulative effect of the staining cycles, the magnified schematic (panel B) progressively adds color with each

step. This represents the stable, covalent binding of each Opal dye to its target antigen's location, even after the primary and secondary antibodies are removed by microwave-based stripping. The dashed lines between each step in the diagram represent the stripping process, emphasizing the tissue's readiness for the next staining cycle. (C) Counterstaining and Mounting: Following the six staining cycles, the tissue section is counterstained with DAPI (to visualize cell nuclei) and mounted with a coverslip for imaging. This mIHC protocol allows for the simultaneous detection and visualization of six different antigens (TIM3, LAG3, PD1, CD68, CD3, and CK) within a single human CRC tissue section.

2.5 Library slides preparation

Six slides were prepared for spectral library generation using a CD8 antibody (Leica Biosystems, Cat# NCL-L-CD8-4B11, RRID: AB_563624, 1:50 dilution), with each slide stained with a single, distinct Opal fluorophore. In addition, an unstained slide was prepared for autofluorescence assessment, and a slide was stained with DAPI. No primary or secondary antibodies were used on the autofluorescence or DAPI-only slides, **Figure 14**.

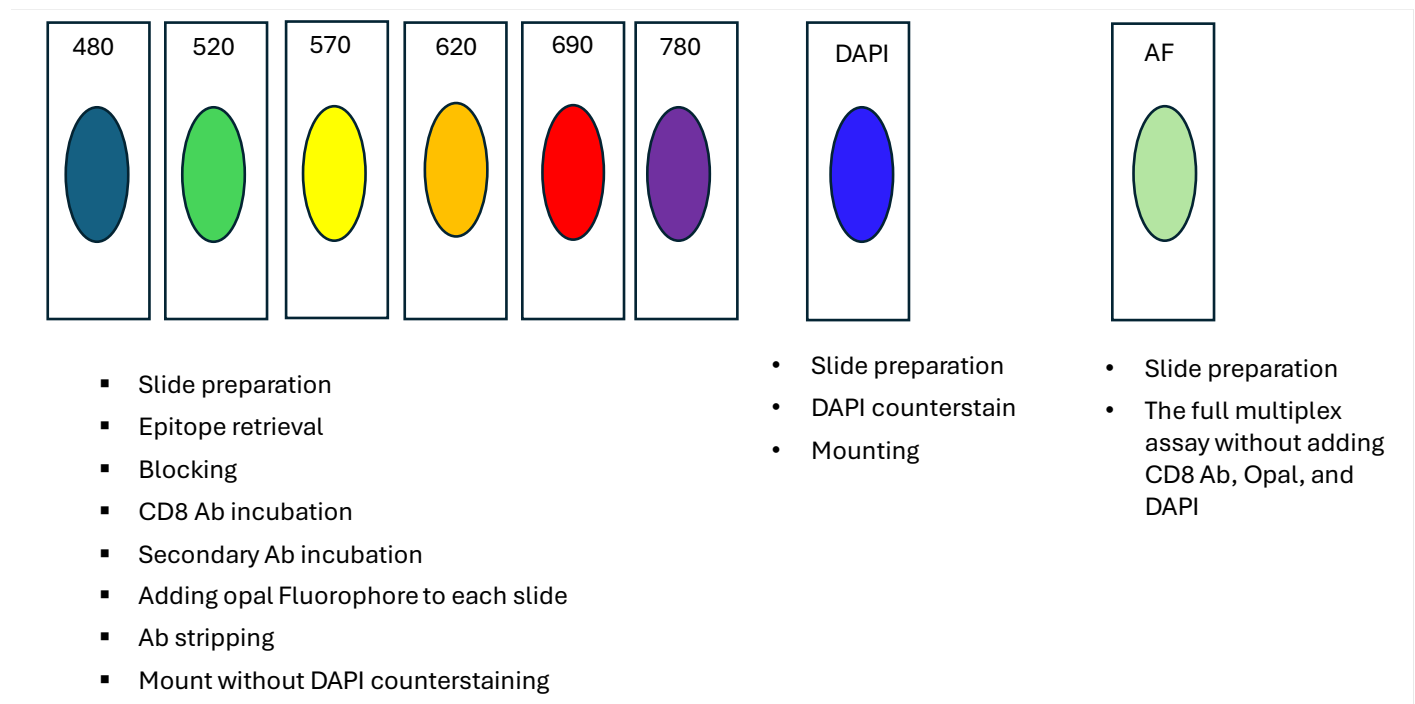


Figure 14. Schematic diagram of single-plex staining procedures for generating a spectral library.

The image illustrates the steps involved in preparing single-plex slides for spectral library construction, each stained with a different Opal fluorophore (Opal 480, 520, 570, 620, 620, 690, and 780). In addition, DAPI and AF slides were also prepared to unmix DAPI and remove autofluorescence.

2.6 Image acquisition, Scanning, and InForm training

The TMA slides were scanned with Phenolmager HT system (Akoya Biosciences) at 20X magnification. Images were annotated via Phenochart (version 2.2; Akoya Biosciences, Marlborough, MA, USA) (Akoya Biosciences). Using the captured spectral data and the spectral library, the TMA core images were decomposed into individual fluorophore components via the InForm software (version 3.0; Akoya Biosciences, Marlborough, MA, USA). In the next step, images were trained via machine learning algorithms of InForm software package in three steps, including tissue segmentation (Tumour-epithelium and Stroma), cell segmentation (DAPI as nuclear signal, CD3 as membrane marker, and CD68 as cytoplasmic marker), and phenotype classifications in one schema. CD3 positive cells are trained as CD3+/LAG3+, CD3+/PD1+, CD3+/TIM3+, CD3+/LAG3+/PD1+, CD3+/LAG3+/TIM3+, CD3+/TIM3+/PD1+, CD3+/LAG3+PD1+TIM3+, and Non ExhaustedCD3+. CD68 positive cells are trained as CD68+/LAG3+, CD68+/PD1+, CD68+/TIM3+, CD68+/PD1+/TIM3+/ Non exhausted CD68. CK positive cells are trained as CK epithelium and finally cells without CD3 and CD68 were trained as exhausted others (if they have expression of any exhaustion markers) and non-exhausted others (if they don't have the expression of exhaustion markers).

Data was exported from InForm in single cell level all manually assessed agree with machine learning training. InForm results then processed with R statistical software. Phenoptr package (<https://github.com/akoyabio/phenoptr>) used for the quantification and spatial determination of cells in the cores.

2.7 Drop-out and stripping efficiency test

Multiplex immunohistochemistry (IHC) is susceptible to several potential sources of error, including signal carry-over, bleed-through, and incomplete antibody stripping. **Carry-over** refers to the persistence of Antibody from a previous staining cycle into subsequent cycles, leading to false-positive signals. This can result from residual antibody bound to the tissue section due to high concentration or long incubation time. **Inefficient antibody stripping** can further exacerbate carry-over by failing to completely remove antibodies from previous cycles. **Bleed-through** occurs when high signal intensity in one channel is detected in adjacent channels. This is particularly problematic when channels are spectrally close, such as DAPI and 480 nm, or 520 nm and 570 nm. Saturated signals, often caused by excessive primary antibody or fluorophore concentration, prolonged incubation times, or high exposure times during image acquisition, significantly increase the risk of bleed-through.

To minimize signal saturation and bleed-through during optimization, we aimed to maintain Opal dye signal intensities between 10 and 30 for 520, 570, 690 channels, with a target range of 1 and 10 for the dimmest Opal dye, 780. The brightest Opal dye, 480, was allowed to have a higher acceptable mean signal intensity of up to 50. By optimizing signal intensities within these parameters, we aimed to minimize bleed-through. To specifically assess the potential for signal carry-over, dropout tests were performed for the TIM3 and LAG3 antibodies. These antibodies were selected due to their similar staining patterns observed in subsequent cycles, raising concerns about possible carry-over.

The dropout tests were conducted as follows: Tissue sections were stained with the first primary antibody (e.g. anti-TIM3) and Opal 690. A second cycle without primary antibody was completed using a different Opal dye. The TMA slides were scanned with Phenoimager HT system, (Akoya Biosciences) at 20X magnification. Providing no carry over of the first cycle was present no signal should be detected in the channel corresponding to the second cycle.

The primary objective of antibody stripping in mIHC is to eliminate all antibodies bound to the tissue section from previous staining cycles. This ensures that signals detected in subsequent staining rounds are exclusively derived from the antibodies applied in the current round, preventing signal carry-over and false-positive results. To assess the effectiveness of our standard microwave-based stripping protocol in removing the antibodies, the following protocols were performed. After completing a standard staining cycle with the anti-TIM3 antibody, the Opal detection step was intentionally omitted. Microwave treatment was then performed as usual, followed by a cooling period. Subsequently, an Opal dye (570), was applied to the section and incubated for 10 minutes. The section was then washed with TBST, counterstained with DAPI, and mounted. This approach allows us to determine if any residual TIM3 antibody remains bound to the tissue after stripping. If stripping is complete, no signal should be detected on channel 570 in a full multiplex experiment.

2.8 Statistical analysis

Cell Density Analysis: Cell densities for each phenotype were quantified from the mIHC images using InForm software (version 3.0; Akoya Biosciences, Marlborough, MA, USA). Comparison between cell density of desired phenotypes in stroma and intraepithelial compartments was done using the Wilcoxon signed-rank test in SPSS software (version 29.0; IBM Corp, Armonk, NY, USA). Comparisons of cell densities between different tissue regions (adjacent normal vs. tumour-associated cores) within each patient were

performed using the Wilcoxon signed-rank test with Holm-Bonferroni correction for multiple comparisons in SPSS software (version 29.0; IBM Corp., Armonk, NY, USA). Comparison of cell densities between unpaired groups (MSI vs. MSS and R-CRC vs. L-CRC) were done via Mann Whitney U test in R (version 4.4.1; R Core Team, Vienna, Austria). Graphs of cell densities were generated using GraphPad Prism (version 10.0; GraphPad Software, San Diego, CA, USA). Heatmaps visualizing the density of desired phenotypes across different cores of individual patients were generated using ggplot2 and reshape2 packages in R (version 4.4.1; R Core Team, Vienna, Austria).

Survival Analysis: For survival analysis, the average cell density of each phenotype was calculated across tumour-associated cores (IM, CT, and LS) for each patient. Optimal cut-off points of these average cell densities were determined using X-tile software (version 3.4.7; Yale University, New Haven, CT, USA). The cut-off points were then used to dichotomize the cell density data into "high" and "low" expression groups for each phenotype using SPSS software (version 29.0; IBM Corp., Armonk, NY, USA). Survival curves were generated using R (version 4.4.1; R Core Team, Vienna, Austria) with the 'survival', 'survminer', and ggplot2 packages. The Kaplan-Meier method was used to estimate survival probabilities, and differences in survival between the high and low density groups were assessed using the log-rank test. Statistical significance for these analyses was defined as a p-value < 0.05.

To investigate potential differences in the prognostic value of the desired cell densities between different tumour locations and MMR status, patients were categorized into two groups based on the primary tumour location: right-sided or left-sided CRC (CRC) and High MMR (MSS) and Low MMR (MSI). Then, within each group, the average cell density of desired phenotype was calculated across tumour-associated cores (IM, CT, and LS) for each patient. Optimal cut-off points, dichotomization, and survival analysis were done as mentioned before. The same methodology was used to investigate prognostic value of the desired cell densities between different section, including AN, CT, IM, and LS.

The prognostic significance of average cell densities within tumour-related cores, was determined with multivariate Cox proportional hazards regression on SPSS (version 29.0; IBM Corp., Armonk, NY, USA). The model included the following covariates: sex, MMR status, vascular invasion, TNM stage, presence of metastases, tumour sidedness, and dichotomized interested cell density. Optimal cut-off points for dichotomizing cell densities into "high" and "low" expression groups were determined using X-tile software (version 3.4.7; Yale University, New Haven, CT, USA).

Correlation Analysis: Spearman's rank correlation coefficients were calculated to assess the correlation between different cell densities. An overall correlation matrix, including all

phenotypes, was generated and visualized using R (version 4.4.1; R Core Team, Vienna, Austria) with the corrplot package. For specific pairwise correlations of interest, Spearman's rank correlation coefficients were calculated using SPSS software (version 29.0; IBM Corp., Armonk, NY, USA).

Spatial and neighborhood Analysis: Cytomap software (version 1.4.21) was used to identify and define distinct tissue regions based on cell density and spatial distribution.

Figure and Image Generation: For image and figure generation, Biorender and Figjam were utilized.

AI using: AI writing assistance was used in preparing this manuscript. Gemini Advanced (Google) and Grammarly aided in proofreading for only grammar and clarity.

Chapter 3: Result

3.1 Optimizing mIHC panel

This study focused on optimizing the mIHC staining protocols for TIM3, LAG3, PD1, CD68, CD3, and CK antibodies to permit the study of T-cell exhaustion in FFPE human CRC sections. Previous students had established optimized protocols for PD1, CD68, CD3, CK, TIM3, and LAG3 monoclonal antibodies. Hence, initial experiments with TIM3 and LAG3, based on prior protocols, utilized overnight incubation at 4°C for both LAG3 and TIM3 Abs. However, further optimization in multiplex panels revealed that a significantly shorter incubation time of 1 hour at room temperature for both TIM3 and LAG3 resulted in improved signal intensity with a reduced background. Antigen retrieval buffer optimization was also performed for TIM3 and LAG3 to have a better signal to background intensity. Additionally, PD1 chromogenic staining was performed alongside TIM3 and LAG3 to help characterize their expression patterns within the tissue.

3.1.1 TIM3 Ab optimization

Initial mIHC experiments on FFPE human CRC tissue revealed challenges in achieving optimal staining quality for the anti-TIM3 antibody. Through an overnight incubation protocol at 4°C in the initial panels, we observed high background staining, in the 690 channel paired with TIM3 Ab (**Figure 15**). This elevated background raised concerns for potential false-positive signals and signal carry-over.

To address these issues, we undertook a comprehensive optimization of the TIM3 staining protocol. First, we evaluated the impact of antigen retrieval buffer pH on staining quality by comparing the results of heat-induced epitope retrieval using buffers at pH 6 and pH 9 via chromogenic IHC (**Figure 16**). Secondly, background signal intensity in chromogenic IHC was reduced by decreasing the incubation time from overnight at 4°C to 1 hour at room temperature. (**Figure 17**). Third, to directly assess the potential for signal carry-over, a two-cycle dropout test was performed. In the first cycle, the tissue was stained with TIM3 antibody paired with Opal 690. The second cycle included only Opal 480 reagent, omitting any primary antibody. In the absence of carry-over, no signal should be detected on the 480 channel. However, a persistent signal in the 480 channel, indicating carry-over of the TIM3 signals from the first cycle, **Figure 19**. This carry-over effect is likely attributed to either an excessively high concentration of Opal 690 dyes or TIM3 antibodies, or to

insufficient antibody stripping between cycles. Consequently, the efficiency of microwave-based antibody stripping was assessed, **Figure 20**.

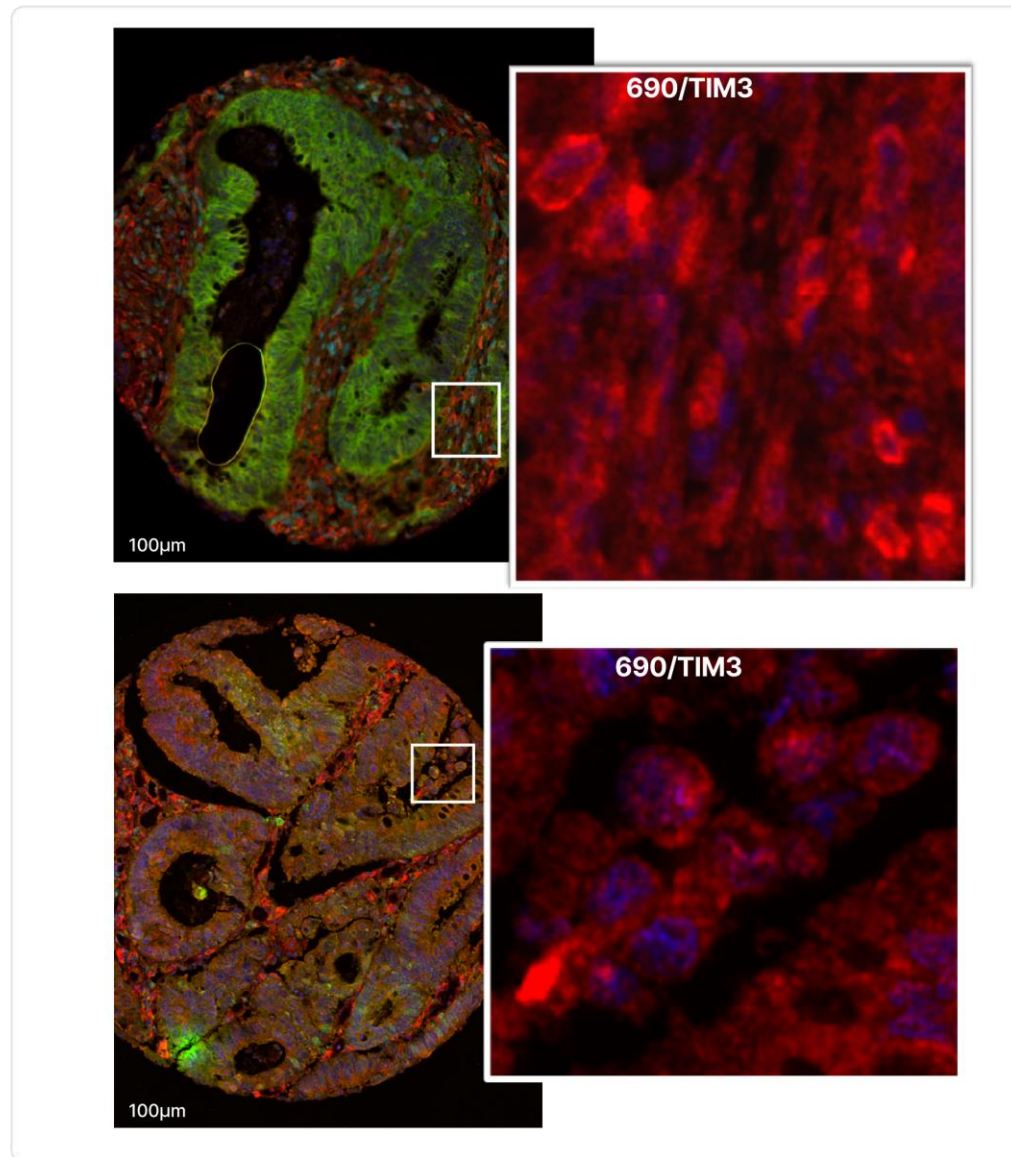


Figure 15. High background staining observed with overnight incubation of TIM3 antibody in a mIHC panel on human CRC tissue from two cores (patients).

(Left) Representative image of tissue sections stained TIM3 (Red, detected at 690 nm). TIM3 antibody was used at the first position in a 1:400 dilution and incubated overnight at 4°C. Magnified view of the boxed region, showing 690 channels. Although positive cells are clear, the high background staining, in the 690 nm channel for TIM3 was detected, which could potentially lead to false-positive interpretation of TIM3 expression and carry over to other channels.

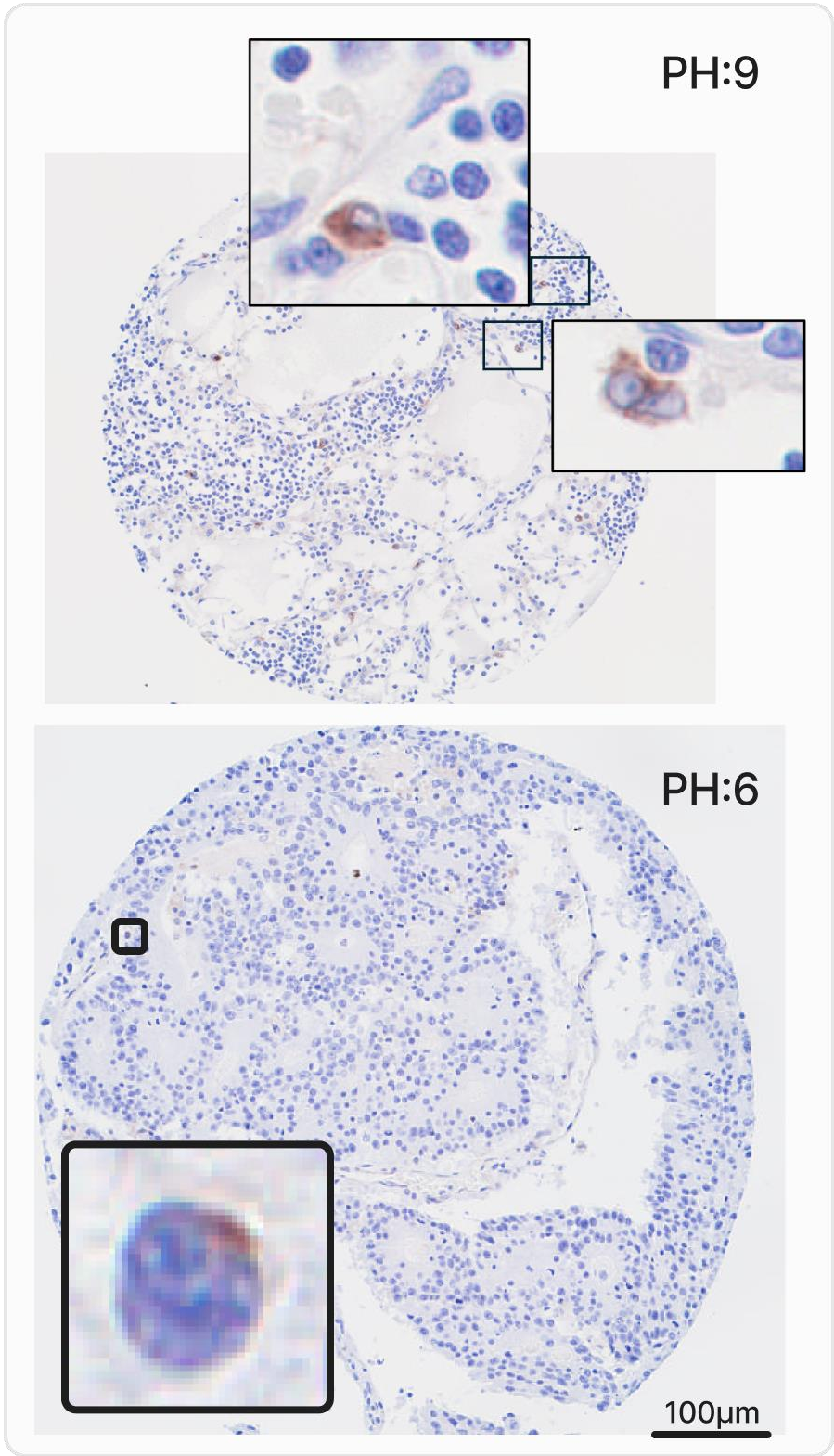


Figure 16. Comparison of TIM3 IHC staining in human CRC tissue (one patient) using antigen retrieval buffers at pH 6 and pH 9, showed PH9 as the optimized PH.

Sections from same patients in two different tests were subjected to heat-induced epitope retrieval with either a pH 6 (Citrate-based buffer)(bottom) or pH 9 (top) (EDTA-based buffer). IHC staining was performed using an anti-TIM3 antibody at a 1:100 dilution and a 1-hour incubation at room temperature. A weak signal for TIM3 was observed with the pH 6 buffer compared to the strong staining of pH 9 buffer. Insets show magnified views of representative cells, highlighting the difference in staining intensity.

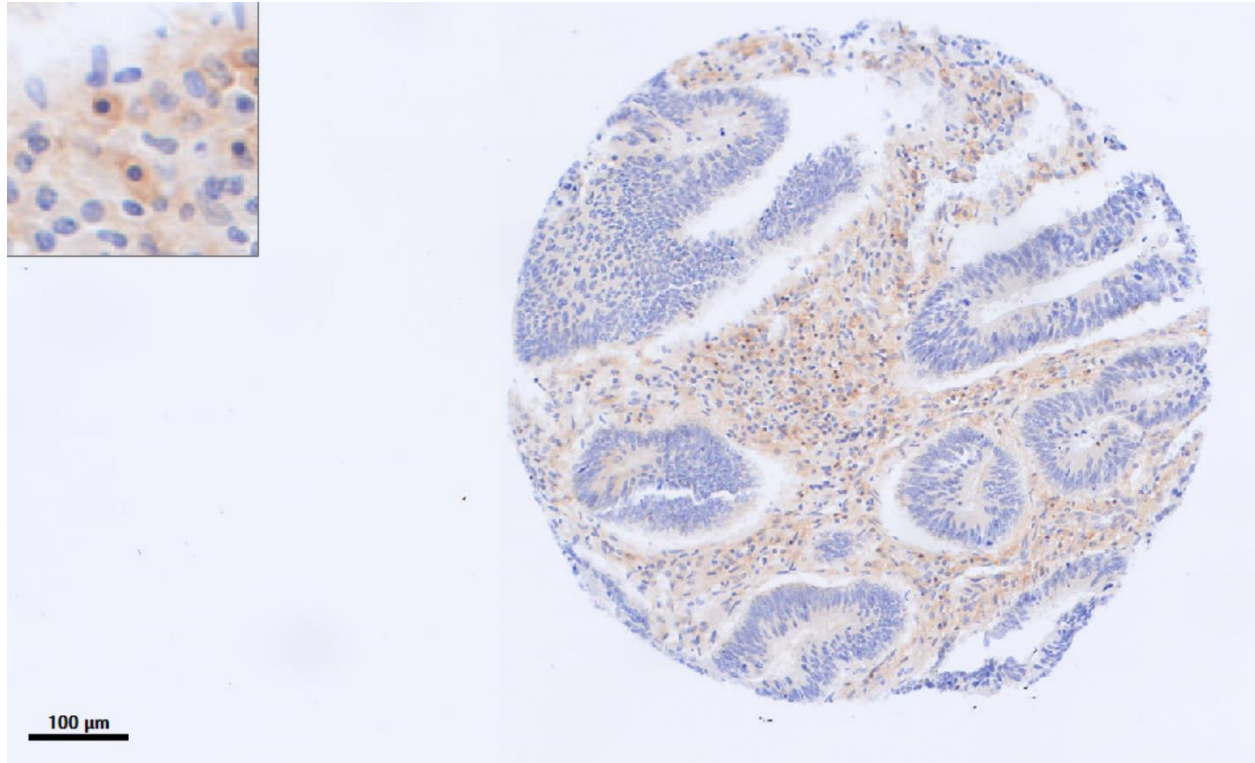


Figure 17. High background observed with overnight incubation of TIM3 antibody on human CRC tissue (one core).

IHC staining for TIM3 was performed on a human CRC tissue section using an anti-TIM3 antibody at a 1:200 dilution and an overnight incubation at 4°C after heat-induced epitope retrieval with a pH 9 buffer. While some specific staining is apparent (inset, magnified view), there is substantial background staining throughout the tissue section, potentially obscuring accurate interpretation of TIM3 expression.

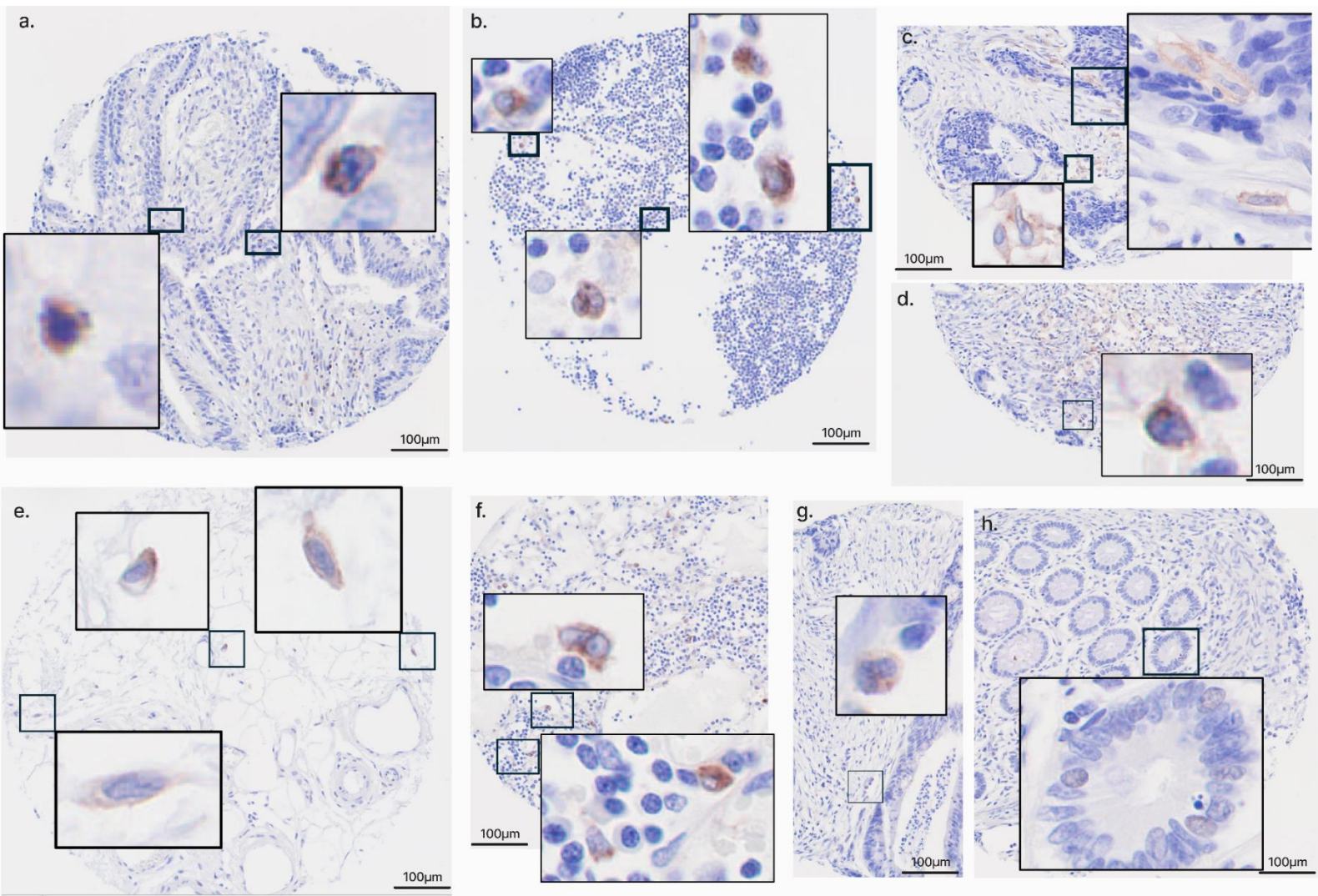


Figure 18. TIM3 IHC staining on CRC human tissue sections using a 1-hour incubation at room temperature and pH 9 antigen retrieval in different cores (patients).

Final Optimized TIM3 IHC staining. Representative images from different tissue cores (patients), demonstrating predominantly cytoplasmic and membranous staining patterns with minimal to no background staining in most cores. (h) In some cores (h), nuclear staining of tumour cells was also observed.

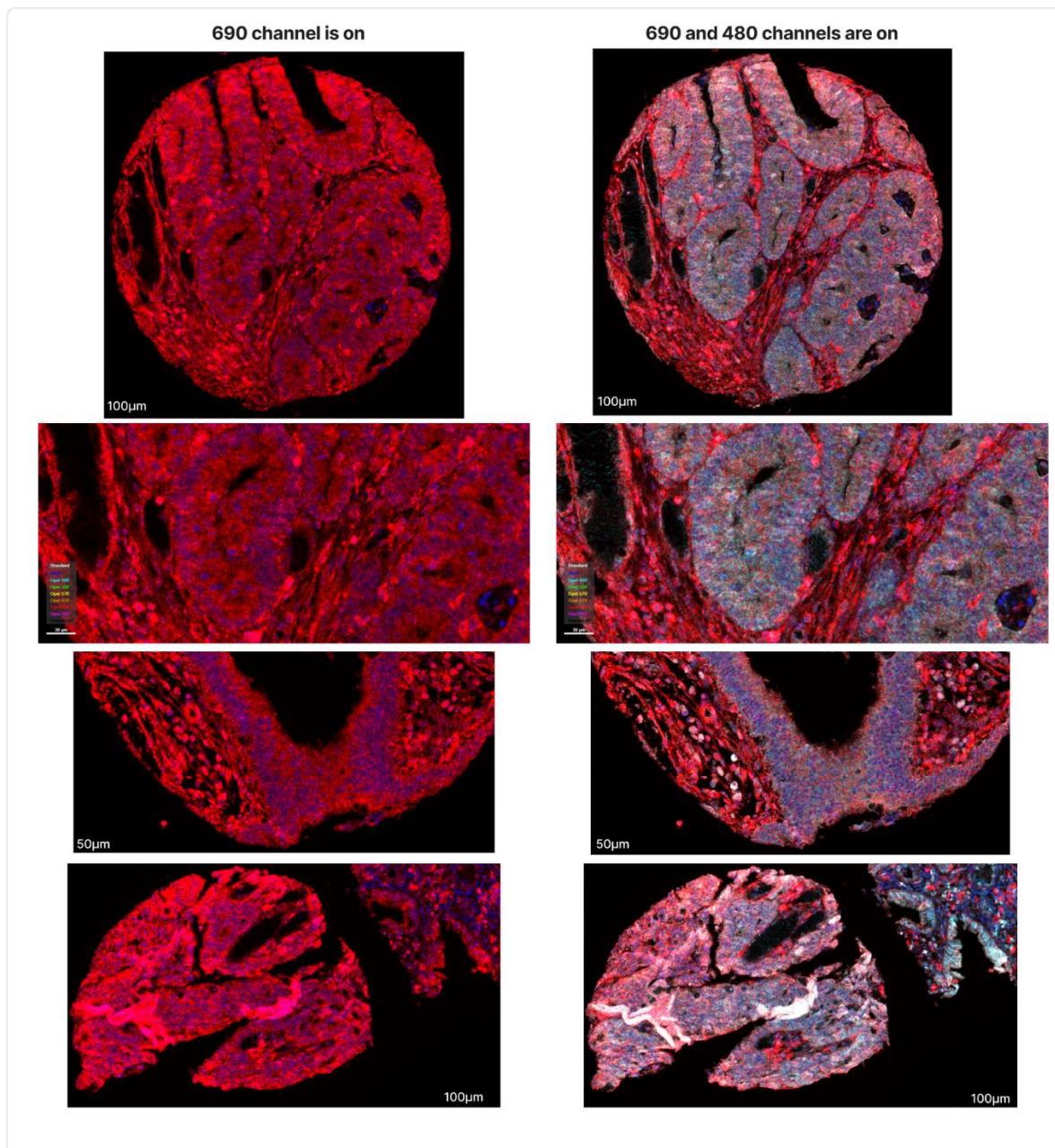


Figure 19. Dropout test demonstrated signal carry-over in a two-cycle mIHC experiment targeting TIM3 on CRC tissue sections.

In the first cycle, tissue sections were stained with an anti-TIM3 antibody in a 1:400 dilution and incubated overnight at 4°C, detected using Opal 690 (red, left column). The second cycle included only Opal 480 (cyan, right column) without any primary antibody. Images in the left column show the signal from the 690 channel of the first cycle. Images in the right column show the combined signal from both 480 and 690. Ideally, no signal should be detected in the 480 channel in the absence of a primary antibody. However, a persistent signal observed on the 480 channel that mirrors the staining pattern seen on the 690 channel indicating carry-over of the TIM3 signal, likely due to either an excessively high concentration of Opal 690 or TIM3 antibody in the first cycle, or to insufficient antibody stripping between cycles. The carry-over effect suggests that in a standard multiplex panel, a portion of the signal attributed to the second antibody (e.g. LAG3) might originate from residual TIM3 antibody from the previous cycle, leading to potential false-positive results.

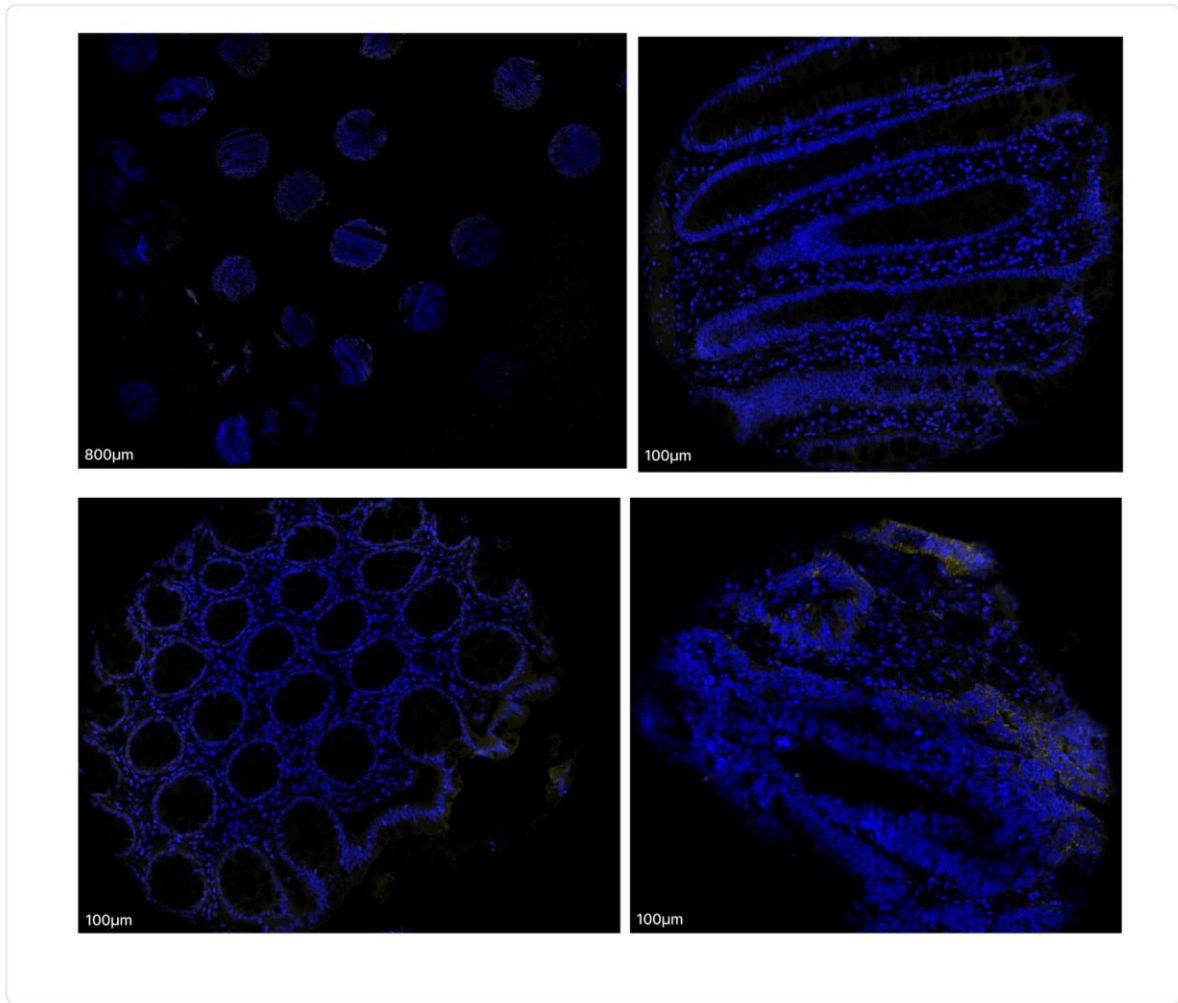


Figure 20. Evaluation of microwave-based antibody stripping efficiency in a mIHC panel using a TIM3 antibody on CRC tissue sections in different patient samples (Cores).

To assess stripping efficiency, a modified staining protocol was employed. In the first cycle, tissue sections were stained with a TIM3 antibody. No Opal dye was added following the antibody incubation in this cycle. Microwave treatment was then performed like the standard multiplex protocol. After cooling, the sections were incubated with Opal 570 for 10 minutes, washed with TBST, and counterstained with DAPI. Representative images show DAPI (blue) and Opal 570 (yellow) channels. In the majority of the tissue cores (top left, top right, and bottom left images), no Opal 570 signal was detected, indicating effective stripping of the TIM3 antibody. A slight signal was observed in only two out of 100 cores (bottom right image, yellow), which is considered negligible. These results demonstrate the overall effectiveness of the microwave-based stripping protocol in removing antibodies between cycles in this multiplex panel.

In conclusion, the TIM3 antibody (Ab) was successfully optimized for the first position in the panel, utilizing a 1:100 dilution, 1-hour incubation at 37°C, and a pH of 9.0. This Ab was effectively paired with Opal 690 at a 1:100 dilution.

3.1.2 LAG3 Ab Optimization

Using an initial overnight incubation protocol at 4°C for the LAG3 antibody paired with Opal 480, a high background staining was observed (**Figure 21**). In addition, the high mean signal intensity of LAG3 (>100) presented a risk of saturated signals, signal bleed-through into other channels, and carry over. An evaluation of antigen retrieval buffer pH, comparing pH 6 and pH 9 and the effect of reducing antibody incubation time from overnight at 4°C to 1 hour at room temperature was conducted, **Figure 22, Figure 23**.

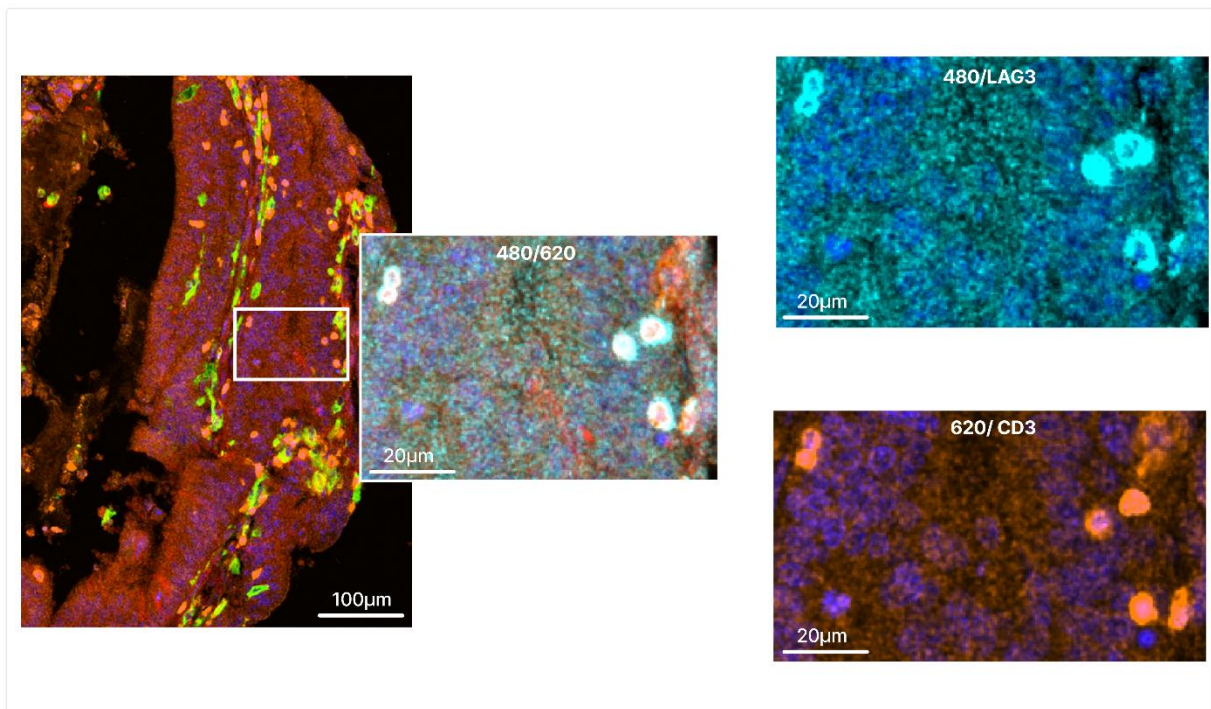


Figure 21. High background staining observed with overnight incubation of LAG3 antibody in a mIHC panel on human CRC tissue in one core (patient).

(Left) Representative image of a tissue section stained LAG3 (cyan, detected at 480) and CD3 (orange, detected at 620). The LAG3 antibody was used at the second position in a 1:100 dilution and incubated overnight at 4°C. Center is the magnified view of the boxed region, showing multiple channels. (Right) Single-channel images extracted from the center panel, with the top showing the 480 channel (LAG3, cyan) and the bottom showing the 620 channel (CD3, orange). The high background staining, in the 480 channel for LAG3 was detected, which could potentially lead to false-positive interpretation of LAG3 expression and bleed through to other channels.

Further examination of the multiplex staining results revealed a concerning similarity in the staining patterns of LAG3 and PD1, detected just after LAG3 in the multiplex panel. Dropout test, shown in **Figure 25**, showed signals on the 570 channel that closely resembled the LAG3 staining pattern from the previous cycle. Given previous experiments demonstrated the effectiveness of stripping protocol (**Figure 20**), the persistent signal strongly suggests that the carry-over is not due to residual LAG3 antibody. Instead, it likely results from an excess of Opal 480 used in the LAG3 detection. Decreasing the concentration of Opal 480 in the full multiplex panel showed satisfactory results, **Figure 26**.

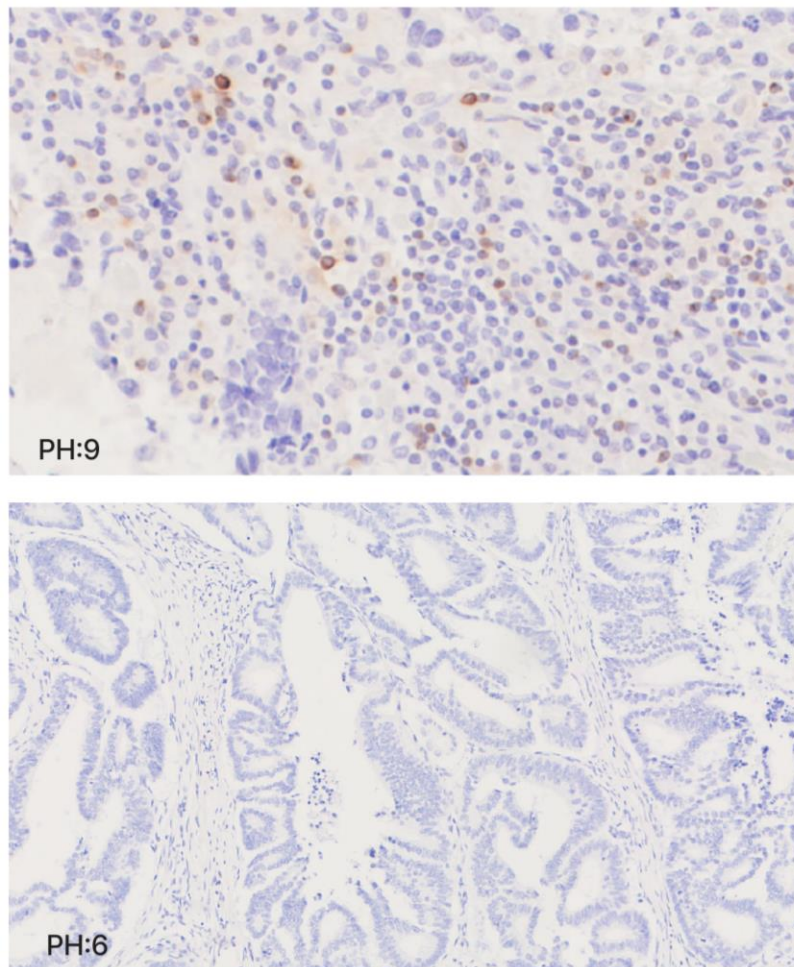


Figure 22. Optimization of pH for LAG3 IHC Staining in Colorectal Cancer in two different cores (patients) showed PH9 as the optimized PH.

The LAG3 antibody was used at a 1:100 dilution with a 1-hour incubation at room temperature. Two different pH levels were tested for antigen retrieval: pH 9 and pH 6. At pH 9, positive staining is observed, indicating successful antigen retrieval and antibody binding. At pH 6, no positive staining is observed, suggesting that this pH is not optimal for antigen retrieval with this particular antibody, concentration, incubation time, and tissue.

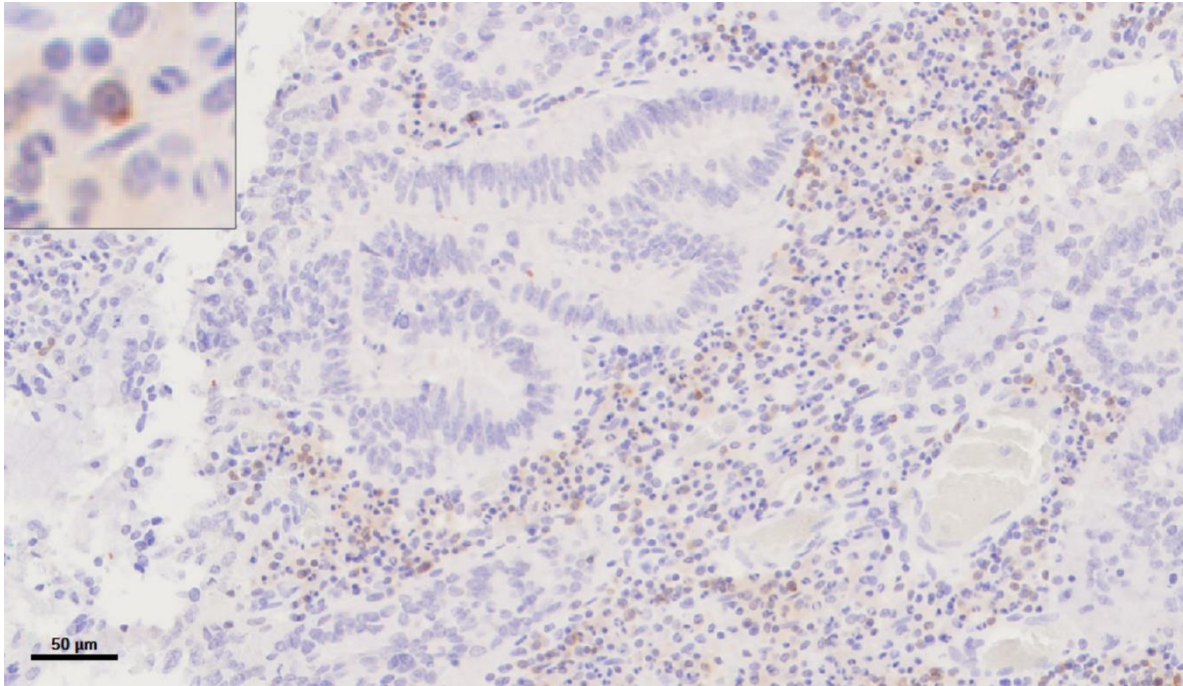


Figure 23. Overnight Incubation for LAG3 IHC in a CRC core (patient).

IHC was performed on human CRC tissue using the LAG3 antibody with overnight incubation at 4°C, a 1:100 dilution, and pH 9 antigen retrieval. Positive staining (brown cytoplasmic and membrane pattern) is observed.

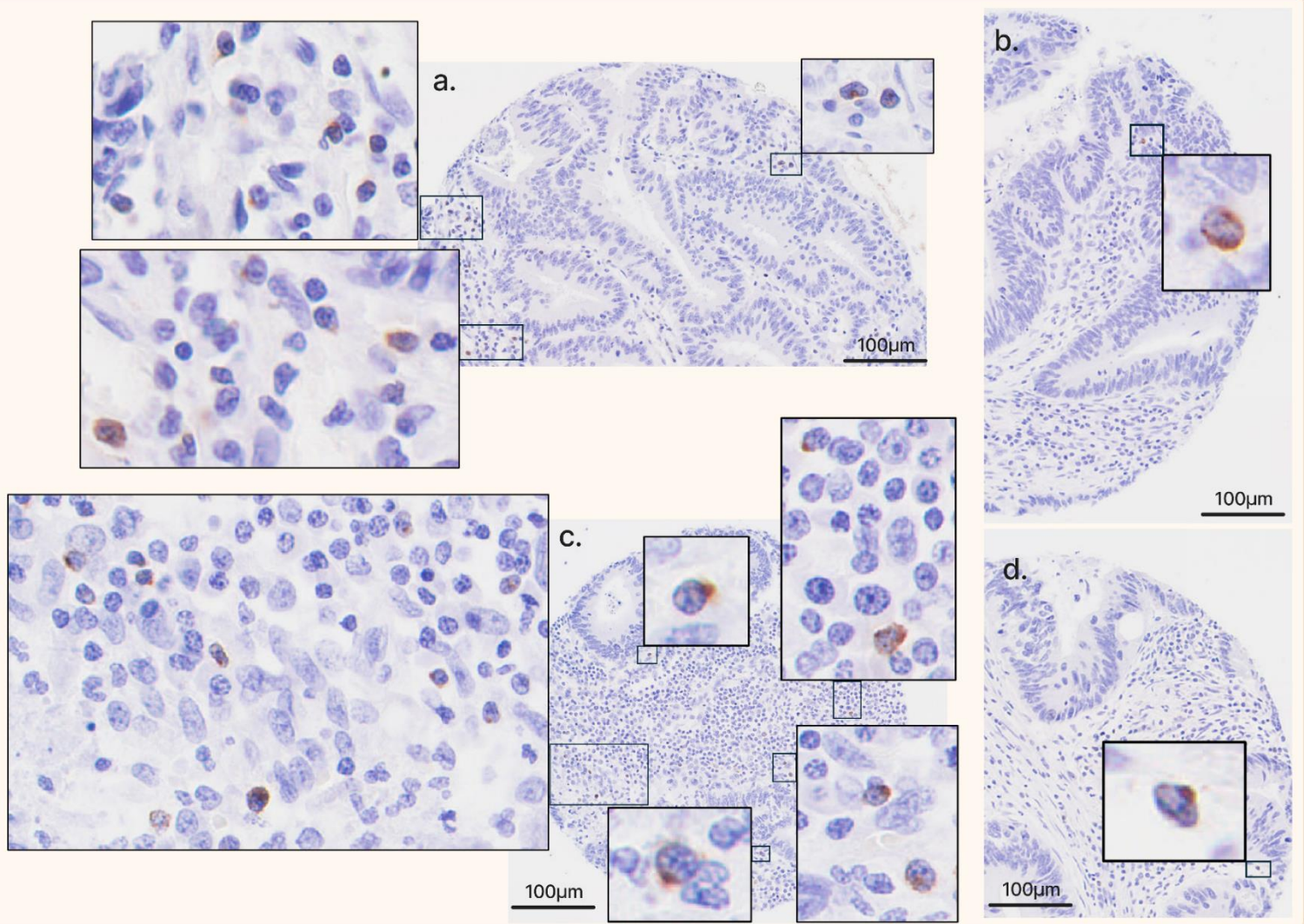


Figure 24. Subcellular Localization of LAG3 (1:100. PH:9, 1h incubation) in CRC Tissue as Demonstrated by Chromogenic IHC in different cores (patients).

The final optimized situation for LAG3 antibody was 1:100 dilution with a 1-hour incubation at room temperature and antigen retrieval at pH 9. Different subcellular staining patterns are observed, suggesting dynamic localization of LAG3. (c,d): Examples of predominantly cytoplasmic LAG3 staining, potentially representing vesicular localization, as indicated by the dot-like pattern (see insets for higher magnification). The circular membrane staining(b) in some cells may represent LAG3 localization to the cell surface following activation. Images show clear backgrounds. Insets show higher magnification views of selected areas, highlighting the subcellular staining patterns.

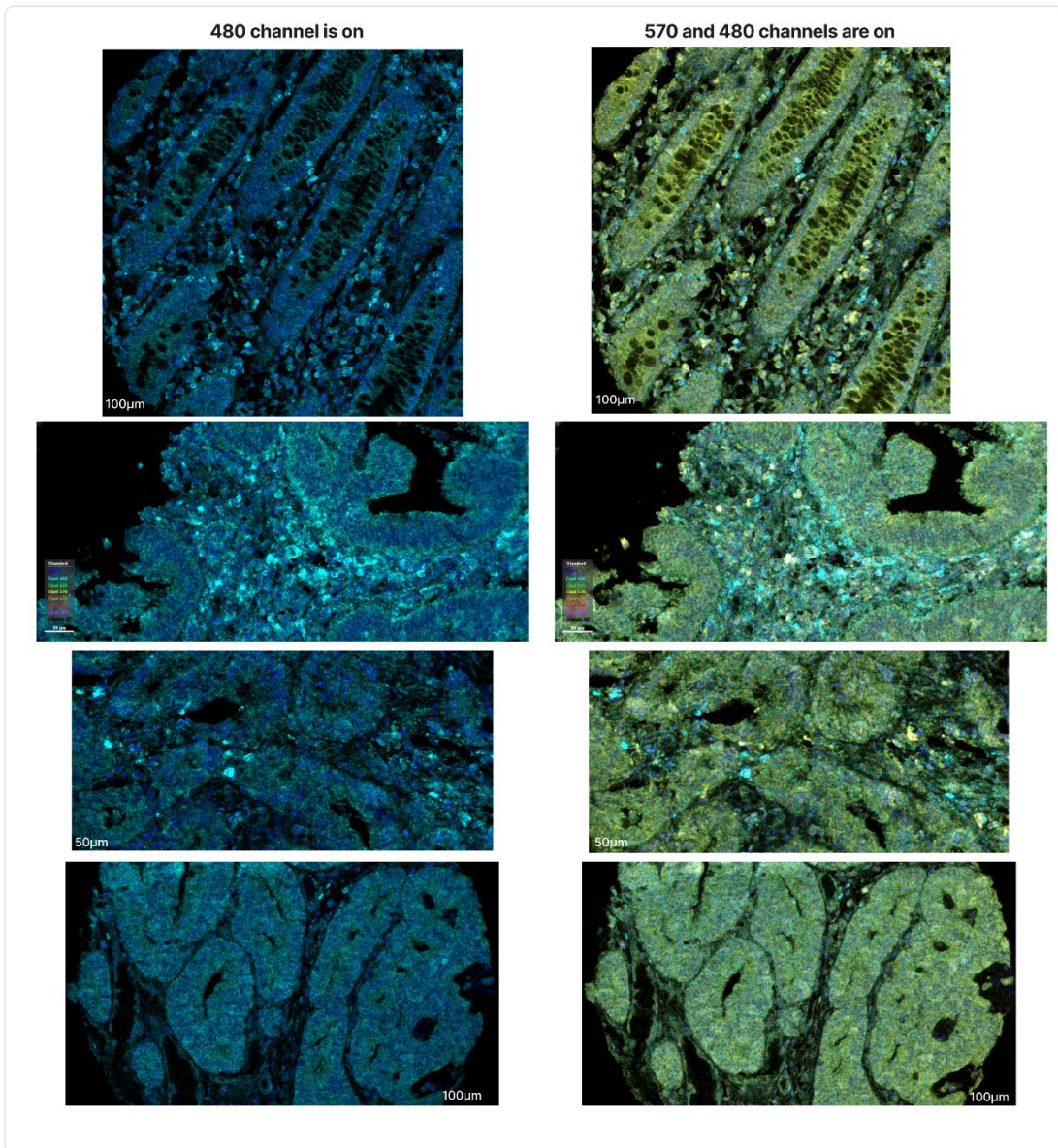


Figure 25. Dropout test demonstrated signal carry-over in a two-cycle IHC experiment targeting LAG3 on FFPE human CRC cores.

In the first cycle, CRC tissue sections were stained with a LAG3 antibody (diluted 1:100 and incubated overnight at 4°C) and detected using Opal 480 (cyan, left column). The second cycle included only Opal 570 (yellow, right column) without any primary antibody. Images in the left column show the signal from the 480 channel after the first cycle. Images in the right column show the combined signal from both the 480 and 570 channels after the second cycle. Ideally, no signal should be detected in the 570 channel in the absence of a primary antibody. However, a persistent signal observed in the 570 channel that mirrors the staining pattern seen in the 480 channel, indicating carry-over of the LAG3 signal to next cycles.

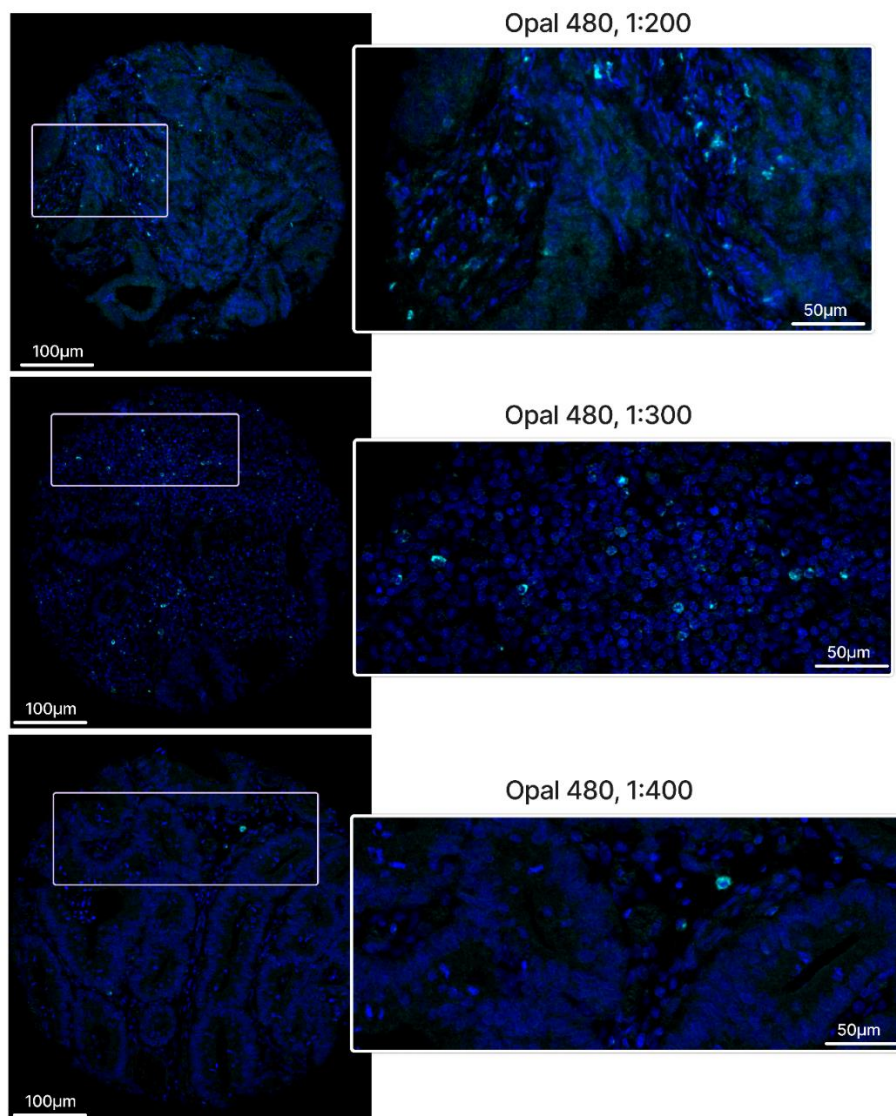


Figure 26. Optimization of Opal 480 concentration for LAG3 detection in a mIHC panel on human CRC tissue sections in different cores (patients).

FFPE human CRC tissue sections were stained with a LAG3 antibody and visualized using different dilutions of Opal 480 in different multiplex panels. (Top) Opal 480 at 1:200 dilution. (Middle) Opal 480 at 1:300 dilution. (Bottom) Opal 480 at 1:400 dilution. Left-hand images show an overview of each tissue section, while right-hand images show magnified views of the boxed regions. While the 1:200 dilution resulted in high background, the 1:300 dilution yielded acceptable background in most tissue cores. However, the mean signal intensity for LAG3 at the 1:300 dilution was 54 (range: 35-120), exceeding the target maximum of 50 and raising concerns about potential bleed-through into adjacent channels or signal carry-over to subsequent cycles. The 1:400 dilution of Opal 480 demonstrated minimal background and a mean LAG3 signal intensity of 35.6 (range: 21-69), falling within the acceptable range. Therefore, the 1:400 dilution of Opal 480 was selected as the optimal concentration for LAG3 detection in this multiplex panel.

In conclusion, the LAG3 antibody (Ab) was successfully optimized for the second position in the panel. This optimization involved a 1:100 dilution, 1-hour incubation at 37°C, and a pH of 9.0. The Ab was effectively paired with Opal 480 at a 1:400 dilution.

3.1.3 PD1 Ab Optimization

PD1 Ab associated with higher background in the initial panels, **Figure 27**. This mostly came from previous cycles, and was decreased after optimization of TIM3 and LAG3 Ab. To find the pattern of PD1 expression in the tumour and immune cells, chromogenic IHC was done which showed different patterns for the expression of PD1 in which epithelial tumour cells exhibited a nuclear staining pattern compared to the cytoplasmic pattern of immune cells, **Figure 28**.

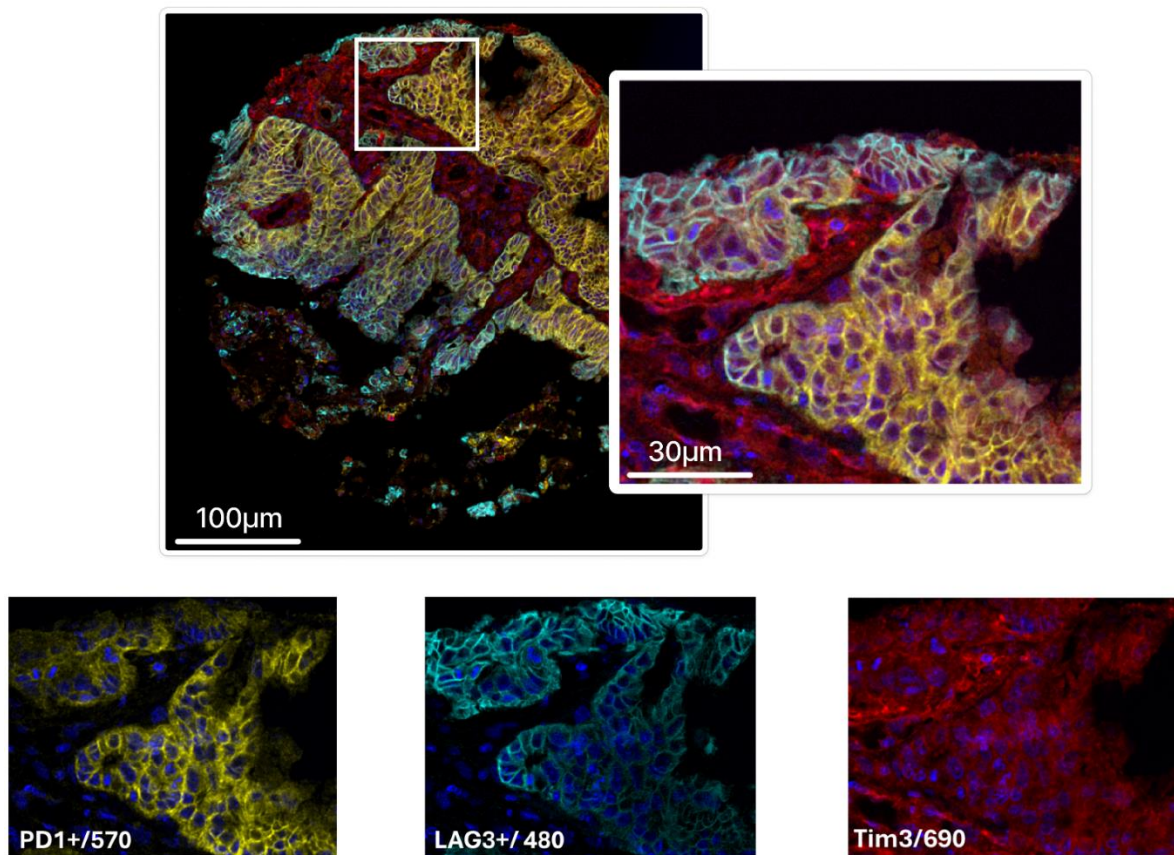


Figure 27. mIHC optimization of human CRC tissue showing high background of PD1, LAG3, and TIM3 in initial panels in one core.

FFPE human CRC tissue sections were stained with a mIHCpanel targeting PD1 (1:200, 1 hour incubation, second position), LAG3 (1:100, overnight incubation at 4°C, first position), and TIM3 (1:400, overnight incubation at 4°C, third position) using Opal reagents (Top Left). Image showing PD1 (yellow), LAG3 (cyan), and TIM3 (red), with nuclei counterstained with DAPI (blue). (Top Right) Magnified view of the boxed region in the top left panel. (Bottom) Individual channels for PD1/Opal 570 (yellow), LAG3/Opal 480 (cyan), and TIM3/Opal 690 (red). Note the presence of high background staining, particularly for TIM3, PD1 and LAG3 is obvious.

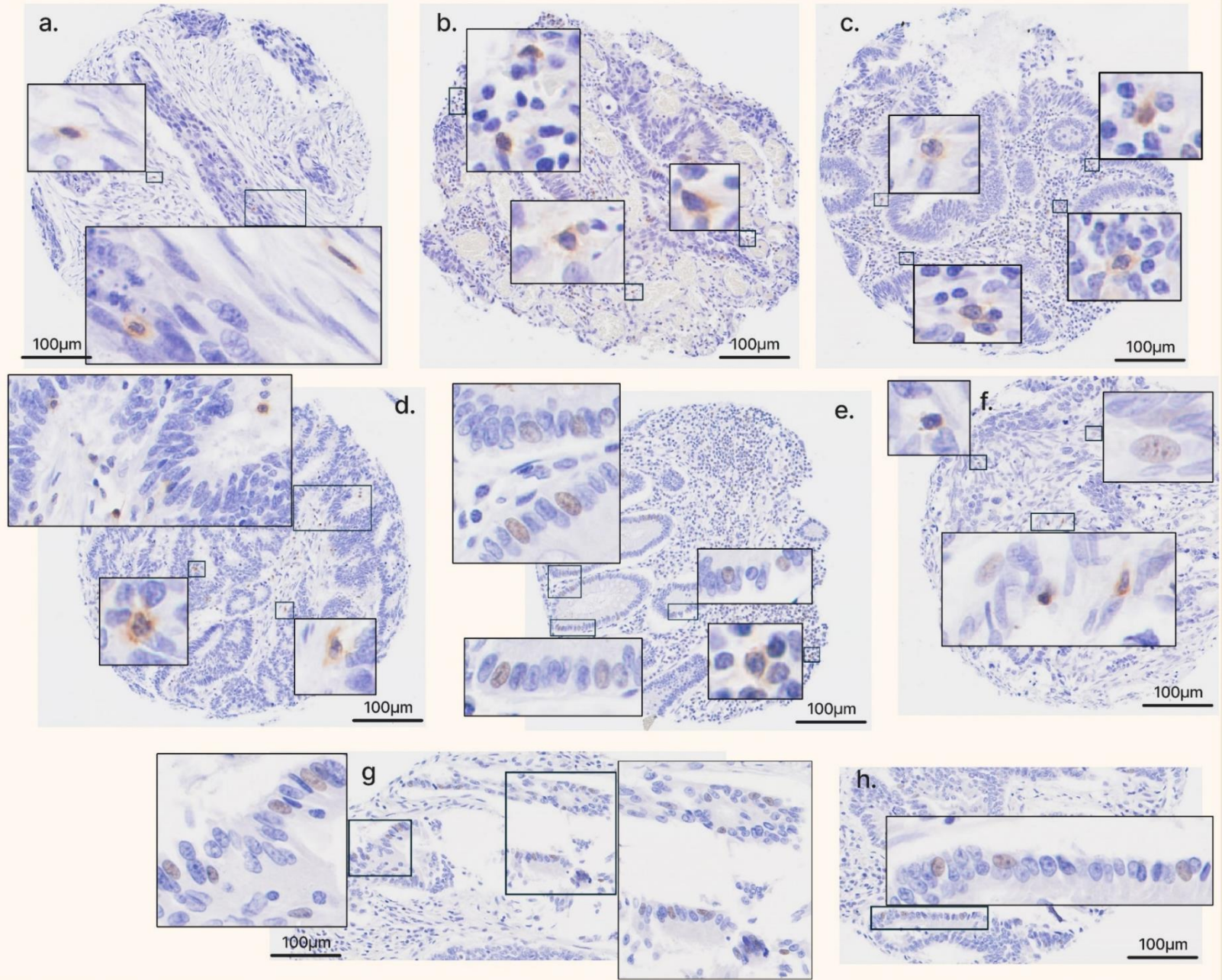


Figure 28. Optimization of PD1 (1:200, PH:9, 1h incubation) immunohistochemical staining in human CRC tissue sections in different cores (patients) reveals cytoplasmic/membrane staining in immune cells and possible nuclear staining in tumour cells.

IHC was performed on human CRC tissue sections to assess the expression pattern of PD1. Sections were stained with an anti-PD1 antibody for 1 hour at room temperature with pH 9 buffer. Detection was performed using DAB chromogen and hematoxylin counterstain. (a-d) Representative images showing predominantly cytoplasmic and/or membrane staining patterns in cells. (e,g,h) Representative images showing nuclear staining patterns in tumour cells.

In conclusion, the PD1 antibody (Ab) was successfully optimized for the third position in the panel. This optimization involved a 1:200 dilution and a 1-hour incubation at 37°C and pH 9.0. The Ab was effectively paired with Opal 570 at a 1:100 dilution.

Multiplex panel Optimization

Following Akoya's guidelines, individual antibodies were first optimized with chromogenic IHC. This optimization informed the selection of appropriate Opal fluorophores for each antibody. Low abundance targets were paired with brighter fluorophores, such as Opal 570 and 480, while high abundance targets were assigned to dimmer fluorophores, such as Opal 690. For potentially co-expressed markers on a cell, spectrally separated Opals, were chosen to minimize the risk of bleed-through. However, based on extensive experience in mIHC within the Tumour Immunology group at the University of Nottingham, it has been demonstrated that optimal single-plex slides often did not translate well to multiplex panels. Therefore, we moved directly to optimizing a multiplex panel. Akoya recommends a signal-to-background ratio (SNR) of 10:1, with signal intensities for most Opal dyes between 10-30. Exceptions include Opal 480, where intensities up to 50 are acceptable, and Opal 780, where intensities between 1-10 are acceptable. In the final optimized panel, Opal signal intensities were within the recommended ranges after testing and refining multiple panel configurations, **Table 4, Figure 29**. Besides checking the specific expected pattern, signal intensity and background were visually assessed in up to 50 cells across multiple cores for each panel, guiding subsequent panel design. This repetitive process ultimately yielded an optimized panel (**Table 4**) with balanced signal intensities and minimal background (**Table 5**), which was then used for staining the official slide set in the current project. The optimized multiplex panel demonstrated good overall performance, with acceptable signal-to-background ratios for antibodies (**Figure 30-44**).

Ab	Ab dilution	Incubation	AR, PH	Opal	Opal Dilution	Exposure Time
LAG3	1/100	Overnight, 4C	9	620	1/150	70 ms
CD3	1/300	1h, RT	6	480	1/150	5.9 ms
PD1	1/200	1h, RT	9	570	1/100	150 ms
CK	1,4000	1h, RT	9	780	1/150	150 ms

Ab	Dilution	Incubation	AR, PH	Opal	Dilution	Exposure Time
LAG3	1/100	Overnight, 4C	9	620	1,100	70 ms
PD1	1,200	1h, RT	9	520	1,100	37.8 ms
Tim3	1,400	Overnight, 4C	9	690	1,100	90 ms
CD3	1,300	1h, RT	6	480	1,200	4.95 ms
CK	1,200	1h, RT	9	780	1,150	150 ms

Ab	Dilution	Incubation	AR, PH	Opal	Dilution	Exposure Time
LAG3	1, 100	Overnight, 4C	9	480	1, 100	12.6 ms
PD1	1, 200	1h, RT	9	570	1, 100	150 ms
Tim3	1, 400	Overnight, 4C	9	690	1, 100	78.5 ms
CD68	1, 300	1h, RT	6	520	1, 150	44 ms
CD3	1, 300	1h, RT	6	620	1, 100	70 ms
CK	1, 200	1h, RT	9	780	1, 150	150 ms

Ab	Dilution	Incubation	AR, PH	Opal	Dilution	Exposure Time
LAG3	1, 100	Overnight, 4C	9	520	1,100	70ms
PD1	1, 200	1h, RT	9	480	1,100	15ms
Tim3	1, 400	Overnight, 4C	9	690	1,100	150ms
CD68	1, 300	1h, RT	6	570	1,100	150ms
CD3	1, 300	1h, RT	6	620	1,100	70ms
CK	1, 200	1h, RT	9	780	50	150ms

Ab	Dilution	Incubation	AR, PH	Opal	Dilution	Exposure Time
LAG3	1, 100	Overnight, 4C	9	480	1, 100	150ms
PD1	1, 200	1h, RT	9	570	1, 100	15ms
Tim3	1, 200	Overnight, 4C	9	690	1, 100	150ms
CD68	1, 300	1h, RT	6	520	1**300	70ms
CD3	1, 300	1h, RT	6	620	1, 100	70ms
CK	1, 200	1h, RT	9	780	1, 150	

Ab	Dilution	Incubation	AR, PH	Opal	Dilution	Exposure Time
Tim3	1, 400	Overnight, 4C	9	690	1, 100	150ms
LAG3	1, 100	Overnight, 4C	9	480	1, 100	15ms
PD1	1, 200	1h, RT	9	570	1, 100	150ms
CD68	1, 300	1h, RT	6	520	1**300	70ms
CD3	1, 300	1h, RT	6	620	1, 100	70ms
CK	1, 200	1h, RT	9	780	1, 150	150ms

Ab	Dilution	Incubation	AR, PH	Opal	Dilution	Exposure Time
Tim3	1, 400	Overnight, 4C	9	690	1, 100	150ms
LAG3	1, 100	Overnight, 4C	9	480	1, 150	15ms
PD1	1, 200	1h, RT	9	570	1, 100	150ms
CD68	1, 300	1h, RT	6	520	1,150	70ms
CD3	1, 300	1h, RT	6	620	1, 150	70ms
CK	1, 200	1h, RT	9	780	1, 150	150ms

Ab	Dilution	Incubation	AR, PH	Opal	Dilution	Exposure Time
Tim3	1, 400	Overnight, 4C	9	690	1, 100	150ms
LAG3	1, 100	Overnight, 4C	9	480	1, 200	15ms
PD1	1, 200	1h, RT	9	570	1, 100	150ms
CD68	1, 300	1h, RT	6	520	1,150	70ms
CD3	1, 300	1h, RT	6	620	1, 200	70ms
CK	1, 200	1h, RT	9	780	1, 150	150ms

Ab	Dilution	Incubation	AR, PH	Opal	Dilution	Exposure Time
Tim3	1, 100	1h, RT	9	690	1, 100	50
LAG3	1, 100	1h, RT	9	480	1,200	10
PD1	1, 200	1h, RT	9	570	1, 100	45
CD68	1, 300	1h, RT	6	520	1,150	25
CD3	1, 300	1h, RT	6	620	1, 200	30
CK	1, 200	1h, RT	9	780	1, 150	70

Ab	Dilution	Incubation	AR, PH	Opal	Dilution	Exposure Time
Tim3	1, 300	1h, RT	9	690	1, 100	50
LAG3	1, 100	1h, RT	9	480	1,200	10
PD1	1, 200	1h, RT	9	570	1, 100	45
CD68	1, 300	1h, RT	6	520	1,150	25
CD3	1, 300	1h, RT	6	620	1, 200	30
CK	1, 200	1h, RT	9	780	1, 150	70

Ab	Dilution	Incubation	AR, PH	Opal	Dilution	Exposure Time
Tim3	1, 100	1h, RT	9	690	1, 100	50
LAG3	1, 100	1h, RT	9	480	1,300	10
PD1	1, 200	1h, RT	9	570	1, 100	45
CD68	1, 300	1h, RT	6	520	1,150	25
CD3	1, 300	1h, RT	6	620	1, 200	30
CK	1, 200	1h, RT	9	780	1, 150	70

Ab	Dilution	Incubation	AR, PH	Opal	Dilution	Exposure Time
Tim3	1, 100	1h, RT	9	690	1, 100	50
LAG3	1, 100	1h, RT	9	480	1,400	10
PD1	1, 200	1h, RT	9	570	1, 100	45
CD68	1, 300	1h, RT	6	520	1,150	25
CD3	1, 300	1h, RT	6	620	1, 200	30
CK	1, 200	1h, RT	9	780	1, 150	70

Figure 29. Optimization of a six-plex immunofluorescence panel for human CRC tissue sections.

The table details the various panels tested, including antibody (Ab) dilutions, incubation times, antigen retrieval (AR) conditions, Opal pairings, Opal dilutions, and exposure times. Each panel aimed to refine staining parameters to achieve optimal signal intensity and minimal background.

Table 4. Antibody and Opal Reagent Incubation Details for the Optimized mIHC Panel in Human CRC Tissue Sections.

Ab	Dilution	Incubation	AR, PH	Opal	Dilution
Tim3	1;100	1h, RT	9	690	1; 100
LAG3	1; 100	1h, RT	9	480	1;400
PD1	1; 200	1h, RT	9	570	1; 100
CD68	1; 300	1h, RT	6	520	1;150
CD3	1; 300	1h, RT	6	620	1; 200
Pan CK	1; 200	1h, RT	9	780	1; 150

Table 5. Signal and background statistics for the optimized mIHC panel in human CRC tissue sections.

Ab	Signal Mean	Signal Range	Background Mean	Background Range
Tim3	13.82	6-18	2.14	1.2-3
LAG3	35.6	21-69	3.1	0-9
PD1	13.175	7-20	1.78	1-3
CD68	27.4	17-46	3.19	1-5
CD3	25.3	11-42	1.25	0-3
Pan CK	7.2	1.5-11	0.1	0-1

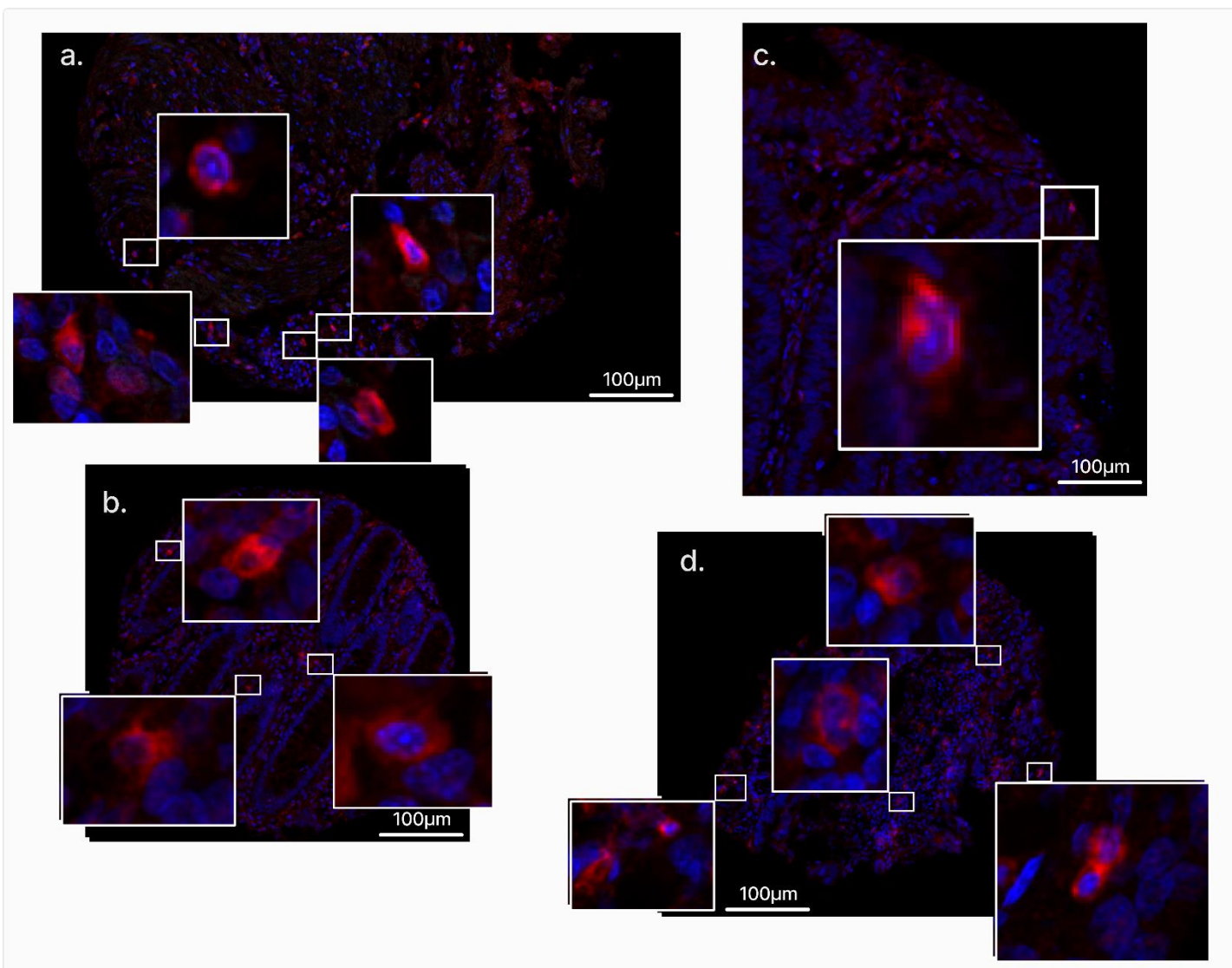


Figure 30. Representative images of TIM3 (Opal 690) expressions in human CRC tissue sections in different cores (patients) stained with the optimized mIHC panel (Table 4).

FFPE human CRC tissue sections were stained with a multiplex panel that included a TIM3 antibody (1:100 dilution) paired with Opal 690 (red) in the first position. Different regions of interest are shown, highlighting the predominantly cytoplasmic and membranous staining pattern of TIM3 in immune cell infiltrates. Insets show magnified views of representative cells.

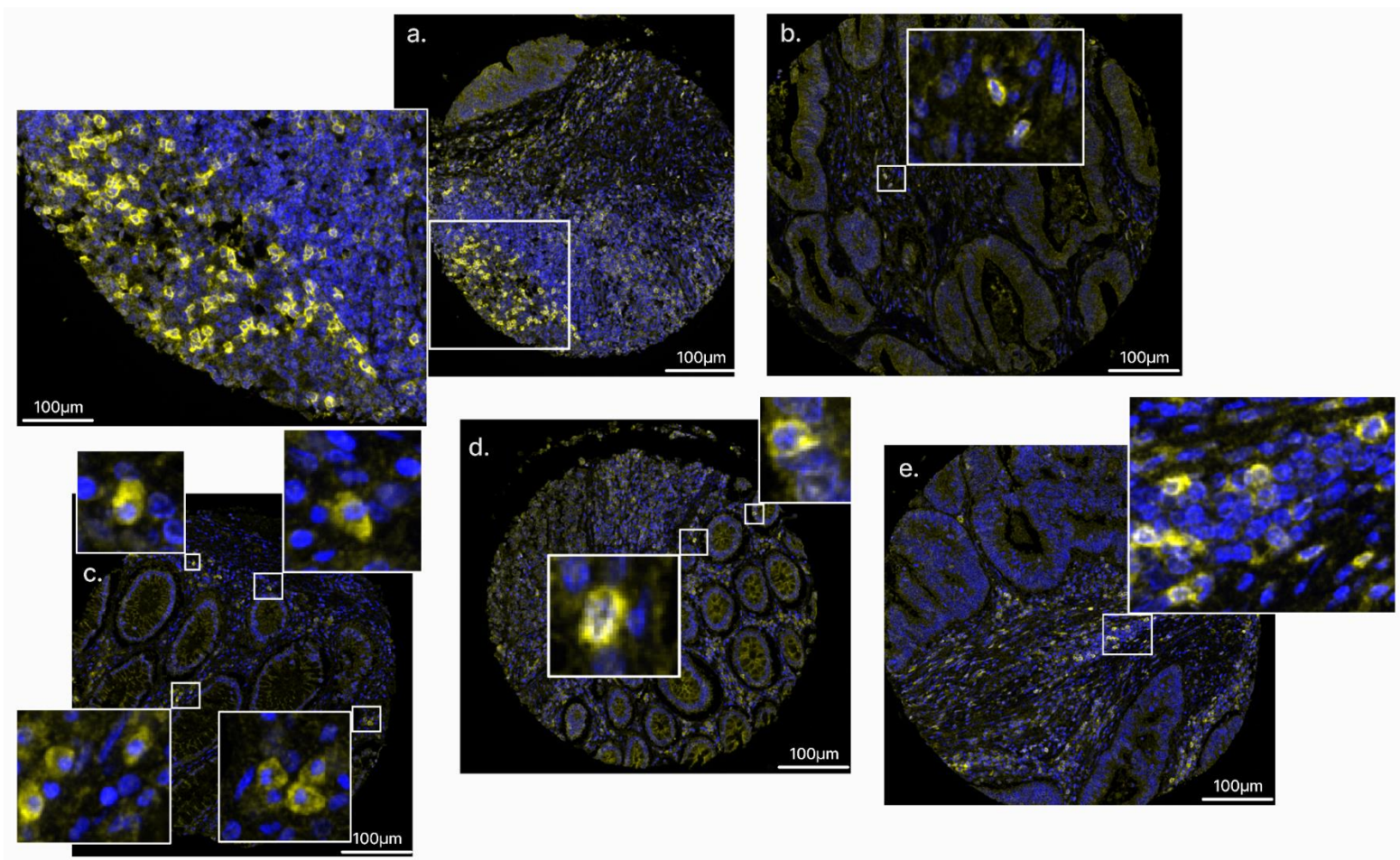


Figure 31. Representative images of PD1 (Opal 570) expression in human CRC tissue sections in different cores (patients) stained with the optimized mIHC panel (Table 4).

FFPE human CRC tissue sections were stained with a multiplex panel that included a PD1 antibody paired with Opal 570 (yellow) in the third position. (a-e) Different regions of interest are shown, highlighting the predominantly membranous and cytoplasmic staining pattern of PD1 in immune cells within the regions. Insets show magnified views of representative cells.

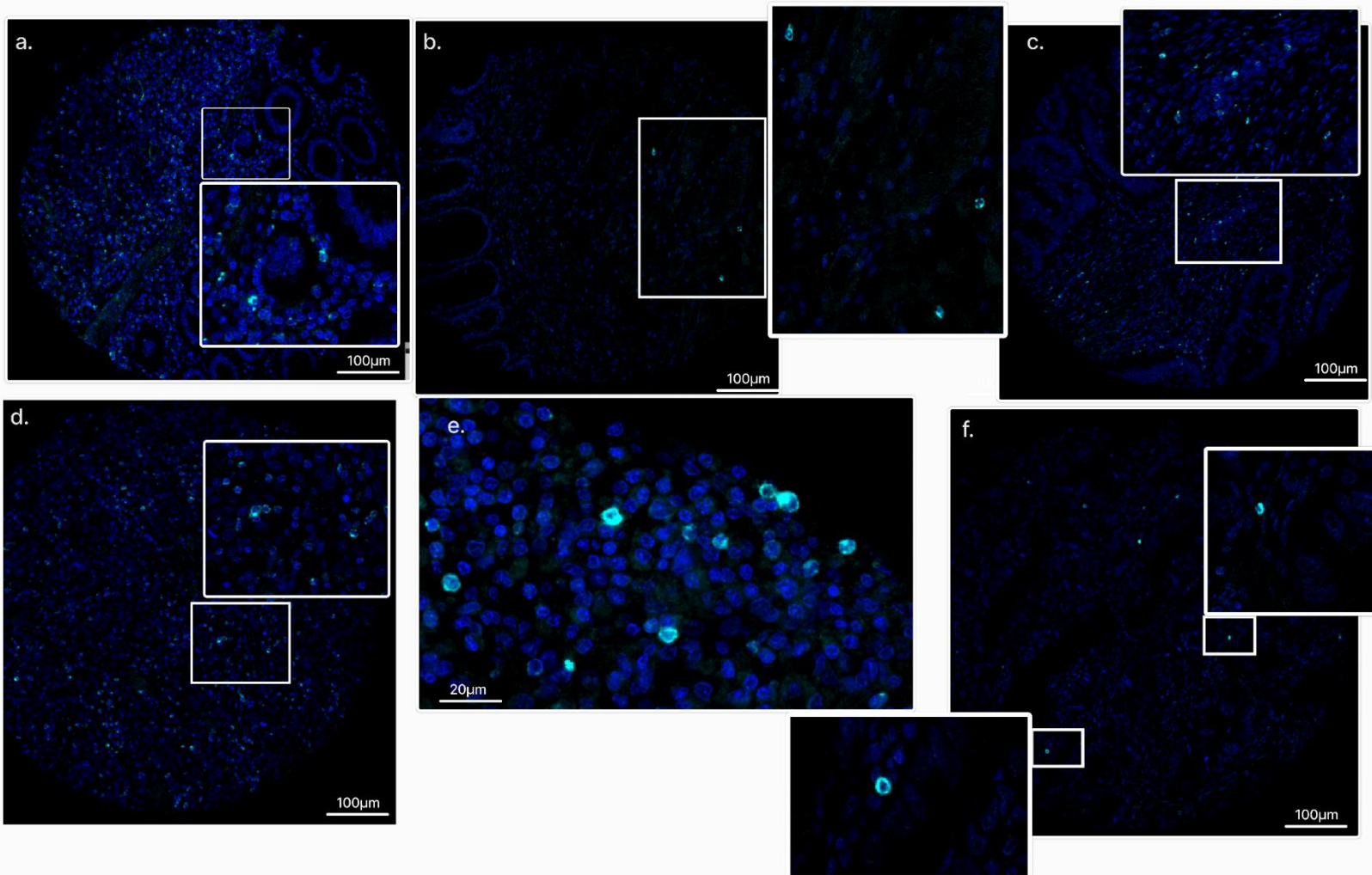


Figure 32. Representative images of LAG3 (Opal 480) expression in human CRC tissue sections in different cores (patients) stained with the optimized mIHC panel (Table 4).

FFPE human CRC tissue sections were stained with the multiplex panel that included the LAG3 antibody (1:100 dilution) paired with Opal 480 (cyan) in the second position. Nuclei were counterstained with DAPI (blue). Different regions of interest are shown, highlighting the predominantly cytoplasmic in intracellular staining pattern of LAG3 in related cells within the regions. Insets show magnified views of representative cells.

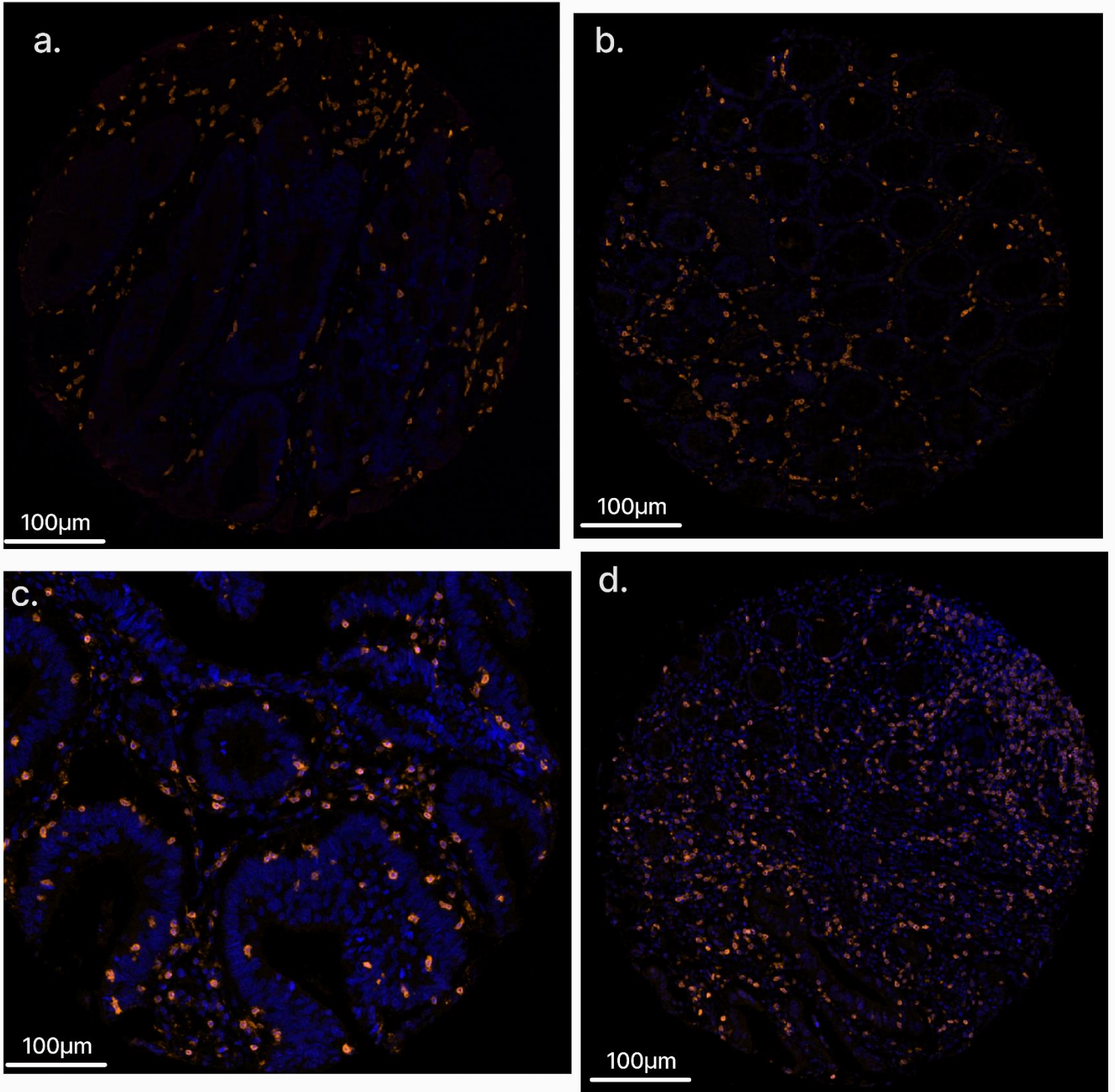


Figure 33. Representative images of CD3 (Opal 620) expression in human CRC tissue sections in different cores (patients) stained with the optimized mIHC panel (Table 4).

FFPE human CRC tissue sections were stained with a multiplex panel that included the CD3 antibody (1:300 dilution) paired with Opal 620 (orange) in the fifth position. (a-d) Different regions of interest are shown, highlighting the predominantly membranous staining pattern of CD3 in lymphocytes or other CD3 positive cells within the intraepithelial and stromal compartments.

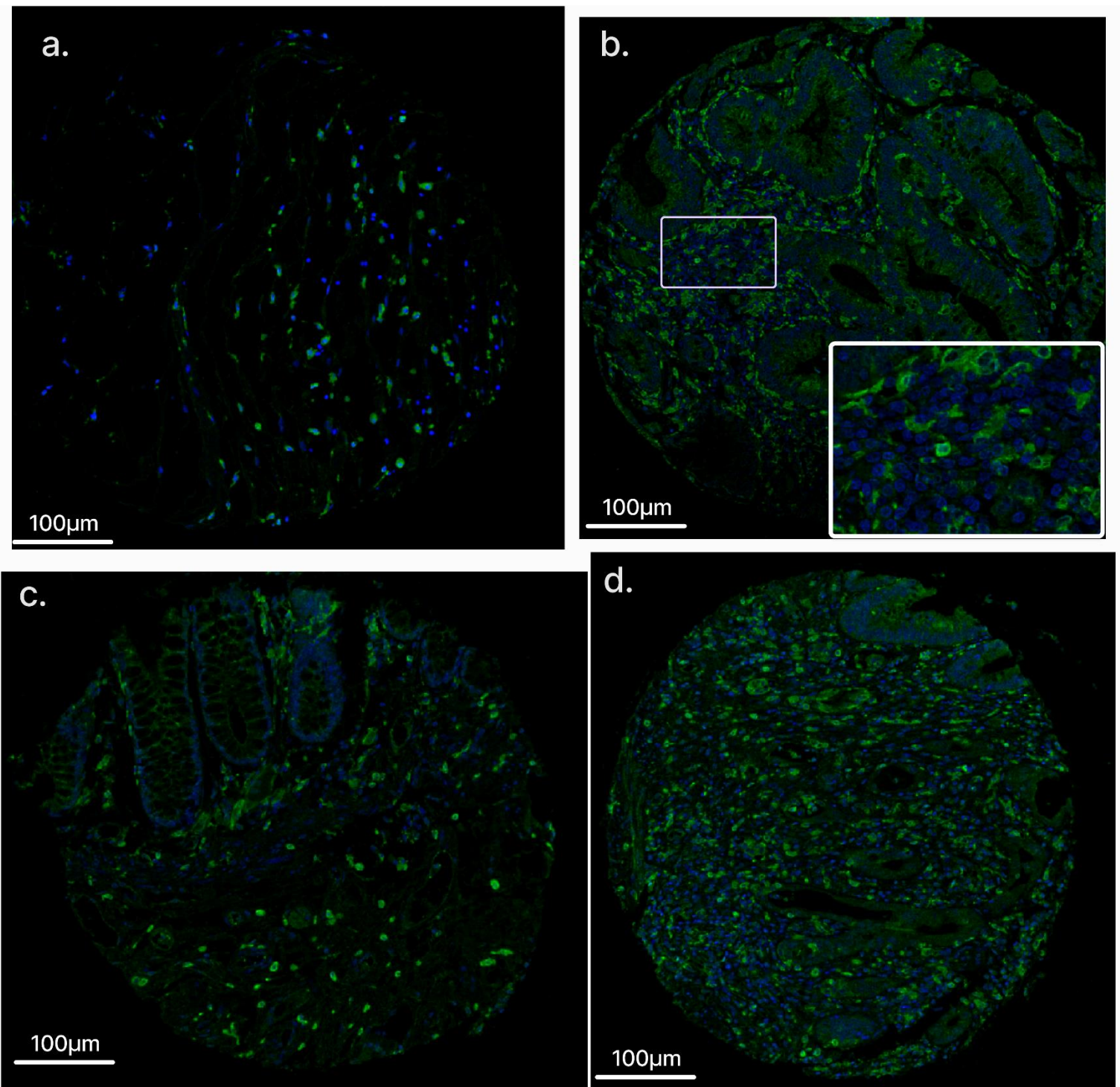


Figure 34 . Representative images of CD68 (Opal 520) expression in human CRC tissue sections in different cores (patients) stained with the optimized mIHC panel (Table 4).

FFPE human CRC tissue sections were stained with the multiplex panel that included the CD68 antibody (1:300 dilution) paired with Opal 520 (green) in the fourth position. (a-d) Different regions of interest are shown, highlighting the predominantly cytoplasmic staining pattern of CD68 in macrophages and other positive cells within the intraepithelial and stromal compartments. (b) Magnified inset highlights the morphology of CD68-positive cells.

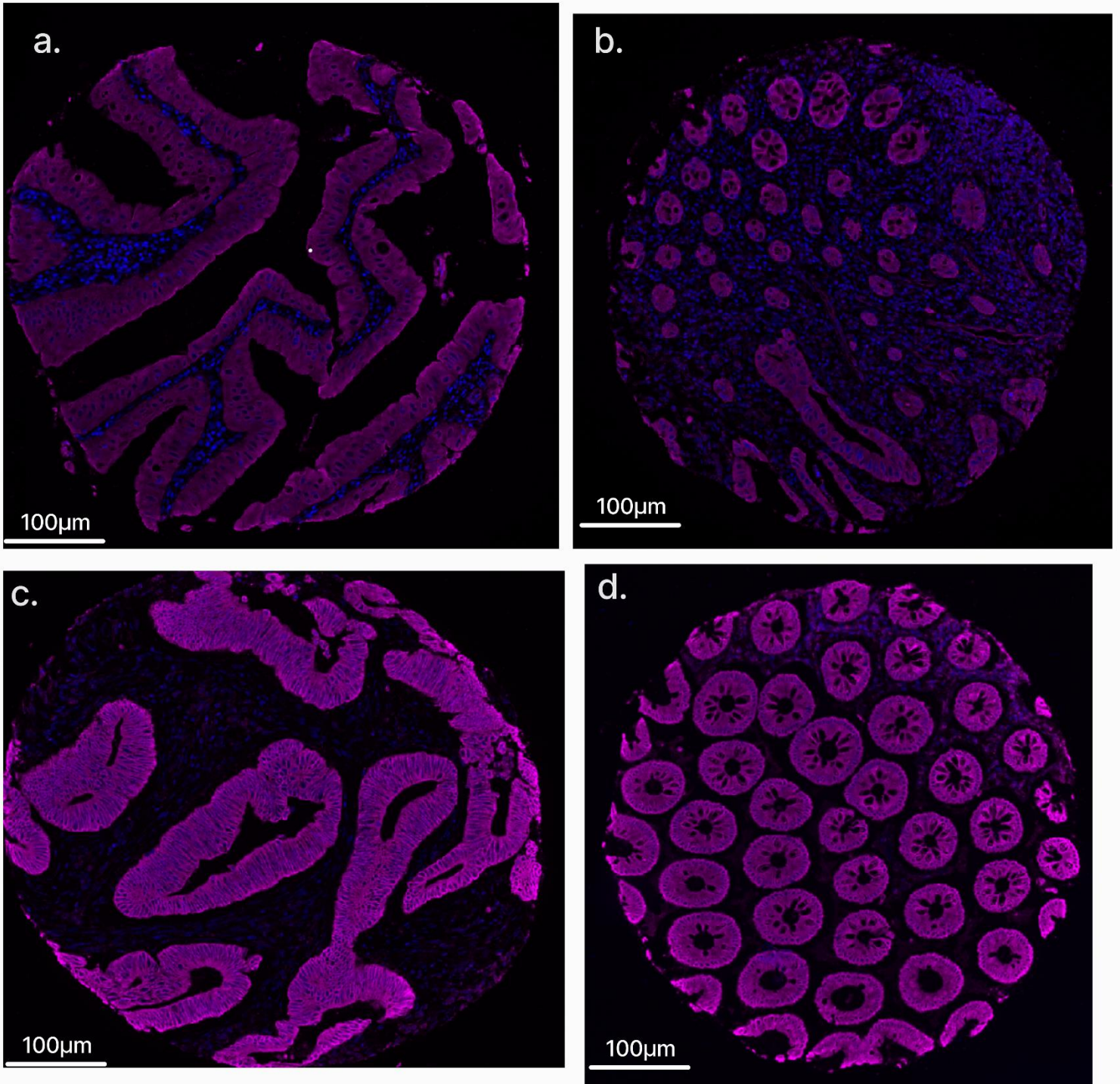


Figure 35. Representative images of CK (Opal 780) expression in human CRC tissue sections in different cores (patients) stained with the optimized mIHC panel (Table 4).

FFPE human CRC tissue sections were stained with the multiplex panel that included the Pan Cytokeratin antibody (1:200 dilution) paired with Opal 780 (magenta) in the sixth position. (a-d) Different regions of interest are shown, highlighting the strong cytoplasmic staining pattern of CK in epithelial cells within the tissue.

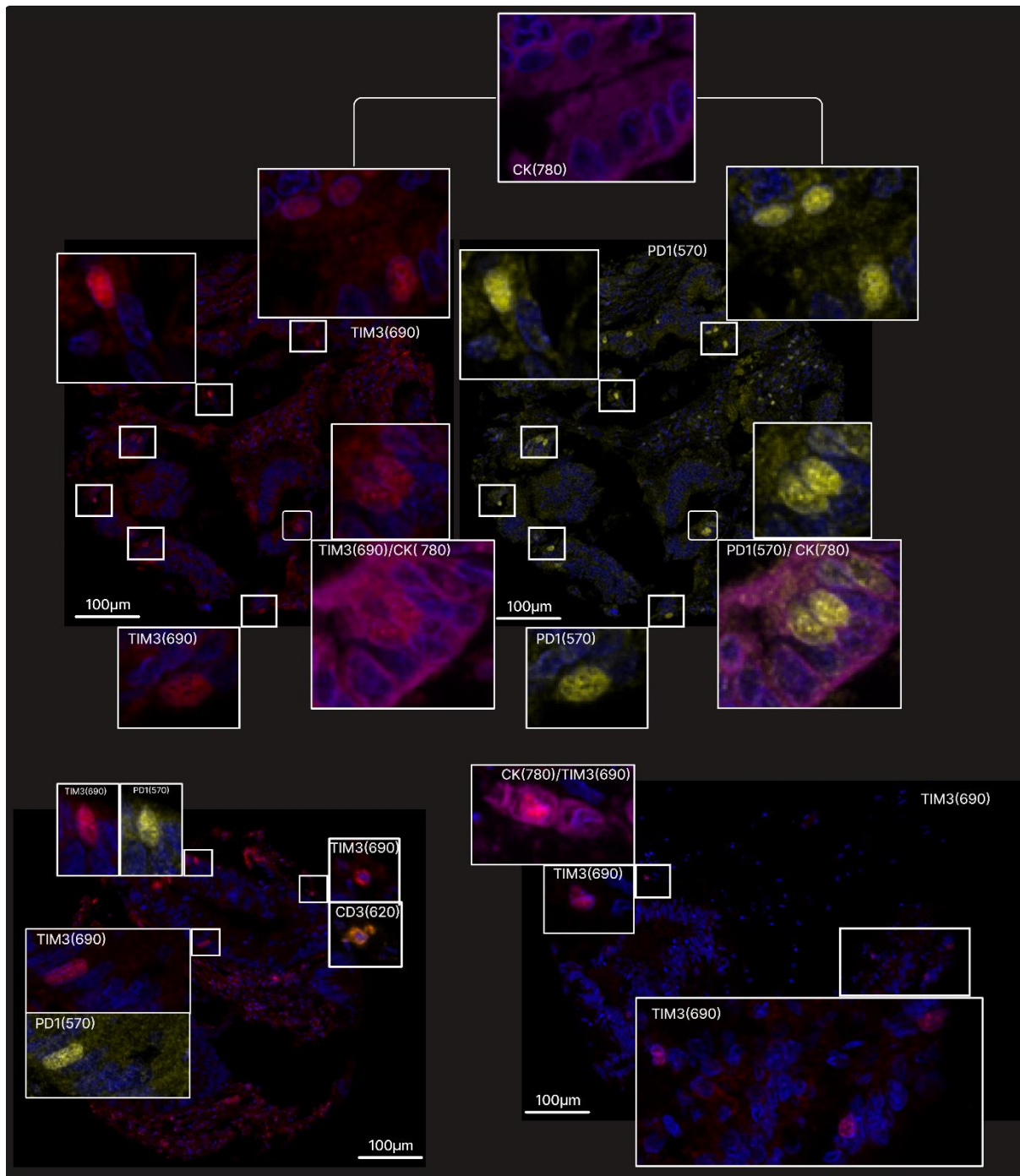


Figure 36. Nuclear expression of TIM3 and PD1 in Cytokeratin-positive (CK+) epithelial cells in human CRC tissue sections in different cores (patients) stained with the optimized multiplex panel (Table 4).

mIHC staining was performed on FFPE human CRC tissue sections using the optimized panel. The image shows representative regions of interest demonstrating the subcellular localization of TIM3 (Opal 690, red), PD1 (Opal 570, yellow), and CK (Opal 780, magenta) in CK+ epithelial cells. The bottom left panel also shows CD3 staining (Opal 620, orange). Insets highlight examples of nuclear TIM3 and PD1 staining within CK+ cells. The bottom left panel includes an inset demonstrating membranous TIM3 staining on CD3+ cell, in contrast to the nuclear pattern observed in CK+ cells.

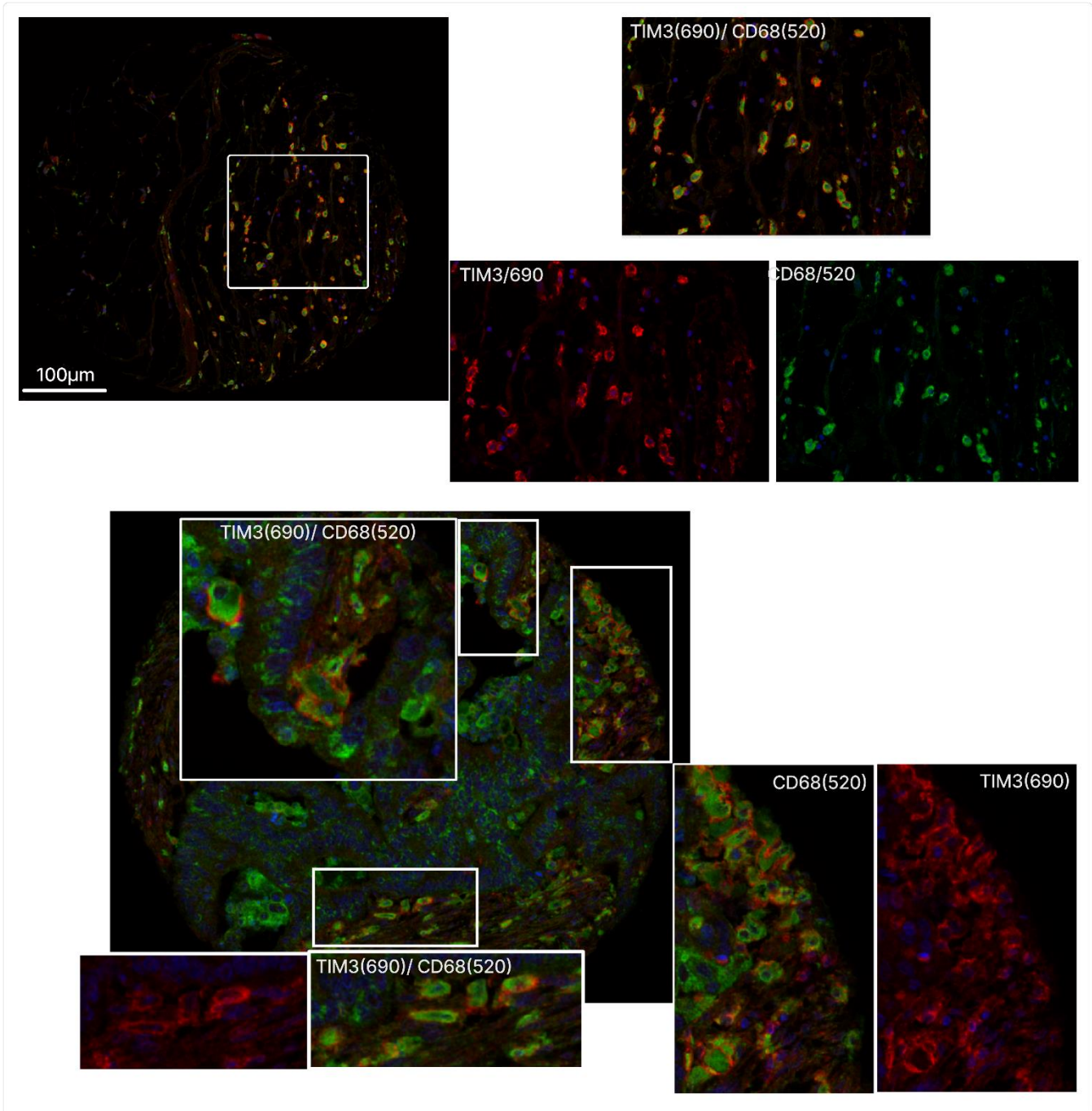


Figure 37. Co-expression of TIM3 and CD68 on macrophages in human CRC tissue sections in two different cores as demonstrated by the optimized mIHC panel (Table 4).

FFPE human CRC tissue sections were stained with the optimized multiplex panel including antibodies against TIM3 (1:100 dilution) and CD68 (1:300 dilution). The images show representative regions demonstrating the co-localization of TIM3 (Opal 690, red) and CD68 (Opal 520, green) in macrophages. Insets show magnified views of co-expressing cells.

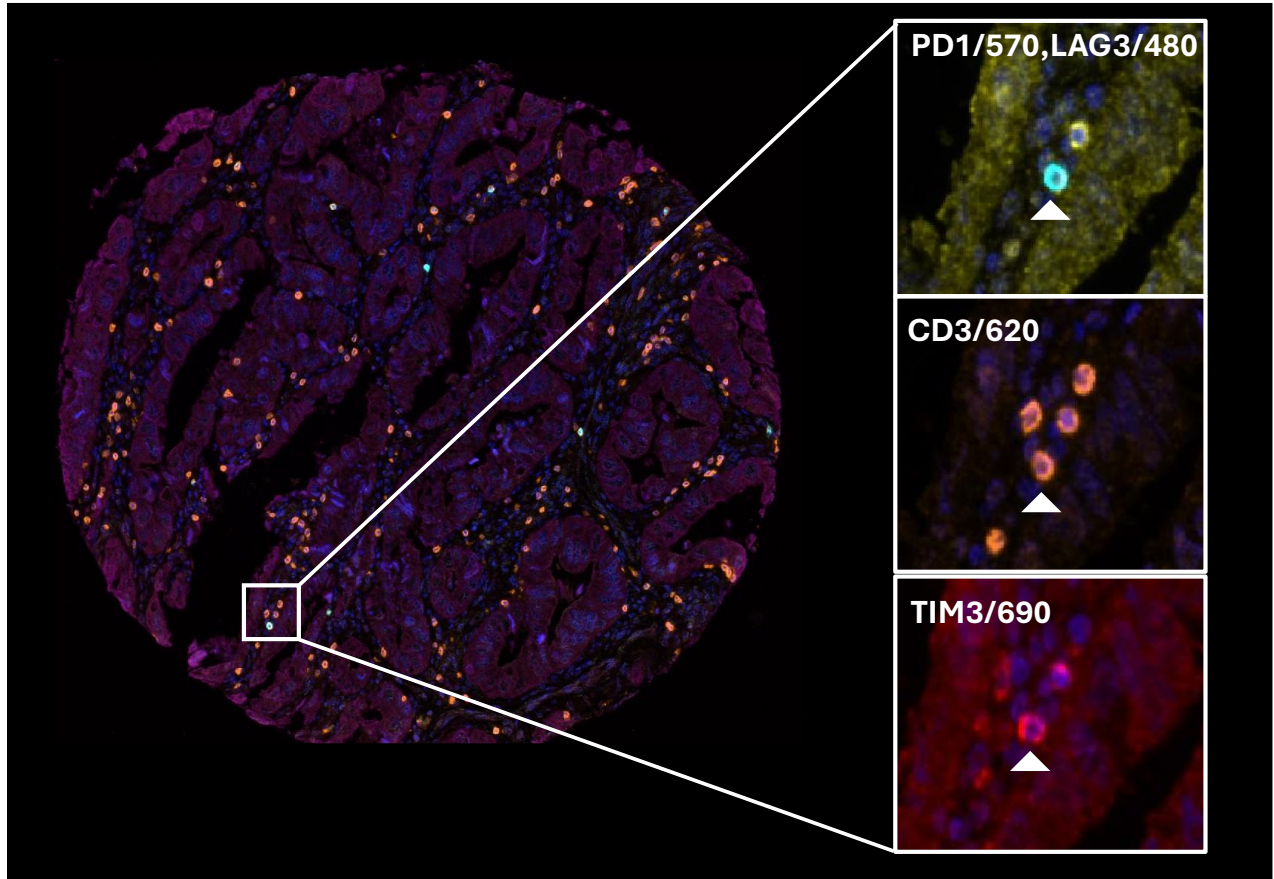


Figure 38. Co-expression of TIM3 and LAG3 on a CD3 cell in human CRC tissue section in one core (patient) stained with the optimized mIHC panel (Table 4).

Formalin-fixed paraffin-embedded (FFPE) human colorectal cancer (CRC) tissue sections were stained with an optimized mIHC panel. The images show representative regions demonstrating the co-localization of TIM3 (Opal 690, red) and LAG3 (Opal 480, cyan) in the marked CD3 cell (Opal620, orange). Magnified views (insets) highlight co-expressing cells, with the white arrowheads indicating a cell co-expressing TIM3 and LAG3.

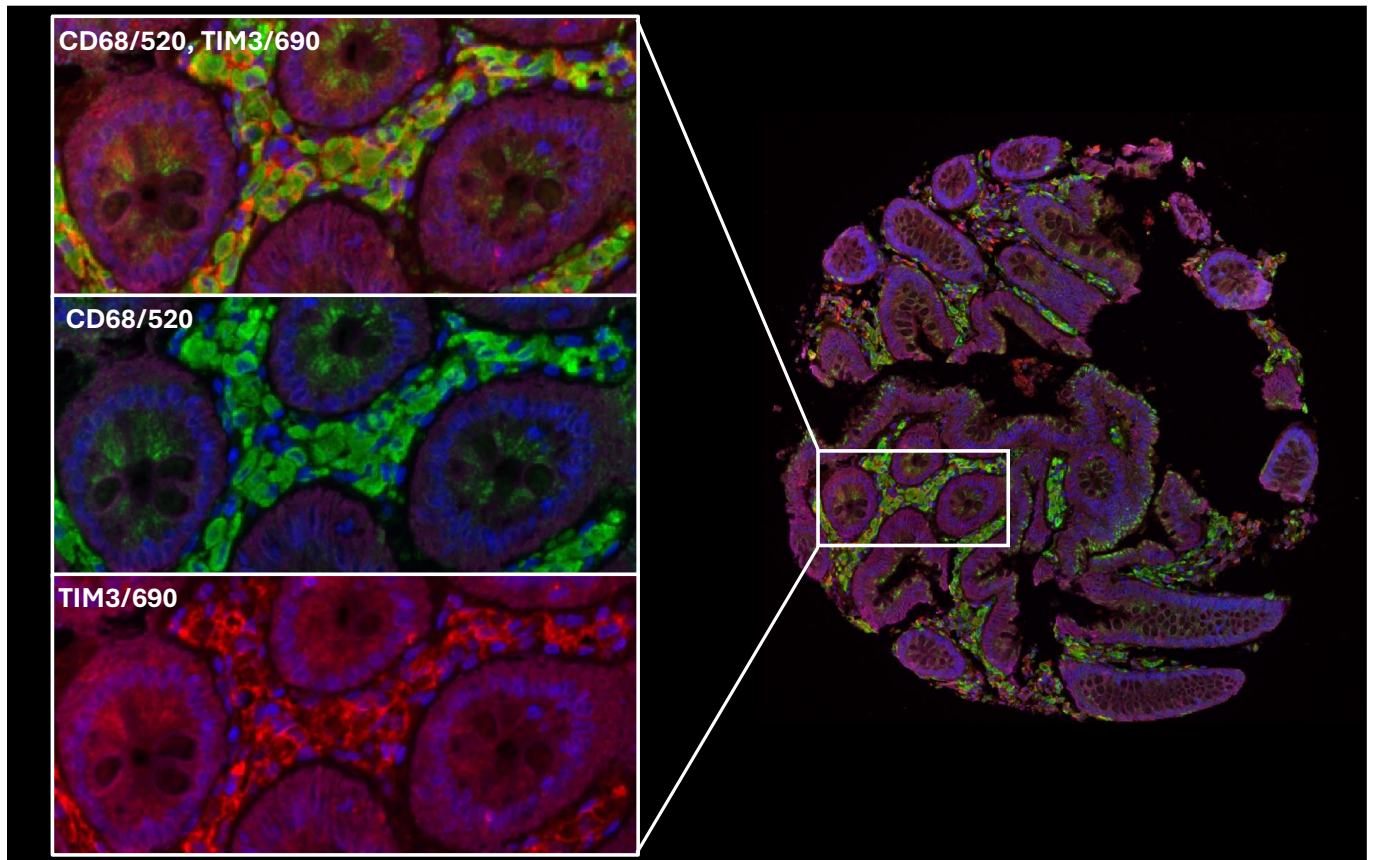


Figure 39. Co-expression of TIM3 and CD68 on macrophages in human CRC tissue section in one core (patient) stained with mIHC panel (table 4).

FFPE human colorectal cancer tissue sections were stained with an optimized mIHC panel including antibodies against TIM3 and CD68. The main image shows a representative overview of the tissue, while the insets on the left provide a magnified view of a region of interest. The top inset shows the co-localization of TIM3 (Opal 690, red) and CD68 (Opal 520, green), with co-expressing cells appearing in yellow/orange. The middle inset isolates the CD68 (green) signal, which marks macrophages. The bottom inset isolates the TIM3 (red) signal, showing cells expressing this marker. Nuclei are counterstained with a nuclear stain (blue), and the entire image demonstrates the presence and co-localization of these two markers within the tumor microenvironment.

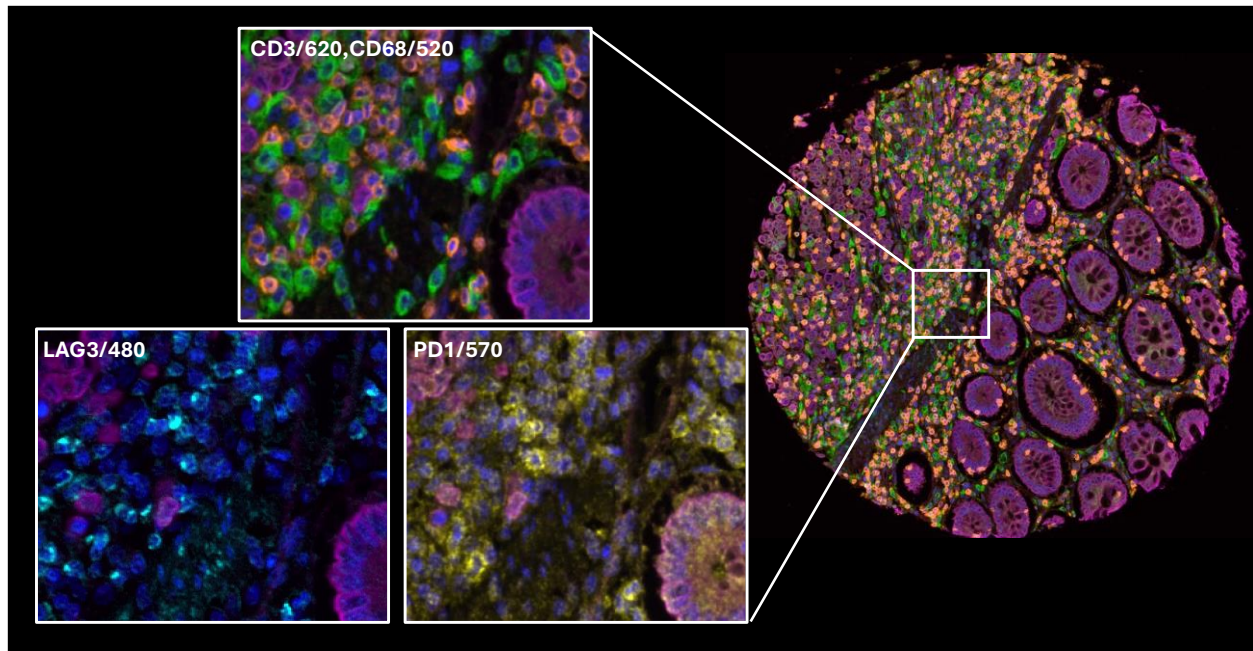


Figure 40. Spatial distribution and co-localization of multiple immune markers in human CRC tissue section in one core (patient) stained with the optimized mIHC panel (Table 4).

This representative image of a FFPE colorectal cancer tissue section, stained with an mIHC panel, illustrates the complex cellular landscape of the tumor microenvironment. The overview image highlights a tumor region rich in immune cells adjacent to epithelial tissue. The magnified inset in the top left shows the co-localization of CD3 (Opal 620, orange) and CD68 (Opal 520, green), demonstrating the presence of distinct immune cell populations. The magnified inset on the bottom left highlights cells expressing the immune checkpoint marker LAG3 (Opal 480, cyan), while the inset on the bottom right shows cells expressing another key immune checkpoint marker, PD1 (Opal 570, yellow). This figure collectively reveals the spatial organization and intricate relationships of different immune cell types and checkpoint markers within the CRC tissue.

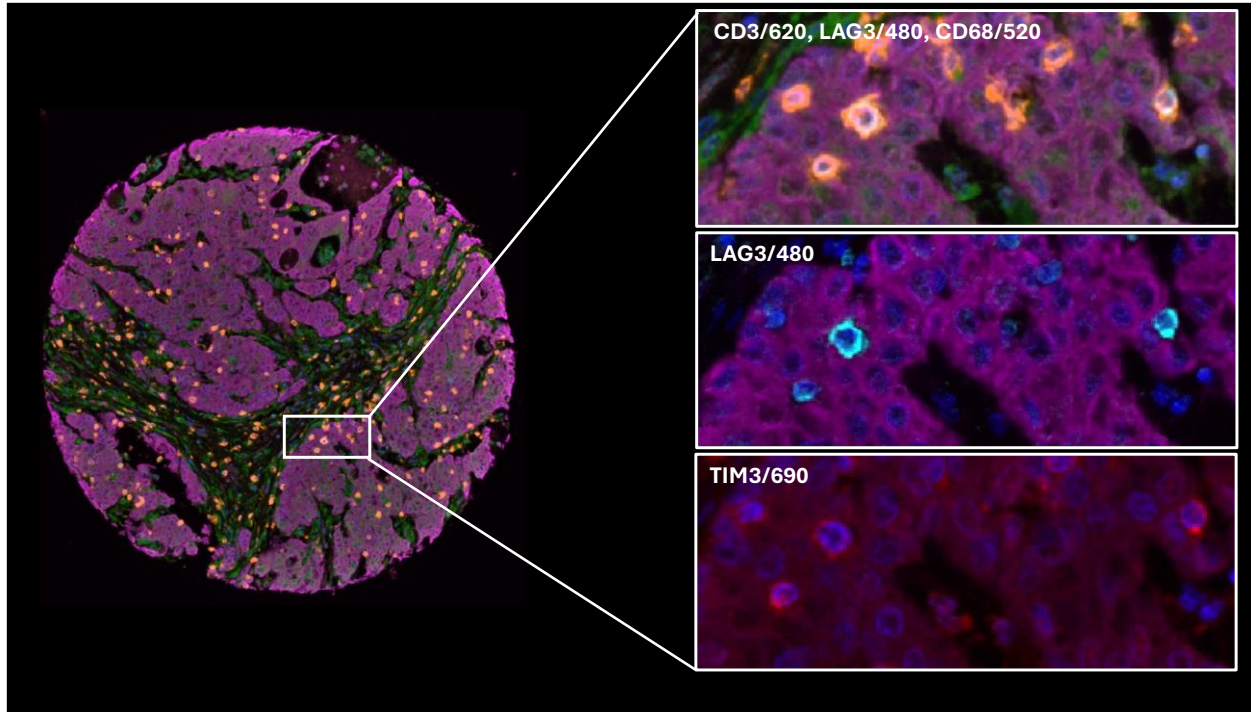


Figure 41. Co-expression of immune markers CD3, LAG3 and TIM3 on lymphocyte and CD68 expressing macrophages in human CRC tissue section in one core (patient) stained with the optimized mIHC panel (Table 4).

A representative image of a FFPE colorectal cancer tissue section stained with an optimized mIHC panel. The main image provides an overview of the tissue, while the magnified insets on the right highlight specific staining patterns. The top inset shows the co-localization of CD3 (Opal 620, orange), LAG3 (Opal 480, cyan), and CD68 (Opal 520, green). The middle inset isolates the staining for LAG3 (Opal 480, cyan), showing a population of cells expressing this immune checkpoint marker. The bottom inset isolates the staining for TIM3 (Opal 690, red), highlighting another population of immune checkpoint-positive cells. The entire figure illustrates the complex spatial relationships of these immune markers within the tumor microenvironment.

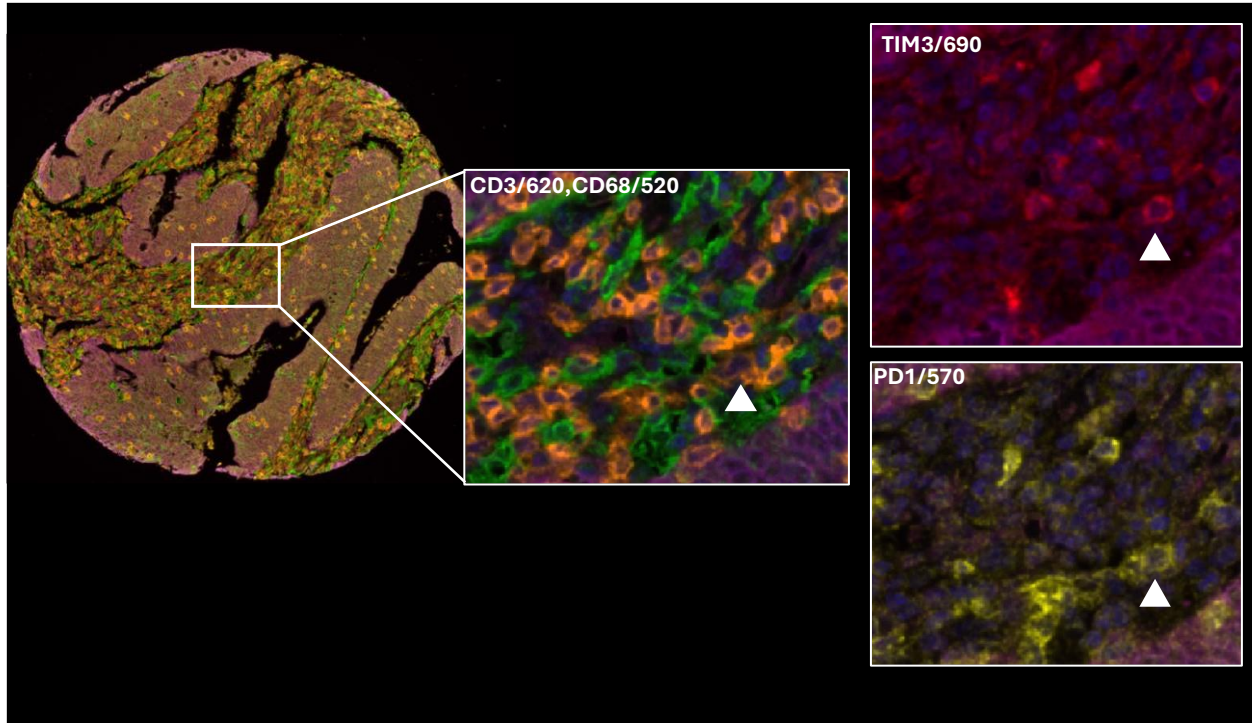


Figure 42. Co-expression of immune checkpoint markers PD1 and TIM3 on lymphocytes within human CRC tissue section in one core (patient) stained with the optimized mIHC panel (Table 4).

This representative image of a FFPE colorectal cancer tissue section, stained with an optimized mIHC panel, illustrates the complex cellular landscape of the tumor microenvironment. The central magnified inset shows the co-localization of the T-cell marker CD3 (Opal 620, orange) and the macrophage marker CD68 (Opal 520, green). The white arrowhead points to a cell co-expressing both markers. The magnified inset on the top right highlights the expression of TIM3 (Opal 690, red), and the magnified inset on the bottom right highlights the expression of PD1 (Opal 570, yellow). The image demonstrates the presence of a lymphocyte population expressing both of these key immune checkpoint markers, PD1 and TIM3, within the tumor microenvironment, as indicated by the white arrowheads in each of the right-hand insets. This co-expression pattern suggests a population of exhausted T-cells.

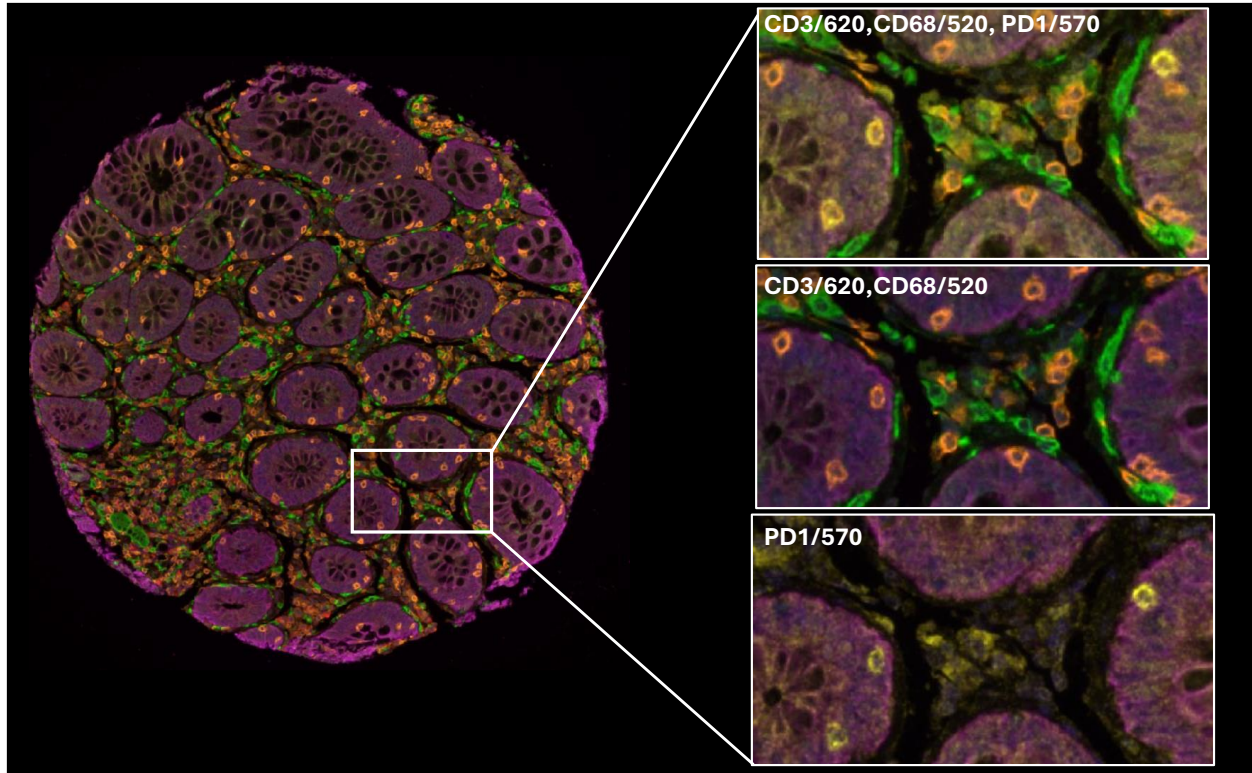


Figure 43. Co-localization of T-cells and macrophages with PD1-expressing cells in human CRC tissue section in one core (patient) stained with the optimized mIHC panel (Table 4).

A representative image of a FFPE colorectal cancer tissue section stained with an optimized mIHC panel. The main image provides an overview of the tissue, highlighting the epithelial tissue and the surrounding tumor stroma rich in immune cells. The magnified top inset shows the co-localization of CD3 (Opal 620, orange), CD68 (Opal 520, green), and PD1 (Opal 570, yellow), illustrating the complex immune cell landscape. The middle inset further clarifies the co-localization of the T-cell marker CD3 and the macrophage marker CD68. The bottom inset isolates the staining for PD1 (Opal 570, yellow), highlighting the presence of PD1-expressing cells within the tumor microenvironment. This figure collectively reveals the spatial relationships between T-cells, macrophages, and PD1-positive immune cells within the CRC tissue.

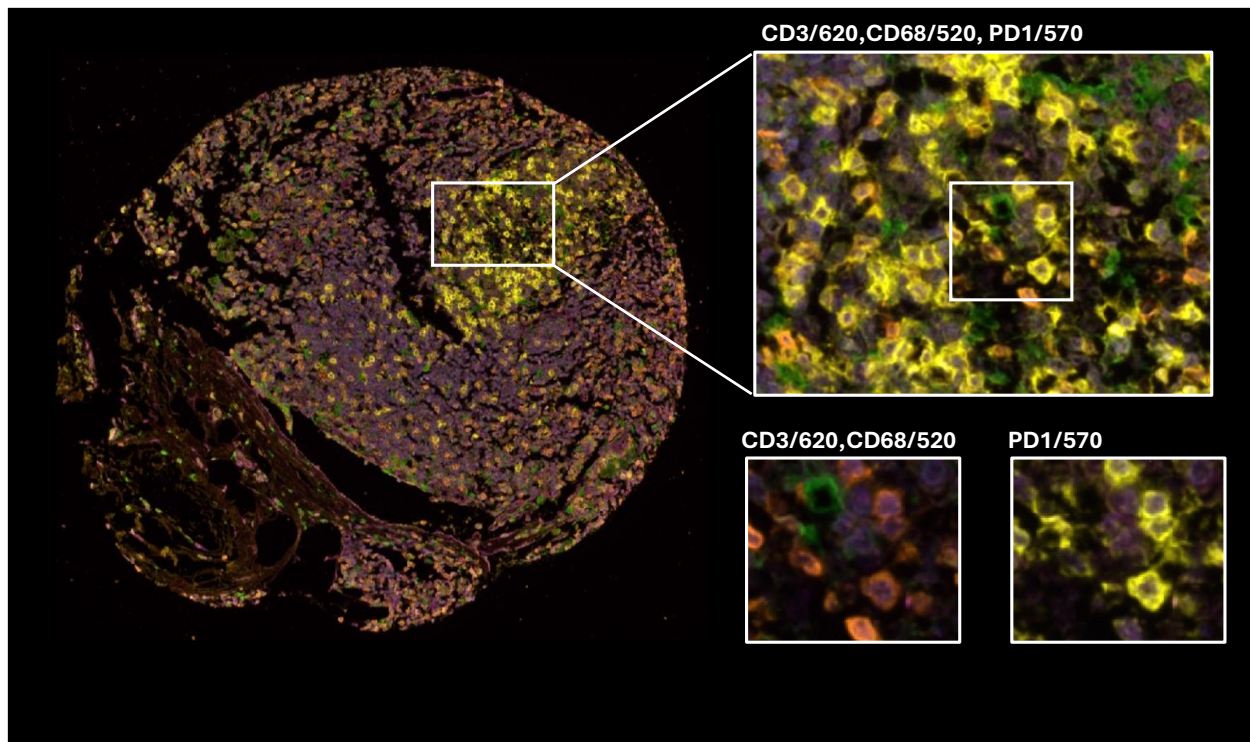


Figure 44. Co-expression of PD1 with T-cell and macrophage markers in a region of high immune infiltration in human CRC tissue section in one core (patient) stained with the optimized mIHC panel (Table 4).

A representative image of a FFPE human colorectal cancer tissue section stained with an optimized mIHC panel, showing an area of dense immune infiltration. The magnified top inset displays the co-localization of the T-cell marker CD3 (Opal 620, orange), the macrophage marker CD68 (Opal 520, green), and the immune checkpoint marker PD1 (Opal 570, yellow). This inset highlights a region with abundant PD1-expressing cells, many of which appear to co-express CD3. The bottom left inset isolates the staining for CD3 and CD68, showing their respective populations, while the bottom right inset exclusively shows the PD1-expressing cell population. This figure emphasizes a highly inflamed area within the tumor microenvironment characterized by a significant presence of immune cells, particularly those expressing the immune checkpoint PD1.

3.2 Library slides

To enable spectral unmixing of mIHC images, a spectral library was successfully generated using single-plex control slides. Each control slide was generated with an anti-CD8 antibody and a single Opal fluorophore. Additionally, a DAPI-only slide and an unstained slide for autofluorescence assessment were successfully prepared, **Figure 45**.

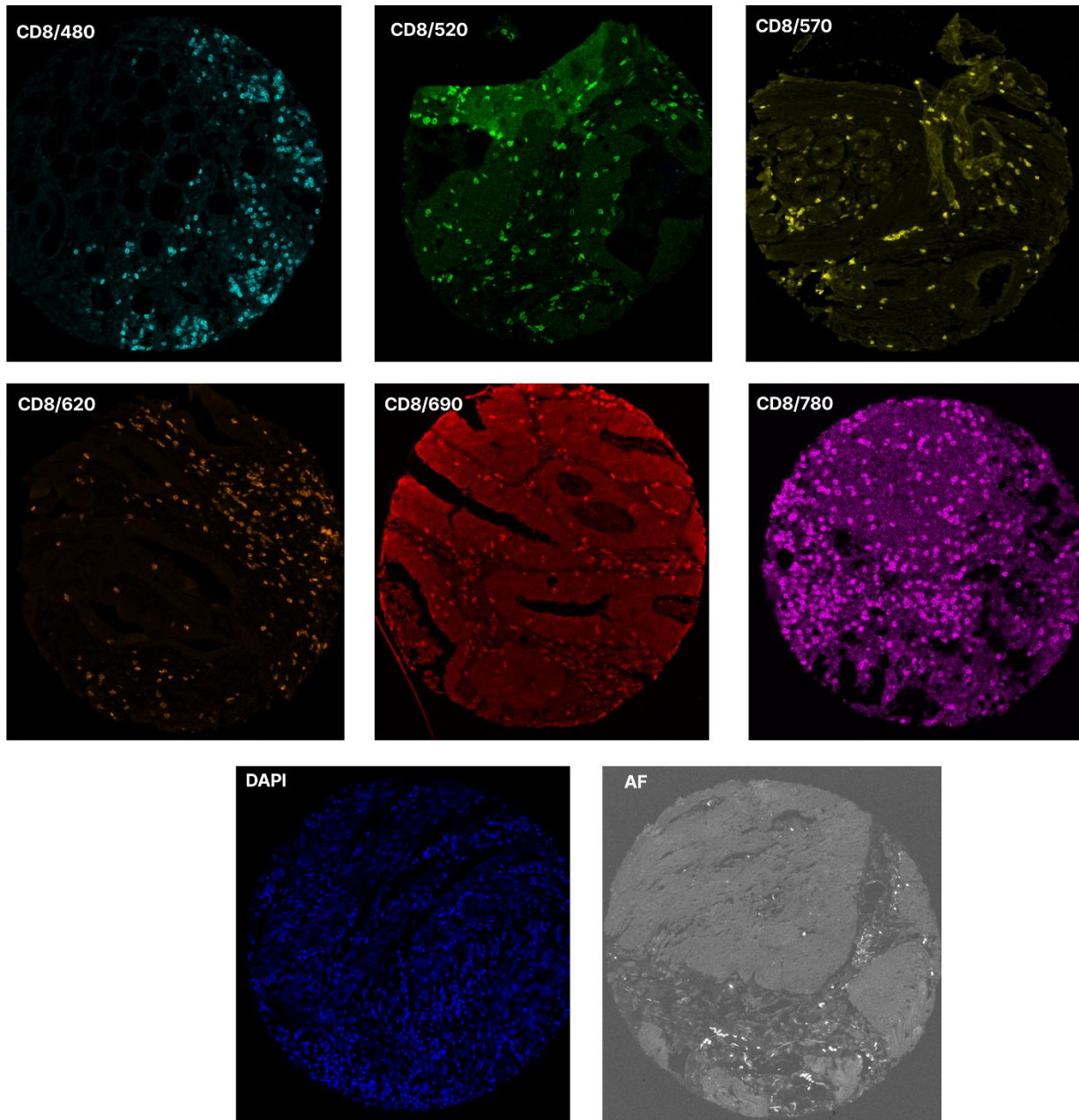


Figure 45. Single-channel images of a spectral library slide prepared for mIHC with an anti-CD8 antibody (each core belongs to a sperate slide).

FFPE human colorectal tissue sections were stained with an anti-CD8 antibody (1:50 dilution) and individual Opal dyes to generate a spectral library for subsequent unmixing of multiplex images using InForm software. The following channels are shown: Top Row: Opal 480 (cyan), Opal 520 (green), Opal 570 (yellow). Middle Row: Opal 620 (orange), Opal 690 (red), Opal 780 (magenta). Bottom Row: DAPI (blue), and Autofluorescence (AF, gray).

3.3 Staining and Scanning

Official staining was done on 15 slides according to the optimized panel and scanned with Phenomager HT system (Akoya Biosciences). After each slide scanning the quality of scanning was checked visually. **Figure 46** shows the whole process of multiplex IHC from optimization to the interpretation of the result in this project.

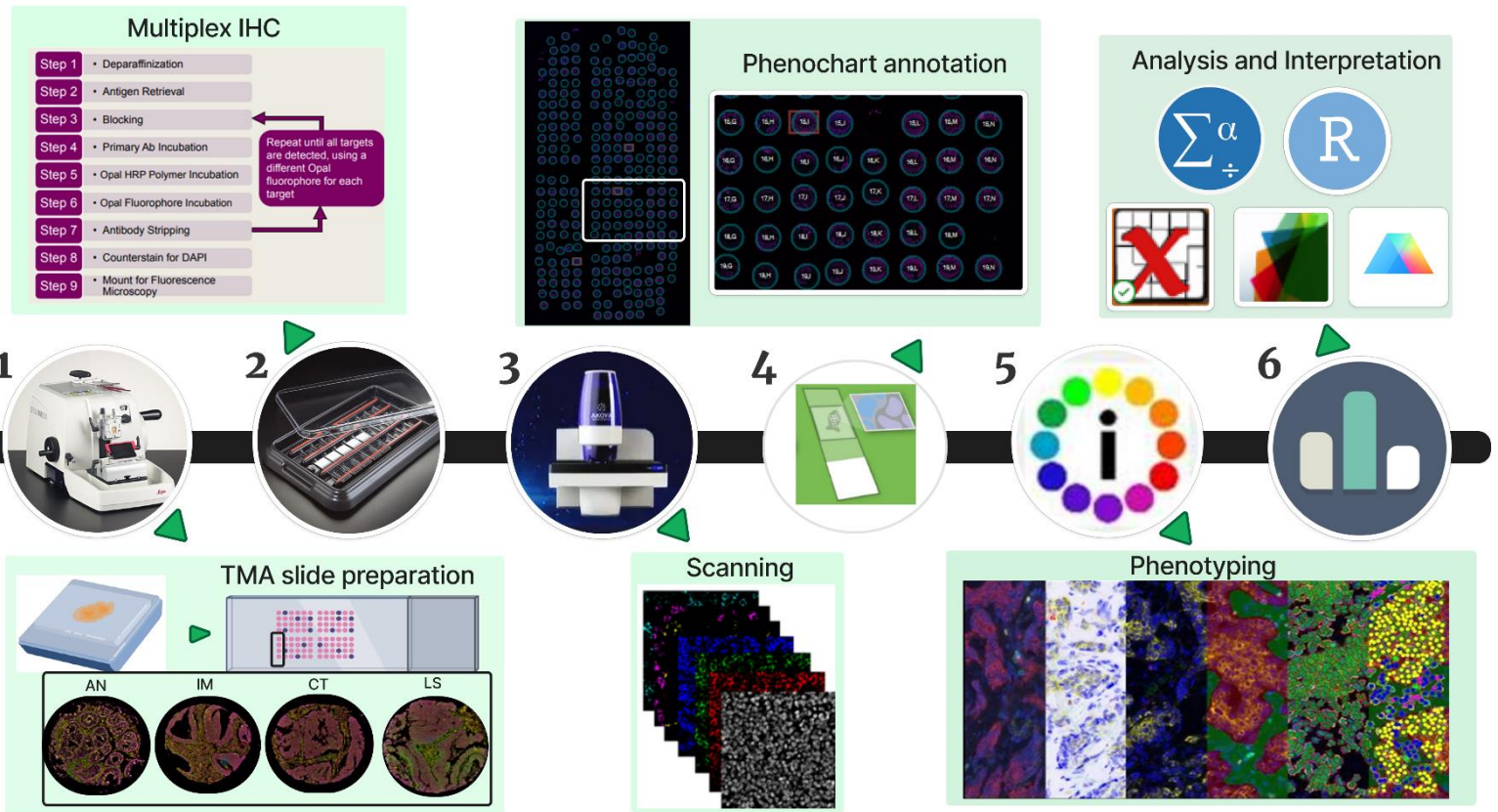


Figure 46. Overview of the Workflow for Multiplex Immunohistochemical Analysis of CRC Tissue Microarrays.

Step 1: Tissue Preparation and TMA Slide Creation. FFPE tissue blocks were sectioned at 5 μm thickness using a microtome. TMA slides were prepared, with each slide containing multiple cores. The inset in Step 1 illustrates a representative TMA slide with four cores from a single patient. Step 2: mIHC Staining. Step 3: Slide Scanning. Stained TMA slides were scanned at high resolution using the Phenomager HT 2.0 (Akoya Biosciences) platform. Step 4: Image Annotation. Phenochart software (Akoya Biosciences) was used for image annotation. Regions of interest (ROIs) were manually annotated for subsequent analyses (training set) and batch analysis. Step 5: InForm Training. The InForm software (Akoya Biosciences) was used to train an algorithm for cell, tissue segmentation and phenotypic identification based on the provided training set. Step 6: Data Analysis. Image analysis and data processing were performed using a combination of softwares, including SPSS, R, X-tile, Cytomap, and GraphPad Prism. This included quantification of cell densities, spatial analysis, and statistical comparisons.

3.4 Initial InForm training output

Through a comprehensive InForm training, we successfully trained an algorithm to remove the autofluorescence from slide and segment tissue to stromal and intraepithelial compartment based on the CK signaling and the shape of cells. In the next step, the training algorithm correctly segmented cells based on the nuclear (DAPI), cytoplasmic (CD68), and membrane (CD3) signaling from each other; and finally, successfully distinguished 16 different phenotypes from each other in the training set (3 cores per slide), **Figure 47** and **Figure 48**. The training set then successfully mapped to the whole slide through Batch analysis. The results of the batch were checked randomly in several cores per slides and the correctness of training map was confirmed.

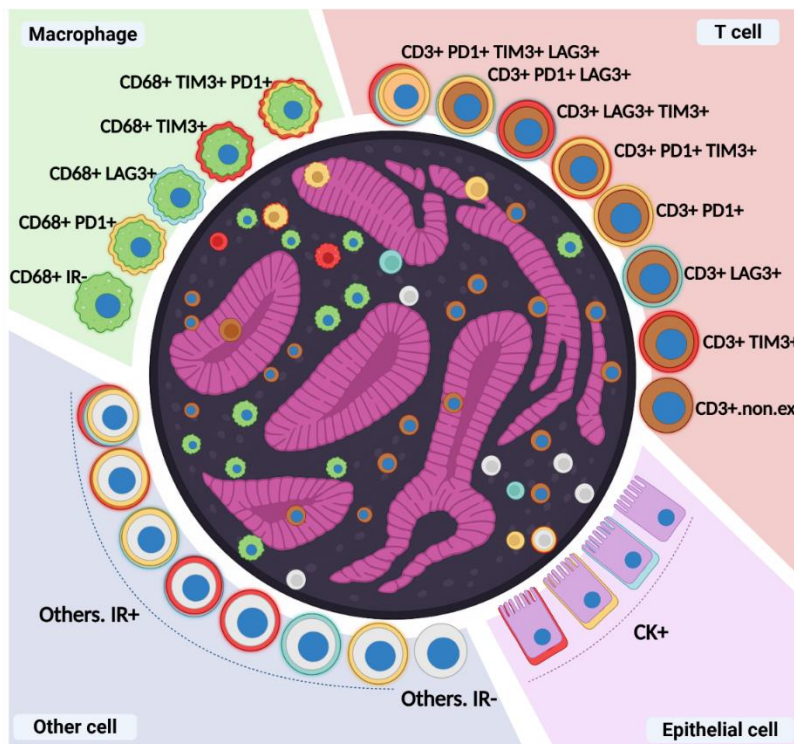


Figure 47. Schematic diagram illustrating the cell phenotypes identified and quantified using InForm software, categorized into Macrophages, T cells, Epithelial cells, and Other cell types, based on marker expression.

Images were trained via machine learning algorithms of InForm software package in three steps, including tissue segmentation (Tumor-epithelium and Stroma), cell segmentation (DAPI as nuclear signal, CD3 as membrane marker, and CD68 as cytoplasmic marker), and phenotype classifications in one schema. CD3 positive cells are trained as CD3+/LAG3+, CD3+/PD1+, CD3+/TIM3+, CD3+/LAG3+/PD1+, CD3+/LAG3+/TIM3+, CD3+/TIM3+/PD1+, CD3+/LAG3+PD1+TIM3+, and Non ExhaustedCD3+. CD68 positive cells are trained as CD68+/LAG3+, CD68+/PD1+, CD68+/TIM3+, CD68+/PD1+/TIM3+/ Non exhausted CD68. CK positive cells are trained as CK epithelium and finally

cells without CD3 and CD68 were trained as exhausted others (if they have expression of any exhaustion markers) and non-exhausted others (if they don't have the expression of exhaustion markers).

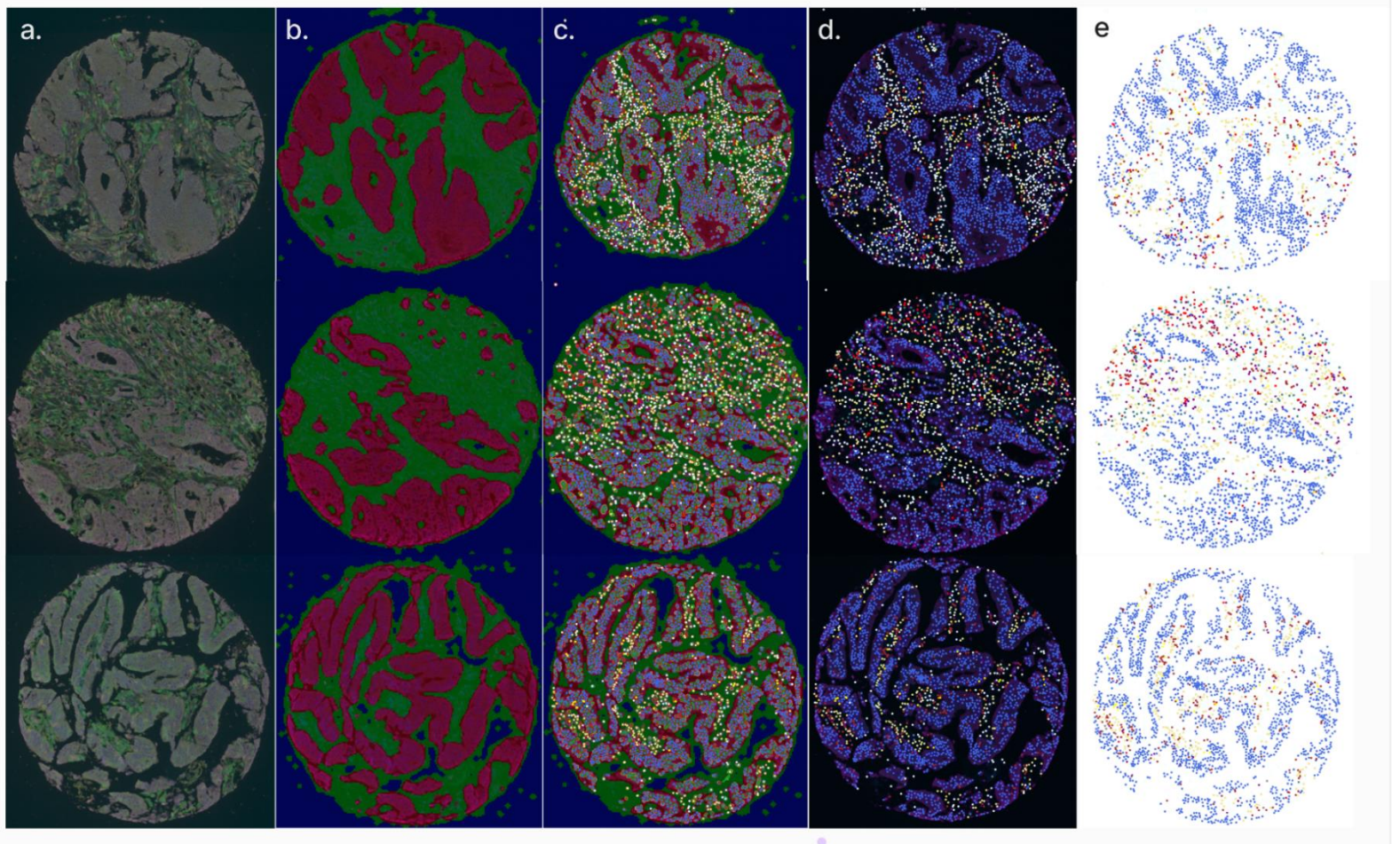


Figure 48. InForm image analysis workflow for adaptive tissue segmentation, cell segmentation, and phenotyping of mIHC images of human CRC tissue sections in three different cores (patients) stained with the optimized mIHC panel (Table 4).

The training set consisted of 45 manually annotated images (3 images from each of the 15 slides) (a) Slide preparation and autofluorescence removal. Raw multispectral images were processed to remove autofluorescence and unmixed spectrally based on library slides. (b) Tissue segmentation. Tissue sections were segmented into epithelial tumour regions (red) and stroma (green) using a machine-learning algorithm trained on CK expression (Opal 780) and morphological features. (c) Cell segmentation. Individual cells were segmented based on nuclear (DAPI), membranous (CD3), and cytoplasmic (CD68) markers using InForm's cell segmentation algorithm. (d) Phenotype training. Within one schema, an algorithm was trained to identify 16 different cell phenotypes based on the staining patterns of each marker. Weak or non-specific signals were excluded from the training data. (e) Phenotype mapping. The trained algorithm was applied to segment and phenotype cells across all tissue cores. Each dot represents an individual cell, colored according to its assigned phenotype. Due to the large number of phenotypes and some similarity in assigned colors, two separate images are shown to highlight the different phenotype color assignments.

3.5 Analysis of the result of multiplex panel

3.5.1 Cell density analysis within tumour related cores, including IM, CT, and LS

Overview of cell phenotype densities in stromal and intraepithelial compartments of human CRC tissue sections is represented in, **Figure 49**. Subsequent detailed descriptions and statistical comparisons of individual cell types will come in the following sections.

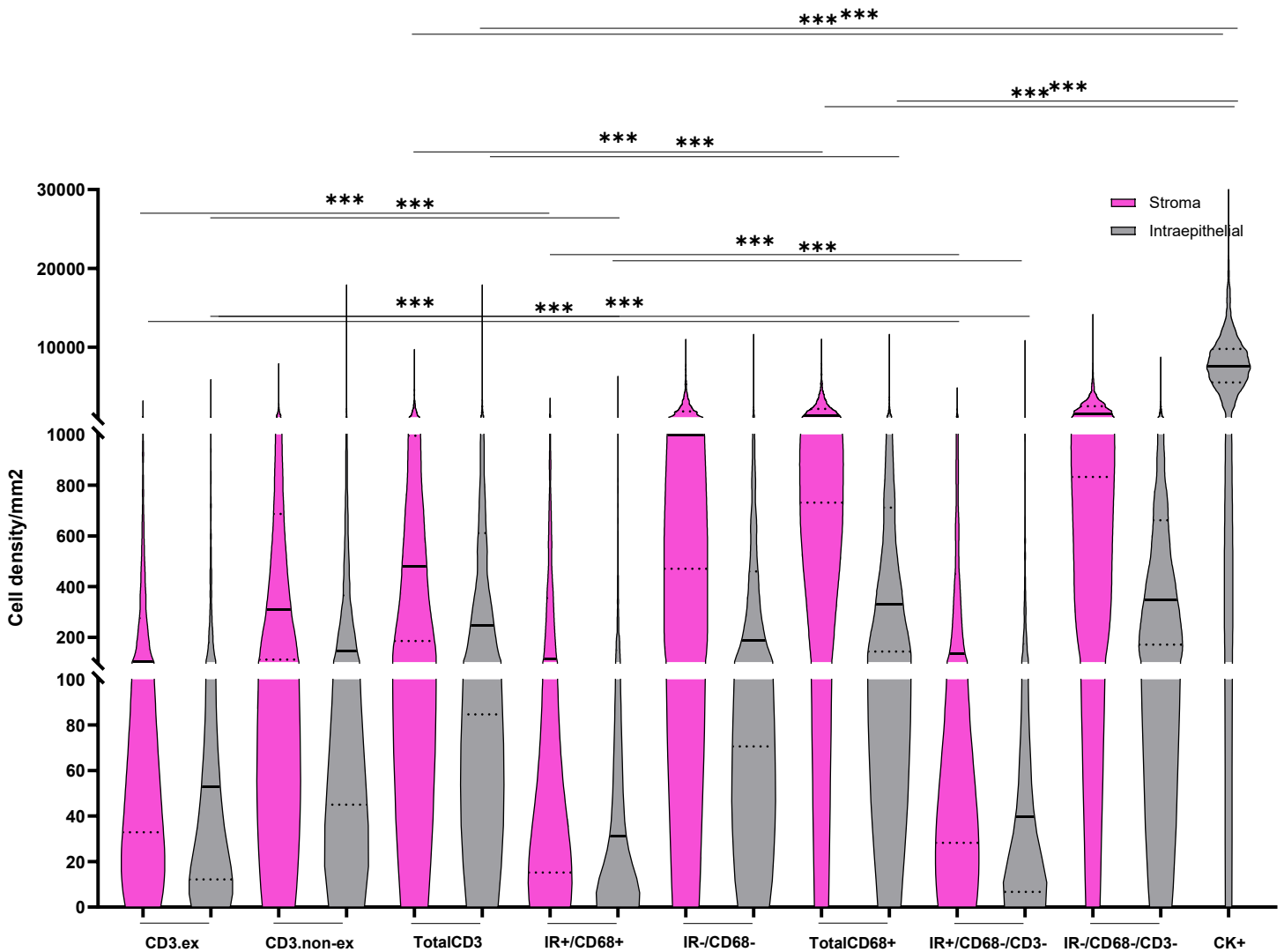


Figure 49. Differential densities of immune cell subsets and epithelial cells between stromal and intraepithelial regions in human CRC tissue sections showing higher density of cells in stromal compartment compared to intraepithelial compartments.

Violin plots illustrate the distribution of cell densities (cells/mm²) for various cell populations. Data are presented separately for stroma (pink) and intraepithelial (grey) regions. Cell populations are categorized as follows: CD3+ cells expressing at least one exhaustion marker (LAG3, PD1, or TIM3) (CD3.ex); all CD3+ cells without expression of exhaustion markers (CD3.non-ex); total CD3+ cells (TotalCD3); CD68+ cells expressing immune regulatory (IR) markers (LAG3, PD1, or TIM3) (IR+/CD68+); CD68+ cells not expressing IR markers (IR-/CD68-); total CD68+ cells (TotalCD68+); cells negative for CD68 and CD3 but positive for IR markers (IR+/CD68-/CD3-); cells negative for CD68, CD3, and IR markers (IR-/CD68-/CD3-); and cytokeratin-positive epithelial cells (CK+). The horizontal black lines within the violins represent the median; dotted lines represent the upper and lower quartiles. Note: The y-axis is segmented with different scales to improve visualization of the full range of density values.

1.1.1.1. The balance of CD3 cells subsets.

Higher densities of total CD3+ cells were observed in the stroma compared to the intraepithelial regions ($p < 0.001$, **Figure 50**), irrespective of their exhaustion status. Furthermore, stromal and intraepithelial CD3.non-ex cells (lacking LAG3, PD1, and TIM3 expression) were significantly more abundant than CD3.ex cells (expressing at least one of these markers) ($p < 0.001$, **Figure 50**^{Figure 51}). Examination of the CD3.ex populations (**Figure 51**) revealed low densities of LAG3+ single-positive cells in both compartments. PD1+ and TIM3+ single-positive cells and a population of PD1+TIM3+ cells were more prevalent, notably in the stroma (**Figure 51**).

CD3 Cell Density in CRC TME

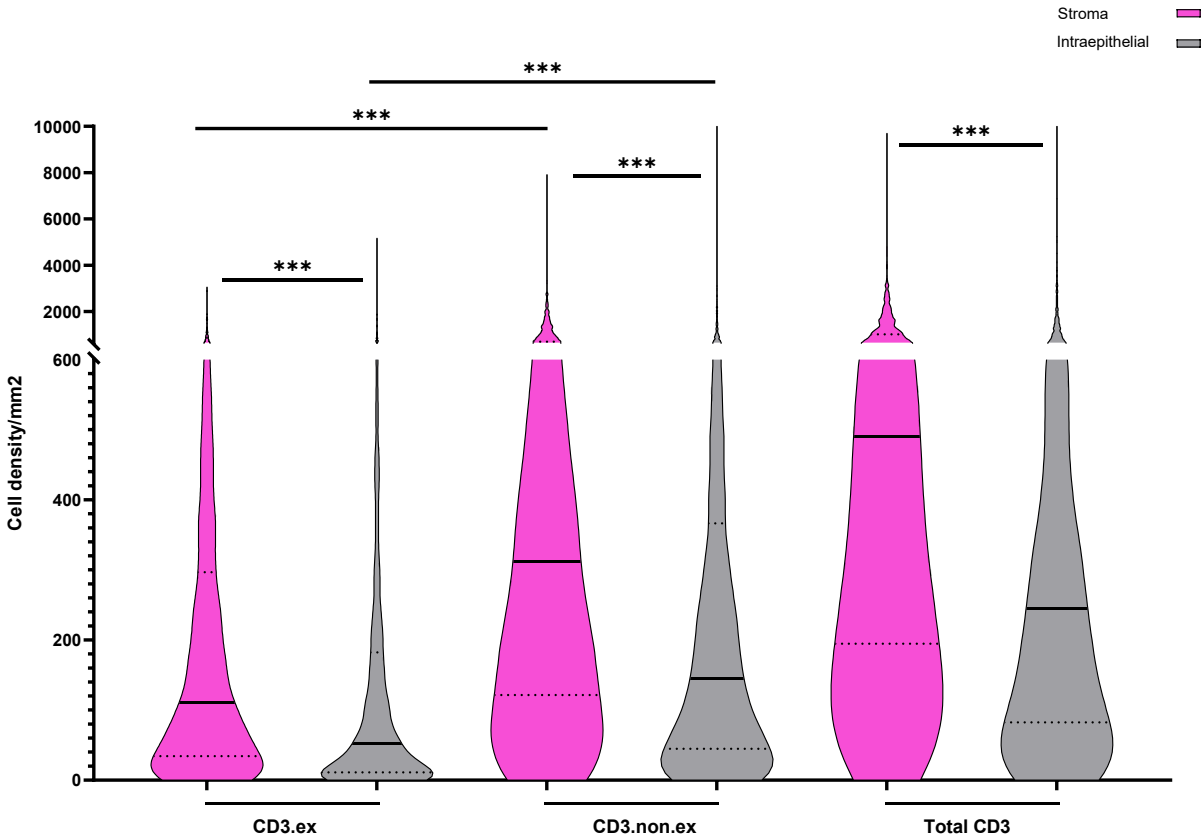


Figure 50. Significantly higher densities of both exhausted and non-exhausted CD3+ cells in the stromal compartment compared to the intraepithelial regions of human CRC tissue sections.

Violin plots show the distribution of CD3+ cell densities (cells/mm²) in stroma (pink) and intraepithelial (grey) regions. CD3+ cells were further categorized based on the expression of exhaustion markers: "CD3.ex" represents CD3+ cells expressing at least one exhaustion marker (LAG3, PD1, or TIM3); "CD3.non-ex" represents CD3+ cells not expressing any of these exhaustion markers; and "Total CD3" represents all CD3+ cells regardless of exhaustion marker expression. The horizontal black lines within the violins represent the median. The dotted horizontal lines represent the upper and lower quartiles. The y-axis is divided into two segments with different scales to improve visualization of both low- and high-density values. Statistical comparisons between stroma and tumour regions for each CD3+ T cell population were performed using the Wilcoxon signed-rank test. All comparisons showed statistically significant differences with p-values less than 0.001(***).

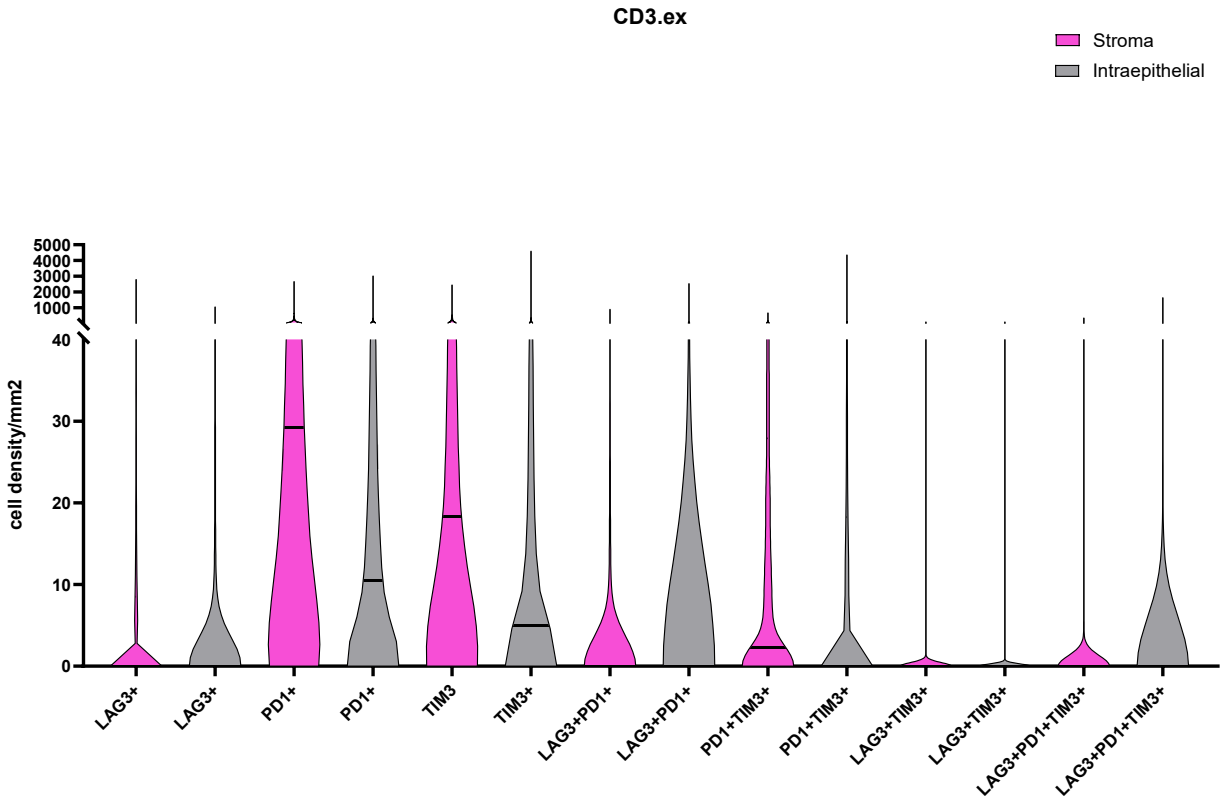


Figure 51. Densities of CD3+ cell phenotypes expressing exhaustion markers in stromal and intraepithelial regions of human CRC tissue sections.

Violin plots showing the distribution of cell densities (cells/mm²) for CD3+ cell phenotypes, defined by their expression of the exhaustion markers LAG3, PD1, and TIM3 for stroma (pink) and intraepithelial (grey) regions. CD3.ex indicates that all populations are a subset of CD3+ cells that express at least one of these markers. The specific combinations of markers for each phenotype are indicated on the x-axis (e.g., LAG3+PD1+ represents CD3+ T cells that are double-positive for LAG3 and PD1). The horizontal lines within the violins represent the median. The dotted horizontal lines represent the upper and lower quartiles. Note: The y-axis is divided into two segments with different scales to improve visualization of both low- and high-density values.

3.5.1.1 The balance of macrophage subsets.

We investigated the expression of immune checkpoint regulatory (IR) molecules on macrophages in colorectal cancer. Given the limited understanding of the function of these molecules in macrophages and evidence suggesting roles beyond exhaustion (e.g., higher TIM3 expression in quiescent macrophages and M2 macrophages), we refer to these cells as IR-positive (IR+) or IR-negative (IR-) macrophages instead of exhausted macrophages. Analysis revealed significantly higher densities of both IR+ and IR- macrophages in the stroma compared to the intraepithelial, **Figure 52**. Furthermore, the cell density of IR negative macrophages were higher compared to IR+ macrophages in both

regions. Among the IR+ macrophage populations, TIM3 expressions were particularly notable. Furthermore, while single-positive PD1+ macrophages were found at low densities, the second most abundant IR+ macrophage population consisted of double-positive macrophages for PD1 and TIM3, **Figure 53**.

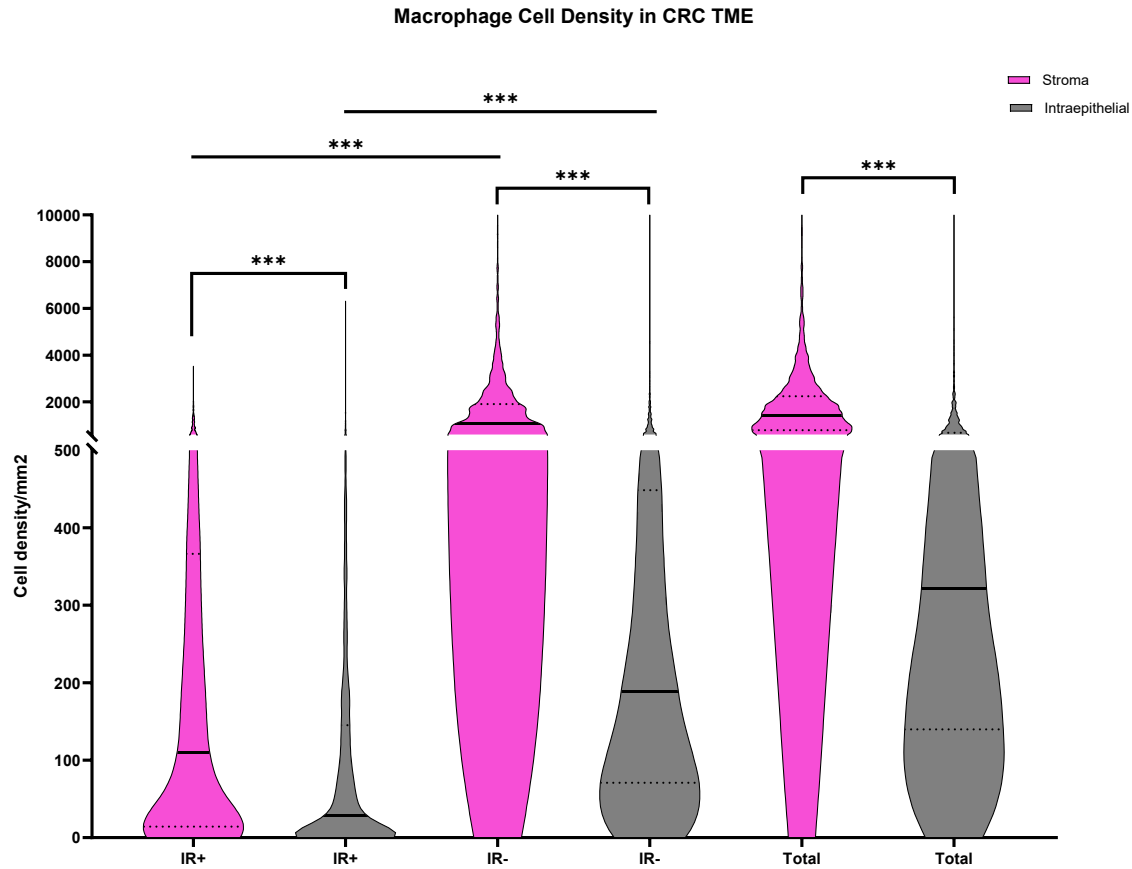


Figure 52. Higher Density of macrophages in stromal compartment compared to Intraepithelial compartments.

Violin plots showing the distribution of macrophage densities (cells/mm²) in CRC tissue categorized by location: stroma (pink) and intraepithelial (grey) compartments. Macrophages are further classified based on the expression of immune regulatory (IR) markers: IR+ (positive for at least one IR marker), IR- (negative for all IR markers), and total macrophages (Total). The horizontal black lines within the violins represent the median. The dotted horizontal lines represent the upper and lower quartiles. Comparisons between stroma and tumour areas for each macrophage subset were made using the two-sided Wilcoxon signed-rank test. All comparisons yielded statistically significant differences ($p < 0.001$), indicated by ***. Note: The y-axis is linear but divided into two segments with different scales to improve visualization of both low- and high-density values.

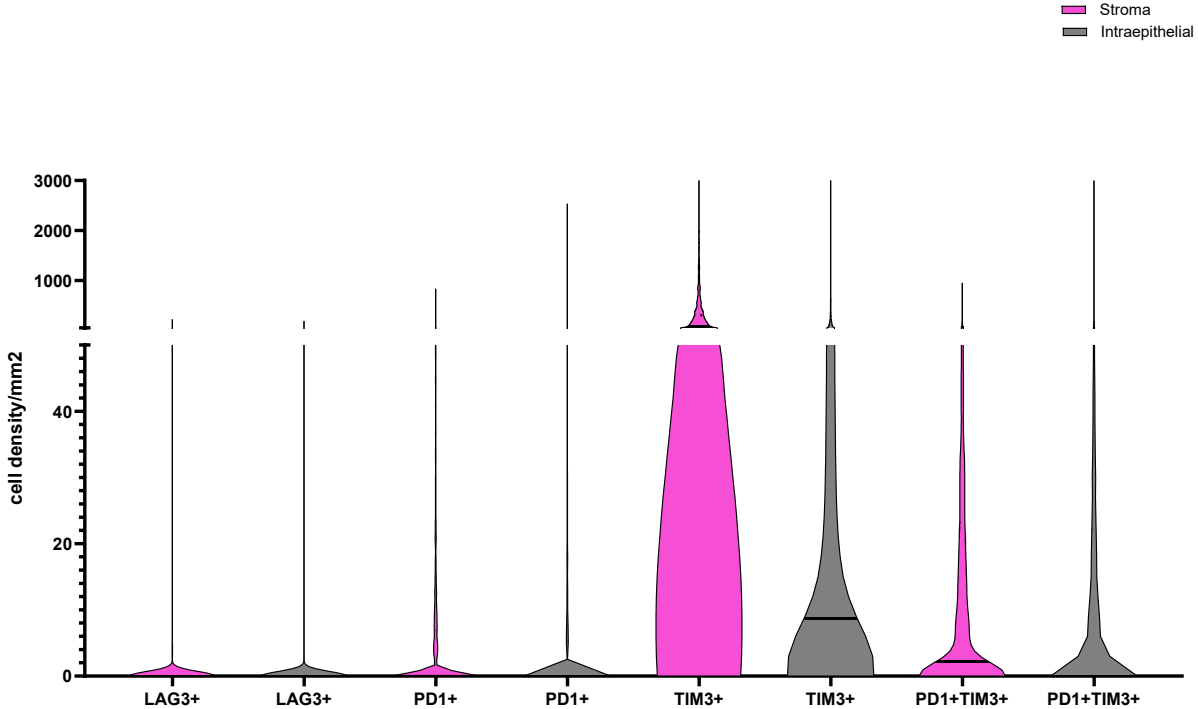


Figure 53. Densities of macrophage expressing immune checkpoint inhibitors (IR) in stromal and Intraepithelial regions of human CRC tissue sections.

Violin plots showing the distribution of cell densities (cells/mm²) for various IR+ macrophage phenotypes. Data are presented separately for stroma (pink) and tumour (grey) regions. IR+ macrophage phenotypes are defined as CD68+ cells expressing at least one of the following markers: LAG3+, PD1+, or TIM3+. The specific phenotypes shown are single-positive CD68+LAG3+, single-positive CD68+PD1+, single-positive CD68+TIM3+, double-positive CD68+PD1+TIM3-, and double-positive CD68+PD1+TIM3+. The horizontal lines within the violins represent the median. The dotted horizontal lines represent the upper and lower quartiles. Note: The y-axis is divided into two segments with different scales to improve visualization of both low- and high-density values.

3.5.1.2 The main exhaustion markers in macrophages and CD3 cells

Analysis of immune checkpoint molecule expression on CD3+ cells and CD68+ macrophages revealed marked differences in the densities of PD1 and TIM3 expression, **Figure 54**. The density of PD1+ cells was significantly higher in T- cells compared to macrophages ($p < 0.001$, **Figure 54**). Conversely, TIM3+ cell density was significantly higher in macrophages ($p < 0.001$, **Figure 54**).

Within the CD3+ cell population, PD1+ cell density was higher than TIM3+ cell density, although this difference did not reach statistical significance ($p = 0.38$). Both PD1+ and TIM3+ cell densities were significantly higher than that of LAG3+ cells in CD3+ cells ($p < 0.001$ for both comparisons, **Figure 54**).

Within the CD68+ macrophage population, TIM3+ cells exhibited significantly higher density compared to both PD1+ and LAG3+ cells ($p < 0.001$, **Figure 54**). Similar to CD3+ cells, LAG3+ cell density was significantly lower than the two other markers in macrophages ($p < 0.001$, **Figure 54**). Notably, LAG3+ cell density was low in both T-cells and macrophages, but nevertheless significantly higher in CD3+ cells ($p < 0.001$, **Figure 54**).

In order to find the proportion of each training phenotypes in CD68 and CD3 cells, we calculated the proportion of each exhaustion marker in each cell types in different sections represented in a stacked bar chart. **Figure 55** and **Figure 56** show the proportion of each training phenotype within CD68 or CD3 cells.

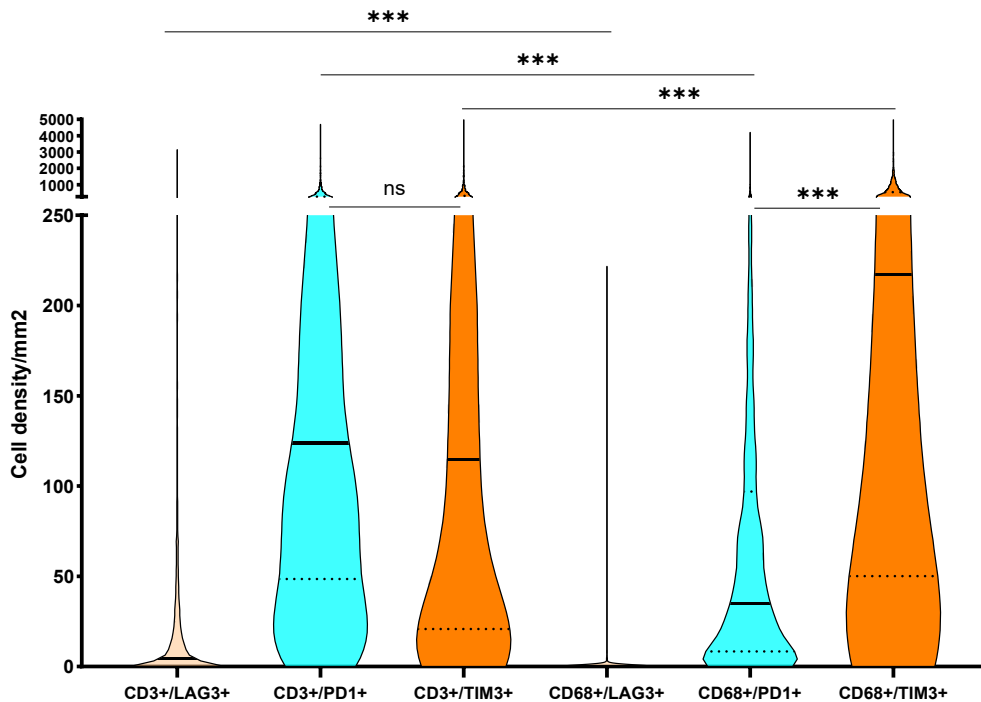


Figure 54. Comparison of exhaustion marker cell densities between CD3+ and CD68+ cells showed higher Tim3 on macrophages compared to T cells.

Violin plots showing the distribution of LAG3, PD1, and TIM3 cell densities (cells/mm²) in CD3+ (left) and CD68+ (right) cells. The horizontal black lines within the violins represent the median. Comparison between the two cell types for each marker were made using the two-sided Wilcoxon signed-rank test. Significance levels are indicated as follows: * $p < 0.05$, ** $p < 0.01$, *** $p < 0.001$, ns = not significant. For LAG3: CD3+ vs. CD68+, $p < 0.001$ (***) ; For PD1: CD3+ vs. CD68+, $p < 0.001$ (***) ; For TIM3: CD3+ vs. CD68+, $p < 0.001$ (***) . Furthermore, within CD3 cells, PD1 vs. TIM3, PD1 vs. LAG3, and LAG3 vs. TIM3 was $p < 0.38$ (ns), $p < 0.001$ (***) , and $p < 0.001$ (***) , respectively. Within CD68 positive cells significant levels for PD1 vs. TIM3, PD1 vs. LAG3, and LAG3 vs. TIM3 was $p < 0.001$ (***) in each comparison. Note: Cells expressing multiple markers are included in the density calculations for each marker they express. Note: The y-axis is divided into two segments with different scales to improve visualization of both low- and high-density values.

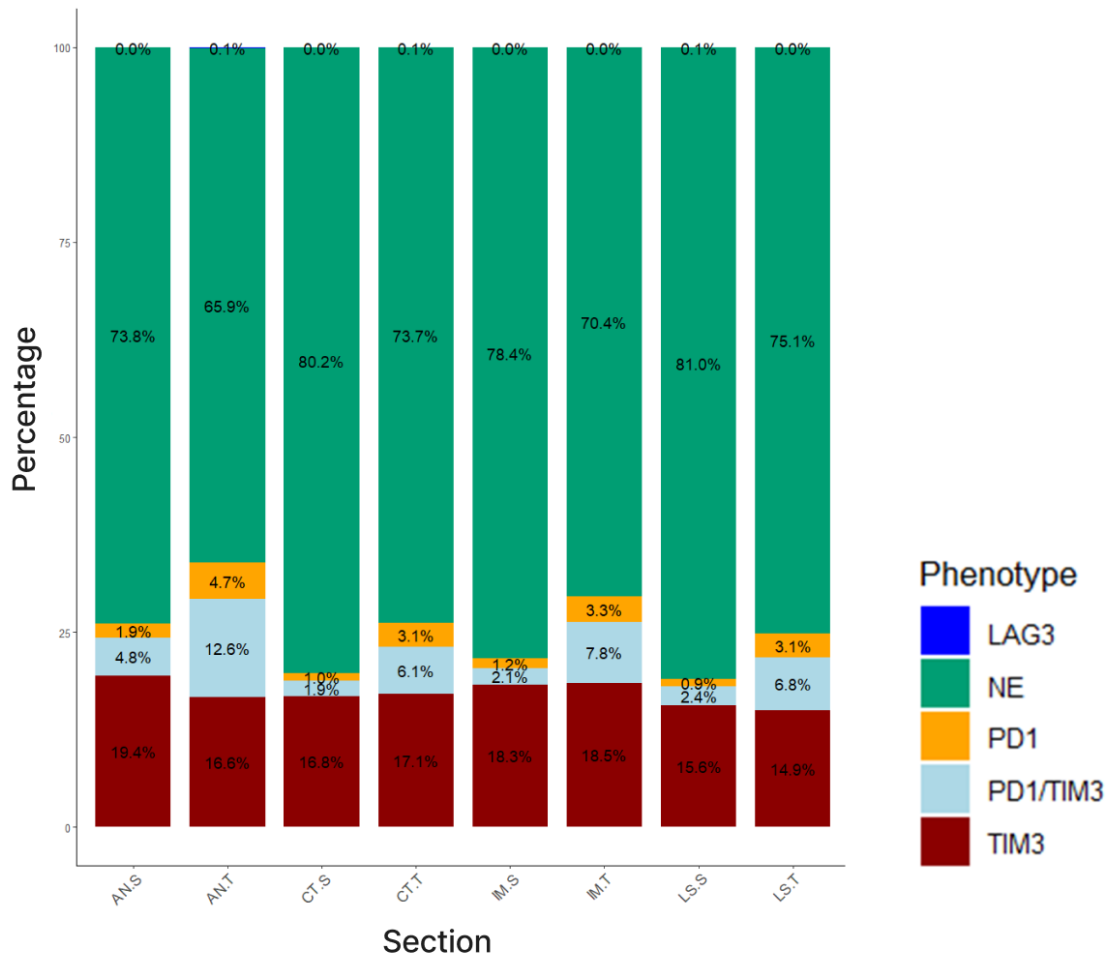


Figure 55. The percentage of different phenotypes of macrophage according to the Inform training.

S: Stroma, T: intraepithelial, AN: adjacent normal, IM: invasive margin, CT: center of the tumour, LS: Luminal side.

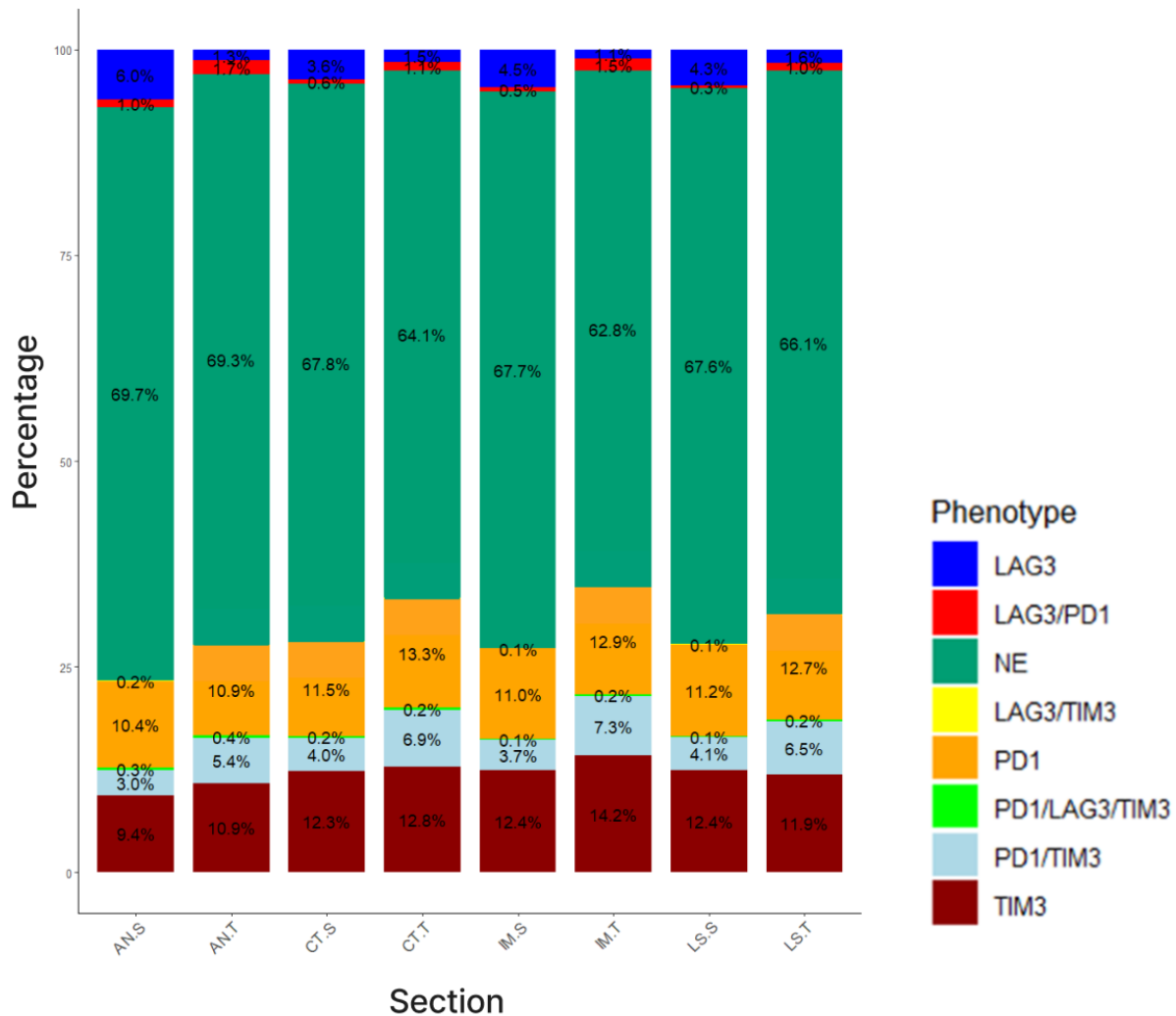


Figure 56. The percentage of different phenotypes of CD3 cells according to the Inform training.

S: Stroma, T: intraepithelial, AN: adjacent normal, IM: invasive margin, CT: center of the tumour, LS: Luminal side.

3.5.2 Correlation analysis

3.5.2.1.1 Positive correlation between immune cells and exhaustion.

To investigate the relationships between different cell populations within the tumour microenvironment of CRC tissue sections, we performed Spearman rank correlation analysis on the densities of different phenotypes across tissue cores, **Figure 57**

Stromal Compartment Correlations: Several significant correlations were observed within the stromal compartment. Notably, a strong positive correlation was found between

the density of total CD3+ cells (Total.CD3.S) and non-exhausted CD3+ cells (CD3.non.ex.S) ($\rho = 0.93$). Furthermore, a positive correlation was also observed between the density of CD3.ex cells and Total.CD3.S ($\rho = 0.78$). A moderate positive correlation was observed between total CD68+ cells (Total.CD68.S) and CD68.IR-.S ($\rho = 0.26$). There was also a moderate positive correlation between CD3.ex cells and Others.IR+.S ($\rho = 0.57$). A negative correlation was observed between Total.CD68.S and CD68.IR+.S ($\rho = -0.24$).

Intraepithelial Compartment Correlations: Within the tumour compartment, a strong positive correlation was observed between Total.CD3.T and both CD3.non.ex.T ($\rho = 0.89$) and CD3.ex.T ($\rho = 0.80$). CD68.IR+.T also correlated strongly with CD3.ex.T ($\rho = 0.62$). CD68.IR-.T and Total.CD68.T had a strong positive correlation. ($\rho = 0.79$). Additionally, there was a moderate positive correlation between CD3.ex.T and Others.IR+.T ($\rho=0.60$).

Inter-Compartment Correlations: There were also notable correlations between cell populations in the stroma and intraepithelial compartments. For example, CD3.ex cells in the stroma (CD3.ex.S) were positively correlated with CD3.ex cells in the epithelium (CD3.ex.T) ($\rho = 0.65$) and Others.IR+.T. Similarly, CD3.non.ex.S positively correlated with CD3.non.ex.T ($\rho = 0.55$).

Figure 58 and **Figure 59** shows the scatter plots of spearman correlation between the total CD3 and total CD68 in the stoma and exhaustion densities.

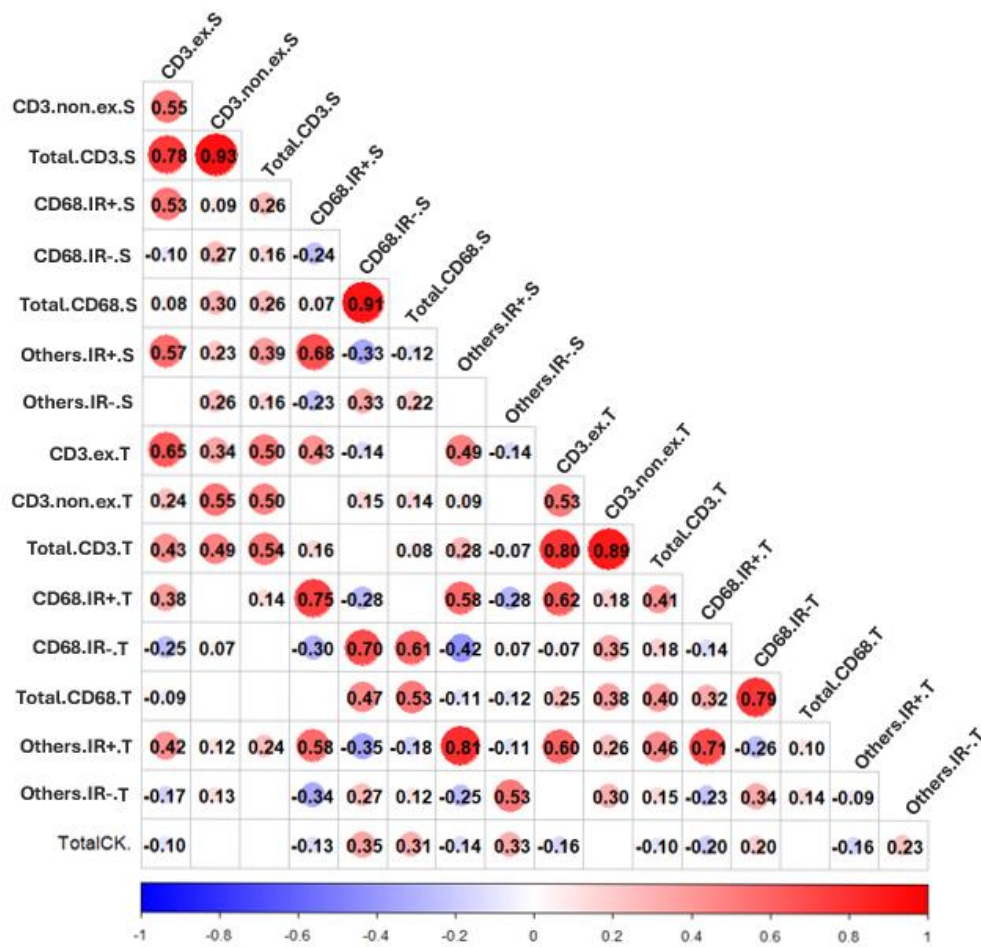


Figure 57. Spearman rank correlation matrix of cell densities showing the correlation between exhausted T cells and IR+ macrophages.

The matrix displays Spearman's rank correlation coefficients (ρ) between the densities of different cell populations identified by mIHC and quantified using inForm software. Each cell in the matrix represents the correlation between two cell populations, with the color intensity indicating the strength and direction of the correlation (red for positive, blue for negative). The size of each circle is proportional to the magnitude of the correlation coefficient. Correlation coefficients are shown only for correlations with a statistically significant p-value ($p < 0.05$); non-significant correlations are left blank. **S**: Stroma, **T**: Intraepithelial Tumour, **CD3.ex**: CD3+ cells expressing at least one exhaustion marker (LAG3, PD1, or TIM3), **CD3.non-ex**: CD3+ cells not expressing exhaustion markers (LAG3, PD1, or TIM3), **TotalCD3**: Total CD3+ cells, **IR+**: Cells expressing at least one immune regulatory marker (LAG3, PD1, or TIM3), **IR-**: Cells not expressing immune regulatory markers, **TotalCD68**: Total CD68+ cells, **CK+**: Cytokeratin-positive cells. **Others.IR+**: cells negative for CD3 and CD68 but positive for at least one exhaustion marker (LAG3, PD1, or TIM3). **Others.IR-**: cells negative for CD3 and CD68 not expressing exhaustion markers (LAG3, PD1, or TIM3).

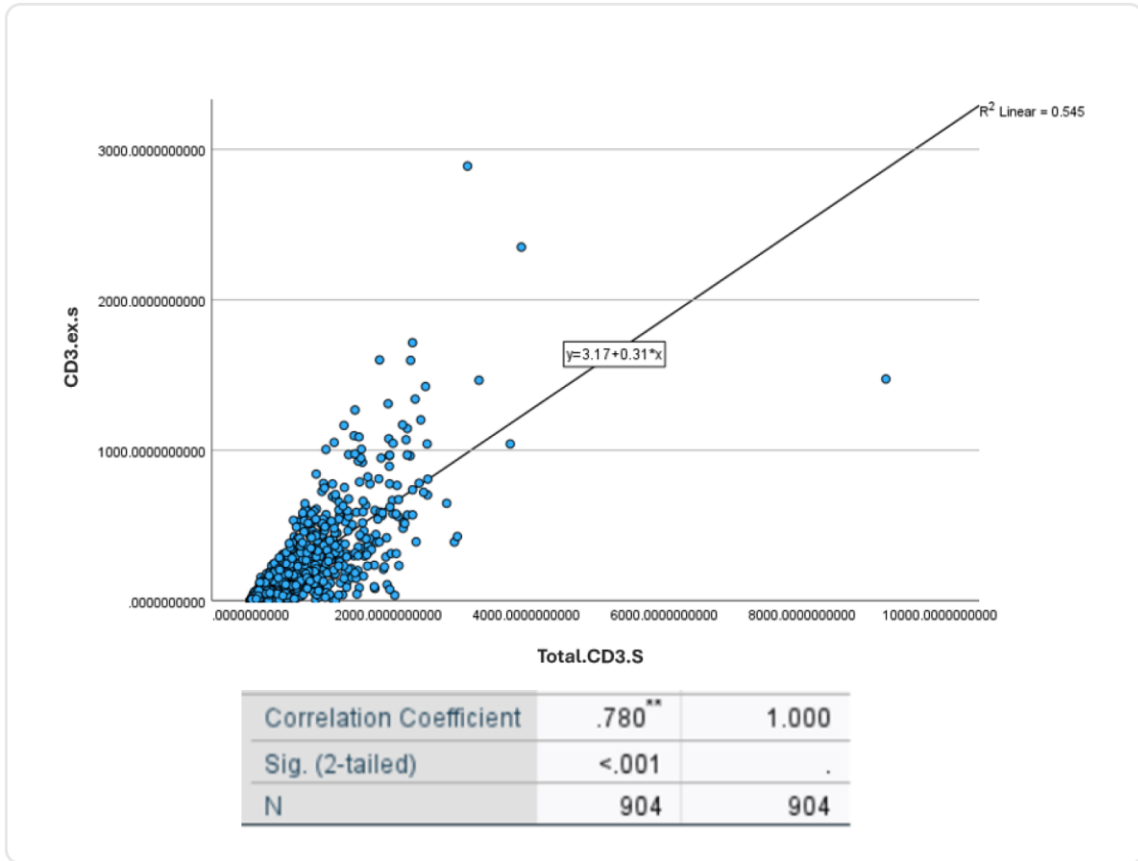


Figure 58. There is a positive correlation between CD3.ex and Total CD3 cells.

(Top) Scatter plot showing the relationship between average total CD3+ cell density (Total.CD3.S, x-axis) and the average density of CD3.ex cells (CD3+ cells expressing at least one exhaustion marker - LAG3, PD1, or TIM3; CD3.ex.S, y-axis) in the stroma. Each dot represents the average cell densities across three tumour-related cores from a single patient. The black line represents the linear regression fit, with the equation $y = 3.17 + 0.31x$. The R-squared value for the linear regression is 0.545, indicating that approximately 54.5% of the variance in average CD3.ex cell density is explained by average total CD3+ cell density. (Bottom) Spearman's rank correlation coefficient between average CD3.ex cell density and average total CD3+ cell density in the stroma. The correlation coefficient (rho) is 0.780, with a statistically significant p-value of < 0.001 , indicating a strong positive correlation. N = 904 patients.

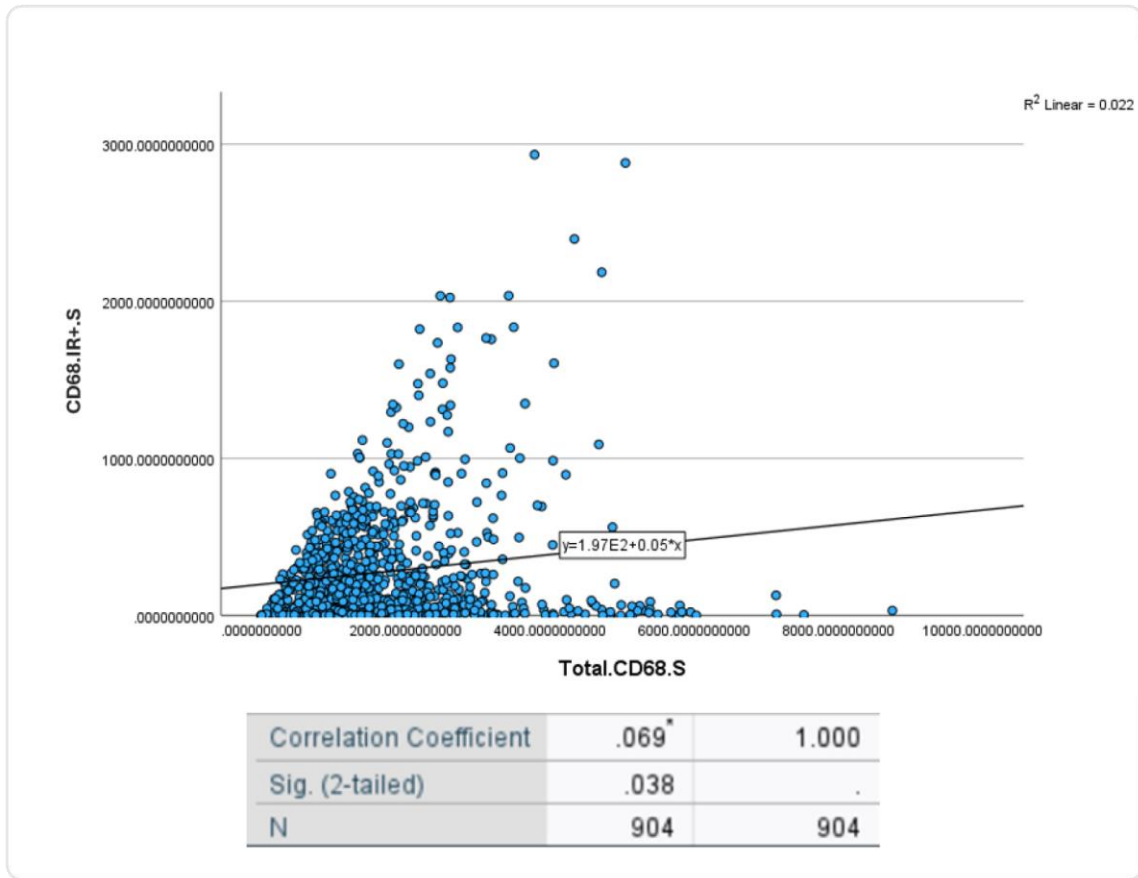


Figure 59. There is weak positive correlation between stromal CD68.IR+ and total CD68 in the stromal compartment.

(Top) Scatter plot showing the relationship between average total CD68+ cell density (Total.CD68.S, x-axis) and the average density of CD68.IR+ cells (CD68+ cells expressing at least one immune regulatory marker - LAG3, PD1, or TIM3; CD68.IR+.S, y-axis) in the stroma. Each dot represents the average cell densities across three tumour-related cores from a single patient. The black line represents the linear regression fit, with the equation $y = 8.7E2 + 0.057x$. The R-squared value for the linear regression is 0.003, indicating that only approximately 0.3% of the variance in average CD68.IR+ cell density is explained by average total CD68+ cell density. (Bottom) Spearman's rank correlation coefficient between average CD68.IR+ cell density and average total CD68+ cell density in the stroma. The correlation coefficient (rho) is 0.069, with a p-value of 0.038, indicating a weak positive correlation that is statistically significant. N = 904 patients.

3.5.3 Comparison of cell density between adjacent normal and tumour regions

3.5.3.1 CD3 positive cells

3.5.3.1.1 CD3.non.ex

Analysis of non-exhausted CD3+ T cell densities revealed contrasting patterns between the stromal and intraepithelial compartments of normal and tumour regions, **Figure 60**. Within the intraepithelial region, the density of CD3.non.ex cells was lower in tumour-related cores (IM vs AN, $p < 0.001$; CT vs AN, $p < 0.001$; LS vs AN, $p < 0.001$). Conversely, no significant differences in CD3.non.ex cell densities were observed in the stromal compartment when comparing AN cores to IM ($p < 0.56$), CT ($p < 0.99$), or LS ($p < 0.29$) cores (**Figure 60**). Within the tumour-related regions, there was a significant higher cell density of CD3.non.ex cells in stromal LS compared IM. In addition, intraepithelial CD3.non.ex cells density in IM was significantly higher than CT.

Heatmap analysis was used to illustrate the distribution of non-exhausted T-cells within the stromal and epithelium of all patients. Higher cell density of stromal LS was highlighted **Figure 61**. According to the spearman correlation, there was a weak positive correlation between CD3.non.ex. cell density in different sections, **Figure 62**.

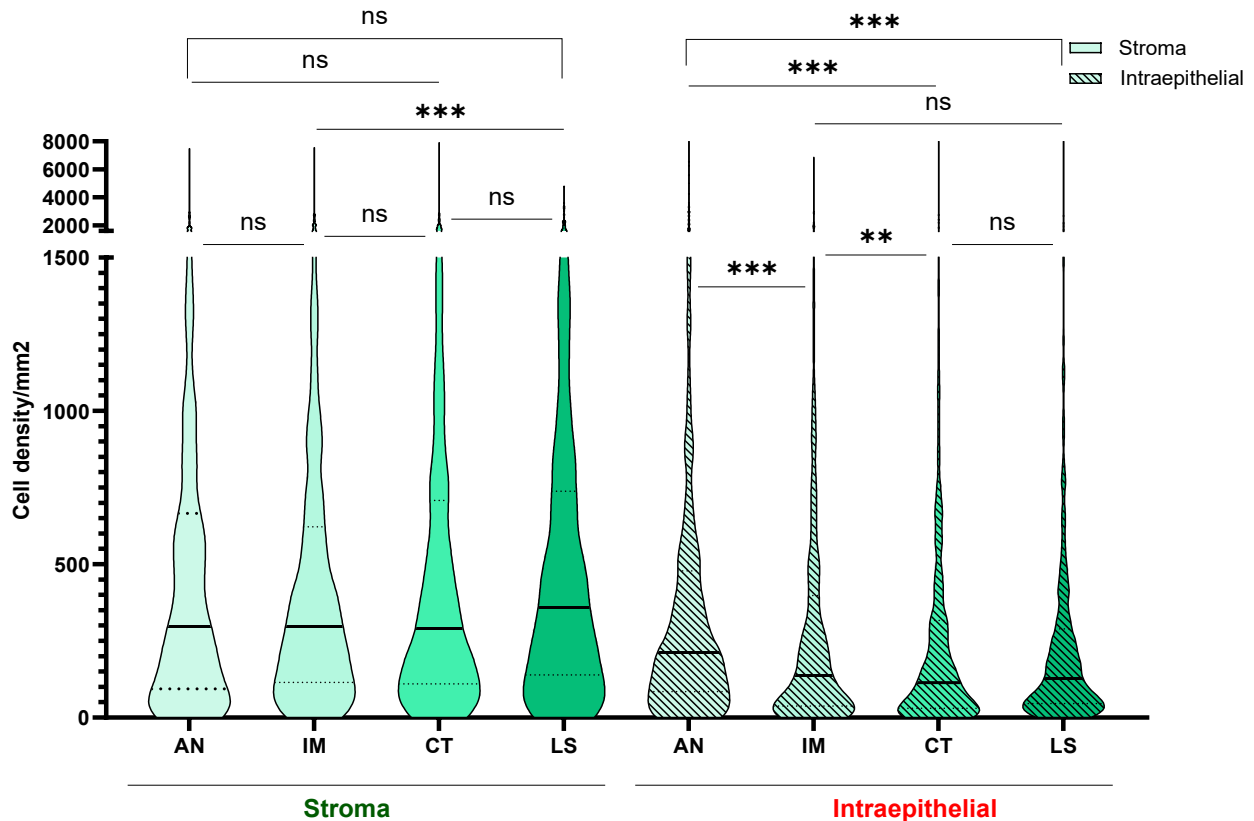


Figure 60. Comparison of non-exhausted CD3 cell densities in stroma and intraepithelial regions of adjacent normal and tumour-related cores showed a higher density of T cells in intraepithelial compartment of adjacent normal compared to tumor related cores.

Violin plots showing the distribution of CD3 cells densities (cells/mm²) in adjacent normal (AN), invasive margin (IM), core of tumour (CT), and luminal side (LS) cores within stroma (plain graphs) and intraepithelial (hatched graphs) compartments. The horizontal black lines within the violins represent the median. Comparisons between AN and tumour-related cores within each region were made using the two-sided Wilcoxon signed-rank test with Holm-Bonferroni correction. Significance levels are indicated as follows: * $p < 0.05$, ** $p < 0.01$, *** $p < 0.001$. Within the stroma, the following comparisons were made: AN vs. IM, $p < 0.56$ (ns); AN vs. CT, $p < 0.99$ (ns); AN vs. LS, $p < 0.29$ (ns); IM vs. CT, $p < 0.07$ (ns); LS vs. CT, $p < 0.3$ (ns); IM vs. LS, $p < 0.001$ (***). Within the intraepithelial compartment, the following comparisons were made: AN vs. IM, $p < 0.001$ (***); AN vs. CT, $p < 0.001$ (***); AN vs. LS, $p < 0.001$ (***); IM vs. CT, $p < 0.01$ (**), LS vs. CT, $p < 0.4$ (ns); IM vs. LS, $p < 0.1$ (ns). Note: The y-axis is divided into two segments with different scales to improve visualization of both low- and high-density values.

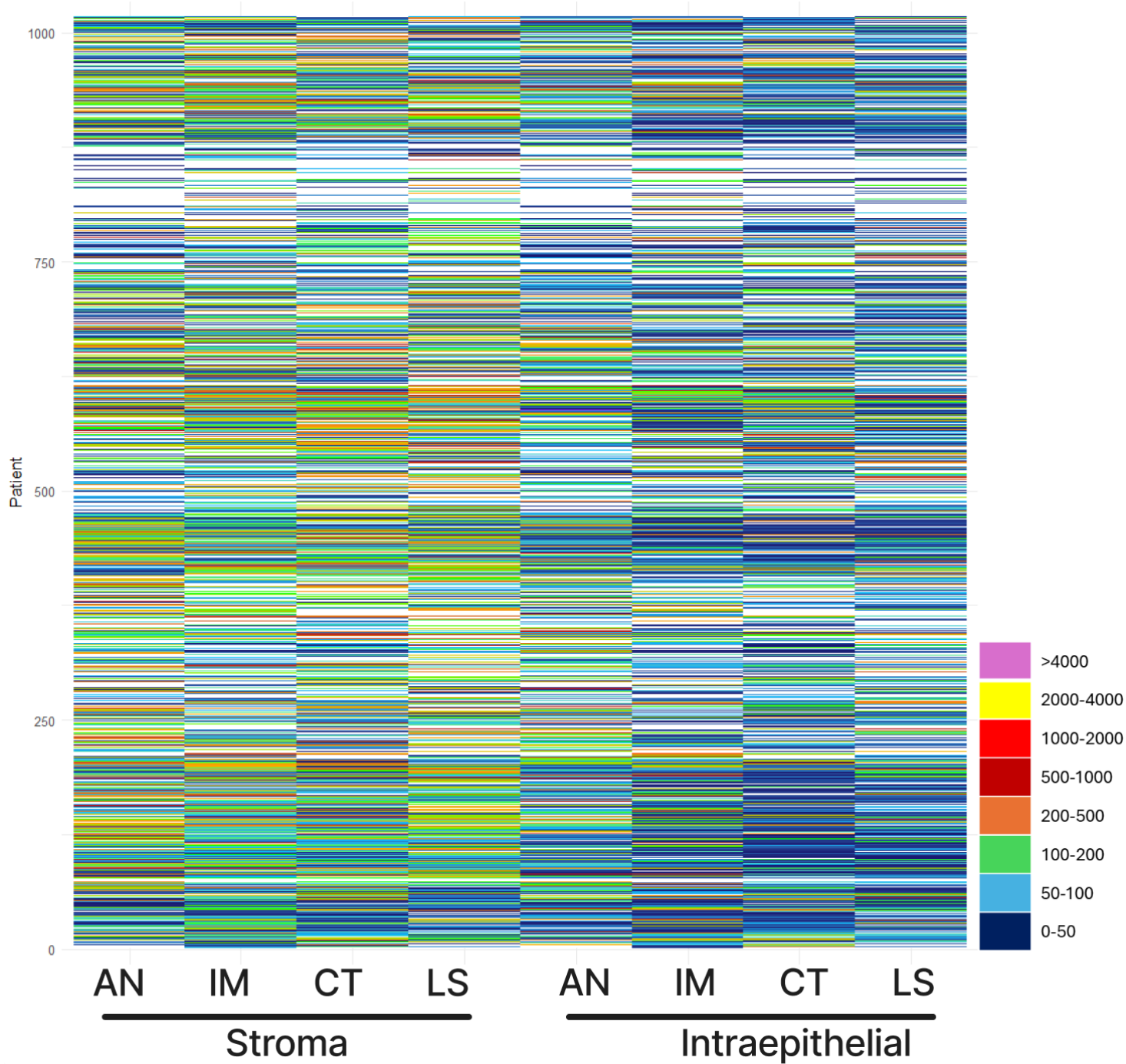


Figure 61. Heatmap of non-exhausted CD3+ cell density in colorectal cancer.

Each row represents an individual patient, and each column represents a distinct tissue core. The color intensity corresponds to the density of non-exhausted CD3+ cells, as indicated by the scale bar. white tiles indicate missing data.

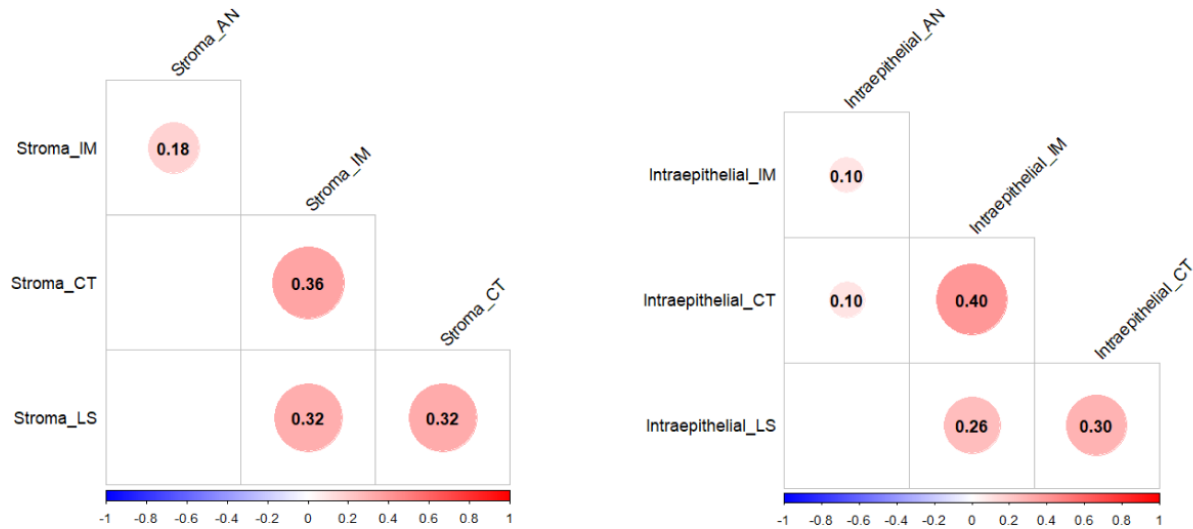


Figure 62. Spearman correlation analysis of CD3.non.ex densities within the tumour microenvironment of colorectal cancer, performed on the entire patient cohort.

Correlations are shown separately for stromal and intraepithelial compartments across four regions: adjacent normal (AN), invasive margin (IM), tumour center (CT), and luminal side (LS). Each cell in the matrix represents the correlation between two cell populations, with the color intensity indicating the strength and direction of the correlation (red for positive, blue for negative). The size of each circle is proportional to the magnitude of the correlation coefficient. Correlation coefficients are shown only for correlations with a statistically significant p-value ($p < 0.05$); non-significant correlations are left blank.

3.5.3.1.2 Total CD3.ex

Analysis of exhausted CD3+ T cell (CD3.ex) densities revealed significant differences between adjacent normal (AN) and tumour-related cores in the stromal compartment of Human CRC tissue sections (**Figure 63**). Specifically, the density of CD3.ex cells was lower in the stroma of AN cores compared to the stroma of invasive margin (IM) ($p = 0.035$), center of the tumour (CT) ($p = 0.008$), and luminal side (LS) cores ($p = 0.005$). However, no significant differences in CD3.ex cell densities were observed when comparing the intraepithelial regions of AN cores to the corresponding tumour regions. Further analysis revealed significantly higher densities of CD3.ex cells in the IM compared to both the CT and LS regions, however, in the stroma luminal side showed significant higher cell density compared to the IM. The heatmap visualization (**Figure 64**) demonstrated substantial inter-patient heterogeneity highlighting the diverse immune profiles present within the cohort. No correlation was found between CD3.ex cell densities in the normal and tumour regions

in either the stromal or intraepithelial compartments. However, a significant association was observed between CD3.ex densities in all tumour-associated regions within both compartments, **Figure 65**.

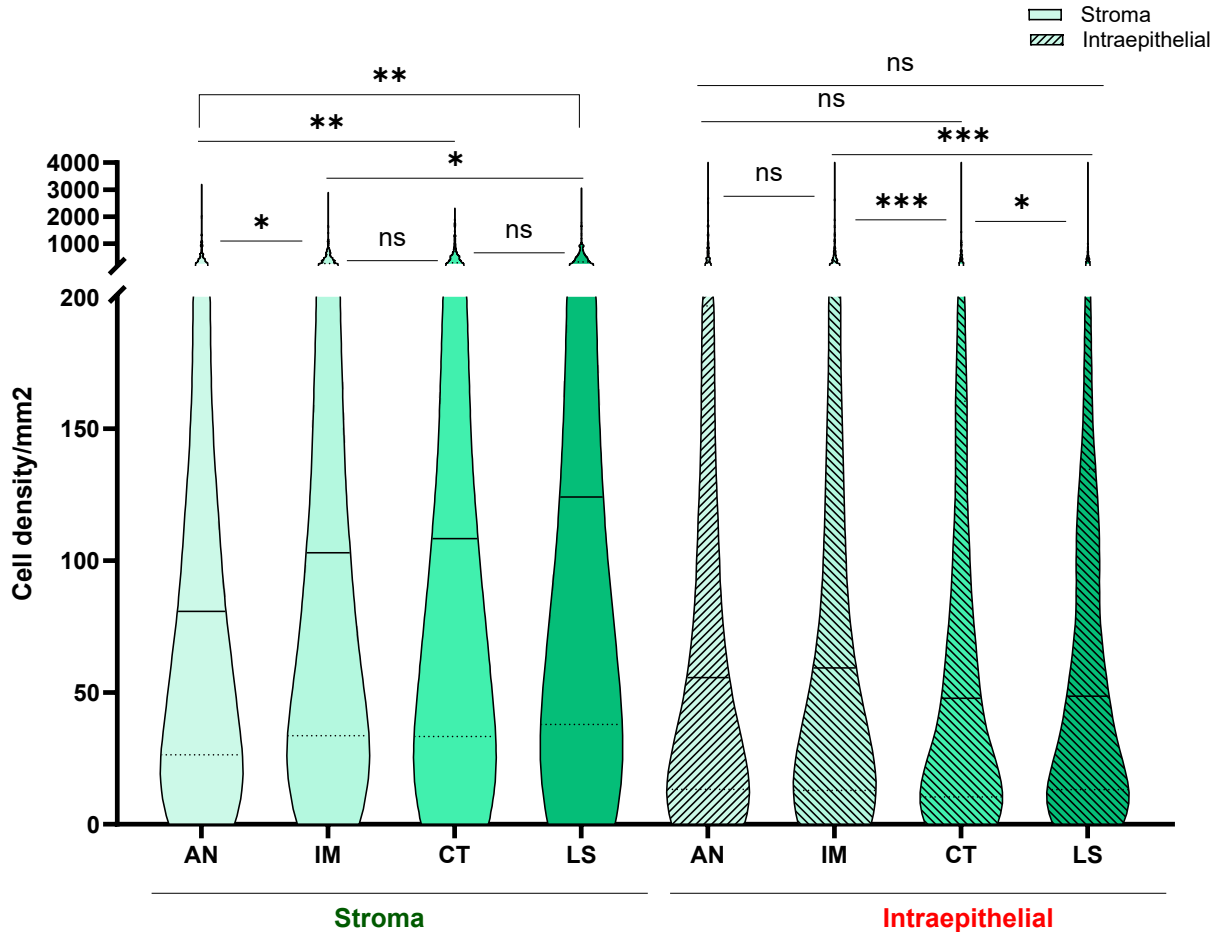


Figure 63. Higher density of CD3.ex in the stromal compartment of tumor related cores compared to adjacent normal.

Violin plots showing the distribution of CD3 cells densities (cells/mm²) in adjacent normal (AN), invasive margin (IM), core of tumour (CT), and luminal side (LS) cores within stroma (plain graphs) and intraepithelial (hatched graphs) compartments. The horizontal black lines within the violins represent the median. Comparisons between AN and tumour-related cores within each region were made using the two-sided Wilcoxon signed-rank test with Holm-Bonferroni correction. Significance levels are indicated as follows: * $p < 0.05$, ** $p < 0.01$, *** $p < 0.001$. Within the stroma, the following comparisons were made: AN vs. IM, $p < 0.035$ (*); AN vs. CT, $p < 0.008$ (**); AN vs. LS, $p < 0.005$ (**); IM vs. CT, $p < 0.2$ (ns), LS vs. CT, $p < 0.3$ (ns); IM vs. LS, $p < 0.02$ (*). Within the intraepithelial regions, the following comparisons were made: AN vs. IM, $p < 0.4$ (ns); AN vs. CT, $p < 0.25$ (ns); AN vs. LS, $p < 0.07$ (ns); IM vs. CT, $p < 0.001$ (***), LS vs. CT, $p < 0.035$ (*), IM vs. LS, $p < 0.001$ (***). Note: The y-axis is divided into two segments with different scales to improve visualization of both low- and high-density values.

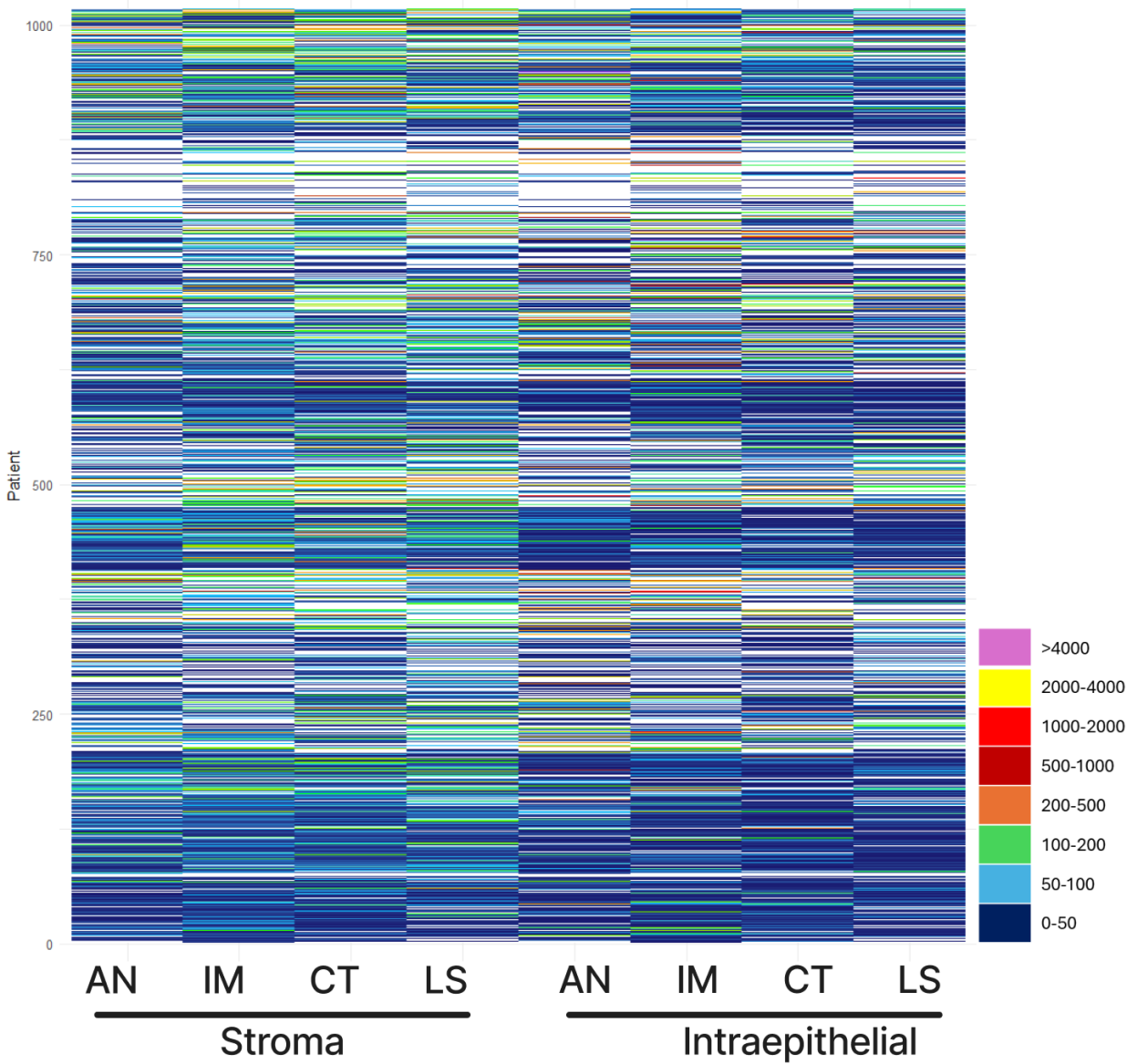


Figure 64. Heatmap of exhausted CD3+ cell density in colorectal cancer.

Each row represents an individual patient, and each column represents a distinct tissue core. The color intensity corresponds to the density of exhausted CD3+ cells, as indicated by the scale bar. white tiles indicate missing data.

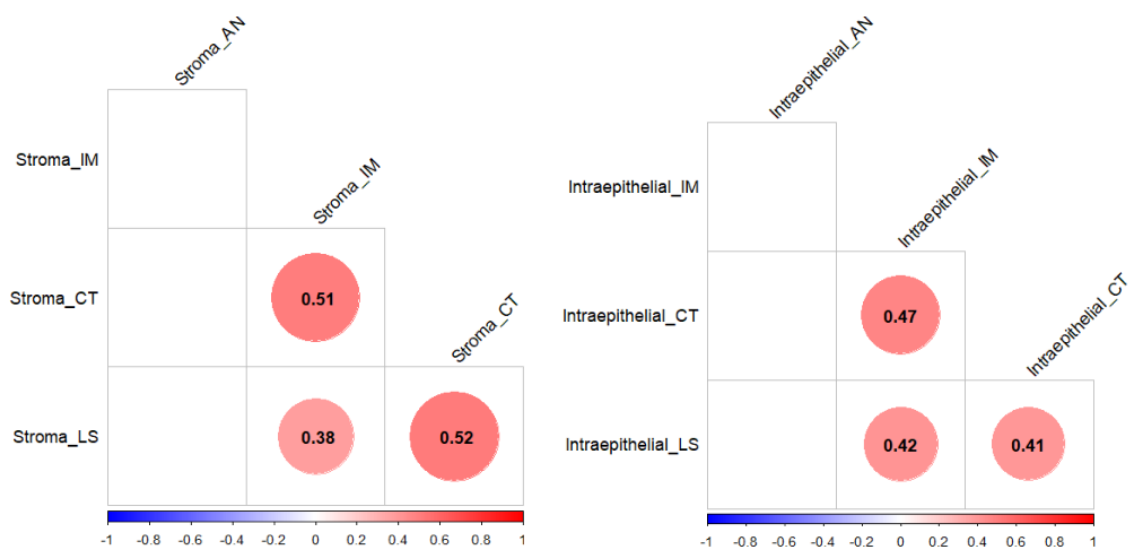


Figure 65. Spearman correlation analysis of CD3.ex densities within the tumour microenvironment of colorectal cancer, performed on the entire patient cohort.

Correlations are shown separately for stromal and intraepithelial compartments across four regions: adjacent normal (AN), invasive margin (IM), tumour center (CT), and luminal side (LS). Each cell in the matrix represents the correlation between two cell populations, with the color intensity indicating the strength and direction of the correlation (red for positive, blue for negative). The size of each circle is proportional to the magnitude of the correlation coefficient. Correlation coefficients are shown only for correlations with a statistically significant p-value ($p < 0.05$); non-significant correlations are left blank.

3.5.3.2 CD3.ex subpopulation

In this chapter violin plot showing the cell density of each exhausted phenotype of CD3 was depicted. Furthermore, heatmap showing the cell density in the cores, and a spearman correlation matrix in both stromal and intraepithelial compartment showing the correlation of phenotypes to give a better understanding of CRC TME. Three phenotypes, including, LAG3/PD1, LAG3, TIM3, and LAG3/TIM3/PD1 had a very low cell density in this project which is not shown with plots.

3.5.3.2.1 PD1+CD3 cell density

Although there was no significant difference between the cell density of CD3 PD1+ cells between AN and tumour related cores in both stromal and intraepithelial compartments,

within tumour related cores a different localization was observed. There was a significantly higher cell density of stromal and intraepithelial PD1+CD3 cells in IM compared to LS ($P < 0.02$ and $P < 0.017$). Furthermore, intraepithelial CD3 PD1+ had higher cell density in IM compared to CT ($P < 0.04$) (**Figure 66**). Heatmap showing the interpatient heterogeneity in the cell density of PD1+CD3+ (**Figure 67**). There was positive correlations in both stromal and intraepithelial cell density of PD1+CD3+ between different sections (**Figure 68**).

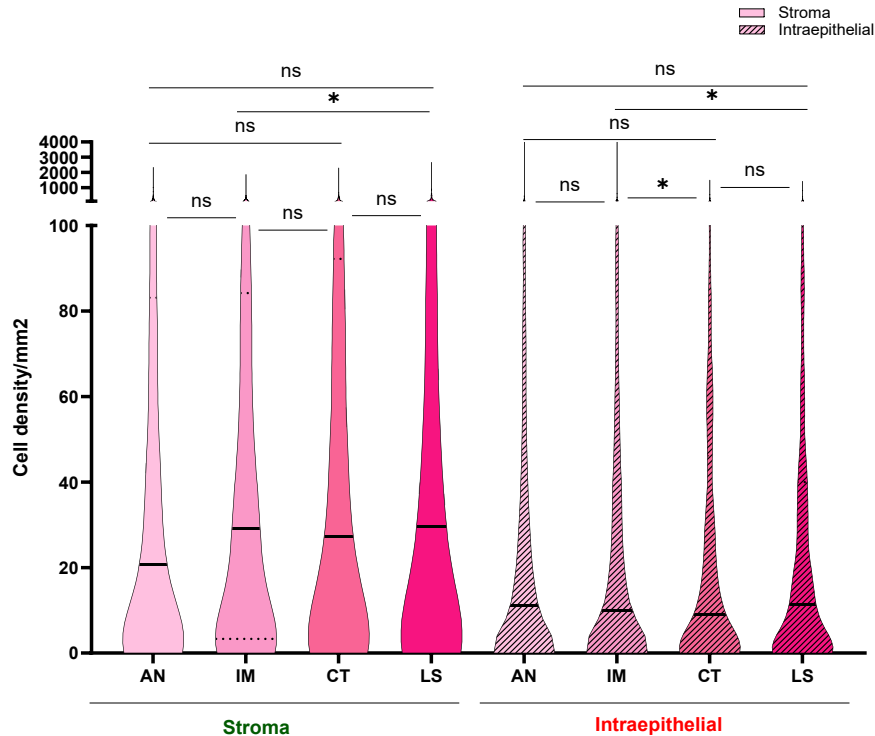


Figure 66. Comparison of PD1+ CD3 cell densities in Stroma and intraepithelial Regions of Adjacent Normal and Tumour-Related Cores.

Violin plots showing the distribution of PD1+CD3 cells densities (cells/mm²) in adjacent normal (AN), invasive margin (IM), core of tumour (CT), and luminal side (LS) cores within stroma (plain graphs) and tumour (hatched graphs). The horizontal black lines within the violins represent the median. Comparisons between AN and tumour-related cores within each region were made using the two-sided Wilcoxon signed-rank test with Holm-Bonferroni correction. Significance levels are indicated as follows: * $p < 0.05$, ** $p < 0.01$, *** $p < 0.001$. Within the stroma, the following comparisons were made: AN vs. IM, $p < 0.5$ (ns); AN vs. CT, $p < 0.1$ (ns); AN vs. LS, $p < 0.1$ (ns); CT vs. IM, $p < 0.3$ (ns); IM vs. LS, $p < 0.02$ (*); CT vs. LS, $p < 0.4$ (ns). Within the intraepithelial compartment, the following comparisons were made: AN vs. IM, $p < 0.9$ (ns); AN vs. CT, $p < 0.2$ (ns); AN vs. LS, $p < 0.2$ (ns); CT vs. IM, $p < 0.04$ (*); IM vs. LS, $p < 0.017$ (*); CT vs. LS, $p < 0.3$ (ns).

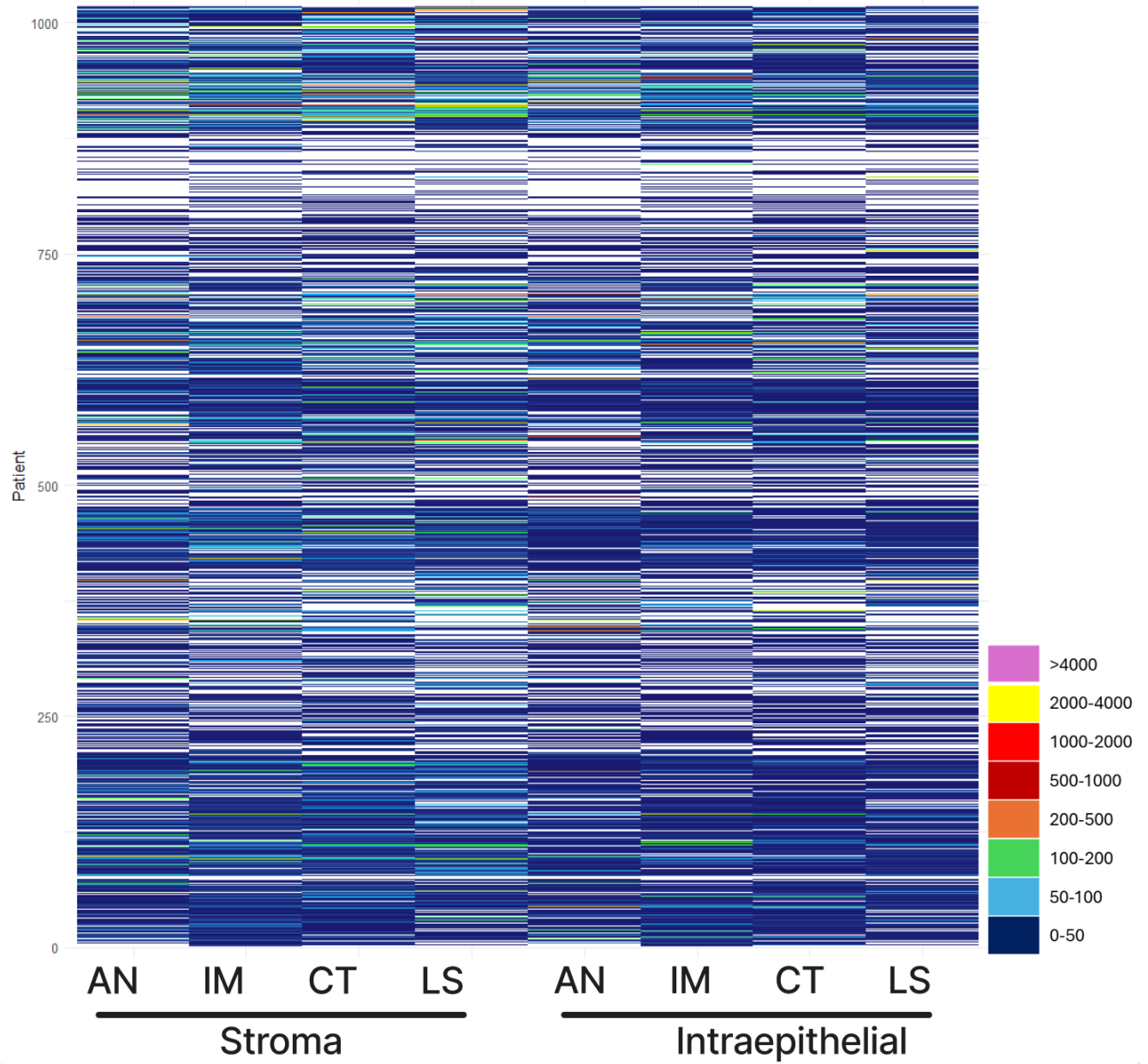


Figure 67. Heatmap of PD1+ CD3+ cell density in colorectal cancer.

Each row represents an individual patient, and each column represents a distinct tissue core. The color intensity corresponds to the density of PD1+ CD3+ cells, as indicated by the scale bar. white tiles indicate missing data.

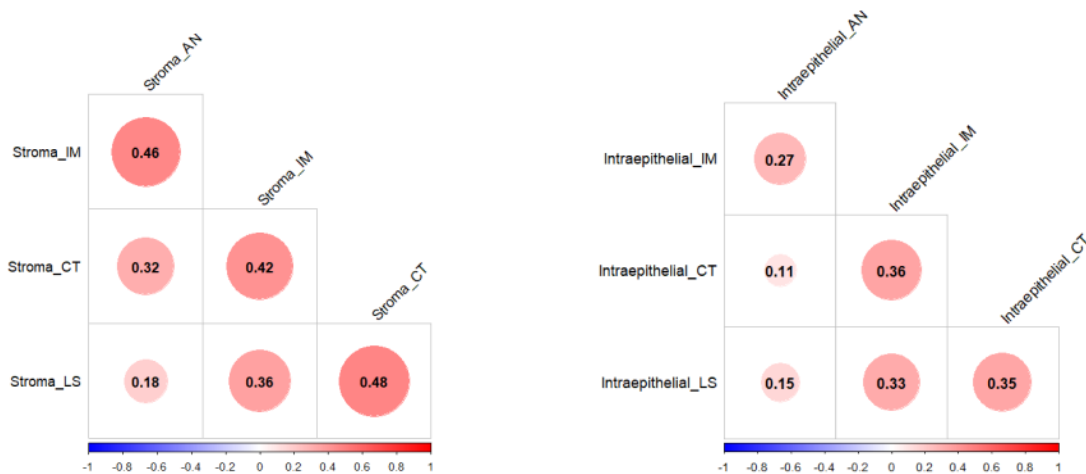


Figure 68. Spearman correlation analysis of PD1+CD3 densities within the tumour microenvironment of colorectal cancer, performed on the entire patient cohort.

Correlations are shown separately for stromal and intraepithelial compartments across four regions: adjacent normal (AN), invasive margin (IM), tumour center (CT), and luminal side (LS). Each cell in the matrix represents the correlation between two cell populations, with the color intensity indicating the strength and direction of the correlation (red for positive, blue for negative). The size of each circle is proportional to the magnitude of the correlation coefficient. Correlation coefficients are shown only for correlations with a statistically significant p-value ($p < 0.05$); non-significant correlations are left blank.

3.5.3.2.2 TIM+CD3 cell density

Although all tumour-related cores showed a significant higher cell density of stromal TIM3+CD3 cells, intraepithelial TIM3+CD3 cells only had significant higher cell density in LS compared to AN. Comparison of tumour related cores, revealed a significant higher cells density of intraepithelial TIM3+CD3 in IM compared to LS and CT (**Figure 69**). Heatmap shows the intra patient heterogeneity between patients (**Figure 70**) and spearman correlation showed a positive correlation between the cell density of TIM3+CD3 between different sections (**Figure 71**).

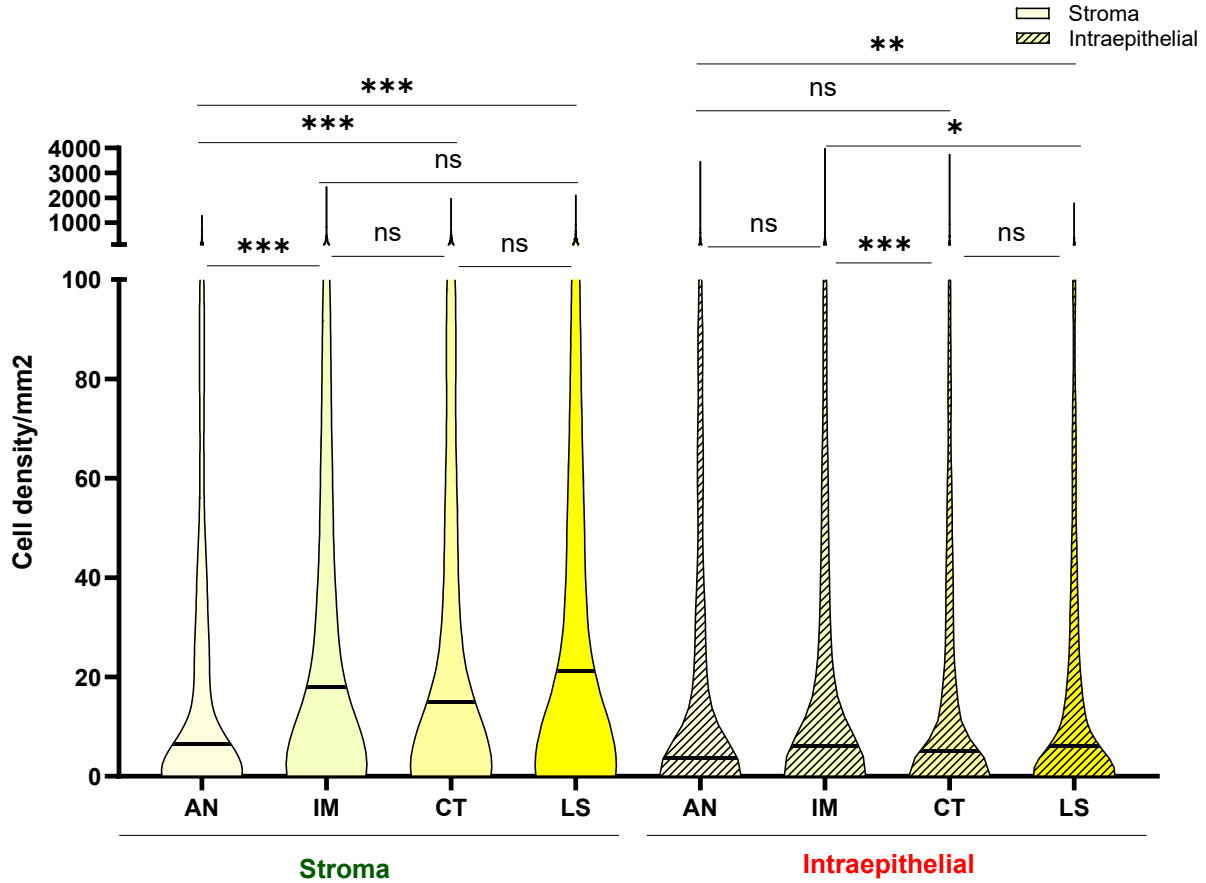


Figure 69. Higher density of stromal Tim3+ CD3 cells in tumor related cores compared to adjacent normal.

Violin plots showing the distribution of TIM3 +CD3 cells densities (cells/mm²) in adjacent normal (AN), invasive margin (IM), core of tumour (CT), and luminal side (LS) cores within stroma (plain graphs) and tumour (hatched graphs). The horizontal black lines within the violins represent the median. Comparisons between AN and tumour-related cores within each region were made using the two-sided Wilcoxon signed-rank test with Holm-Bonferroni correction. Significance levels are indicated as follows: * $p < 0.05$, ** $p < 0.01$, *** $p < 0.001$. Within the stroma, the following comparisons were made: AN vs. IM, $p < 0.001$ (***); AN vs. CT, $p < 0.001$ (***); AN vs. LS, $p < 0.001$ (***); CT vs. IM, $p < 0.7$ (ns); IM vs. LS, $p < 0.07$ (ns); CT vs. LS, $p < 0.2$ (ns). Within the intraepithelial compartment, the following comparisons were made: AN vs. IM, $p < 0.1$ (ns); AN vs. CT, $p < 0.1$ (ns); AN vs. LS, $p < 0.009$ (**); CT vs. IM, $p < 0.001$ (***); IM vs. LS, $p < 0.014$ (*); CT vs. LS, $p < 0.2$ (ns).

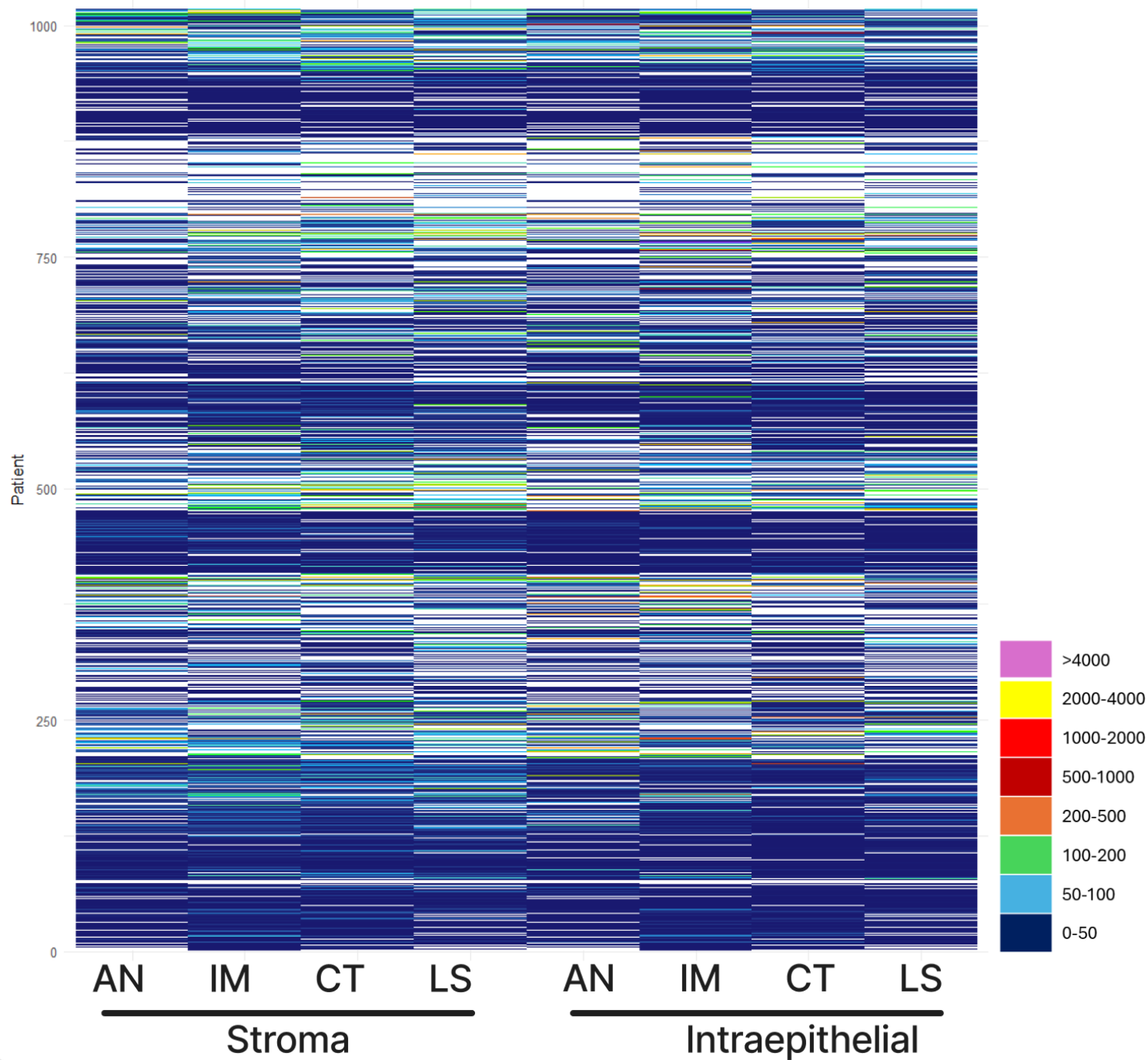


Figure 70. Heatmap of TIM3+ CD3+ cell density in colorectal cancer.

Each row represents an individual patient, and each column represents a distinct tissue core. The color intensity corresponds to the density of TIM3+ CD3+ cells, as indicated by the scale bar. white tiles indicate missing data.

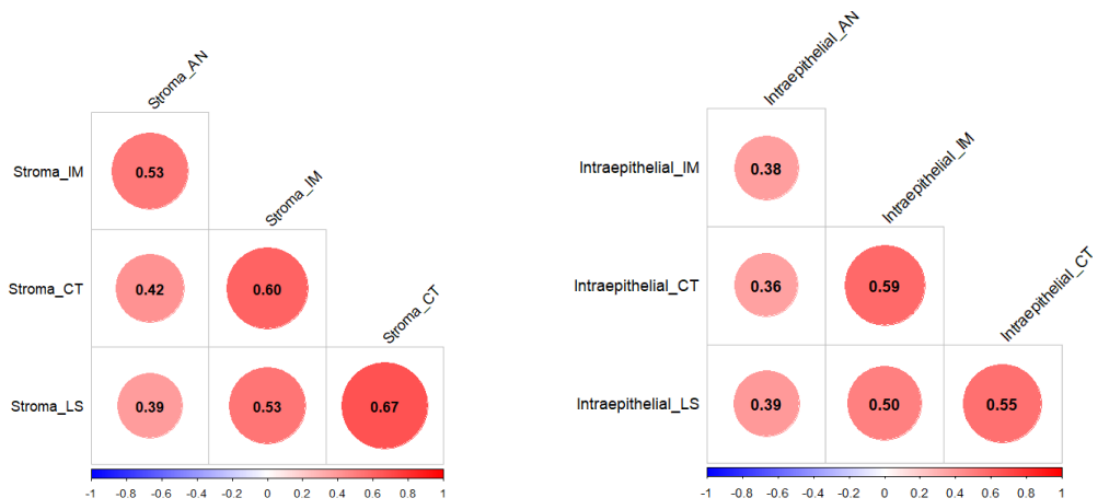


Figure 71. Spearman correlation analysis of TIM3+CD3 densities within the tumour microenvironment of colorectal cancer, performed on the entire patient cohort.

Correlations are shown separately for stromal and intraepithelial compartments across four regions: adjacent normal (AN), invasive margin (IM), tumour center (CT), and luminal side (LS). Each cell in the matrix represents the correlation between two cell populations, with the color intensity indicating the strength and direction of the correlation (red for positive, blue for negative). The size of each circle is proportional to the magnitude of the correlation coefficient. Correlation coefficients are shown only for correlations with a statistically significant p-value ($p < 0.05$); non-significant correlations are left blank.

3.5.3.2.3 LAG3+CD3 cell density

There is no difference in the density of LAG3+CD3 cells between different sections in both stromal and intraepithelial compartments, except there is a higher density of LAG3+CD3 cells in the intraepithelial AN compared to LS (**Figure 72**). Heatmap showing the density of LAG3+CD3+ between different samples (**Figure 73**) and spearman correlation showing the positive correlation between different samples specifically in the stromal compartment, **Figure 74**.

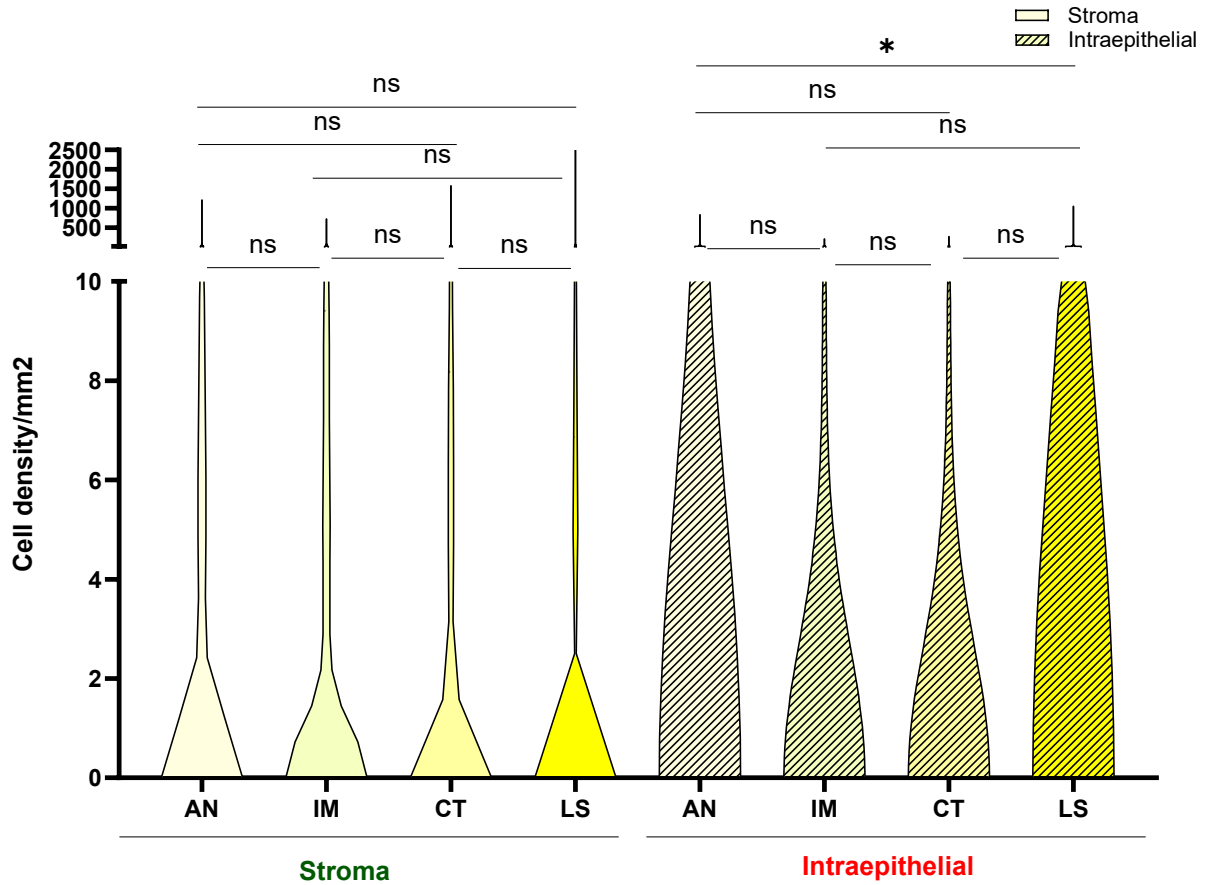


Figure 72. Comparison of LAG3+ CD3 cell densities in stroma and intraepithelial regions of adjacent normal and tumour-related cores.

Violin plots showing the distribution of LAG3+CD3 cells densities (cells/mm²) in adjacent normal (AN), invasive margin (IM), core of tumour (CT), and luminal side (LS) cores within stroma (plain graphs) and tumour (hatched graphs). The horizontal black lines within the violins represent the median. Comparisons between AN and tumour-related cores within each region were made using the two-sided Wilcoxon signed-rank test with Holm-Bonferroni correction. Significance levels are indicated as follows: *p < 0.05, **p < 0.01, ***p < 0.001. Within the stroma, the following comparisons were made: AN vs. IM, p < 0.1 (ns); AN vs. CT, p < 0.08 (ns); AN vs. LS, p < 0.2 (ns); CT vs. IM, p < 0.1 (**); IM vs. LS, p < 0.1 (ns); CT vs. LS, p < 0.2 (ns). Within the intraepithelial compartment, the following comparisons were made: AN vs. IM, p < 0.1 (ns); AN vs. CT, p < 0.06 (ns); AN vs. LS, p < 0.03 (*); CT vs. IM, p < 0.9 (ns); IM vs. LS, p < 0.1 (ns); CT vs. LS, p < 0.1 (ns).

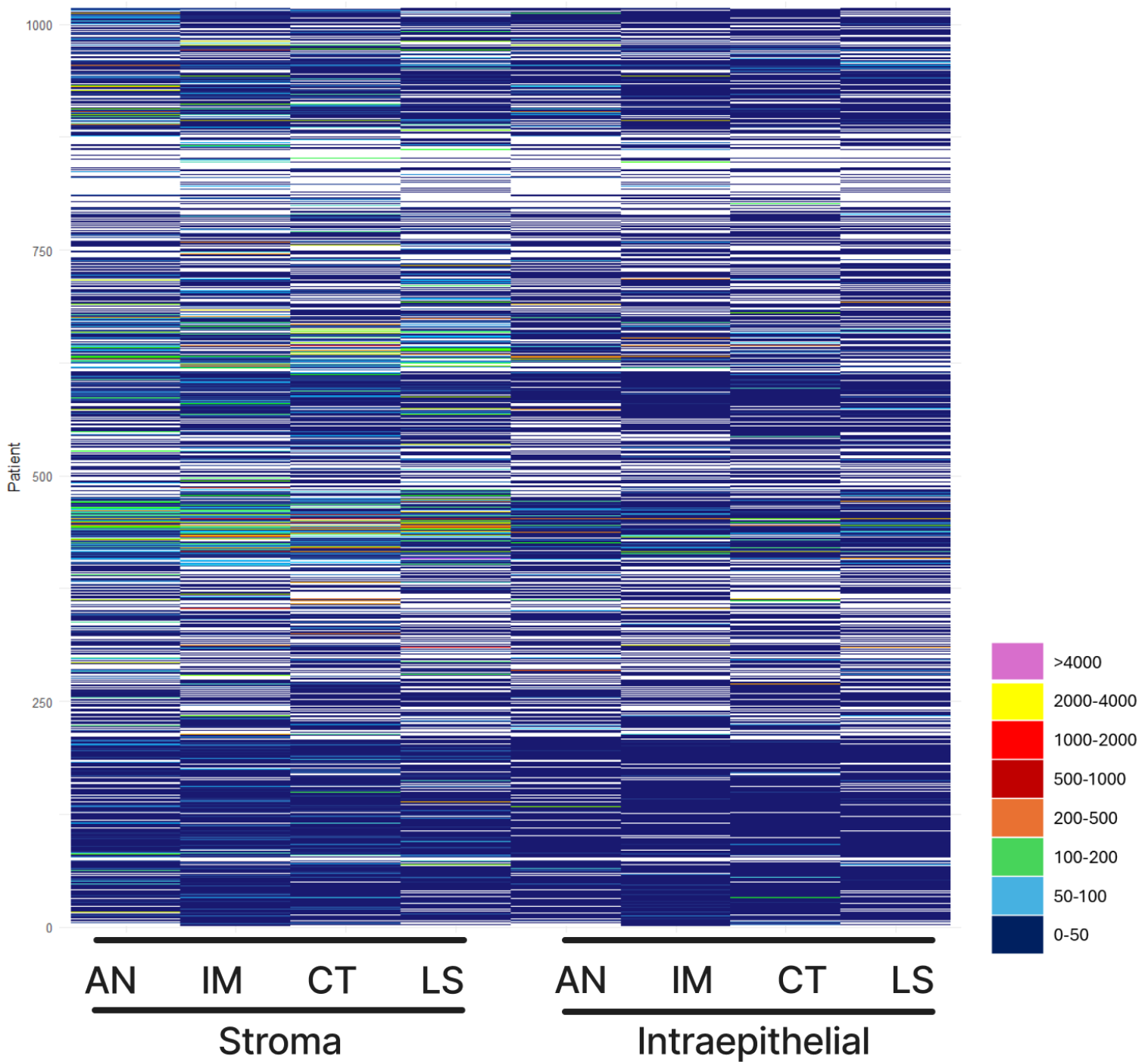


Figure 73. Heatmap of LAG3+ CD3+ cell density in colorectal cancer.

Each row represents an individual patient, and each column represents a distinct tissue core. The color intensity corresponds to the density of LAG3+ CD3+ cells, as indicated by the scale bar. white tiles indicate missing data.

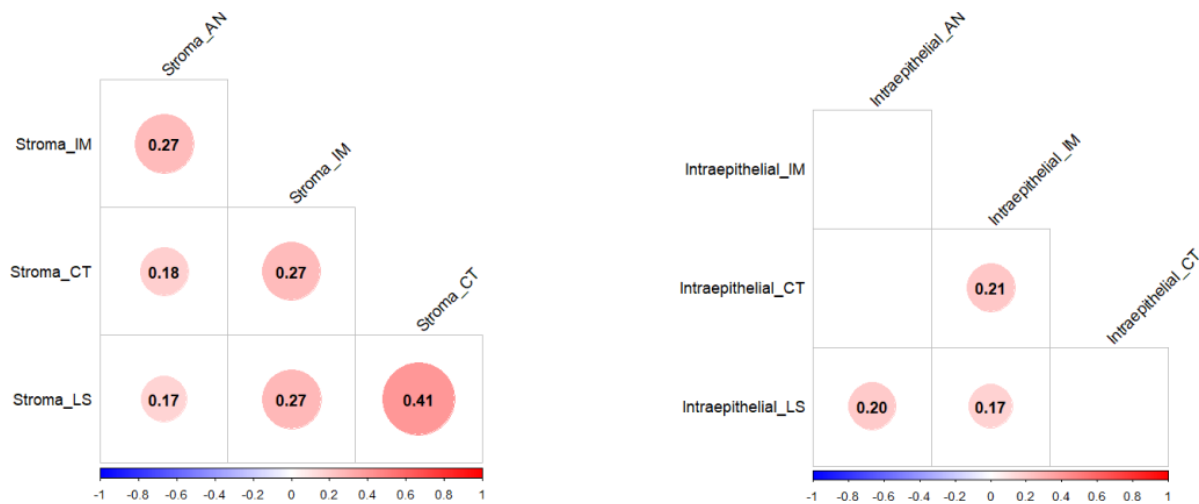


Figure 74. Spearman correlation analysis of LAG3+CD3 densities within the tumour microenvironment of colorectal cancer, performed on the entire patient cohort.

Correlations are shown separately for stromal and intraepithelial compartments across four regions: adjacent normal (AN), invasive margin (IM), tumour center (CT), and luminal side (LS). Each cell in the matrix represents the correlation between two cell populations, with the color intensity indicating the strength and direction of the correlation (red for positive, blue for negative). The size of each circle is proportional to the magnitude of the correlation coefficient. Correlation coefficients are shown only for correlations with a statistically significant p-value ($p < 0.05$); non-significant correlations are left blank.

3.5.3.2.4 PD1+TIM3+CD3 cell density

There was a significant higher cell density of stromal PD1+TIM3+CD3 in tumour related cores compared to AN, however, intraepithelial PD1+TIM3+CD3 only have significant higher cell density in IM compared to AN. Within the tumour related cores, stromal PD1+TIM3+ CD3 in IM was lower than CT and LS. In intraepithelial compartment significant higher cell density of PD1+TIM3+ CD3 in IM compared to LS was observed (**Figure 75**). Heatmap (**Figure 76**) showing intra patient heterogeneity in the PD1+TIM3+ CD3 density. According to the spearman correlation, a positive correlation between the cell density of PD1+ TIM3+ CD3 between different sections were seen (**Figure 77**).

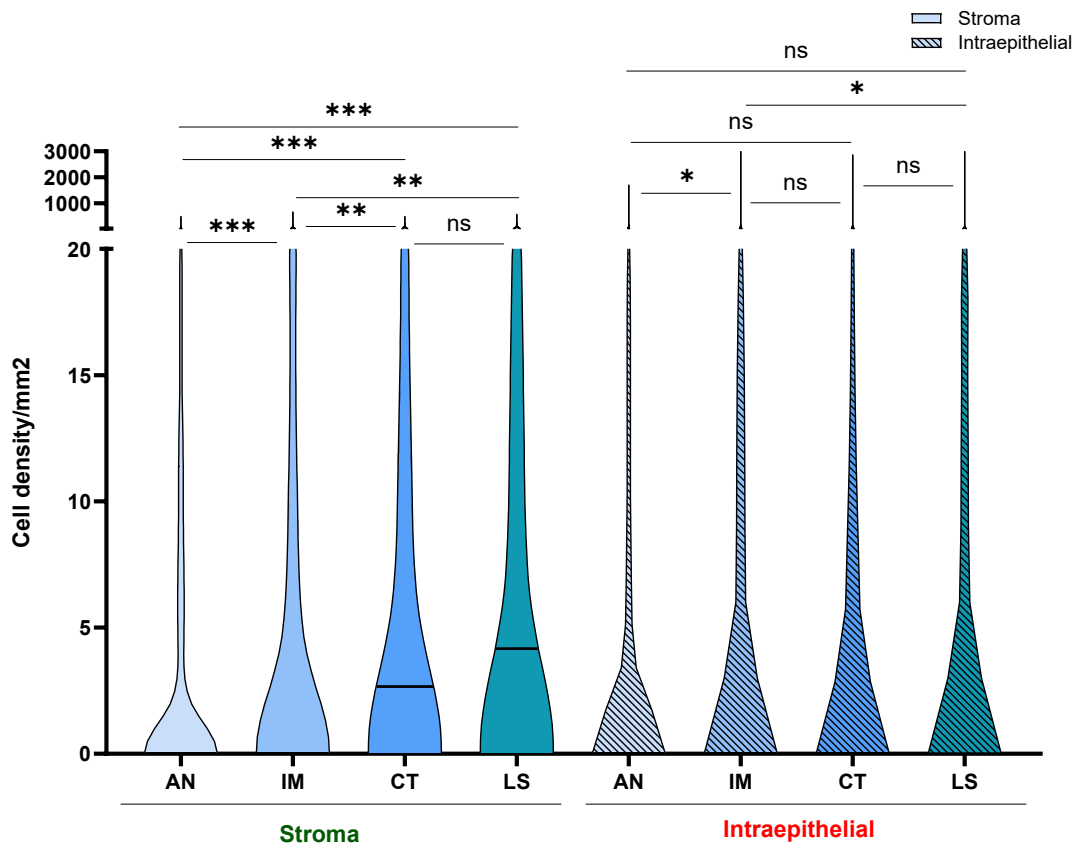


Figure 75. Higher density of TIM3+PD1+ CD3 cell densities in stromal compartment of tumor related cores compared to adjacent normal.

Violin plots showing the distribution of TIM3 PD1+CD3 cells densities (cells/mm²) in adjacent normal (AN), invasive margin (IM), core of tumour (CT), and luminal side (LS) cores within stroma (plain graphs) and tumour (hatched graphs). The horizontal black lines within the violins represent the median. Comparisons between AN and tumour-related cores within each region were made using the two-sided Wilcoxon signed-rank test with Holm-Bonferroni correction. Significance levels are indicated as follows: * $p < 0.05$, ** $p < 0.01$, *** $p < 0.001$. Within the stroma, the following comparisons were made: AN vs. IM, $p < 0.001$ (***) ; AN vs. CT, $p < 0.001$ (***) ; AN vs. LS, $p < 0.001$ (***) ; CT vs. IM, $p < 0.008$ (**) ; IM vs. LS, $p < 0.01$ (*) ; CT vs. LS, $p < 0.9$ (ns). Within the intraepithelial compartment, the following comparisons were made: AN vs. IM, $p < 0.027$ (*) ; AN vs. CT, $p < 0.9$ (ns) ; AN vs. LS, $p < 0.6$ (ns) ; CT vs. IM, $p < 0.1$ (ns) ; IM vs. LS, $p < 0.015$ (*) ; CT vs. LS, $p < 0.055$ (ns).

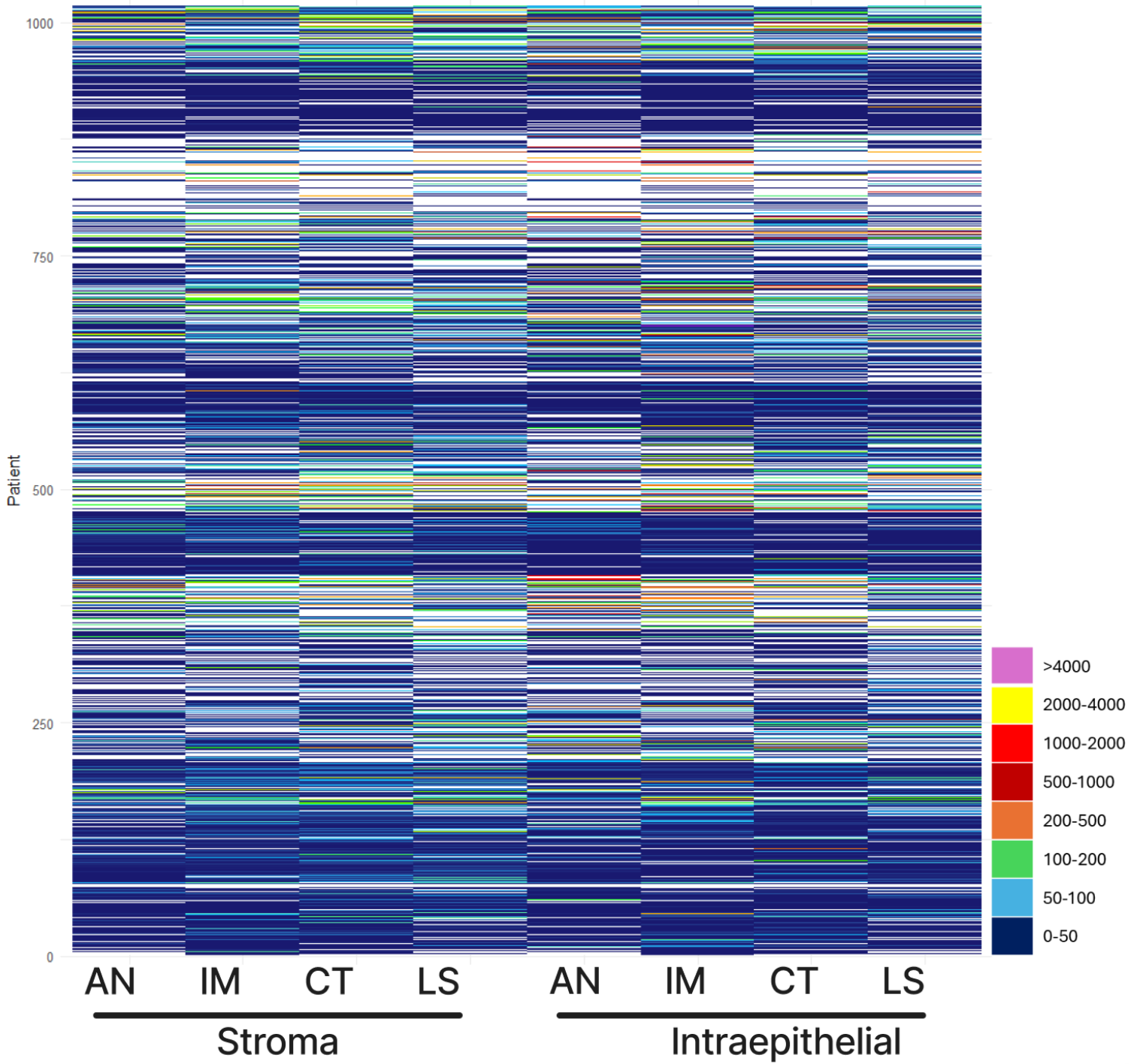


Figure 76. Heatmap of TIM3+PD1+ CD3+ cell density in colorectal cancer.

Each row represents an individual patient, and each column represents a distinct tissue core. The color intensity corresponds to the density of TIM3+ PD1+ CD3+ cells, as indicated by the scale bar. white tiles indicate missing data.

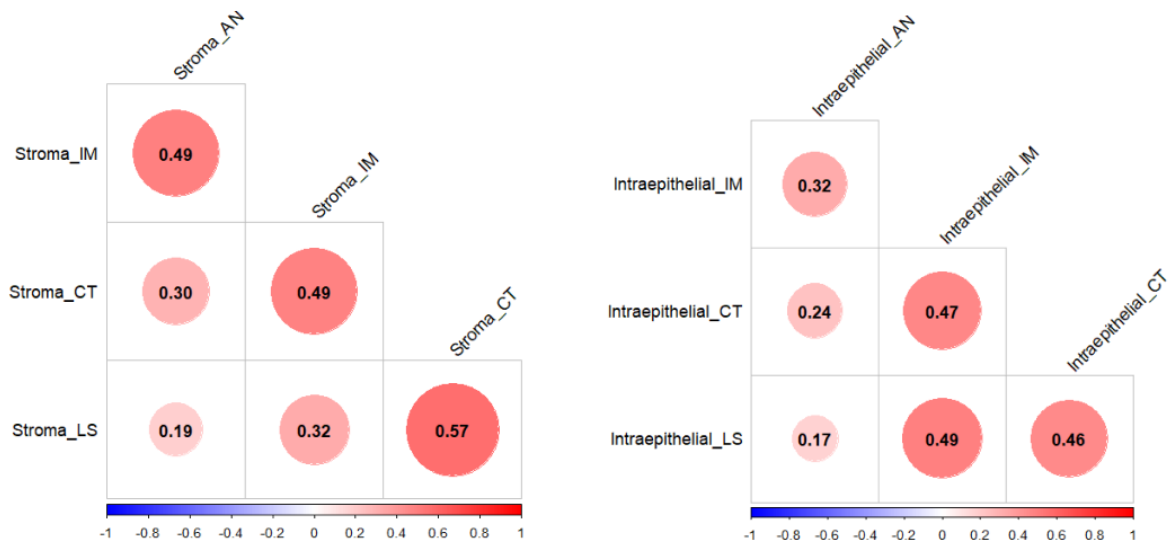


Figure 77. Spearman correlation analysis of TIM3+PD1+ CD3 densities within the tumour microenvironment of colorectal cancer, performed on the entire patient cohort.

Correlations are shown separately for stromal and intraepithelial compartments across four regions: adjacent normal (AN), invasive margin (IM), tumour center (CT), and luminal side (LS). Each cell in the matrix represents the correlation between two cell populations, with the color intensity indicating the strength and direction of the correlation (red for positive, blue for negative). The size of each circle is proportional to the magnitude of the correlation coefficient. Correlation coefficients are shown only for correlations with a statistically significant p-value ($p < 0.05$); non-significant correlations are left blank.

3.5.3.3 CD68 positive cells

3.5.3.3.112. Macrophage without IR

There are highly statistically significant differences in the densities of IR-negative macrophages between the stroma of AN cores and the stroma of all tumour-related cores (IM, CT, and LS) (all p-values < 0.001), in which the stroma of AN cores has a lower density of IR-negative macrophages compared to the stroma of IM, CT, and LS cores. Furthermore, there are also statistically significant lower cell density of IR-negative macrophages when comparing the intraepithelial tumour region of AN cores to the intraepithelial tumour regions of IM, CT, and LS cores. (AN vs. IM: $p < 0.002$, AN vs. CT: $p < 0.05$, AN vs. LS: $p < 0.001$).

Within the tumour related cores, there was a significant lower cell density of stromal IR-negative macrophages in the IM compared to both CT and LS. (**Figure 78**). Heatmap

(Figure 79) showing intra patient heterogeneity in the IR- macrophages density in different cores. Higher densities of IR- macrophages in stroma compared to intraepithelial regions are obvious. Spearman correlation showed a positive correlation between the cell density of IR- macrophages between different sections (Figure 80).

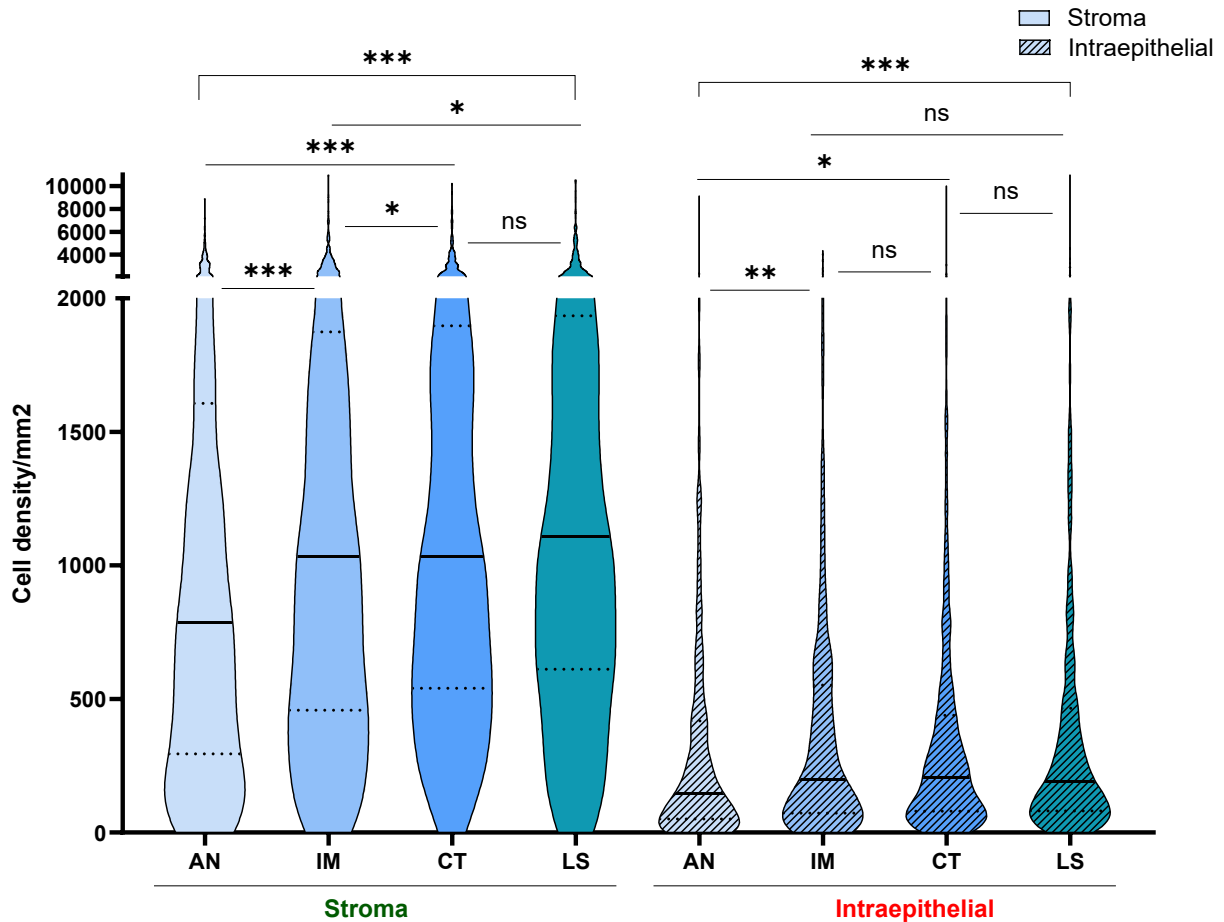


Figure 78. Higher density of macrophages (Excluding IR+ cells) in stromal and intraepithelial regions of tumour-related cores compared to adjacent normal.

Violin plots showing the distribution of macrophage densities (cells/mm²) in adjacent normal (AN), invasive margin (IM), core of tumour (CT), and luminal side (LS) cores within stroma (plain graphs) and tumour (hatched graphs). The horizontal black lines within the violins represent the median. Comparisons between AN and tumour-related cores within each region were made using the two-sided Wilcoxon signed-rank test with Holm-Bonferroni correction. Significance levels are indicated as follows: *p < 0.05, **p < 0.01, ***p < 0.001. Within the stroma, the following comparisons were made: AN vs. IM, p < 0.001 (***); AN vs. CT, p < 0.001 (***); AN vs. LS, p < 0.001 (***); IM vs. CT, p < 0.02 (*), LS vs. CT, p < 0.07 (ns); IM vs. LS, p < 0.024 (*). Within the intraepithelial, the following comparisons were made: AN vs. IM, p < 0.002 (**); AN vs. CT, p < 0.05 (*); AN vs. LS, p < 0.001 (***); IM vs. CT, p < 0.6 (ns), LS vs. CT, p < 0.1 (ns); IM vs. LS, p < 0.2 (ns). Note: The y-axis is divided into two segments with different scales to improve visualization of both low- and high-density values.

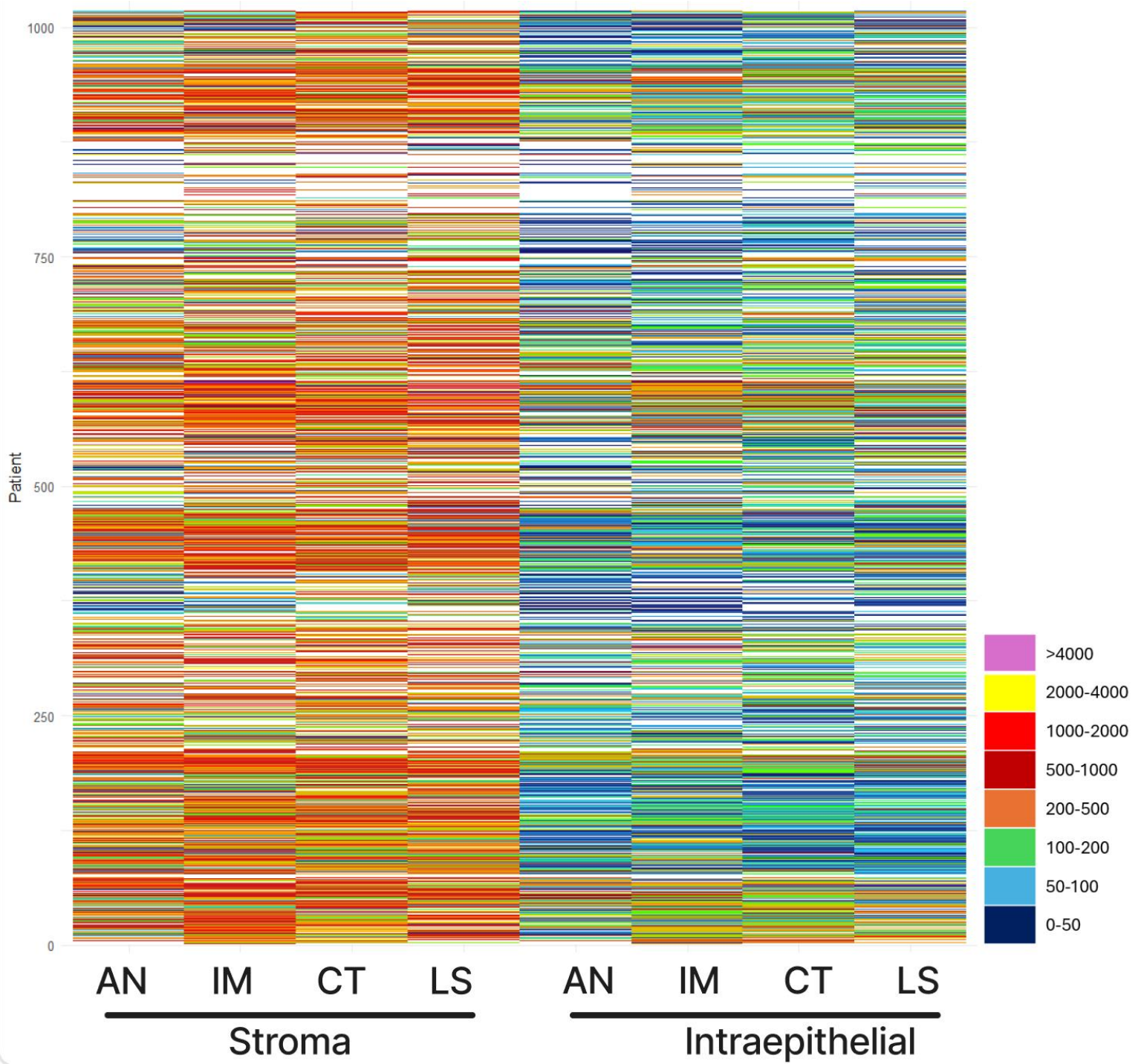


Figure 79. Heatmap of IR- macrophage cell density in colorectal cancer.

Each row represents an individual patient, and each column represents a distinct tissue core. The color intensity corresponds to the density of IR-negative macrophage, as indicated by the scale bar. white tiles indicate missing data.

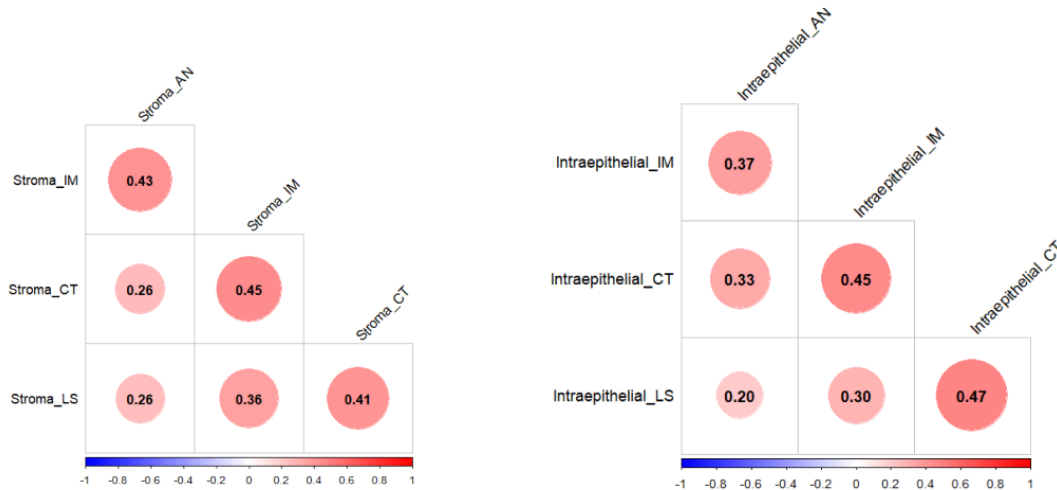


Figure 80. Spearman correlation analysis of CD68.IR negative densities within the tumour microenvironment of colorectal cancer, performed on the entire patient cohort.

Correlations are shown separately for stromal and intraepithelial compartments across four regions: adjacent normal (AN), invasive margin (IM), tumour center (CT), and luminal side (LS). Each cell in the matrix represents the correlation between two cell populations, with the color intensity indicating the strength and direction of the correlation (red for positive, blue for negative). The size of each circle is proportional to the magnitude of the correlation coefficient. Correlation coefficients are shown only for correlations with a statistically significant p-value ($p < 0.05$); non-significant correlations are left blank.

3.5.3.3.211. Total Macrophage with IR

Although There is no statistically significant difference in the density of intraepithelial IR+ macrophages between AN cores and IM cores ($p = 0.252$), there was a highly significant differences in the cell density of this macrophages between AN and both CT ($p < 0.001$) and LS ($p < 0.001$) cores. Specifically, the intraepithelial tumour regions of CT and LS cores have higher densities of IR+ macrophages than the intraepithelial tumour region of AN cores. On the other hand, there are no statistically significant differences in the densities of IR+ macrophages between the stroma of AN cores and the stroma of IM, CT, or LS cores. Within the tumour related cores, IM had a significantly higher cell density of Macrophage with IR compared to LS and CT cores (**Figure 81**). Heatmap (**Figure 82**) showing intra patient heterogeneity in the IR+ macrophages density in different cores. Higher densities of IR+ macrophages in stroma compared to intraepithelial regions are obvious. Spearman correlation showed a positive correlation between the cell density of IR+ macrophages between different sections (**Figure 83**).

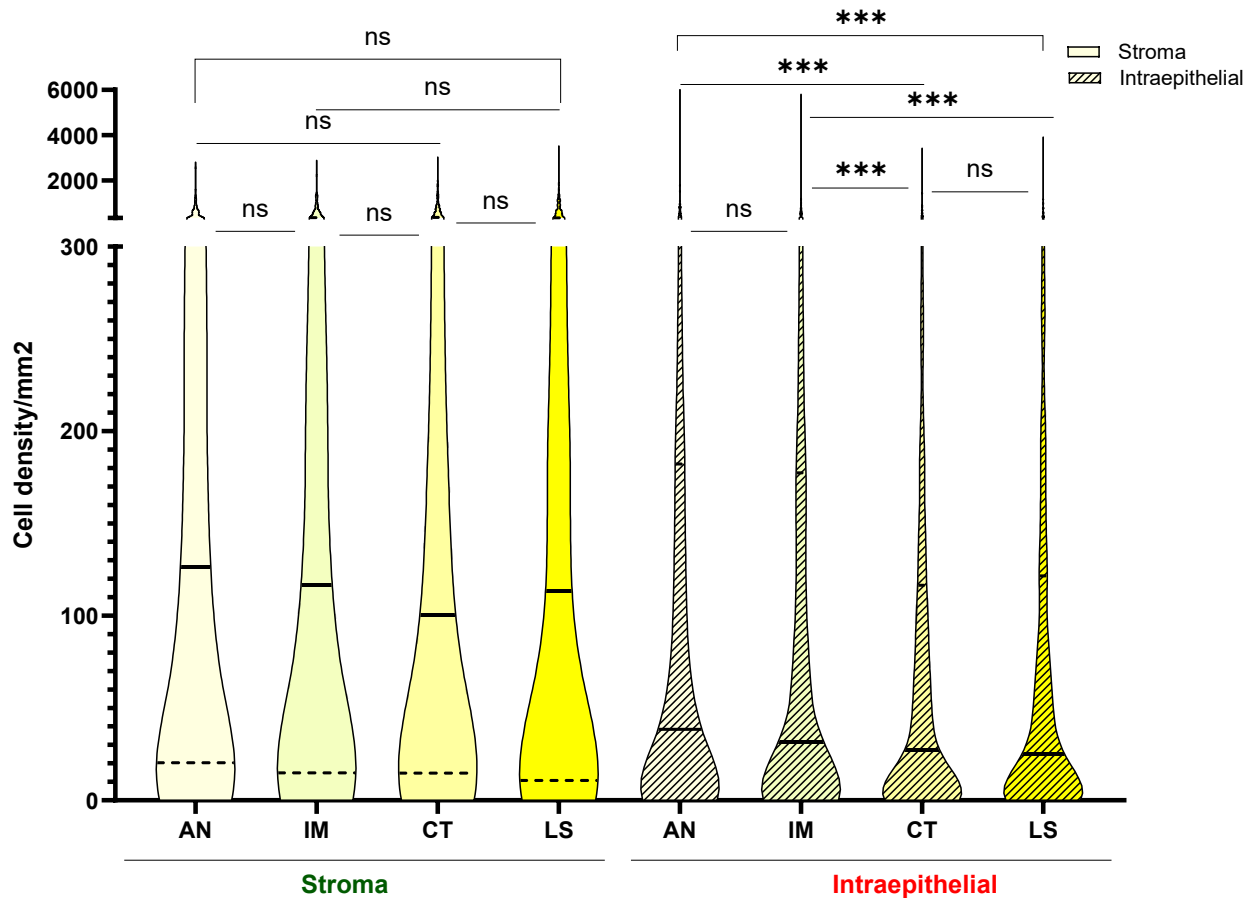


Figure 81. Comparison of macrophage densities (IR+ cells) in stromal and intraepithelial regions of adjacent normal and tumour-related cores of human CRC tissue sections.

Violin plots showing the distribution of macrophage densities (cells/mm²) in adjacent normal (AN), invasive margin (IM), core of tumour (CT), and luminal side (LS) cores within stroma (plain graphs) and tumour (hatched graphs). The horizontal black lines within the violins represent the median. Comparisons between AN and tumour-related cores within each region were made using the two-sided Wilcoxon signed-rank test with Holm-Bonferroni correction. Significance levels are indicated as follows: * $p < 0.05$, ** $p < 0.01$, *** $p < 0.001$. Within the stroma, the following comparisons were made: AN vs. IM, $p < 0.28$ (ns); AN vs. CT, $p < 0.36$ (ns); AN vs. LS, $p < 0.51$ (ns); IM vs. CT, $p < 0.9$ (ns), LS vs. CT, $p < 0.4$ (ns); IM vs. LS, $p < 0.9$ (ns). Within the intraepithelial, the following comparisons were made: AN vs. IM, $p < 0.252$ (ns); AN vs. CT, $p < 0.001$ (***) ; AN vs. LS, $p < 0.001$ (***) ; IM vs. CT, $p < 0.001$ (***) , LS vs. CT, $p < 0.74$ (ns); IM vs. LS, $p < 0.001$ (***) . Note: The y-axis is divided into two segments with different scales to improve visualization of both low- and high-density values.

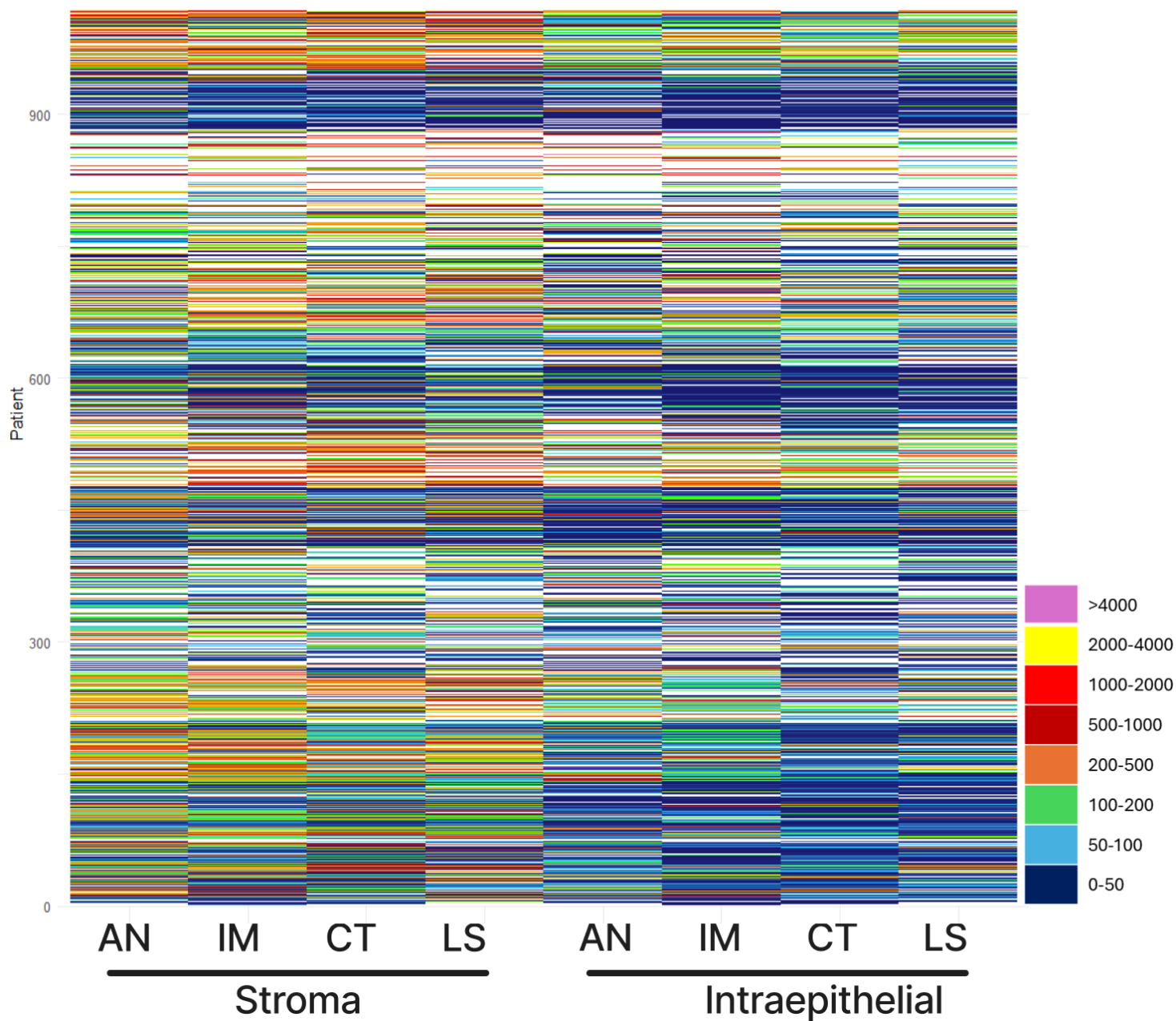


Figure 82. Heatmap of macrophage (IR+) cell density in colorectal cancer.

Each row represents an individual patient, and each column represents a distinct tissue core. The color intensity corresponds to the density of IR+ positive macrophage, as indicated by the scale bar. white tiles indicate missing data.

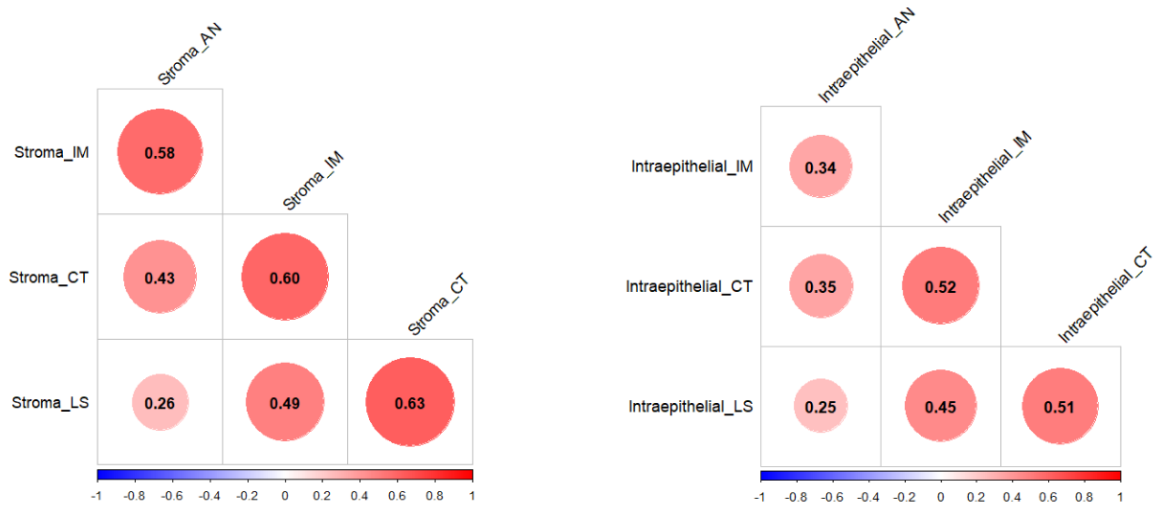


Figure 83. Spearman correlation analysis of IR+CD68 macrophage densities within the tumour microenvironment of colorectal cancer, performed on the entire patient cohort.

Correlations are shown separately for stromal and intraepithelial compartments across four regions: adjacent normal (AN), invasive margin (IM), tumour center (CT), and luminal side (LS). Each cell in the matrix represents the correlation between two cell populations, with the color intensity indicating the strength and direction of the correlation (red for positive, blue for negative). The size of each circle is proportional to the magnitude of the correlation coefficient. Correlation coefficients are shown only for correlations with a statistically significant p-value ($p < 0.05$); non-significant correlations are left blank.

3.5.3.4 IR+ CD68 subpopulation

In this chapter violin plots showing the cell density of each exhausted phenotype of CD68 was depicted. Furthermore, heatmap showing the cell density in the cores, and a spearman correlation matrix in both stromal and intraepithelial compartment showing the correlation of phenotypes to give a better understanding of CRC TME. LAG3+CD68 phenotype had a very low cell density in this project which is not shown with plots.

3.5.3.4.1 PD1+Macrophage

Although there was a significant higher cell density of stromal PD1+Macrophage in AN compared to tumour related cores, intraepithelial PD1+Macrophage showed significant higher cell density in AN compared to CT and LS cores, but not IM cores. Within the tumour related cores, in stromal compartment IM had higher PD1+Macrophage density compared to CT ($P < 0.03$) and in intraepithelial compartment IM had higher CD68 PD1+ density vs. LS

(0.02) (**Figure 84**). In general, PD1+Macrophage had a low cell density which is more obvious in heatmap presented in **Figure 85**. Spearman correlation (**Figure 86**) showed positive correlation between the cell density of PD1+Macrophage in different sections.

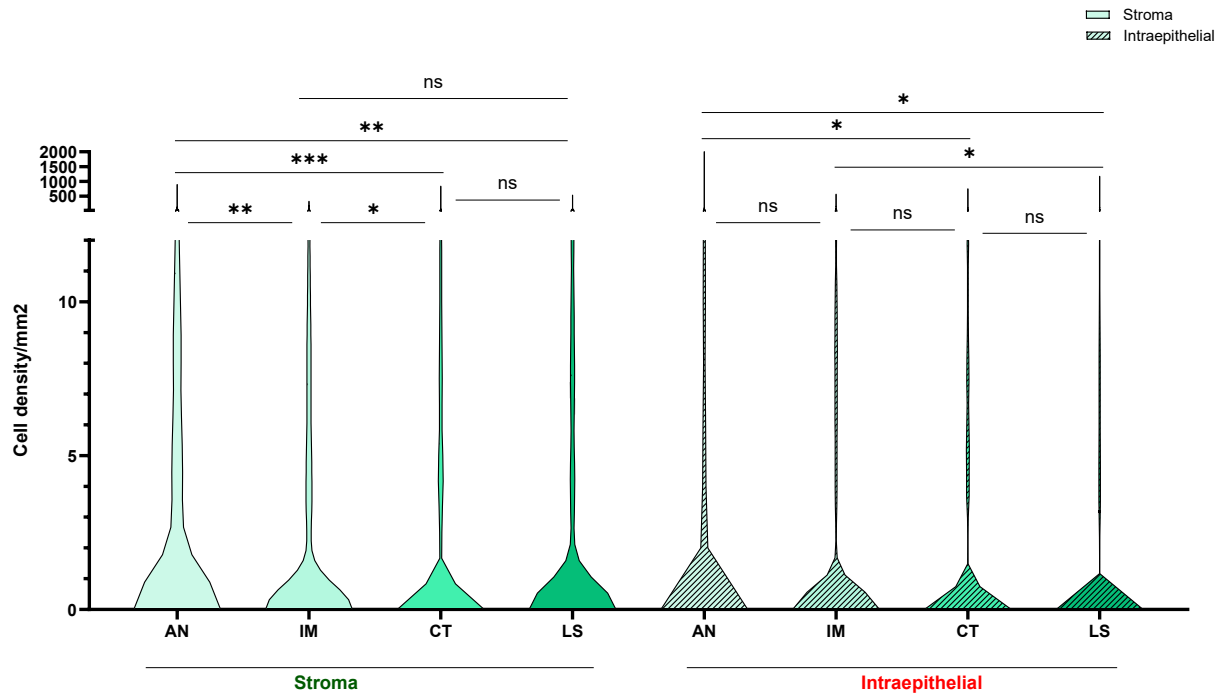


Figure 84. Comparison of PD1+ macrophage cell densities in stromal and intraepithelial regions of adjacent normal and tumour-related cores.

Violin plots showing the distribution of PD1+CD68 cells densities (cells/mm²) in adjacent normal (AN), invasive margin (IM), core of tumour (CT), and luminal side (LS) cores within stroma (plain graphs) and tumour (hatched graphs). The horizontal black lines within the violins represent the median. Comparisons between AN and tumour-related cores within each region were made using the two-sided Wilcoxon signed-rank test with Holm-Bonferroni correction. Significance levels are indicated as follows: * $p < 0.05$, ** $p < 0.01$, *** $p < 0.001$. Within the stroma, the following comparisons were made: AN vs. IM, $p < 0.005$ (**); AN vs. CT, $p < 0.001$ (***); AN vs. LS, $p < 0.001$ (***); CT vs. IM, $p < 0.03$ (*); IM vs. LS, $p < 0.6$ (ns); CT vs. LS, $p < 0.08$ (ns). Within the intraepithelial compartment, the following comparisons were made: AN vs. IM, $p < 0.1$ (ns); AN vs. CT, $p < 0.02$ (*); AN vs. LS, $p < 0.012$ (*); CT vs. IM, $p < 0.06$ (ns); IM vs. LS, $p < 0.02$ (*); CT vs. LS, $p < 0.9$ (ns).

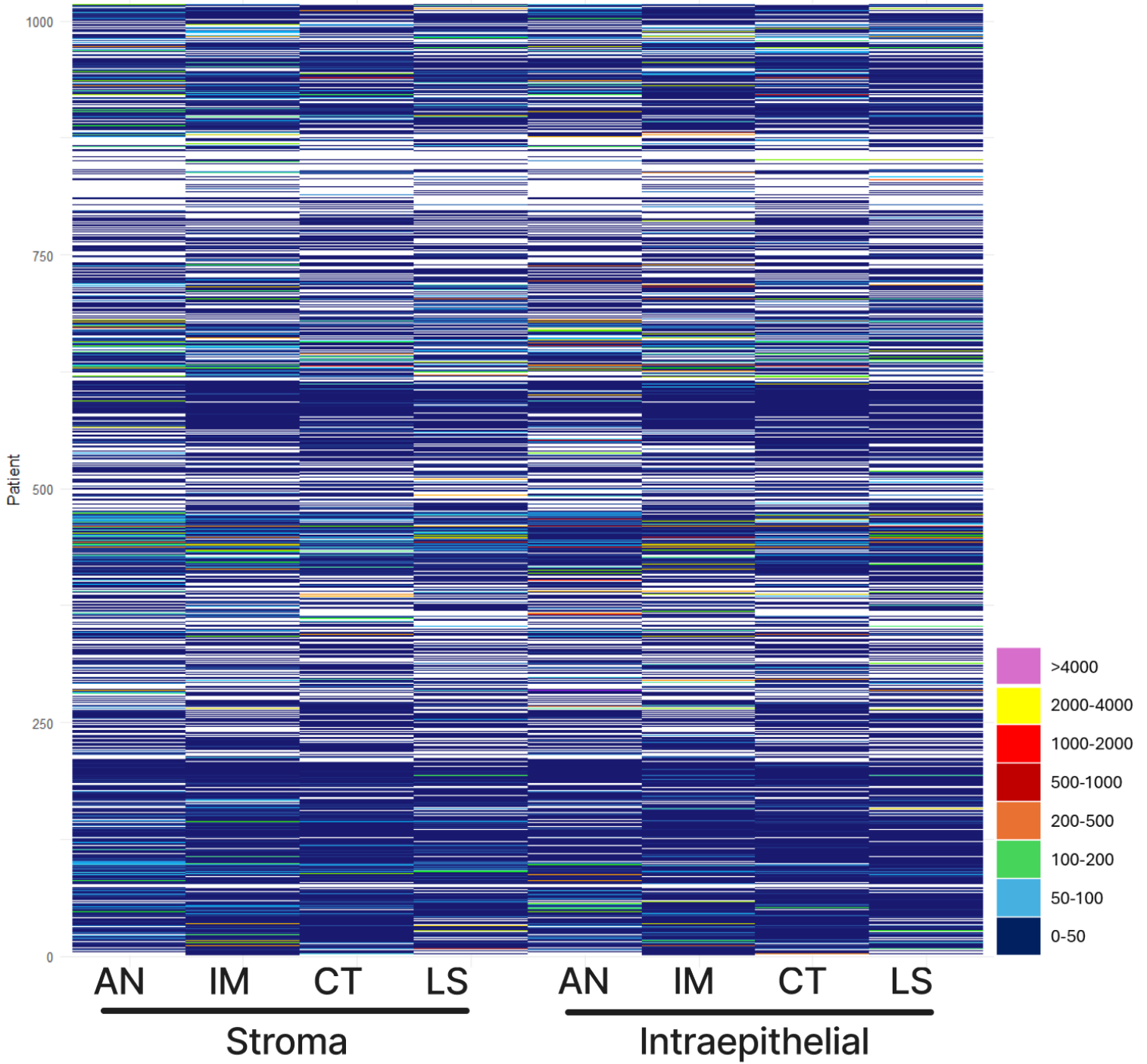


Figure 85. Heatmap of PD1+ macrophage cell density in colorectal cancer.

Each row represents an individual patient, and each column represents a distinct tissue core. The color intensity corresponds to the density of PD1+ macrophage, as indicated by the scale bar. white tiles indicate missing data.

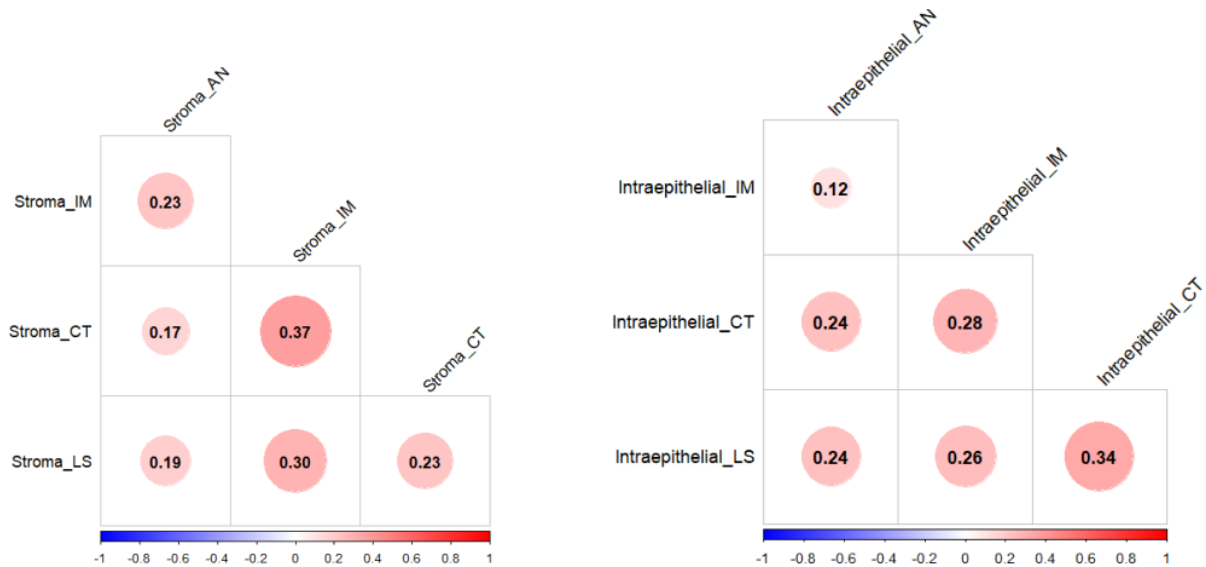


Figure 86. Spearman correlation analysis of PD1+ CD68. densities within the tumour microenvironment of colorectal cancer, performed on the entire patient cohort.

Correlations are shown separately for stromal and intraepithelial compartments across four regions: adjacent normal (AN), invasive margin (IM), tumour center (CT), and luminal side (LS). Each cell in the matrix represents the correlation between two cell populations, with the color intensity indicating the strength and direction of the correlation (red for positive, blue for negative). The size of each circle is proportional to the magnitude of the correlation coefficient. Correlation coefficients are shown only for correlations with a statistically significant p-value ($p < 0.05$); non-significant correlations are left blank.

3.5.3.4.2 TIM3+ Macrophage

Within the stromal compartment, no significant differences in TIM3+ macrophage densities were observed between the AN, IM, CT, and LS regions. However, within the intraepithelial compartment, significant difference was observed. While densities in the AN region did not differ significantly from those in the tumour related sections (IM, CT, LS), the IM exhibited significantly higher TIM3+ macrophage density compared to both the CT ($p < 0.017$) and the LS regions ($p < 0.001$) (**Figure 87**).

The heatmap visualization (**Figure 88**) revealed substantial inter-patient heterogeneity in TIM3+ macrophage density across all regions and compartments. While some patients

exhibited high TIM3+ macrophage densities across multiple regions and compartments, others displayed relatively low densities. Spearman correlation analyses (**Figure 89**) showed statistically significant positive correlations between TIM3+ macrophage densities across all regions in both compartments.

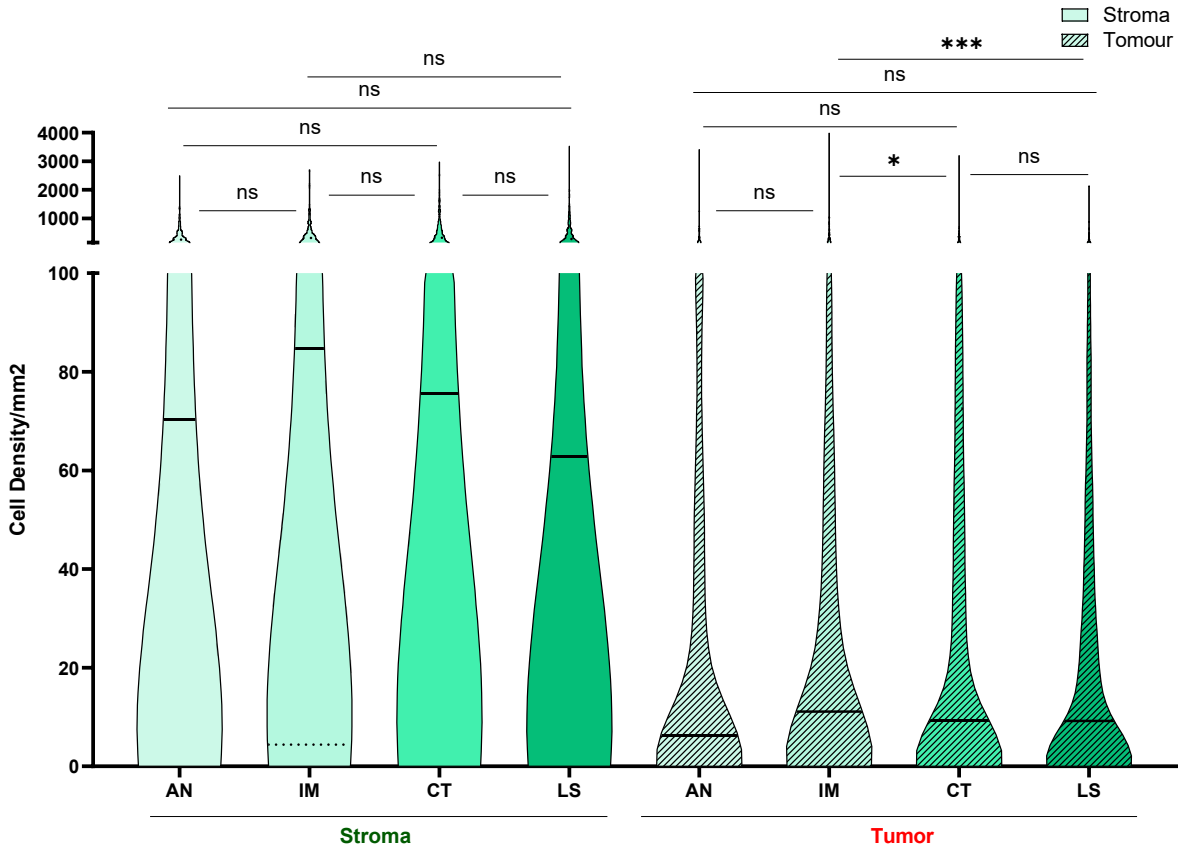


Figure 87. Comparison of CD68 expressing TIM3 cell densities in Stroma and Tumour Regions of Adjacent Normal and Tumour-Related Cores.

Violin plots showing the distribution of CD68 expressing TIM3 cells densities (cells/mm²) in adjacent normal (AN), invasive margin (IM), core of tumour (CT), and luminal side (LS) cores within stroma (plain graphs) and tumour (hatched graphs). The horizontal black lines within the violins represent the median. Comparisons between AN and tumour-related cores within each region were made using the two-sided Wilcoxon signed-rank test with Holm-Bonferroni correction. Significance levels are indicated as follows: * $p < 0.05$, ** $p < 0.01$, *** $p < 0.001$. Within the stroma, the following comparisons were made: AN vs. IM, $p < 0.1$ (ns); AN vs. CT, $p < 0.094$ (ns); AN vs. LS, $p < 0.6$ (ns), IM vs. CT, $p < 0.98$, LS vs. CT, $p < 0.09$, IM vs. LS, $p < 0.69$. Within the tumour, the following comparisons were made: AN vs. CT, $p < 0.091$ (ns); AN vs. LS, $p < 0.1$ (ns), IM vs. CT, $p < 0.017$, LS vs. CT, $p < 0.08$ (ns), IM vs. LS, $p < 0.001$

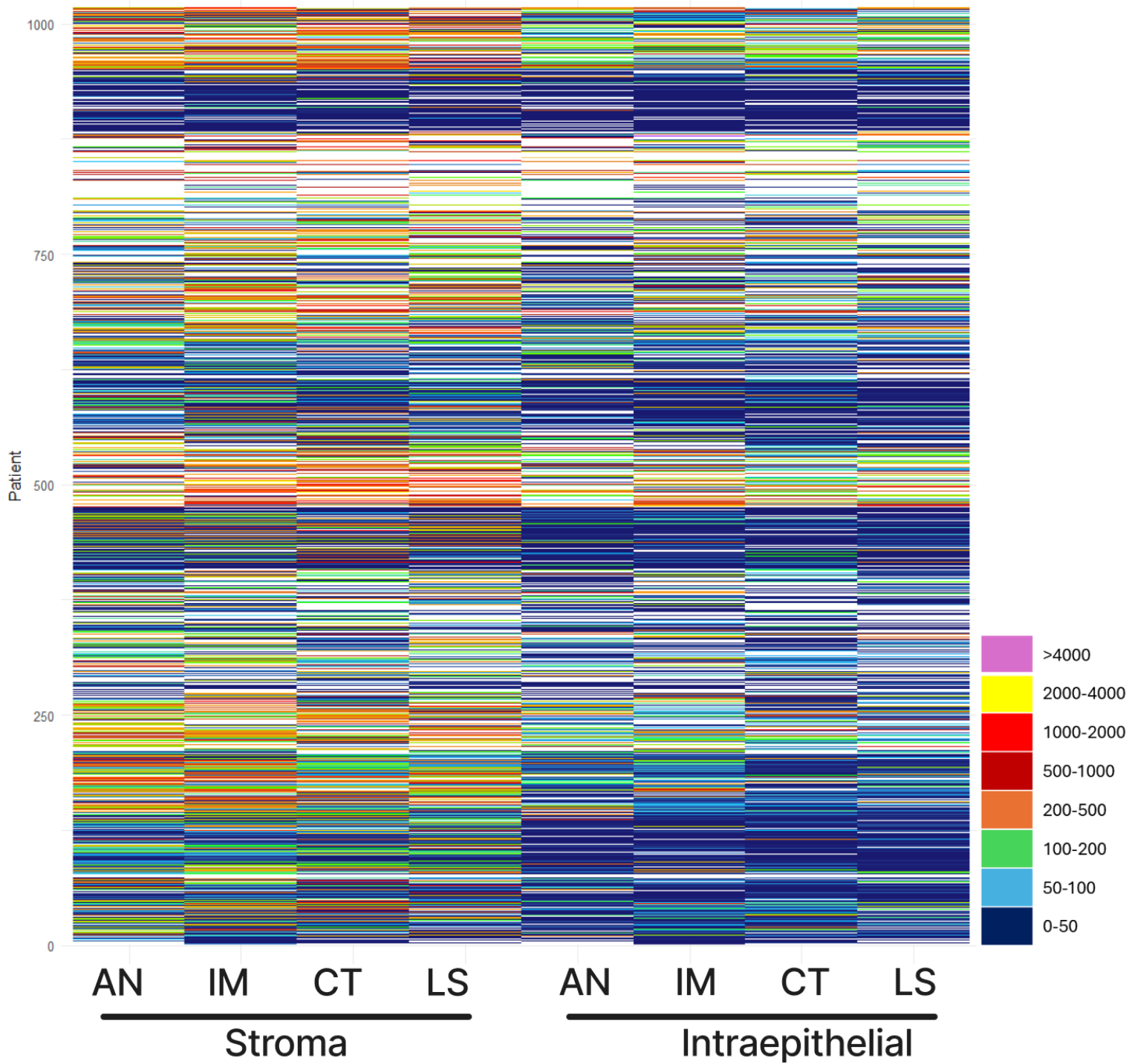


Figure 88. Heatmap of macrophage expressing TIM3 density in colorectal cancer.

Each row represents an individual patient, and each column represents a distinct tissue core. The color intensity corresponds to the density of macrophage expressing TIM3 density, as indicated by the scale bar. white tiles indicate missing data.

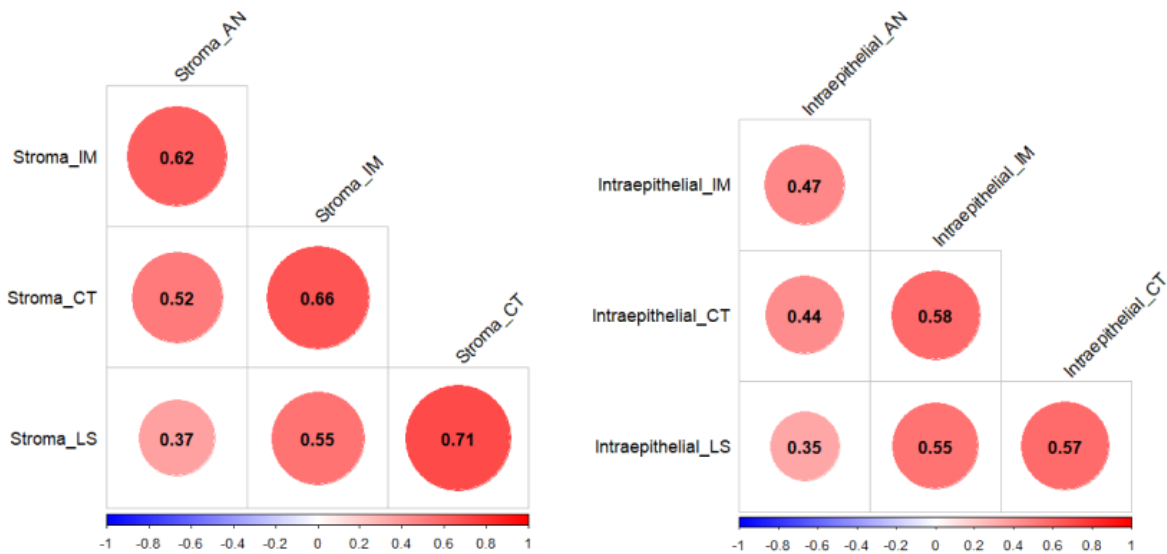


Figure 89. Spearman correlation analysis of TIM3+ macrophage densities within the tumour microenvironment of colorectal cancer, performed on the entire patient cohort.

Correlations are shown separately for stromal and intraepithelial compartments across four regions: adjacent normal (AN), invasive margin (IM), tumour center (CT), and luminal side (LS). Each cell in the matrix represents the correlation between two cell populations, with the color intensity indicating the strength and direction of the correlation (red for positive, blue for negative). The size of each circle is proportional to the magnitude of the correlation coefficient. Correlation coefficients are shown only for correlations with a statistically significant p-value ($p < 0.05$); non-significant correlations are left blank.

3.5.3.4.3 PD1+TIM3+ Macrophage

Violin plot shows a significant higher cell density of PD1+TIM3+ Macrophage in AN, compared to tumour related cores, including CT, IM, and LS in both stroma and intraepithelial compartments. Furthermore, there is a significant difference in the TIM3+/PD+ macrophage in different tumour regions (**Figure 90**). LS had significantly higher cell density over CT and IM in the Stromal region. Conversely, in intraepithelial regions, IM showed higher cell density over CT and LS. Heatmap (**Figure 91**) showing a wide range of PD1+TIM3+ Macrophage densities across patients. Some patients showed lower cell density and others higher cell densities. All spearman correlation between the density of PD1+TIM3+ Macrophage was positive and stroma was slightly stronger than intraepithelial regions (**Figure 92**).

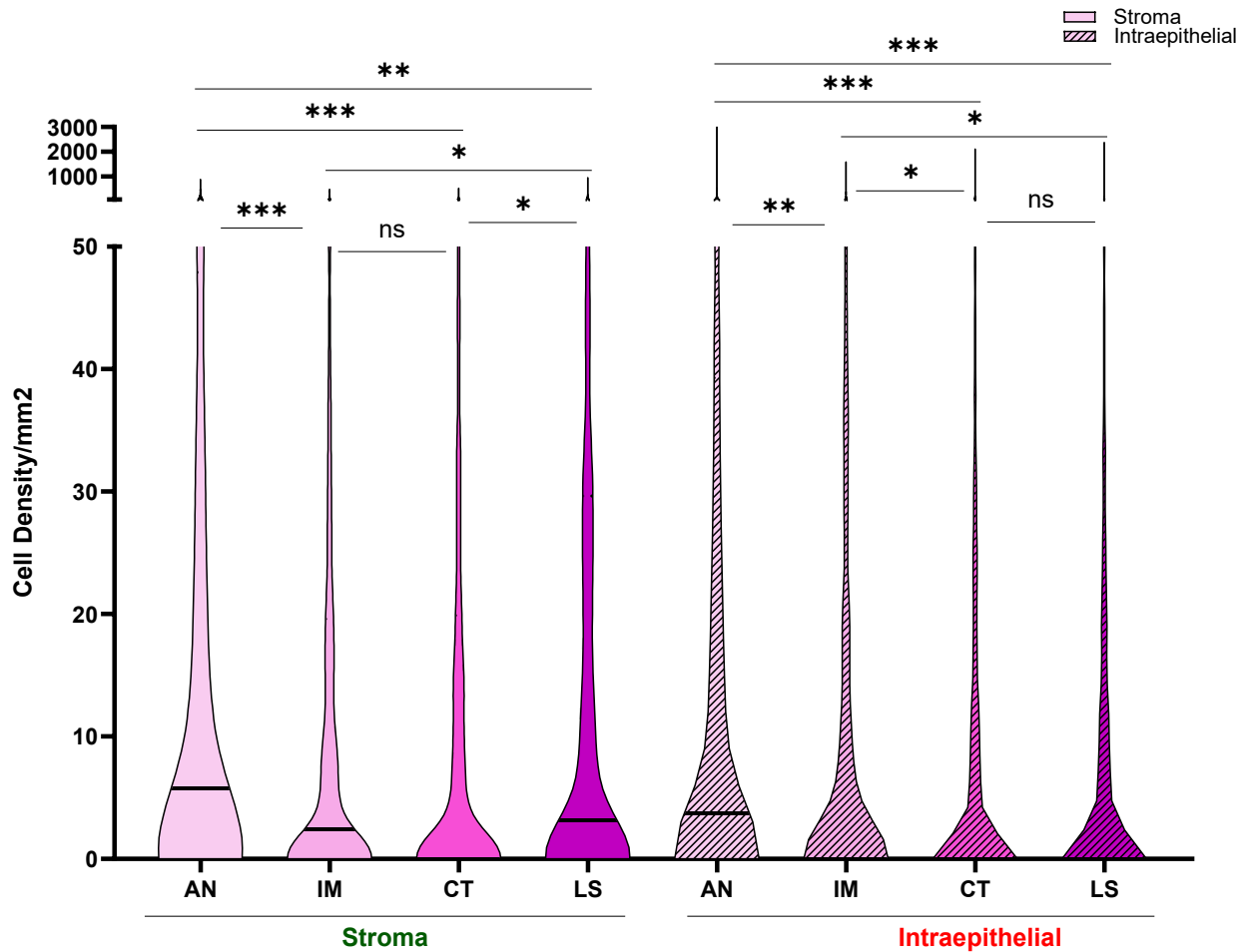


Figure 90. Higher density of TIM3+ PD1+ macrophages densities in stromal and intraepithelial compartments of adjacent normal compared to tumour related cores.

Violin plots showing the distribution of CD68 expressing TIM3 and PD1 cells densities (cells/mm²) in adjacent normal (AN), invasive margin (IM), core of tumour (CT), and luminal side (LS) cores within stroma (plain graphs) and intraepithelial (hatched graphs) compartments. The horizontal black lines within the violins represent the median. Comparisons between AN and tumour-related cores within each region were made using the two-sided Wilcoxon signed-rank test with Holm-Bonferroni correction. Significance levels are indicated as follows: *p < 0.05, **p < 0.01, ***p < 0.001. Within the stroma, the following comparisons were made: AN vs. IM, p < 0.001 (***); AN vs. CT, p < 0.001 (***); AN vs. LS, p < 0.004 (**); IM vs. CT, p < 0.4 (ns); LS vs. CT, p < 0.02 (*); IM vs. LS, p < 0.04 (*). Within the intraepithelial region, the following comparisons were made: AN vs. IM, p < 0.006 (**); AN vs. CT, p < 0.001 (***); AN vs. LS, p < 0.001 (***); IM vs. CT, p < 0.03 (*); LS vs. CT, p < 0.8 (ns); IM vs. LS, p < 0.017 (*).

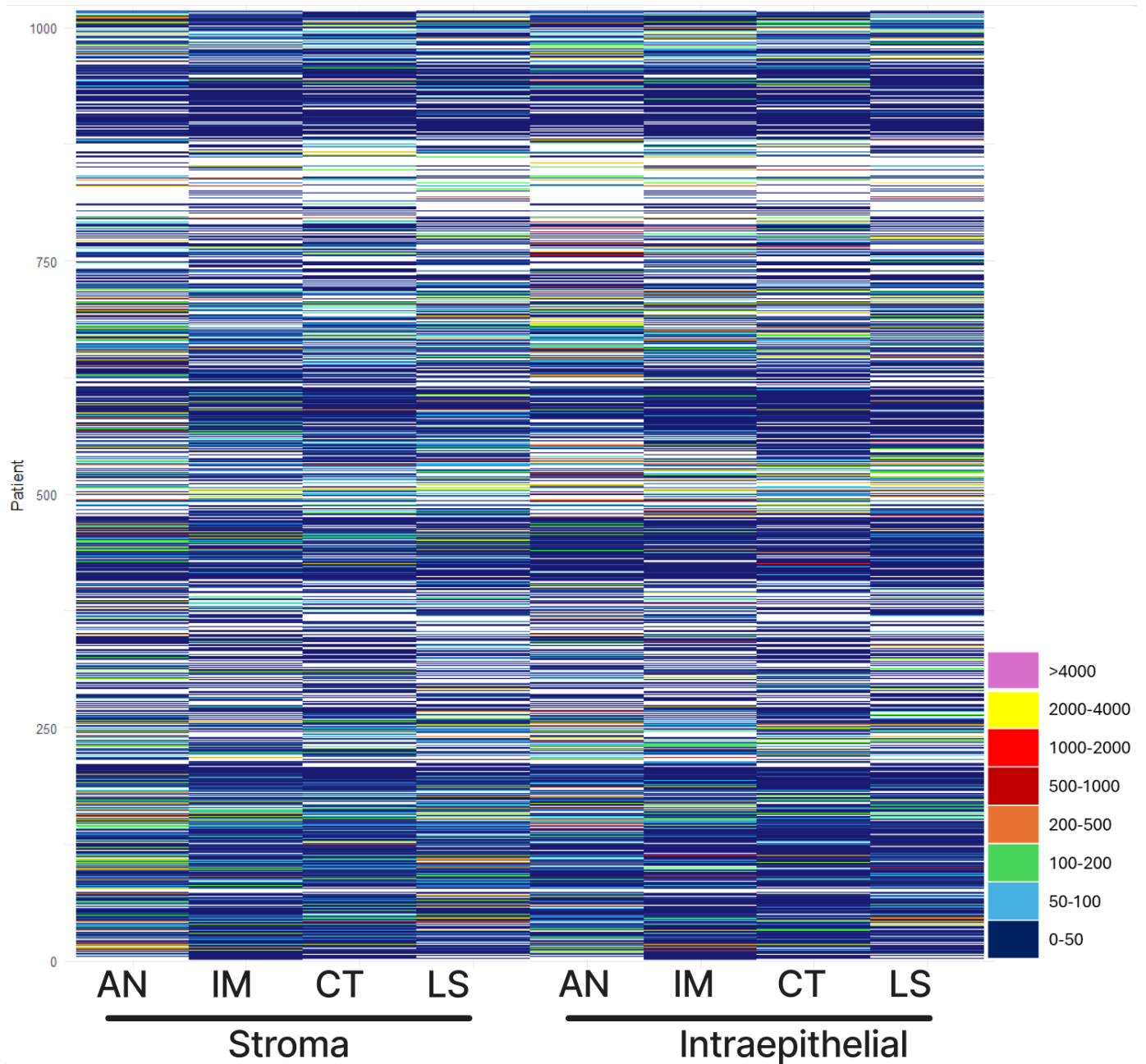


Figure 91. Heatmap of macrophage expressing TIM3/ PD1 density in colorectal cancer.

Each row represents an individual patient, and each column represents a distinct tissue core. The color intensity corresponds to the density of macrophage expressing TIM3/PD1 density, as indicated by the scale bar. white tiles indicate missing data.

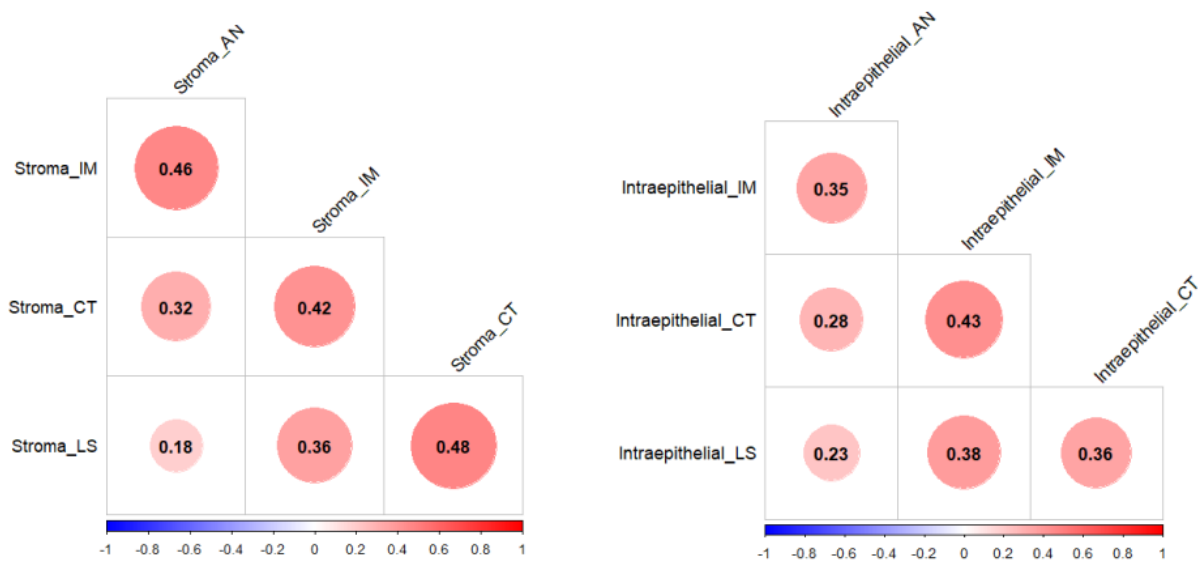


Figure 92. Spearman correlation analysis of TIM3+/PD1 macrophage densities within the tumour microenvironment of colorectal cancer, performed on the entire patient cohort.

Correlations are shown separately for stromal and intraepithelial compartments across four regions: adjacent normal (AN), invasive margin (IM), tumour center (CT), and luminal side (LS). Each cell in the matrix represents the correlation between two cell populations, with the color intensity indicating the strength and direction of the correlation (red for positive, blue for negative). The size of each circle is proportional to the magnitude of the correlation coefficient. Correlation coefficients are shown only for correlations with a statistically significant p-value ($p < 0.05$); non-significant correlations are left blank.

3.5.4 Neighborhood analysis with Cytomap

To characterize the spatial heterogeneity of cell populations within colorectal tumours we used Cytomap (**Figure 93**). Five distinct regions were identified (**Figure 94**).

Region 1 was characterized by a high density of both macrophages (IR+ and IR-) and CD3+ T cells, including both exhausted and non-exhausted subsets, as well as a high density of TIM3+PD1+ cells. This suggests a stroma-rich region with a significant and diverse immune infiltrate. Region 2, also likely representing a stromal compartment, was dominated by other cells and had relatively low densities of macrophage and T cells. Region 3 exhibited a high density of tumour cells expressing immune regulatory markers (IR+), particularly the double-positive TIM3+PD1+ subset. Region 4 showed enrichment for both macrophages expressing immune regulatory markers (CD68.IR+) and other cells expressing immune regulatory markers (Other.IR+). A portion of LAG3+ tumour cells was also present. This may

represent a mixed region, possibly at the tumour-stroma interface, with a potentially immunosuppressive character. Region 5 was notable for its high density of tumour cells lacking immune regulatory markers (Tumour.IR-) and low densities of most immune cell subsets. These findings highlight the spatial heterogeneity of the CRC microenvironment and suggest distinct immune landscapes within different regions. Further investigation is needed to elucidate the functional roles of these different cell populations and their interactions within each region.

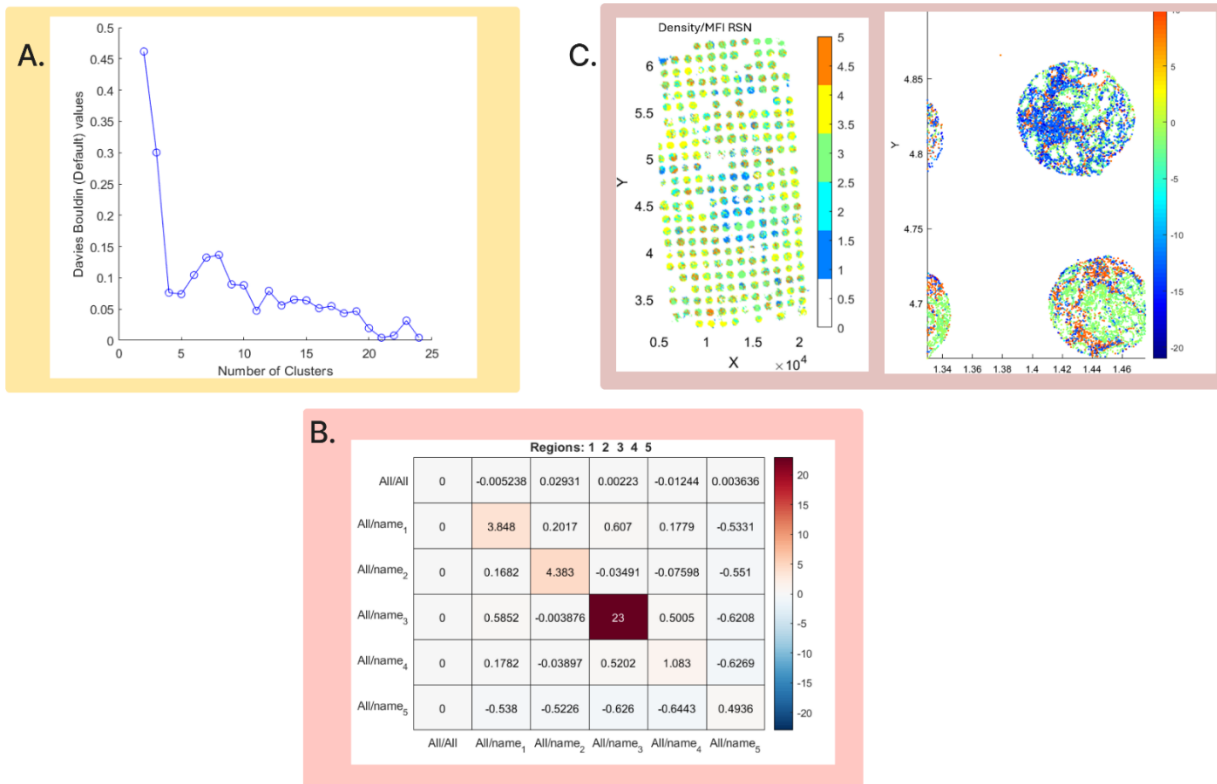


Figure 93. Cytomap analysis of spatial heterogeneity in human CRC tissue sections. (A) Determination of optimal cluster number identified 5 clusters.

The Davies-Bouldin index was calculated for different numbers of clusters (ranging from 2 to 25) to guide the selection of the optimal number of clusters for region identification. Based on the minimum Davies-Bouldin value, the optimal number of clusters was determined to be 5. (B) Heatmap of interactions among 10 nearest neighbors for a sample slide. The heatmap displays the interaction scores between different cell populations across 5 regions. Interaction scores were calculated using the neighborhood analysis function in Cytomap, with a neighborhood radius of 20 pixels. (C) Visualization of region segmentation. (Left) Spatial distribution of the identified regions (clusters) across the tissue section, with each color representing a distinct region, based on the clustering of neighborhoods using k-means clustering. Y-axis and X-axis demonstrate the coordinates of each region within a core. (Right) Magnified view of a representative region, highlighting the spatial arrangement of cells within that region. (D) Heatmap showing the average cell densities of each cell population (CD3+, CD68+, CK+, and other cells) within each of the 5 identified regions.

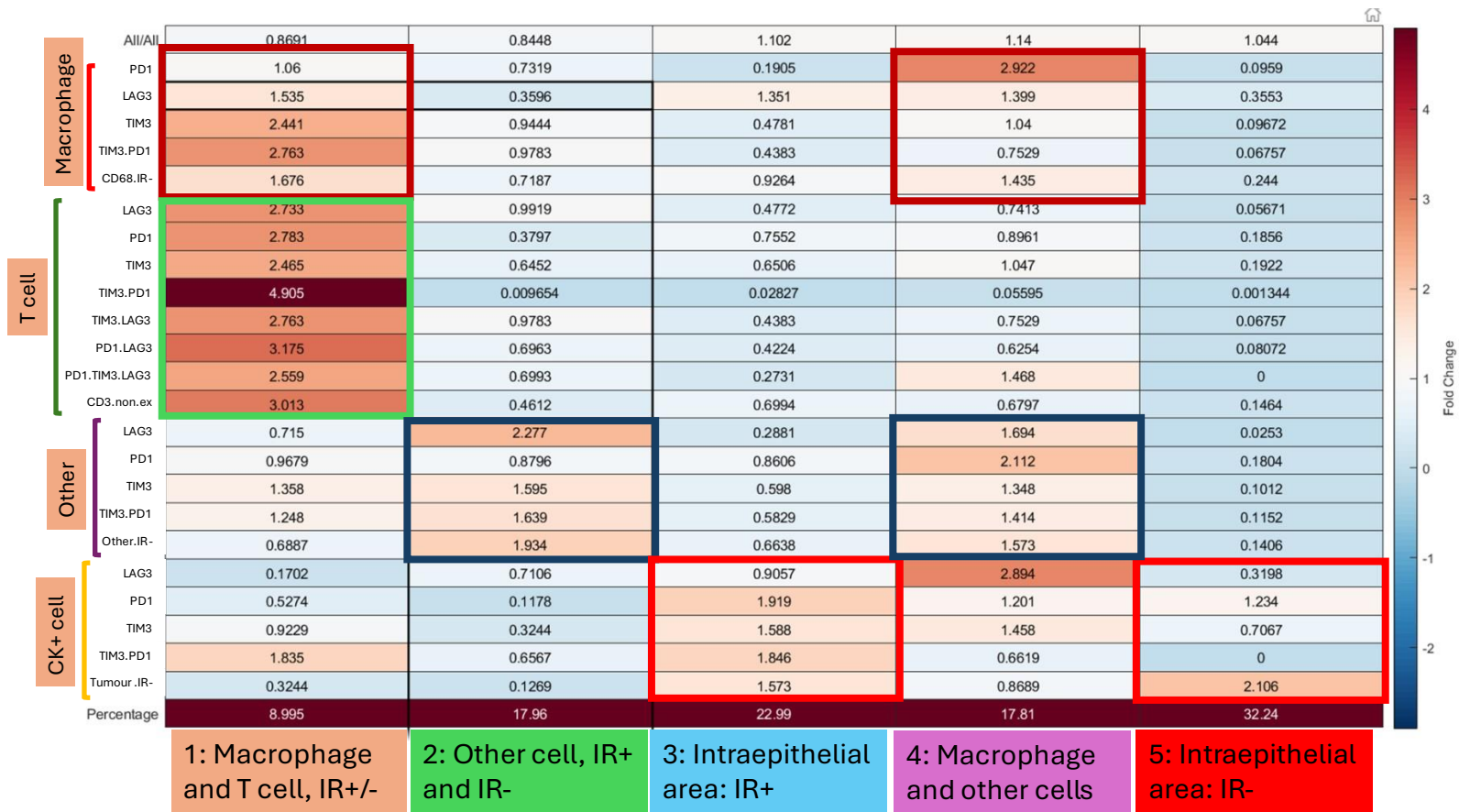


Figure 94. Fold-change in cell population densities across five distinct regions in human CRC tissue sections showing 5 different regions.

The heatmap displays the fold-change in density for various cell populations across five regions identified through spatial analysis using Cytomap. Rows represent specific cell populations, and columns represent the five regions.

3.5.5 Survival analysis regarding the cell density

3.5.5.1 Univariate survival analysis of the densities of CD3+ and CD68+ cells in tumour related cores.

3.5.5.1.1 CD3 positive cells

3.5.5.1.1.1 Total CD3 cells in tumour-related cores

To investigate the correlation between total CD3 density and patient survival, independent of confounding variables such as tumour location, MMR status, sidedness, and colorectal

cancer (CRC) stages, we assessed the combined stromal and intraepithelial CD3+ T cell density. Our analysis revealed that a higher density of CD3+ T cells, irrespective of these confounding factors, significantly correlated with improved survival outcomes.

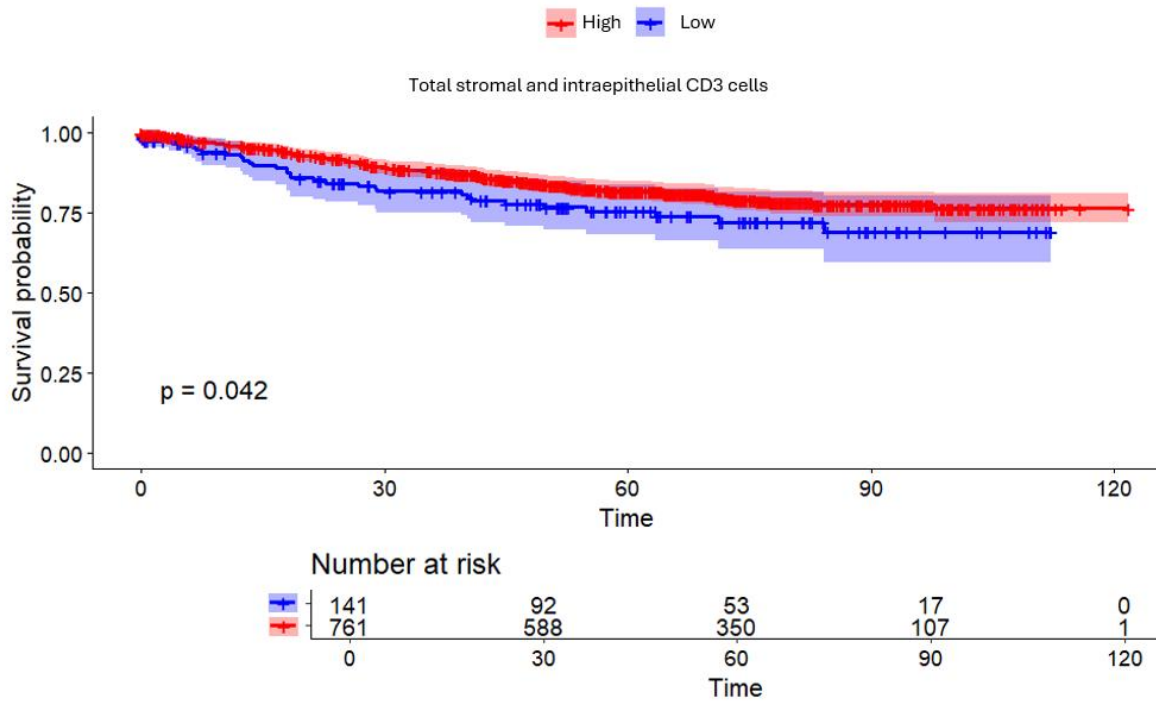


Figure 95. Total CD3 cells correlated with improved survival.

Patients were stratified into two groups, "High" (red) and "Low" (blue), based on the combined density of CD3+ T cells in both stromal and intraepithelial compartments. The optimal cut-off point for dichotomization was determined using X-tile software. The p-value ($p = 0.042$) was calculated using the log-rank test. The number of patients at risk at each time point (in months) is shown below the plot. Shaded areas represent 95% confidence intervals.

3.5.5.1.1.2 Stromal and intraepithelial CD3 cells

Analysis of total stromal CD3+ cell density showed no significant association with overall survival (**Figure 96**, bottom Panel). However, when stratifying by CD3+ cell subsets based on exhaustion marker expression, significant associations emerged. High stromal density of non-exhausted CD3+ cells significantly associated with improved overall survival ($p < 0.013$, (**Figure 96**, Middle Panel). On the other hand, high stromal density of exhausted CD3+ cells was not associated with survival (**Figure 96**, Top Panel).

The high density of total intraepithelial CD3+ cells was significantly associated with improved overall survival ($p < 0.0001$, **Figure 96**, Bottom Panel). This association was even

stronger when considering only non-exhausted subset cells, when high intraepithelial CD3.non.ex density significantly associated with survival ($p < 0.0001$, **Figure 96**, Middle Panel). The higher density of intraepithelial exhausted CD3+ cells showed statistically significant association with overall survival ($p < 0.0051$, **Figure 96**, Top Panel).

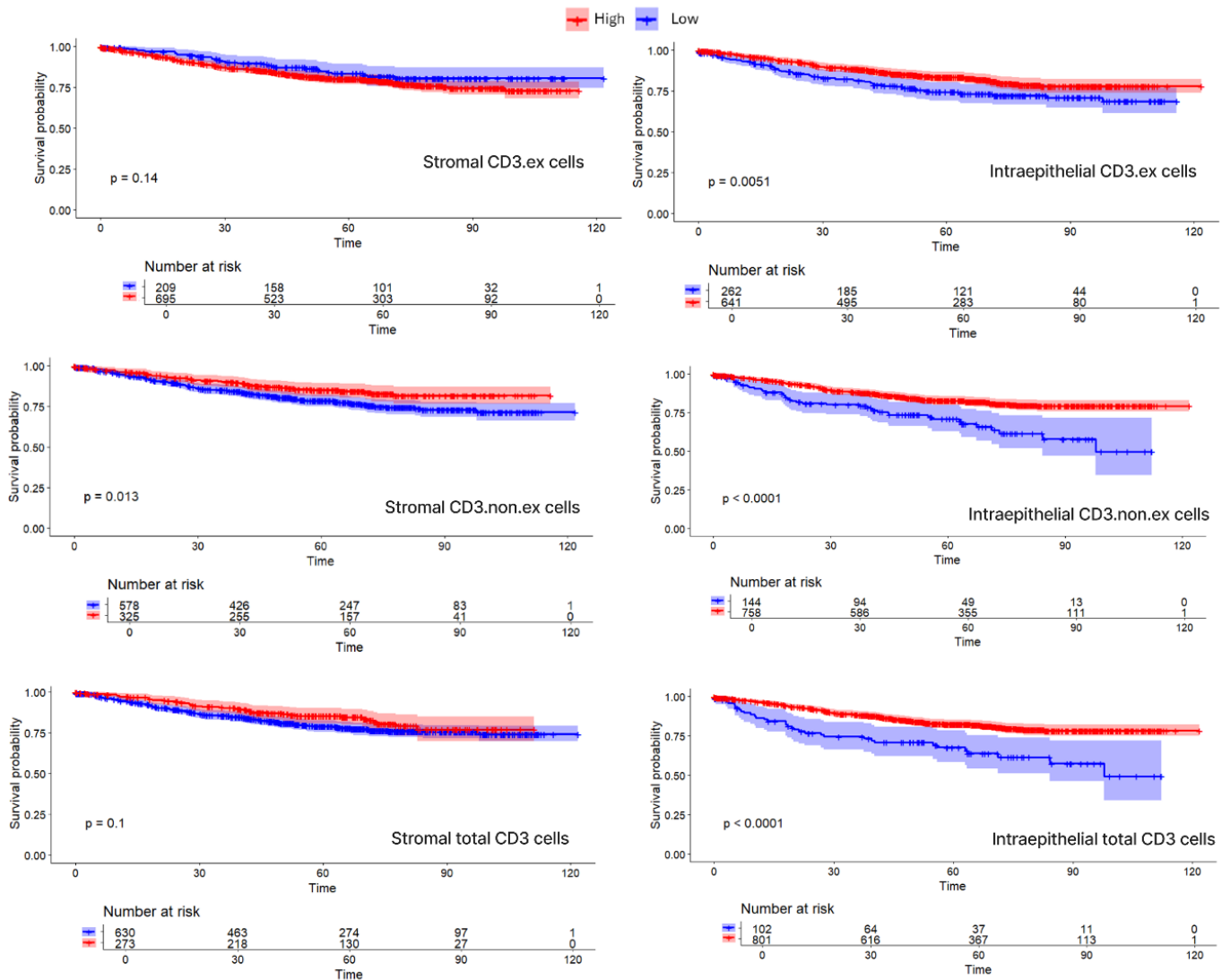


Figure 96. Kaplan-Meier survival curves for overall survival stratified by stromal CD3+ cell density showed intraepithelial CD3 cells correlated with improved survival.

Patients were stratified into "High" (red) and "Low" (blue) groups based on the density of CD3+ cells in the stromal compartment. Optimal cut-off points for dichotomization were determined using X-tile software. CD3.non.ex was defined as CD3+ cells not expressing LAG3, PD1, or TIM3 and CD3.ex was defined as CD3+ cells expressing at least one of these markers. P-values were calculated using the log-rank test. The number of patients at risk at each time point (in months) is shown below each plot. Shaded areas represent 95% confidence intervals.

3.5.5.1.1.3 CD3.ex subpopulations

A higher cell density of PD1+ T cells in both stromal and intraepithelial regions correlated with improved survival. Elevated cell density of intraepithelial PD1+LAG3+ T cells correlated with better survival. However, stromal Tim3 cell density and stromal TIM3+PD1+ CD3+ inversely correlated with reduced survival (**Figure 97, Figure 98**).

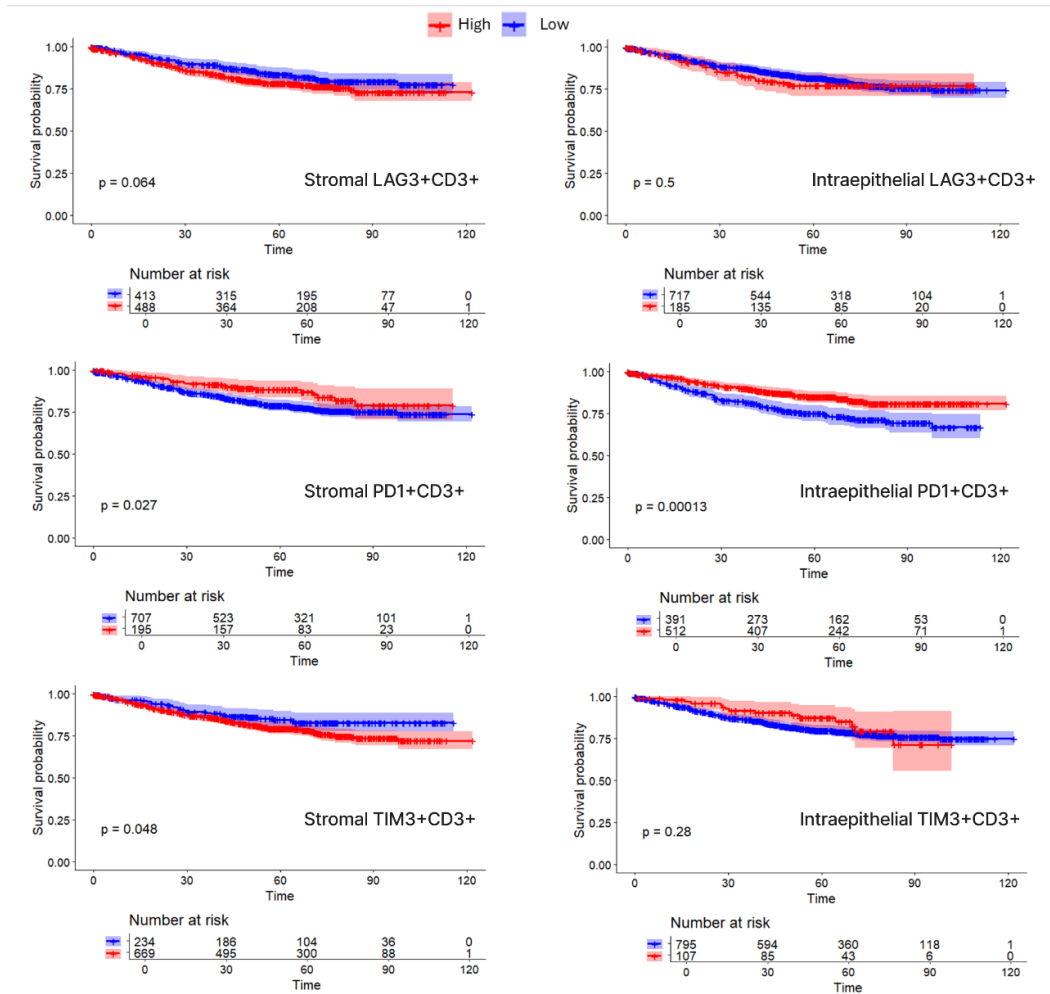


Figure 97. Kaplan-Meier survival curves for overall survival stratified by intraepithelial CD3+ subpopulation showed PD+ CD3 cells correlated with improved survival, although stromal Tim3+ T cells correlated with reduced survival.

Patients were stratified into "High" (red) and "Low" (blue) groups based on the density of CD3+ subpopulation cells (Single positive markers) in the intraepithelial compartment. Optimal cut-off points for dichotomization were determined using X-tile software (Middle). P-values were calculated using the log-rank test. The number of patients at risk at each time point (in months) is shown below each plot. Shaded areas represent 95% confidence intervals.

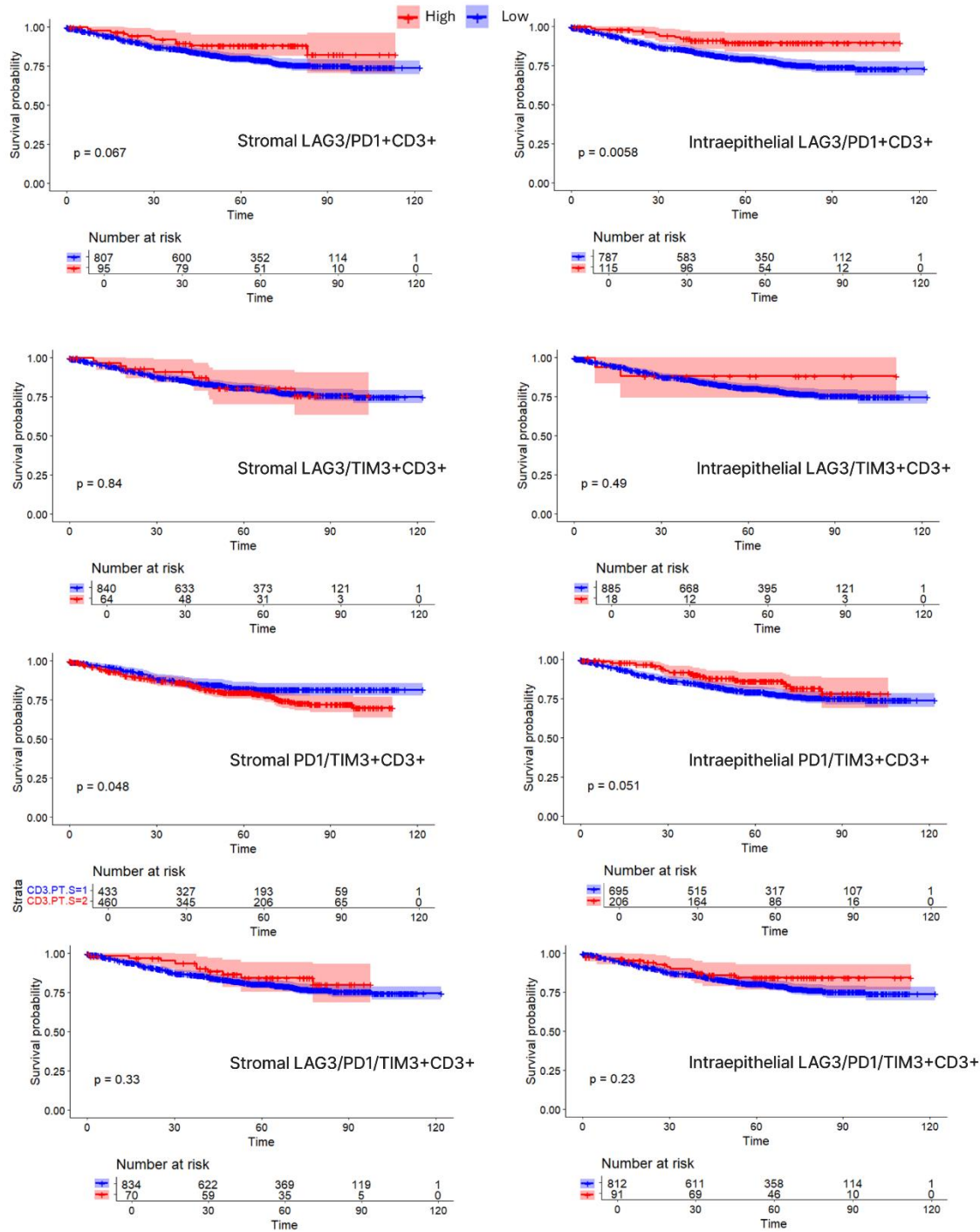


Figure 98. Kaplan-Meier survival curves for overall survival stratified by intraepithelial CD3+ subpopulation cell density showed PD1+Tim3+ T cells correlated with reduced survival.

Patients were stratified into "High" (red) and "Low" (blue) groups based on the density of CD3+ subpopulation cells (Double or triple positive markers) in the intraepithelial compartment. Optimal cut-off points for dichotomization were determined using X-tile software. P-values were calculated using the log-rank test. The number of patients at risk at each time point (in months) is shown below each plot. Shaded areas represent 95% confidence intervals.

3.5.5.1.2 CD68 positive cells

3.5.5.1.2.1 Stromal and intraepithelial macrophages

Analysis of total macrophage density showed no association with overall survival in either the stroma or the intraepithelial compartment. Similarly, the density of CD68.IR- cells showed no association with survival in either the stromal or intraepithelial compartments. Likewise, the density of CD68.IR+ was not significantly associated with overall survival in the stroma or the intraepithelial compartment (**Figure 99**).

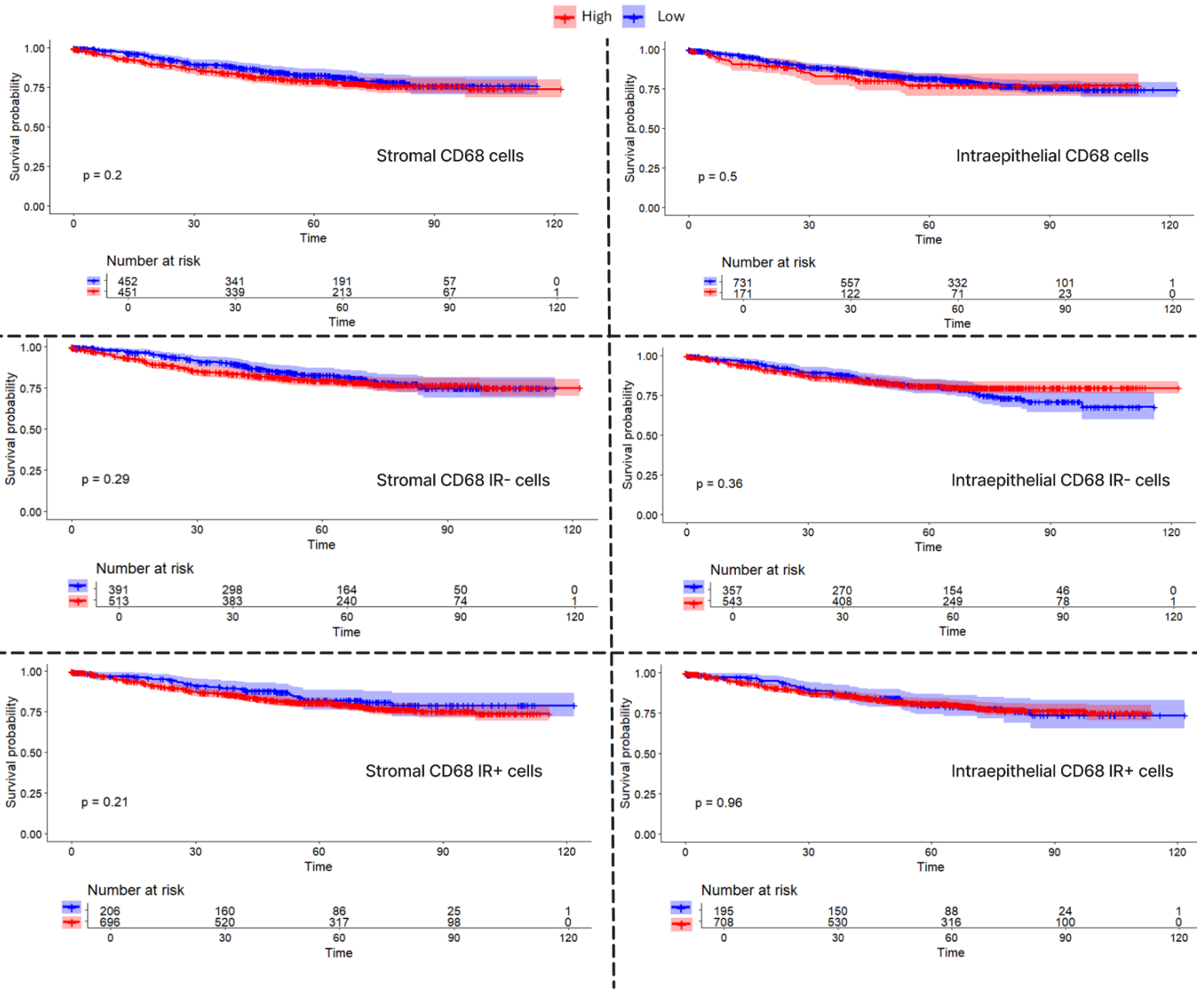


Figure 99. Kaplan-Meier survival curves for overall survival stratified by CD68+ cell density in stromal and intraepithelial compartments showed that total CD68 does not correlate with survival.

Patients were stratified into "High" (red) and "Low" (blue) groups based on the density of CD68+ cells. Optimal cut-off points for dichotomization were determined using X-tile software. CD68.IR- was defined as CD68+ cells not expressing LAG3, PD1, or TIM3, and CD68.IR+ was defined as CD68+ cells expressing at least one of these markers. (Top) Survival curves based on total CD68+ cell density in the stroma (left) and intraepithelial compartment (right). (Middle) Survival curves based on CD68.IR- cell density in the stroma (left) and intraepithelial compartment (right). (Bottom) Survival curves based on CD68.IR+ cell density in the stroma (left) and intraepithelial compartment (right). P-values were calculated using the log-rank test. The number of patients at risk at each time point (in months) is shown below each plot. Shaded areas represent 95% confidence intervals.

3.5.5.1.2.2 IR+ macrophage subpopulation

Analysis of stromal macrophage revealed that high density of CD68+PD1+ cells trended toward improved overall survival, although this association did not reach statistical significance ($p < 0.065$, **Figure 100**, top left panel). However, high stromal density of CD68+TIM3+ cells associated with poor survival ($p < 0.0062$, **Figure 100** middle left panel). Furthermore, high density of CD68+ cells co-expressing both PD1 and TIM3 in the stroma was significantly associated with worse overall survival ($p < 0.035$, **Figure 100**, bottom left panel).

In contrast, within the intraepithelial compartment, no significant associations were found between survival and the density of CD68+PD1+ cells ($p < 0.056$, **Figure 100**, top right panel), CD68+TIM3+ cells ($p < 0.12$, **Figure 100**, middle right panel), or CD68+PD1+TIM3+ cells ($p < 0.22$, **Figure 100**, bottom right panel). It is worth noting that while not statistically significant, CD68+PD1+ cells trended toward significance ($p < 0.056$).

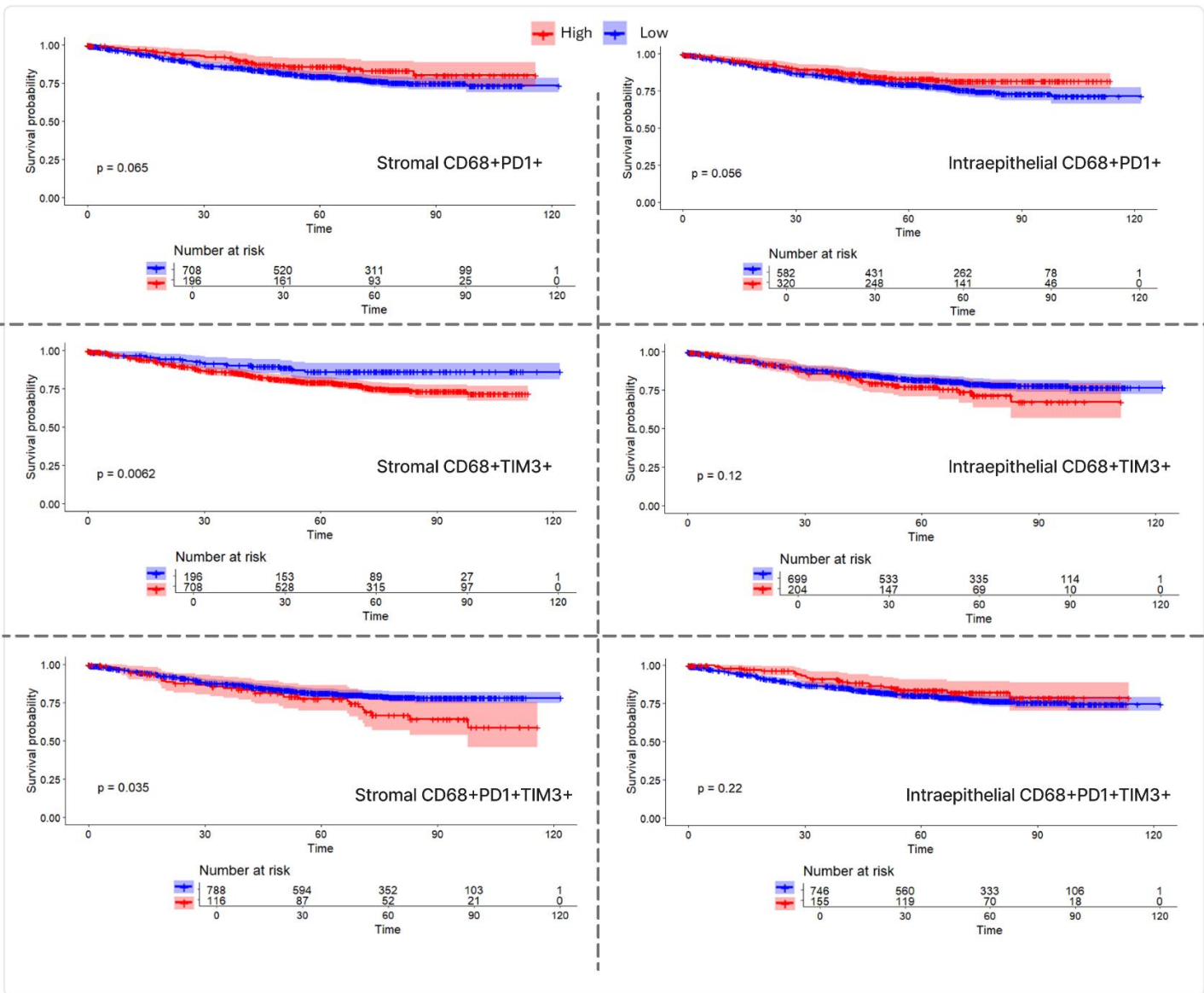


Figure 100. Kaplan-Meier survival curves for overall survival stratified by CD68+ IR+ macrophage subsets in stromal and intraepithelial compartments showed that Tim3 macrophages correlated with reduced survival.

Patients were stratified into "High" (red) and "Low" (blue) groups based on the density of CD68+ macrophages expressing PD1 or TIM3. Optimal cut-off points for dichotomization were determined using X-tile software. (Top) Survival curves based on CD68+PD1+ cell density in the stroma (left) and intraepithelial compartment (right). (Middle) Survival curves based on CD68+TIM3+ cell density in the stroma (left) and intraepithelial compartment (right). (Bottom) Survival curves based on CD68+PD1+TIM3+ cell density in the stroma (left) and intraepithelial compartment (right). P-values were calculated using the log-rank test. The number of patients at risk at each time point (in months) is shown below each plot. Shaded areas represent 95% confidence intervals.

3.5.5.2 Multivariate Cox hazards

Multivariate Cox proportional hazards regression was used to analyze the impact of various immune cell densities on overall survival, adjusting for gender, TNM stage, MMR status, vascular invasion, metastasis, and tumour sidedness.

Analysis of exhausted T cells revealed that a higher density significantly associated with decreased overall survival (HR = 1.745, 95% CI: 1.167 - 2.608, $p < 0.007$). A separate model, examining total T cell infiltrate in the Intraepithelial, revealed high density as protective. [HR=0.6, CI:0.45 – 0.99, P value<0.047]. Regarding the CD3.ex subpopulation, higher densities of TIM3+ and TIM3+PD1+ CD3 within the tumour stroma independently associated with increased hazards of death (HR = 1.69, 95% CI: 1.13 – 2.59, $p < 0.01$; and HR = 1.61, 95% CI: 1.16 – 2.22, $p < 0.001$, respectively).

Higher densities of both TIM3+ macrophages (HR =1.91, 95% CI: 1.19 – 3, $p < 0.007$) and TIM3+PD1+ macrophages (HR =1.72, 95% CI:1.14 – 2.59, $p < 0.009$) inversely associated with survival. These analyses are adjusted for other variables. Overall macrophage density did not herald survival. (Figure 91-94).

Stromal						Intraepithelial					
Variable	B	P.value	HR	95.0% CI for Exp(B)		Variable	B	P.value	HR	95.0% CI for Exp(B)	
				Lower	Upper					Lower	Upper
Sex	0.295	0.077	1.343	0.968	1.863	Sex	0.213	0.197	1.238	0.895	1.712
MMR	-0.146	0.568	0.864	0.522	1.428	MMR	-0.072	0.777	0.930	0.564	1.534
Vascular invasion	0.860	0.000	2.363	1.621	3.446	Vascular invasion	0.798	0.000	2.221	1.520	3.245
TNM stage	-1.108	0.000	0.330	0.213	0.512	TNM stage	-1.050	0.000	0.350	0.225	0.544
Metastases	1.515	0.000	4.548	3.170	6.525	Metastases	1.511	0.000	4.532	3.157	6.507
Sideness	0.156	0.356	1.168	0.840	1.626	Sideness	0.159	0.345	1.173	0.843	1.631
CD3.ex	0.557	0.007	1.745	1.167	2.608	CD3.ex	-0.106	0.528	0.900	0.648	1.249
Variable	B	P.value	HR	95.0% CI for Exp(B)		Variable	B	P.value	HR	95.0% CI for Exp(B)	
Sex	0.237	0.154	1.267	0.915	1.754	Sex	0.231	0.165	1.259	0.909	1.744
MMR	-0.052	0.840	0.950	0.575	1.569	MMR	-0.082	0.749	0.922	0.560	1.518
Vascular invasion	0.835	0.000	2.304	1.573	3.374	Vascular invasion	0.758	0.000	2.135	1.457	3.128
TNM stage	-1.029	0.000	0.357	0.230	0.556	TNM stage	-1.038	0.000	0.354	0.228	0.551
Metastases	1.528	0.000	4.608	3.204	6.628	Metastases	1.498	0.000	4.475	3.109	6.441
Sideness	0.141	0.404	1.152	0.827	1.605	Sideness	0.145	0.394	1.156	0.828	1.613
CD3.non.ex	-0.121	0.503	0.886	0.622	1.263	CD3.non.ex	-0.356	0.058	0.701	0.485	1.012
Variable	B	P.value	HR	95.0% CI for Exp(B)		Variable	B	P.value	HR	95.0% CI for Exp(B)	
Sex	0.208	0.210	1.231	0.890	1.702	Sex	0.207	0.210	1.230	0.890	1.701
MMR	-0.122	0.642	0.885	0.530	1.479	MMR	-0.106	0.676	0.899	0.546	1.482
Vascular invasion	0.801	0.000	2.227	1.526	3.250	Vascular invasion	0.766	0.000	2.151	1.470	3.148
TNM stage	-1.055	0.000	0.348	0.224	0.541	TNM stage	-1.052	0.000	0.349	0.225	0.543
Metastases	1.503	0.000	4.493	3.127	6.456	Metastases	1.470	0.000	4.348	3.022	6.258
Sideness	0.155	0.357	1.168	0.839	1.626	Sideness	0.154	0.361	1.166	0.838	1.623
Total.CD3	-0.074	0.691	0.929	0.646	1.336	Total.CD3	-0.400	0.047	0.671	0.452	0.996

Figure 101. Multivariable cox proportional hazards regression analysis of overall survival in CRC patients showed that total intraepithelial CD3 acts as an independent prognostic factor.

The tables show the results of six separate Cox regression models, each assessing the impact of different CD3+ cell populations on overall survival, adjusted for gender, MMR status, vascular invasion, TNM stage, metastases, and tumour sidedness. Each row represents a predictor variable within a specific model. B: regression coefficient; SE: standard error; HR: hazard ratio; 95% CI: 95% confidence interval. Red boxes highlight the P values. Models analyzed: (1) Stromal exhausted CD3+ T cells (CD3.ex); (2) Intraepithelial exhausted CD3+ T cells (CD3.ex); (3) Stromal non-exhausted CD3+ T cells (CD3.non.ex); (4) Intraepithelial non-exhausted CD3+ T cells (CD3.non.ex); (5) Total Stromal CD3. (6) Total Intraepithelial CD3.

Stromal

Intraepithelial

Variable	B	P.value	HR	95.0% CI for Exp(B)	
				Lower	Upper
Gender	0.222	0.180	1.248	0.903	1.726
MMR	-0.087	0.734	0.917	0.556	1.512
Vascular invasion	0.830	0.000	2.294	1.567	3.358
TNM stage	-1.040	0.000	0.353	0.227	0.549
Metastases	1.508	0.000	4.519	3.137	6.509
Sideness	0.159	0.347	1.172	0.842	1.632
LAG3+CD3	0.139	0.401	1.150	0.830	1.592

Variable	B	P.value	HR	95.0% CI for Exp(B)	
				Lower	Upper
Gender	0.220	0.182	1.246	0.902	1.723
MMR	-0.077	0.763	0.926	0.562	1.527
Vascular invasion	0.809	0.000	2.245	1.539	3.273
TNM stage	-1.057	0.000	0.348	0.224	0.540
Metastases	1.528	0.000	4.610	3.212	6.616
Sideness	0.165	0.328	1.179	0.848	1.641
LAG3+CD3	0.225	0.242	1.252	0.859	1.825

Variable	B	P.value	HR	95.0% CI for Exp(B)	
				Lower	Upper
Gender	0.240	0.148	1.271	0.918	1.759
MMR	-0.007	0.978	0.993	0.599	1.645
Vascular invasion	0.762	0.000	2.144	1.465	3.136
TNM stage	-1.050	0.000	0.350	0.225	0.543
Metastases	1.524	0.000	4.591	3.196	6.595
Sideness	0.142	0.402	1.152	0.827	1.605
PD1+CD3	-0.412	0.085	0.662	0.415	1.058

Variable	B	P.value	HR	95.0% CI for Exp(B)	
				Lower	Upper
Gender	0.211	0.202	1.235	0.893	1.708
MMR	-0.046	0.859	0.956	0.579	1.578
Vascular invasion	0.768	0.000	2.156	1.473	3.156
TNM stage	-1.042	0.000	0.353	0.227	0.549
Metastases	1.486	0.000	4.421	3.078	6.350
Sideness	0.173	0.304	1.189	0.854	1.656
PD1+CD3	-0.289	0.081	0.749	0.541	1.036

Variable	B	P.value	HR	95.0% CI for Exp(B)	
				Lower	Upper
Gender	0.220	0.184	1.246	0.901	1.723
MMR	-0.084	0.742	0.920	0.558	1.514
Vascular invasion	0.814	0.000	2.257	1.549	3.288
TNM stage	-1.064	0.000	0.345	0.222	0.536
Metastases	1.543	0.000	4.677	3.257	6.715
Sideness	0.184	0.274	1.202	0.864	1.672
TIM3+CD3	0.527	0.010	1.694	1.136	2.524

Variable	B	P.value	HR	95.0% CI for Exp(B)	
				Lower	Upper
Gender	0.216	0.190	1.241	0.898	1.716
MMR	-0.074	0.773	0.929	0.563	1.532
Vascular invasion	0.813	0.000	2.255	1.546	3.288
TNM stage	-1.053	0.000	0.349	0.225	0.542
Metastases	1.519	0.000	4.569	3.186	6.552
Sideness	0.157	0.353	1.170	0.840	1.628
TIM3+CD3	-0.206	0.450	0.814	0.477	1.388

Variable	B	P.value	HR	95.0% CI for Exp(B)	
				Lower	Upper
Gender	0.229	0.169	1.257	0.908	1.741
MMR	-0.067	0.792	0.935	0.567	1.541
Vascular invasion	0.836	0.000	2.307	1.576	3.377
TNM stage	-1.027	0.000	0.358	0.230	0.557
Metastases	1.531	0.000	4.622	3.218	6.639
Sideness	0.141	0.404	1.152	0.827	1.605
LAG3.PD1	-0.221	0.482	0.801	0.433	1.484

Variable	B	P.value	HR	95.0% CI for Exp(B)	
				Lower	Upper
Gender	0.215	0.192	1.240	0.897	1.713
MMR	-0.097	0.704	0.908	0.550	1.497
Vascular invasion	0.790	0.000	2.204	1.510	3.217
TNM stage	-1.044	0.000	0.352	0.227	0.546
Metastases	1.497	0.000	4.469	3.115	6.413
Sideness	0.184	0.276	1.202	0.863	1.675
LAG3.PD1	-0.459	0.165	0.632	0.331	1.208

Variable	B	P.value	HR	95.0% CI for Exp(B)	
				Lower	Upper
Gender	0.241	0.148	1.272	0.918	1.763
MMR	-0.102	0.689	0.903	0.547	1.489
Vascular invasion	0.851	0.000	2.341	1.601	3.423
TNM stage	-1.101	0.000	0.332	0.213	0.518
Metastases	1.517	0.000	4.561	3.175	6.550
Sideness	0.134	0.431	1.143	0.820	1.593
PD1.TIM3	0.477	0.004	1.612	1.167	2.226

Variable	B	P.value	HR	95.0% CI for Exp(B)	
				Lower	Upper
Gender	0.195	0.240	1.216	0.877	1.685
MMR	-0.084	0.742	0.919	0.557	1.517
Vascular invasion	0.785	0.000	2.193	1.500	3.206
TNM stage	-1.029	0.000	0.357	0.230	0.556
Metastases	1.539	0.000	4.658	3.244	6.687
Sideness	0.178	0.293	1.195	0.857	1.666
PD1.TIM3	-0.208	0.341	0.812	0.529	1.247

Figure 102. Multivariable cox proportional hazards regression analysis of overall survival in CRC patients showed that Tim3+ T cells and Tim3+PD1+ T cells acts as an independent prognostic factor.

The tables show the results of six separate Cox regression models, each assessing the impact of different CD3.ex subpopulation on overall survival, adjusted for gender, MMR status, vascular invasion, TNM stage, metastases, and tumour sidedness. Each row represents a predictor variable within a specific model. B: regression coefficient; SE: standard error; HR: hazard ratio; 95% CI: 95% confidence interval. Red boxes highlight the P values.

Stromal

Intraepithelial

Variable	B	P.value	HR	95.0% CI for Exp(B)	
				Lower	Upper
Gender	0.244	0.141	1.277	0.922	1.768
MMR	-0.147	0.572	0.863	0.518	1.438
Vascular invasion	0.854	0.000	2.348	1.607	3.431
TNM stage	-1.036	0.000	0.355	0.229	0.551
Metastases	1.554	0.000	4.729	3.290	6.796
Sideness	0.143	0.396	1.153	0.829	1.604
CD68.IR+	0.387	0.059	1.472	0.985	2.199

Variable	B	P.value	HR	95.0% CI for Exp(B)	
				Lower	Upper
Gender	0.240	0.147	1.271	0.919	1.758
MMR	-0.090	0.725	0.914	0.555	1.506
Vascular invasion	0.820	0.000	2.271	1.558	3.309
TNM stage	-1.070	0.000	0.343	0.221	0.532
Metastases	1.542	0.000	4.673	3.253	6.711
Sideness	0.167	0.320	1.182	0.850	1.644
CD68.IR+	0.299	0.126	1.349	0.919	1.978

Variable	B	P.value	HR	95.0% CI for Exp(B)	
				Lower	Upper
Gender	0.228	0.168	1.256	0.908	1.737
MMR	-0.080	0.755	0.923	0.560	1.522
Vascular invasion	0.807	0.000	2.242	1.536	3.271
TNM stage	-1.059	0.000	0.347	0.223	0.539
Metastases	1.516	0.000	4.553	3.173	6.533
Sideness	0.153	0.366	1.165	0.836	1.623
CD68.IR-	0.079	0.634	1.082	0.782	1.497

Variable	B	P.value	HR	95.0% CI for Exp(B)	
				Lower	Upper
Gender	0.202	0.226	1.224	0.882	1.697
MMR	-0.077	0.762	0.926	0.561	1.527
Vascular invasion	0.796	0.000	2.216	1.519	3.232
TNM stage	-1.056	0.000	0.348	0.223	0.541
Metastases	1.524	0.000	4.590	3.191	6.603
Sideness	0.175	0.301	1.191	0.855	1.659
CD68.IR-	-0.094	0.569	0.910	0.658	1.259

Variable	B	P.value	HR	95.0% CI for Exp(B)	
				Lower	Upper
Gender	0.235	0.155	1.265	0.915	1.749
MMR	-0.090	0.724	0.914	0.554	1.507
Vascular invasion	0.801	0.000	2.228	1.527	3.253
TNM stage	-1.056	0.000	0.348	0.224	0.540
Metastases	1.519	0.000	4.566	3.184	6.547
Sideness	0.142	0.403	1.152	0.827	1.605
Total.CD68	0.182	0.263	1.200	0.872	1.652

Variable	B	P.value	HR	95.0% CI for Exp(B)	
				Lower	Upper
Gender	0.230	0.163	1.259	0.911	1.740
MMR	-0.078	0.760	0.925	0.561	1.525
Vascular invasion	0.818	0.000	2.265	1.553	3.304
TNM stage	-1.060	0.000	0.346	0.223	0.538
Metastases	1.515	0.000	4.547	3.170	6.523
Sideness	0.150	0.375	1.161	0.835	1.616
Total.CD68	0.105	0.597	1.111	0.752	1.641

Figure 103. Multivariable cox proportional hazards regression analysis of overall survival in CRC patients showed no independent prognostic impact for total macrophages.

The tables show the results of six separate Cox regression models, each assessing the impact of different CD68+ cell populations on overall survival, adjusted for gender, MMR status, vascular invasion, TNM stage, metastases, and tumour sidedness. Each row represents a predictor variable within a specific model. B: regression coefficient; SE: standard error; HR: hazard ratio; 95% CI: 95% confidence interval. Red boxes highlight the P values. Models analyzed: (1) Stromal CD68 with immune regulator (CD68.IR+); (2) Intraepithelial CD68 with immune regulator (CD68.IR+); (3) Stromal CD68 without immune regulator (CD68.IR-) (4) Intraepithelial CD68 without immune regulator (CD68.IR-); (5) Total Stromal CD68. (6) Total Intraepithelial CD68.

Stromal

Intraepithelial

Variable	B	P.value	HR	95.0% CI for Exp(B)	
				Lower	Upper
Gender	0.213	0.197	1.238	0.895	1.711
MMR	-0.082	0.747	0.921	0.559	1.518
Vascular invasion	0.795	0.000	2.214	1.514	3.237
TNM stage	-1.057	0.000	0.347	0.224	0.539
Metastases	1.509	0.000	4.524	3.152	6.493
Sideness	0.166	0.324	1.181	0.848	1.644
PD1+CD68+	-0.159	0.472	0.853	0.553	1.316

Variable	B	P.value	HR	95.0% CI for Exp(B)	
				Lower	Upper
Gender	0.215	0.193	1.240	0.897	1.714
MMR	-0.062	0.807	0.940	0.570	1.550
Vascular invasion	0.797	0.000	2.218	1.520	3.237
TNM stage	-1.057	0.000	0.347	0.224	0.539
Metastases	1.509	0.000	4.522	3.152	6.487
Sideness	0.161	0.339	1.175	0.844	1.635
PD1+CD68+	-0.192	0.284	0.825	0.581	1.172

Variable	B	P.value	HR	95.0% CI for Exp(B)	
				Lower	Upper
Gender	0.243	0.141	1.276	0.923	1.764
MMR	-0.070	0.782	0.932	0.566	1.535
Vascular invasion	0.834	0.000	2.302	1.580	3.354
TNM stage	-1.064	0.000	0.345	0.222	0.535
Metastases	1.495	0.000	4.459	3.111	6.393
Sideness	0.174	0.301	1.190	0.856	1.655
TIM3+CD68	0.647	0.007	1.910	1.193	3.057

Variable	B	P.value	HR	95.0% CI for Exp(B)	
				Lower	Upper
Gender	0.234	0.159	1.263	0.912	1.748
MMR	-0.067	0.792	0.935	0.567	1.542
Vascular invasion	0.804	0.000	2.235	1.533	3.260
TNM stage	-1.051	0.000	0.349	0.225	0.543
Metastases	1.520	0.000	4.571	3.187	6.556
Sideness	0.153	0.363	1.166	0.838	1.622
TIM3+CD68	0.135	0.459	1.145	0.800	1.639

Variable	B	P.value	HR	95.0% CI for Exp(B)	
				Lower	Upper
Gender	0.223	0.174	1.250	0.906	1.725
MMR	-0.019	0.940	0.981	0.593	1.622
Vascular invasion	0.839	0.000	2.314	1.585	3.377
TNM stage	-1.041	0.000	0.353	0.227	0.548
Metastases	1.544	0.000	4.685	3.267	6.719
Sideness	0.119	0.479	1.127	0.810	1.567
TIM3+PD1+CD68	0.544	0.009	1.722	1.145	2.591

Variable	B	P.value	HR	95.0% CI for Exp(B)	
				Lower	Upper
Gender	0.212	0.199	1.236	0.894	1.709
MMR	-0.079	0.756	0.924	0.560	1.524
Vascular invasion	0.831	0.000	2.296	1.569	3.360
TNM stage	-1.034	0.000	0.356	0.229	0.553
Metastases	1.523	0.000	4.588	3.193	6.591
Sideness	0.170	0.316	1.185	0.851	1.651
TIM3+PD1+CD68	-0.150	0.524	0.861	0.543	1.365

Figure 104. Multivariable cox proportional hazards regression analysis of overall survival showed that Tim3+ macrophages and Tim3+ PD1+ macrophages act as an independent prognostic factor.

The tables show the results of six separate Cox regression models, each assessing the impact of different CD68.IR+ subpopulations on overall survival, adjusted for gender, MMR status, vascular invasion, TNM stage, metastases, and tumour sidedness. Each row represents a predictor variable within a specific model. B: regression coefficient; SE: standard error; HR: hazard ratio; 95% CI: 95% confidence interval. Red boxes highlight the P values.

3.5.6 Prognostic impact of T cell and macrophage density across different tumour regions

The relationship between spatial distribution and patient survival was examined for each region. Cell densities were dichotomized into high and low groups. Survival analysis was performed using the log-rank test, and Kaplan-Meier plots were generated to visualize survival differences.

3.5.6.1 Prognostic value of T cell density

The density of stromal T cells regardless of its exhaustion marker status in the adjacent normal and the invasive margin showed better survival (**Figure 105**). In the center of the tumour, only the density of CD3.non.ex population correlated with survival. In contrast, in the luminal side no association was found. However, in the intraepithelial compartment of different regions, CD3 cells regardless of their exhaustion status, showed improved survival (**Figure 106**).

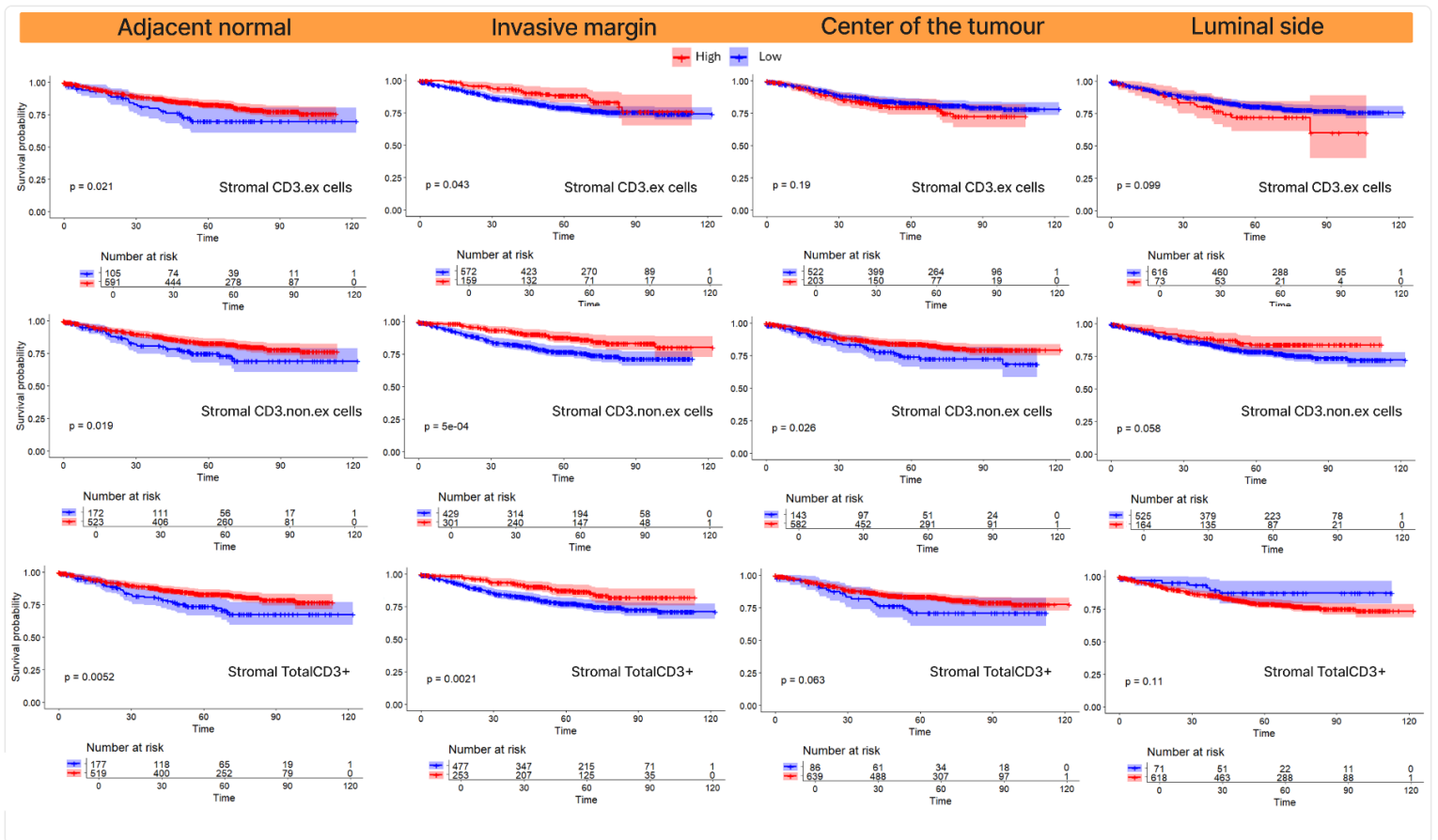


Figure 105. Kaplan-Meier survival curves for CRC patients stratified by stromal CD3+ cell densities in different tumour regions showed that Invasive margin has the most prognostic impact.

Survival curves are shown for patients with high (red) and low (blue) densities of exhausted CD3+ cells (CD3.ex), non-exhausted CD3+ cells (CD3.non.ex), and total CD3+ cells (TotalCD3+) in the adjacent normal tissue (AN), invasive margin (IM), tumour center (CT), and luminal side (LS). P-values were calculated using the log-rank test.

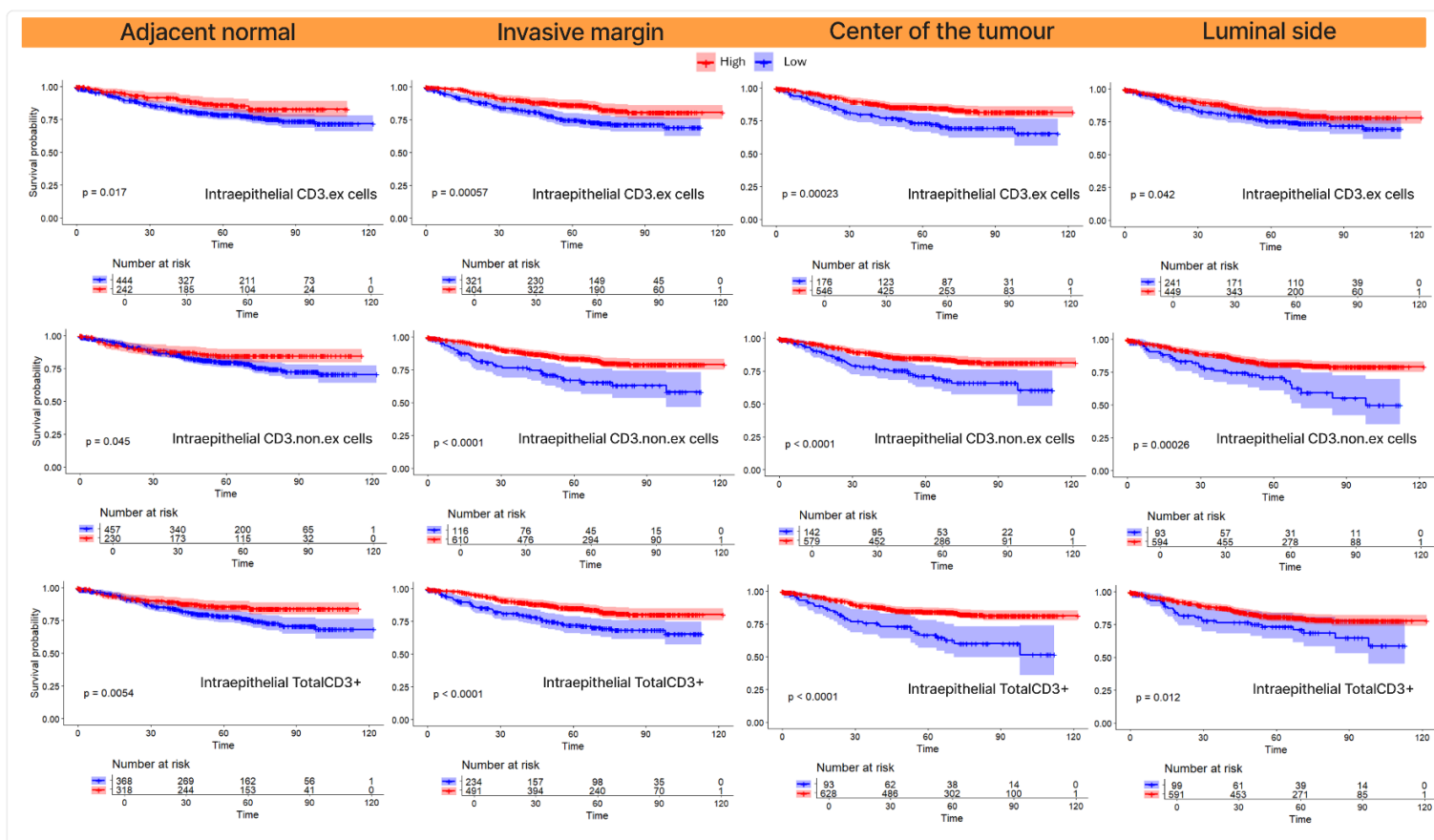


Figure 106. Kaplan-Meier survival curves for CRC patients stratified by intraepithelial CD3+ cell densities in different tumour regions showed that luminal side has the lowest prognostic impact.

Survival curves are shown for patients with high (red) and low (blue) densities of exhausted CD3+ cells (CD3.ex), non-exhausted CD3+ cells (CD3.non.ex), and total CD3+ cells (TotalCD3+) in the adjacent normal tissue (AN), invasive margin (IM), tumour center (CT), and luminal side (LS). P-values were calculated using the log-rank test.

3.5.6.2 Prognostic impact of Exhausted CD3 subpopulation

LAG3+CD3+ higher cell density only in the stromal of adjacent normal was correlated with survival. Both stromal and intraepithelial PD1+CD3+ higher cell densities in the invasive margin and center of the tumour correlated with better survival. However, on the luminal side, only intraepithelial PD1+CD3+ was correlated with better survival. Stromal TIM3+CD3+ higher cell density was correlated with poor survival in the center of the tumour, however, intraepithelial TIM3+CD3+ higher cell density in the invasive margin was

correlated with better survival. Higher cell density of LAG3+PD1+ only on the intraepithelial compartment of invasive margin was correlated with better survival. TIM3+PD1+CD3+ cell density in the stromal compartments of the center of the tumour and luminal side was correlated with poor survival, however in the intraepithelial compartment of invasive margin was associated with good survival (Figure 107, Figure 108).

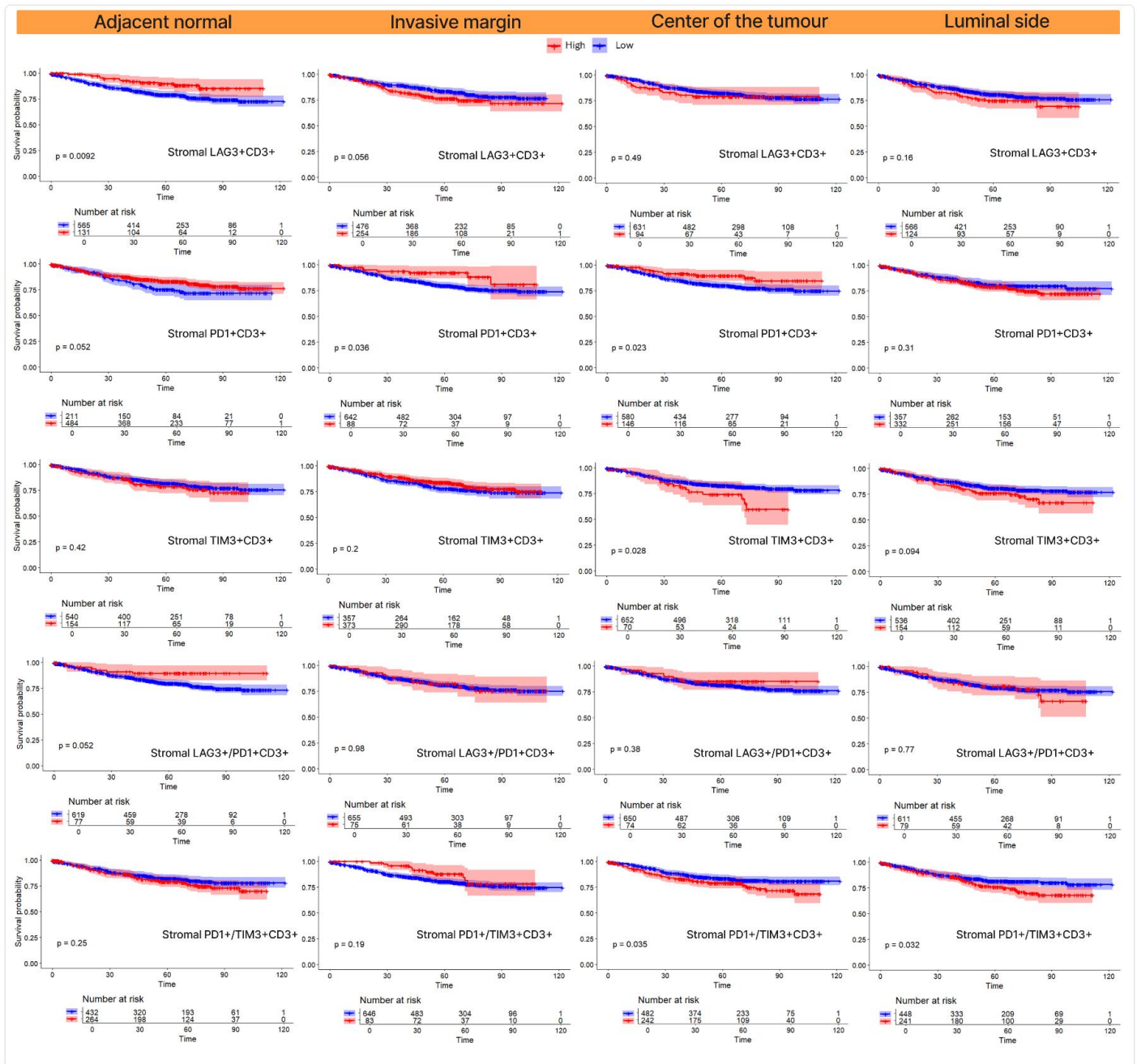


Figure 107. Kaplan-Meier survival curves for CRC patients stratified by stromal CD3+ subpopulation densities in different tumour regions showed that location has an impact on the survival impact.

Survival curves are shown for patients with high (red) and low (blue) densities in the adjacent normal tissue (AN), invasive margin (IM), tumour center (CT), and luminal side (LS). P-values were calculated using the log-rank test.

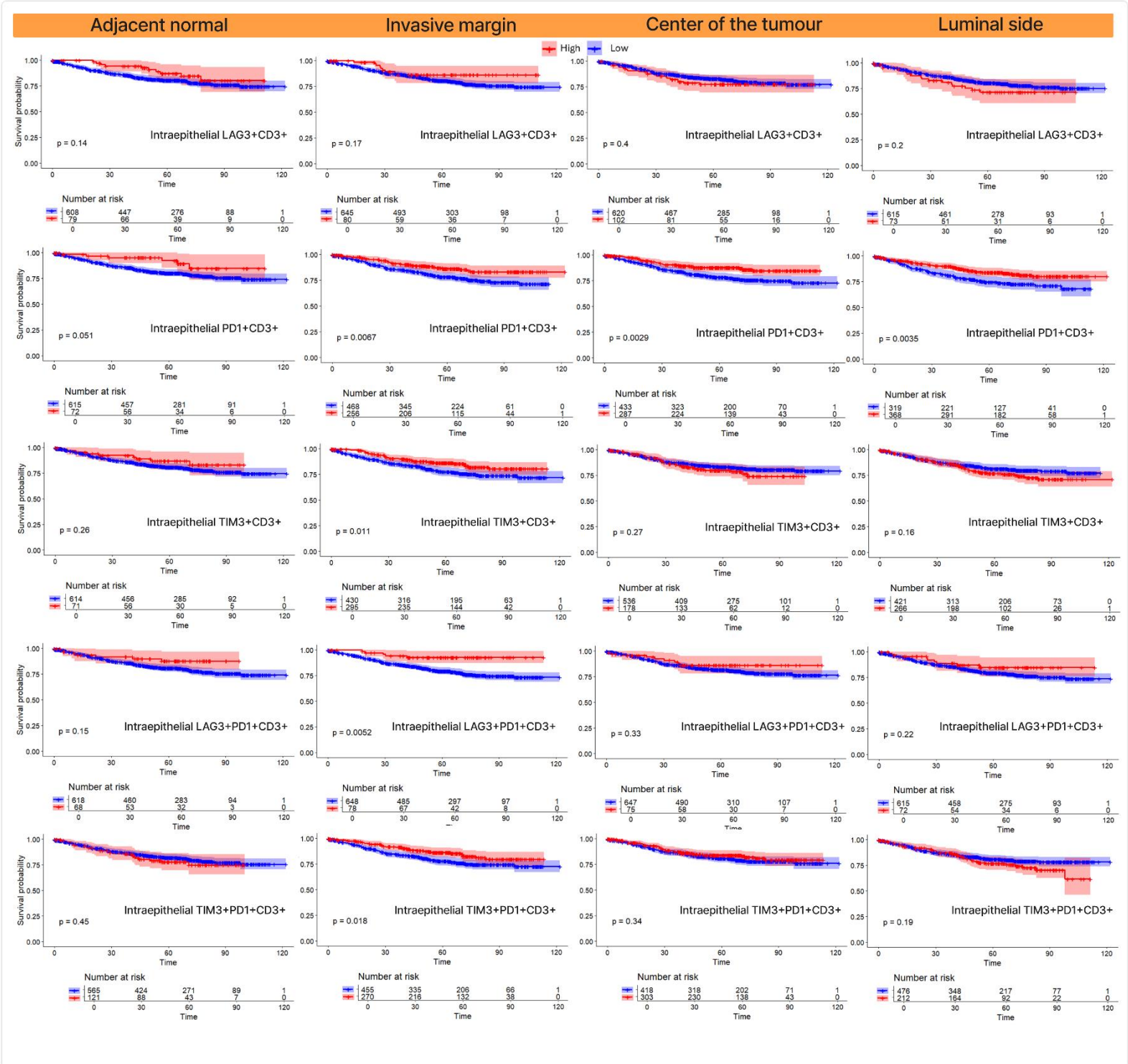


Figure 108. Kaplan-Meier survival curves for CRC patients stratified by intraepithelial CD3+ subpopulation densities in different tumour regions showed that location has an impact on the survival impact.

Survival curves are shown for patients with high (red) and low (blue) densities in the adjacent normal tissue (AN), invasive margin (IM), tumour center (CT), and luminal side (LS). P-values were calculated using the log-rank test.

3.5.6.3 Prognostic impact of macrophage density

The presence of stromal PD1+ macrophages in the invasive margin associated with survival. In contrast lower density of TIM3+CD68+ macrophages in the stromal compartment of center of the tumour and luminal side, plus intraepithelial compartment of adjacent normal showed a poor survival outcome. In both stromal and intraepithelial compartments of invasive margin, TIM3+PD1+ CD68+ macrophages showed good survival. Furthermore, macrophages without immune regulator molecules correlated with better survival only in the intraepithelial compartment of the invasive margin. Total macrophages in the stromal compartment of adjacent normal and intraepithelial compartment of invasive margin correlated with survival (**Figure 109, Figure 110**).

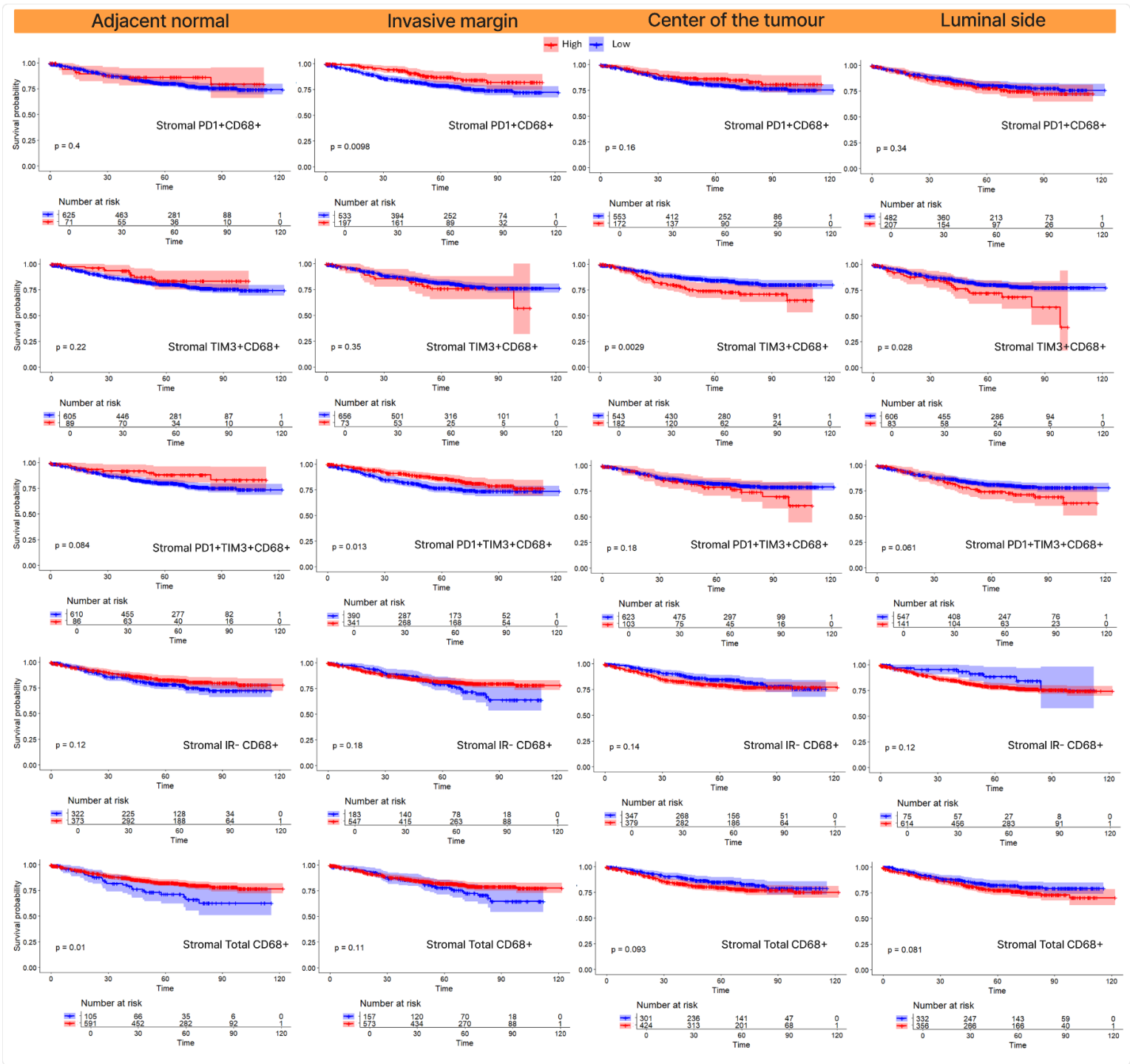


Figure 109. Kaplan-Meier survival curves for CRC patients stratified by stromal CD68+ subpopulation densities in different tumour regions showed that location has an impact on the survival impact.

Survival curves are shown for patients with high (red) and low (blue) densities in the adjacent normal tissue (AN), invasive margin (IM), tumour center (CT), and luminal side (LS). P-values were calculated using the log-rank test.

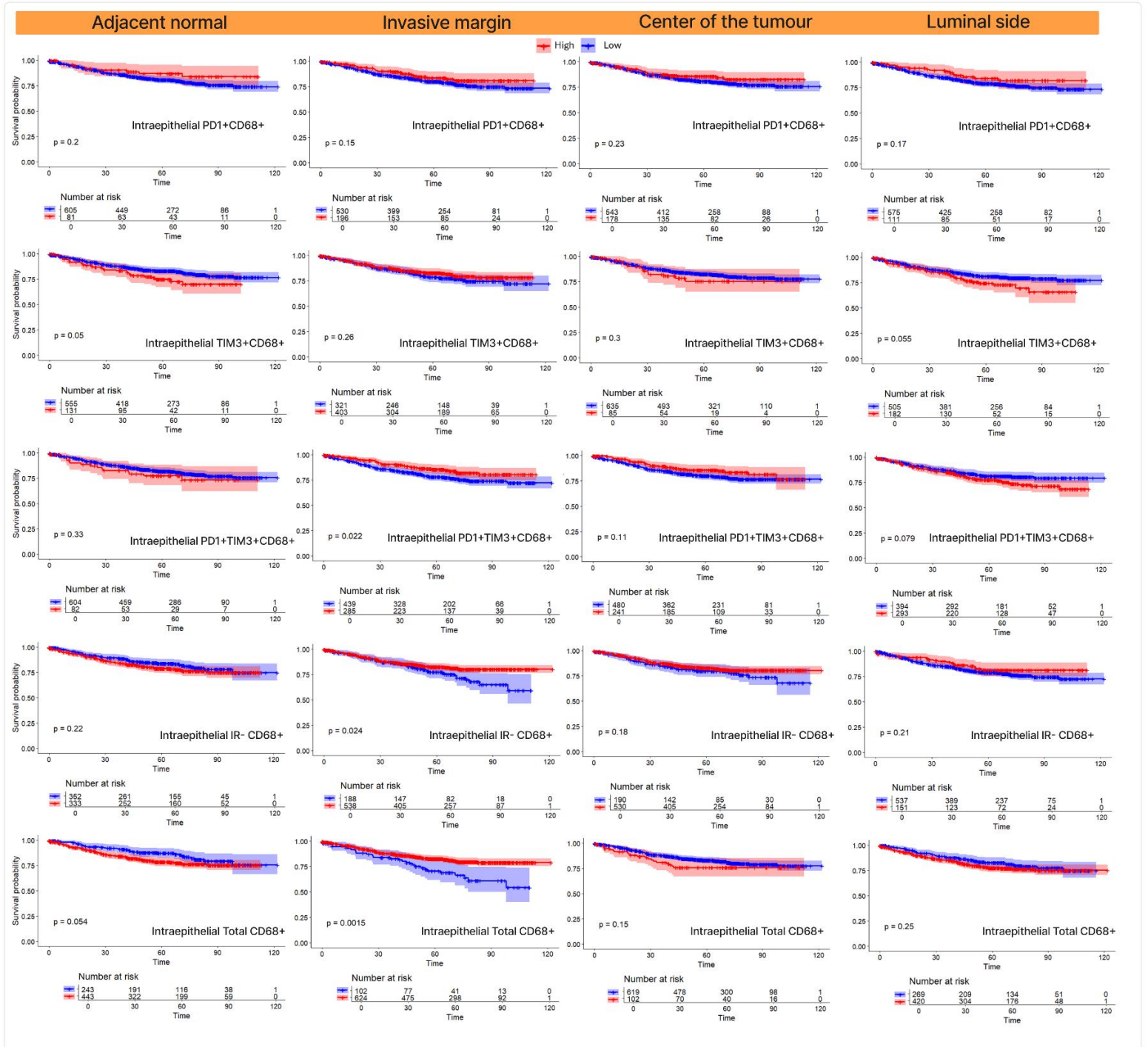


Figure 110. Kaplan-Meier survival curves for CRC patients stratified by intraepithelial CD68+ subpopulation densities in different tumour regions showed that location has an impact on the survival impact.

Survival curves are shown for patients with high (red) and low (blue) densities in the adjacent normal tissue (AN), invasive margin (IM), tumour center (CT), and luminal side (LS). P-values were calculated using the log-rank test.

3.5.7 On the relationship between TNM stage and infiltration by T-cells and macrophage

The TNM staging system is a fundamental prognostic indicator in colorectal cancer, reflecting the extent of tumour progression and metastasis. Given that tumour invasion and dissemination can influence the immune landscape, we analyzed how T cell densities varied across different CRC stages. We analyzed the distribution of leukocytes in tissue sections from patients stratified by TNM stage (I-IV). For each patient, cell densities were averaged across tumour-associated regions, including the IM, CT, and LS. Violin plots were generated to visualize the distribution of cell densities for each phenotype and TNM stage. To assess the prognostic impact of cell density, patients within each TNM stage (I and II) and (III and IV) were dichotomized into "high" and "low" density groups based on an optimal cutoff.

3.5.7.1 T cell density and tumour stage

Violin plots (**Figure 111, Figure 112**) illustrated T-cell infiltration as a prominent feature of low stage CRC. In fact, stromal and intraepithelial PD1+ CD3+ cells density significantly was highest in stage I and had a reduction in density in advanced stages of CRC. CD3.non.ex and total CD3 in both stromal and intraepithelial compartment also had a significantly higher density in early stages compared to advanced stages. Intraepithelial LAG3+ PD1+ CD3 cells also showed a decrease in density.

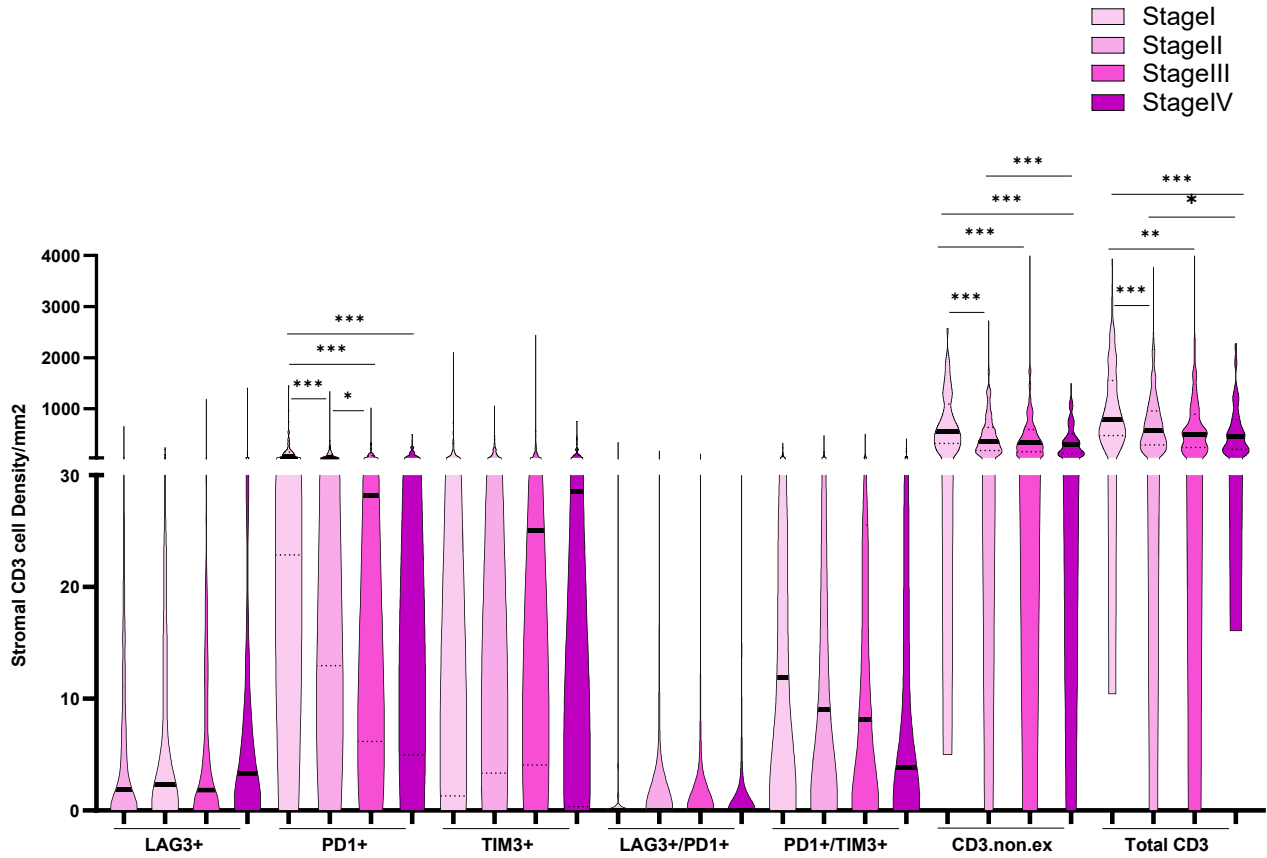


Figure 111. distribution of stromal CD3+ T Cell subset densities across TNM Stages in colorectal cancer showed higher density of CD3 cells in early stages compared to advanced stages.

Violin plots show the density of different CD3+ T cell phenotypes within the stromal compartment of CRC tissue sections, stratified by TNM stage (I-IV). The vertical axis represents cell density expressed as cells per square millimeter (cells/mm²). The horizontal lines within each violin represent the median. Kruskal-Wallis test with the post hoc test compared the cell density between different TNM stages. Only significant values are depicted. PD1+ CD3 density, stage I vs. II, p<0.001(***), stage I vs. III, p<0.001(***) I vs. IV, p<0.19 (***) , Stage II vs. stage III, p<0.038, CD3.non.ex density in stage I vs. II, p<0.001(***), stage I vs. III, p<0.001(***), stage I vs. IV, p<0.001 (***) , Stage II vs. stage IV, p<0.01 (**), Total CD3 density in stage I vs. II, p<0.001(***), stage I vs. III, p<0.001(***), stage I vs. IV, p<0.001 (***) , Stage II vs. stage IV, p<0.012 (*).

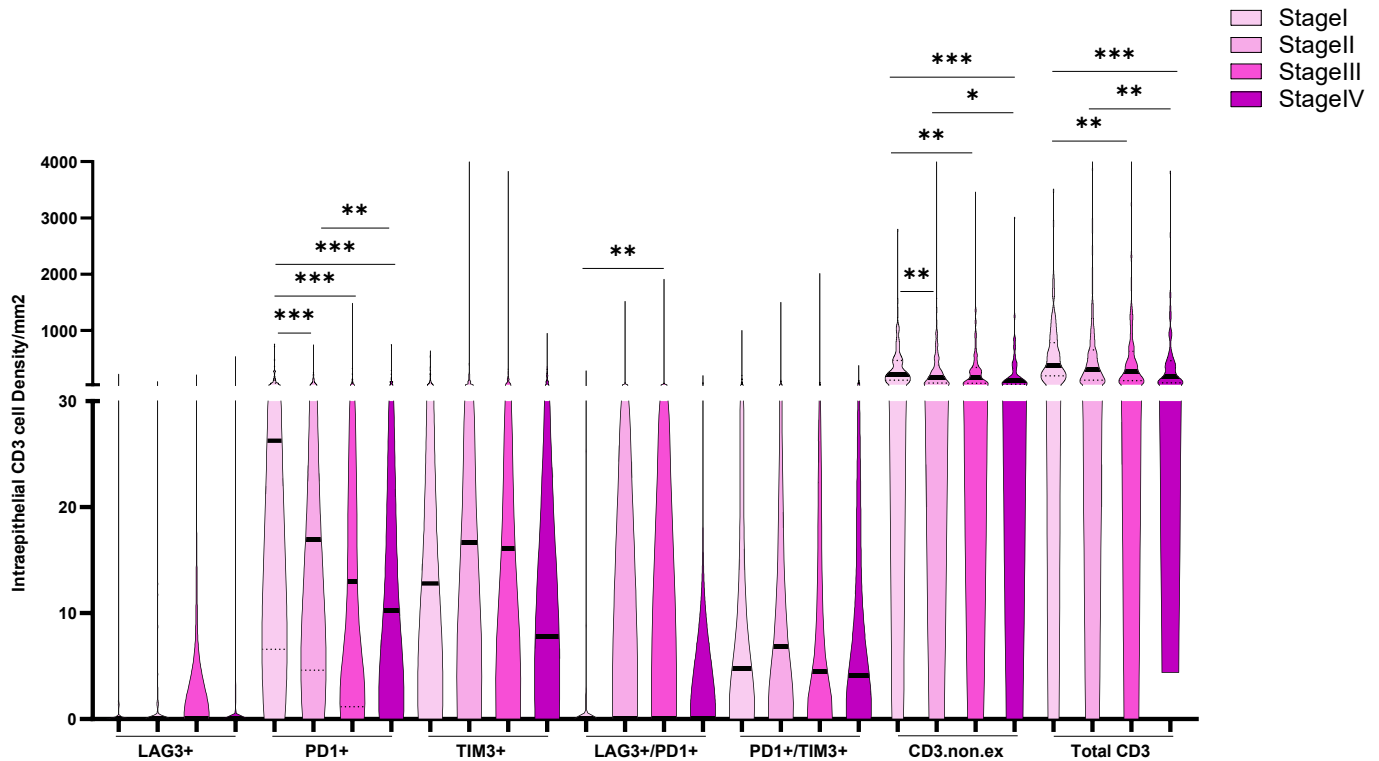


Figure 112. Distribution of intraepithelial CD3+ T Cell subset densities across TNM stages in colorectal cancer showed higher density of CD3 cells in early stages compared to advanced stages.

Violin plots show the density of different CD3+ T cell phenotypes within the stromal compartment of CRC tissue sections, stratified by TNM stage (I-IV). The vertical axis represents cell density expressed as cells per square millimeter (cells/mm²). The horizontal lines within each violin represent the median. Kruskal-Wallis test with the post hoc test compared the cell density between different TNM stages. Only significant values are depicted. PD1+ Cd3 density, stage I vs. II, $p < 0.001$ (***) , stage I vs. III ; $p < 0.001$ (***) , I vs. IV, $p < 0.19$ (***) , stage II vs. stage IV, $p < 0.002$ (**); PD1/LAG3 CD3+ density in stage I vs. III , $p < 0.007$ (**); CD3.non.ex density in stage I vs. II , $p < 0.002$ (**), stage I vs. III , $p < 0.008$ (**), stage I vs. IV, $p < 0.001$ (***) , Stage II vs. stage IV, $p < 0.014$ (*), Total CD3 density, stage I vs. III , $p < 0.005$ (**), stage I vs. IV, $p < 0.001$ (***) , Stage II vs. stage IV, $p < 0.004$ (**).

3.5.7.2 Macrophage infiltration and stage

Although there is significant difference in the cell density of PD1+CD68+ between stage I and II (CRC low stages) and stage IV (CRC high stage) in both stromal and intraepithelial compartment, there is no significant difference in the density of other phenotypes of macrophages in different stages of CRC (**Figure 113, Figure 114**).

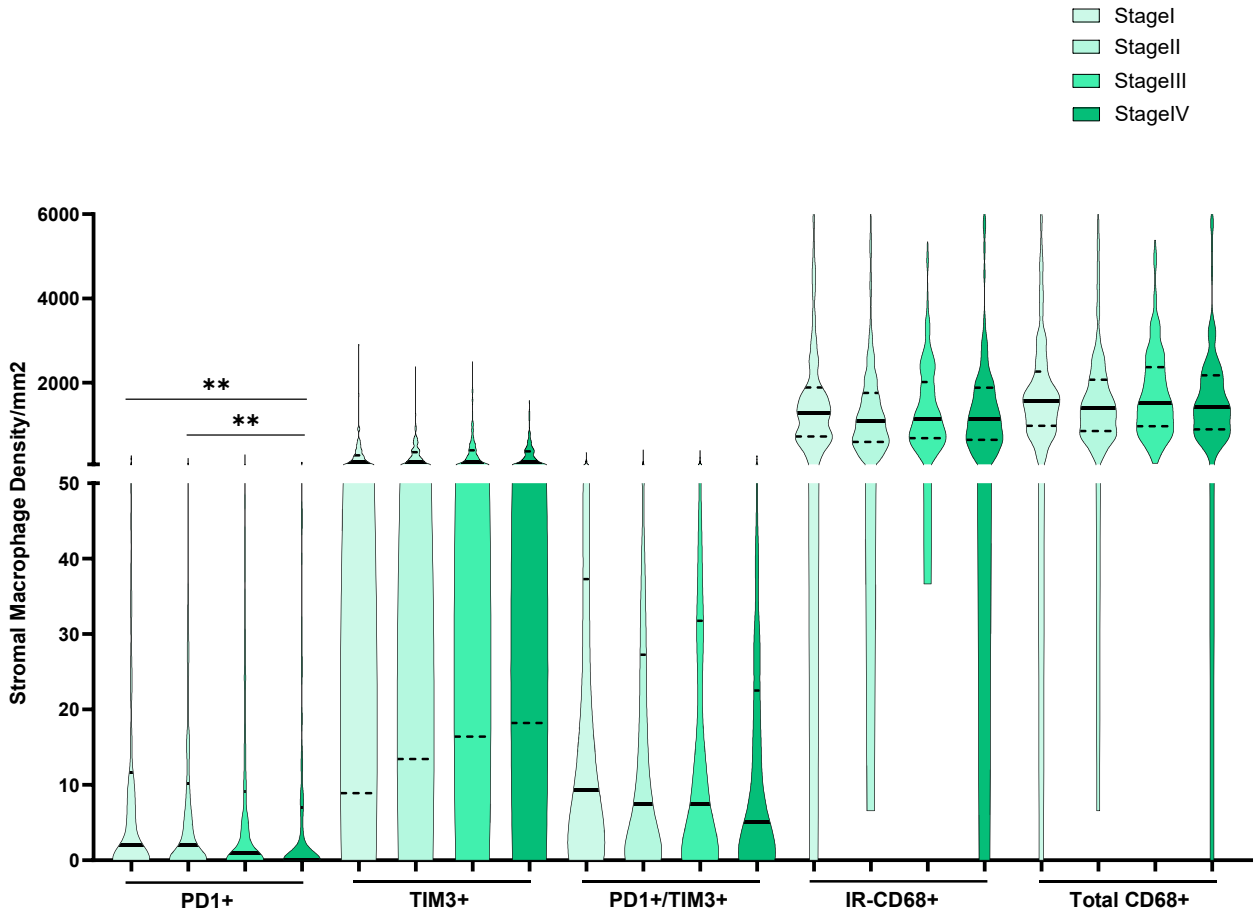


Figure 113. Distribution of stromal CD68+ cell subset densities across TNM stages in colorectal cancer showed there is almost no difference in the density of macrophages between early and advanced stages.

Violin plots show the density of different CD68+ T cell phenotypes within the stromal compartment of CRC tissue sections, stratified by TNM stage (I-IV). The vertical axis represents cell density expressed as cells per square millimeter (cells/mm²). The horizontal lines within each violin represent the median. Kruskal-Wallis test with the post hoc test compared the cell density between different TNM stages. Only significant values are depicted. PD1+ Cd68 density, I vs. IV, $p < 0.008$ (**), stage II vs. stage IV, $p < 0.005$.

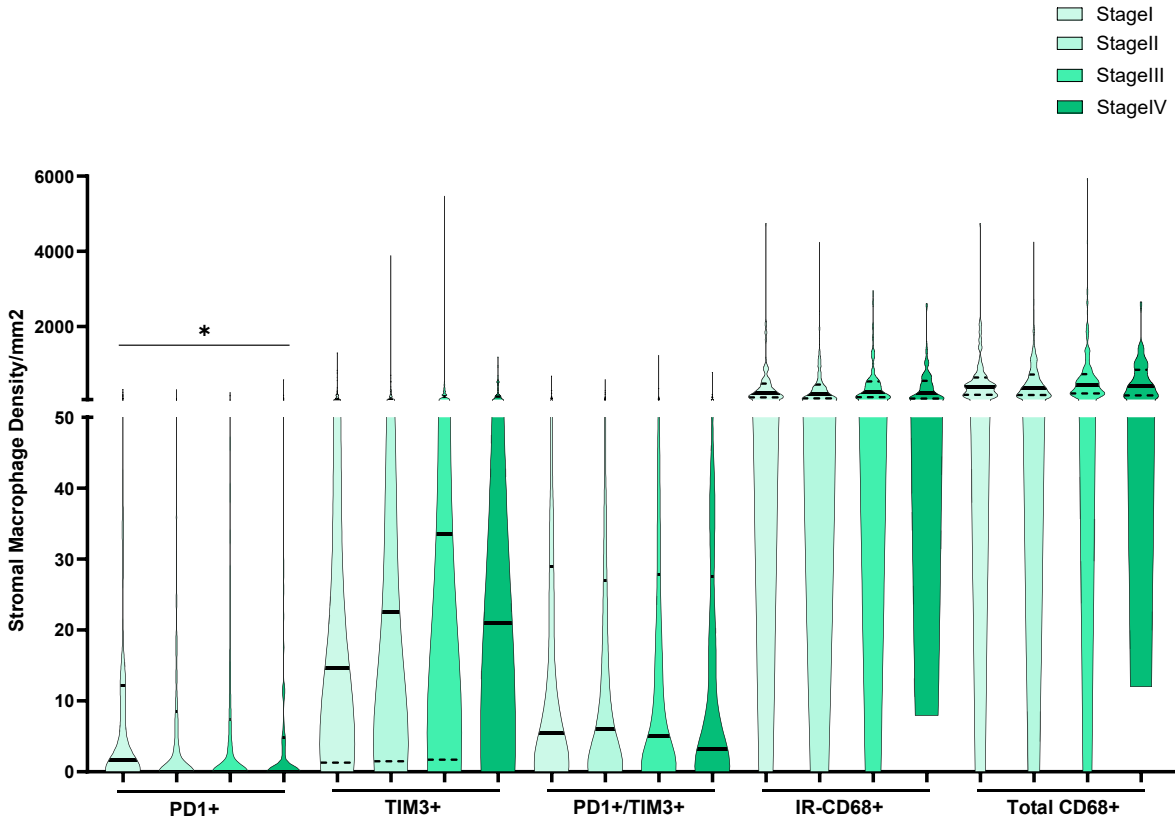


Figure 114. Distribution of intraepithelial CD68+ cell subset densities across TNM Stages in colorectal cancer showed there is almost no difference in the density of macrophages between early and advanced stages.

Violin plots show the density of different CD68+ T cell phenotypes within the stromal compartment of CRC tissue sections, stratified by TNM stage (I-IV). The vertical axis represents cell density expressed as cells per square millimeter (cells/mm²). The horizontal lines within each violin represent the median. Kruskal-Wallis test with the post hoc test compared the cell density between different TNM stages. Only significant values are depicted. PD1+ Cd68 density, I vs. IV, $p < 0.02$ (*).

3.5.7.3 Prognostic impact of T cells and macrophages in different stages.

Stromal CD3.ex cells in both low and high stages of CRC correlated with a poor survival impact (**Figure 115**). However, intraepithelial CD3. Non.ex and total T cells in both low and high stages correlated with improved survival. Regarding CD3.ex subpopulation, PD1+CD3+ cells showed a poor survival in the stromal compartment of low stages CRC and a good survival in the intraepithelial compartment of high-grade CRC. In both low- and high-grade CRC, PD1+TIM3+CD3+ showed poor survival in the stromal compartment (**Figure 116**).

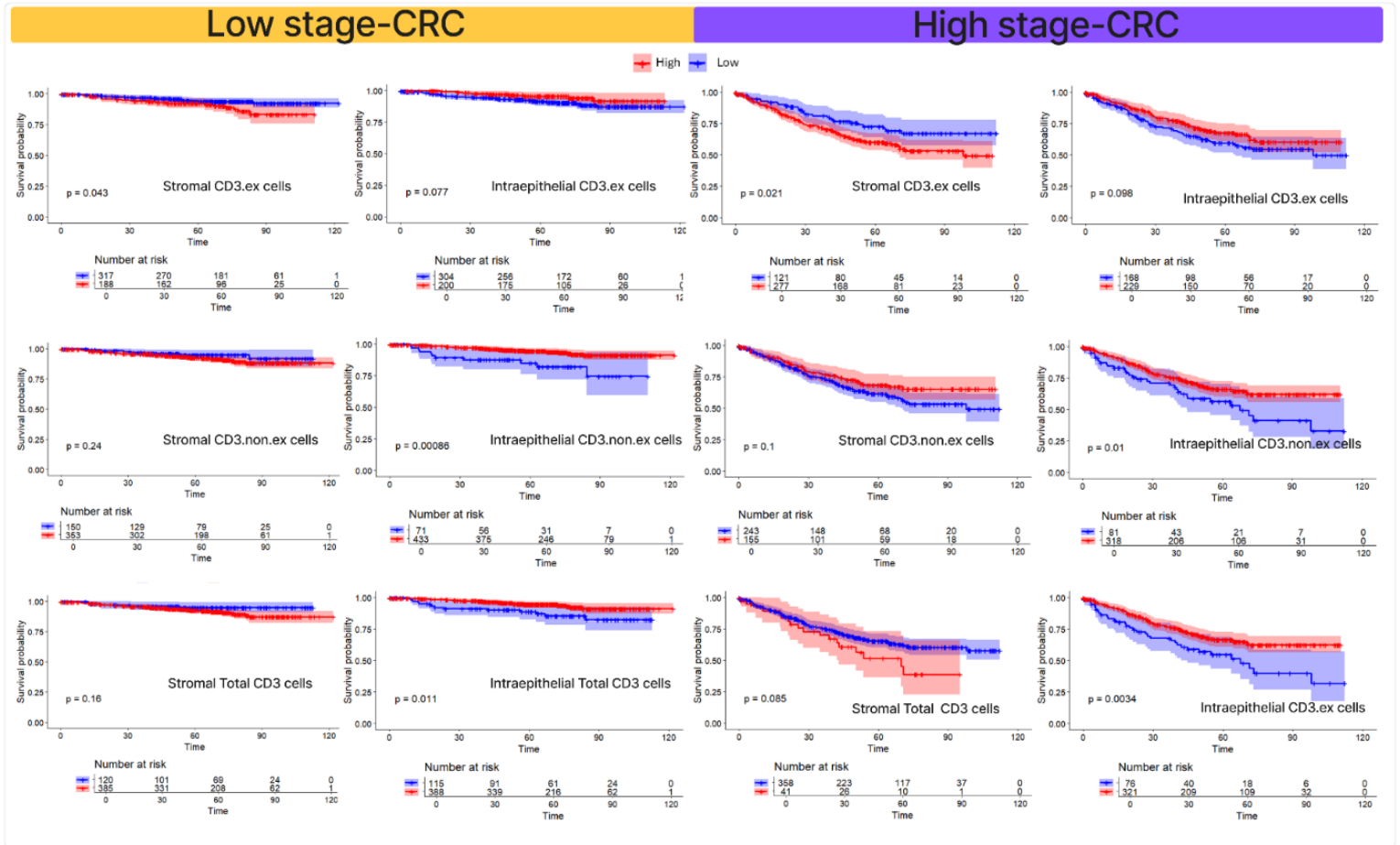


Figure 115. Kaplan-Meier survival curves for overall survival stratified by CD3+ cell density in stromal and intraepithelial compartments of patients with low stage (I, II) and high stage (III, IV) CRC showing there is no impact of tumour stage on CD3 prognostic impact between early and advanced stages.

Patients were stratified into "High" (red) and "Low" (blue) groups based on the density of CD3+ cells, either with or without expression of Immune checkpoint inhibitors. Optimal cut-off points for dichotomization were determined using X-tile software. CD3.ex was defined as CD3+ cells expressing LAG3, PD1, or TIM3. P-values were calculated using the log-rank test. The number of patients at risk at each time point (in months) is shown below each plot. Shaded areas represent 95% confidence intervals.

Low stage-CRC

High stage-CRC

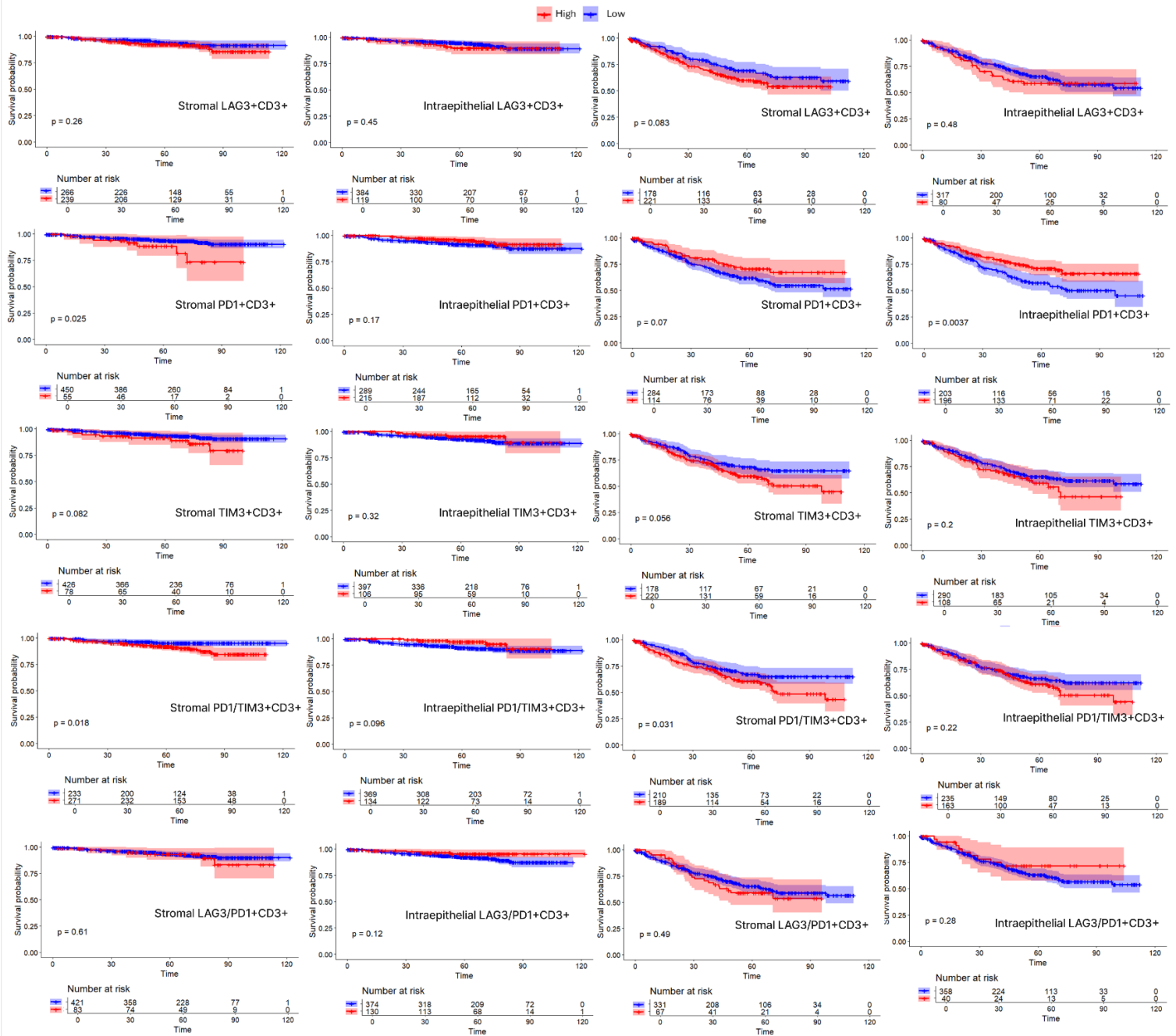


Figure 116. Kaplan-Meier survival curves for overall survival stratified by CD3+ subpopulation cell density in stromal and intraepithelial compartments of patients with low stage (I, II) and high stage (III, IV) CRC showing PD1 CD3 cells in early stage not in the advanced stage of CRC correlated with reduced survival.

Patients were stratified into "High" (red) and "Low" (blue) groups based on the density of CD3+ cells, either with or without expression of Immune checkpoint inhibitors. Optimal cut-off points for dichotomization were determined using

X-tile software. P-values were calculated using the log-rank test. The number of patients at risk at each time point (in months) is shown below each plot. Shaded areas represent 95% confidence intervals.

3.5.7.4 Prognostic impact of macrophages in different stages

IR- macrophage cell density in both low and high grades correlated with better survival, however, in the high stages, TIM3+ CD68+ and TIM3+PD1+ CD68 macrophage cell density correlated with worse overall survival compared to the low stages which there is no association between these two types cell densities and survival outcome (**Figure 117**).

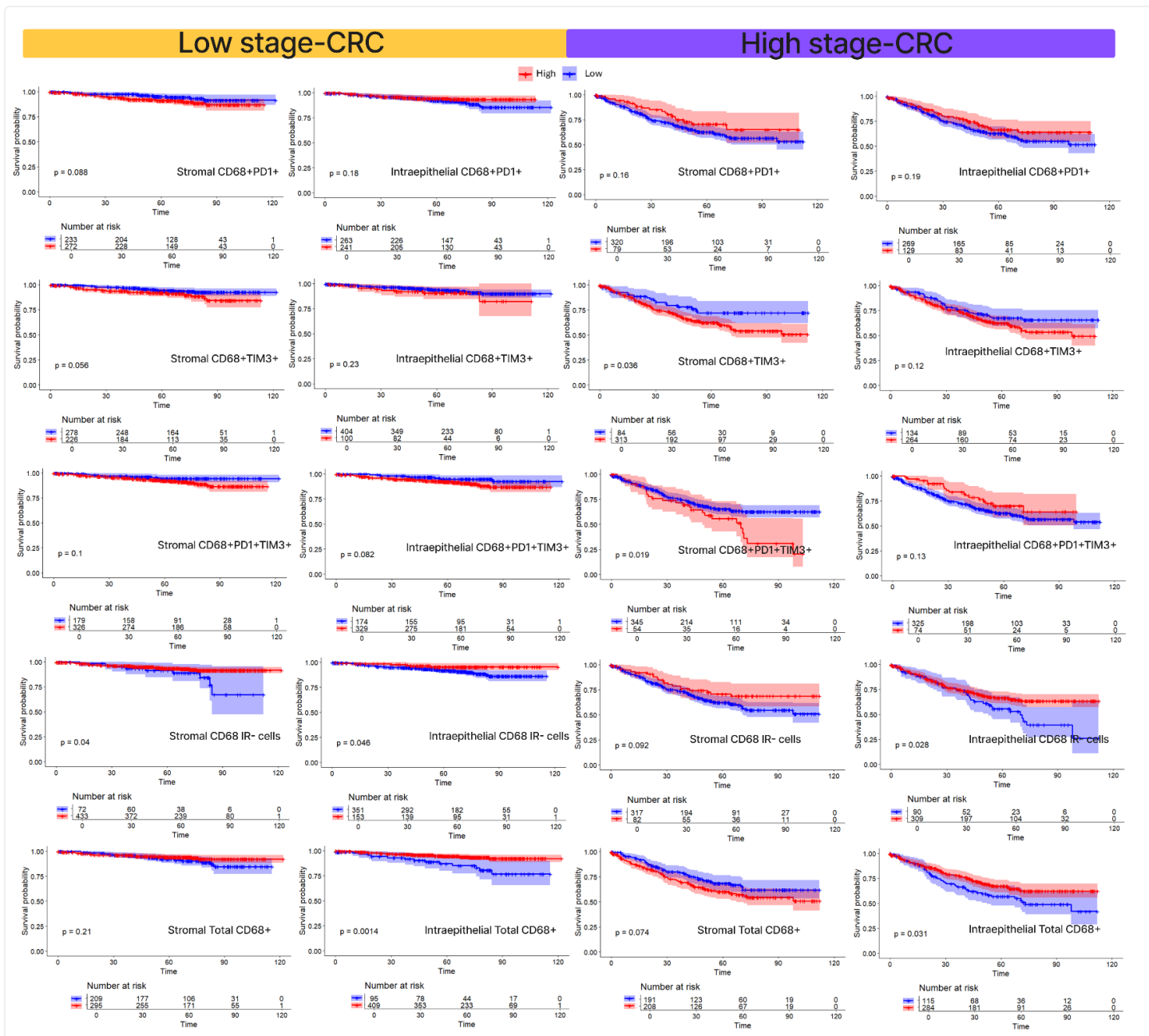


Figure 117. Kaplan-Meier survival curves for overall survival stratified by CD68+ cell density in stromal and intraepithelial compartments of patients with low stage (I, II), stage (III, IV) CRC showing that Tim3 macrophages in the advanced stages, but not early stages correlated with reduced survival.

Patients were stratified into "High" (red) and "Low" (blue) groups based on the density of CD68+ cells, either with or without expression of Immune checkpoint inhibitors. Optimal cut-off points for dichotomization were determined using

X-tile software. P-values were calculated using the log-rank test. The number of patients at risk at each time point (in months) is shown below each plot. Shaded areas represent 95% confidence intervals.

As a summary of the result of this section, while early-stage CRC generally shows a higher density of immune cells than advanced stages, a greater concentration of intraepithelial T cells is consistently linked to a more favorable prognosis in both early and advanced CRC. This positive association is, as anticipated, more pronounced in later stages of the disease.

3.5.8 Tumour sidedness impact on CD3+ and CD68+ cell densities and prognosis

Tumour sidedness in colorectal cancer (CRC) has emerged as a significant factor, correlating with distinct molecular profiles, therapeutic responses, and patient outcomes due to differences in embryological origin and biological characteristics. We therefore investigated whether T cell densities differed between right-sided and left-sided tumours.

3.5.8.1 T cell infiltration in left vs right sided CRC

Both stromal and intraepithelial CD3.ex density in right-sided CRC was higher than left-sided CRC. While stromal CD3.non.ex density in right-sided CRC was lower than left-sided CRC, intraepithelial CD3. non.ex densities was higher in right-sided CRC than left-sided CRC. However, both comparison were not statistically significant (**Figure 118**).

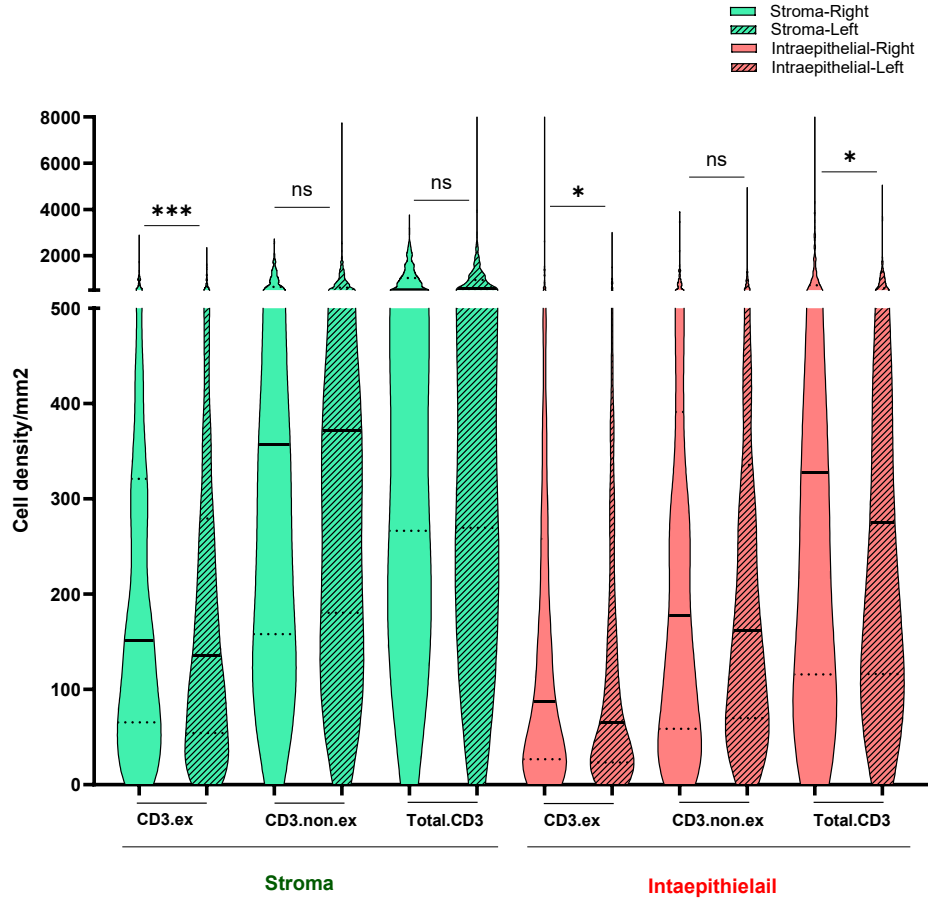


Figure 118. Comparison of CD3 cell densities in Stroma and intraepithelial Regions of Right and left sided CRC showing there is higher density of exhausted CD3 cells on the right sided compared to left sided.

Violin plots showing the distribution of CD3 cells densities (cells/mm²) in Right (plain graphs) and Left (hatched graphs) within stroma (green) and intraepithelial regions (Red). The horizontal black lines within the violins represent the median. Comparisons between groups within each region were made using Mann-Whitney U Test. Significance levels are indicated as follows: *p < 0.05, **p < 0.01, ***p < 0.001. Within the stroma, the following comparisons were made: CD3.ex Right vs. Left, p < 0.001 (***) ; CD3.non.ex.Right vs. Left p < 0.7 (ns); Total.CD3.Right vs. Left, p < 0.5 (ns). Within the intraepithelial compartment, the following comparisons were made: CD3.ex Right vs. Left, p < 0.02 (*); CD3.non.ex.Right vs. Left p < 0.15 (ns); Total.CD3.Right vs. Left, p < 0.02 (ns).

3.5.8.2 Macrophage density in different sides of the CRC

Based on the tumour sidedness, patients divided into two groups in which patients with tumour in ascending colon, cecum, and transverse colon categorized as Right-Sided CRC. On the other hand, patients with tumour in descending colon, rectum, and sigmoid colon

were classified as left-sided CRC. The cell density of desired phenotypes was shown in Figure 85. Data distribution was non-normal and as they are different unrelated patients, Mann Whitney U test was used to compare cell density between left and right-sided CRC. No statistical comparison was seen (**Figure 119**).

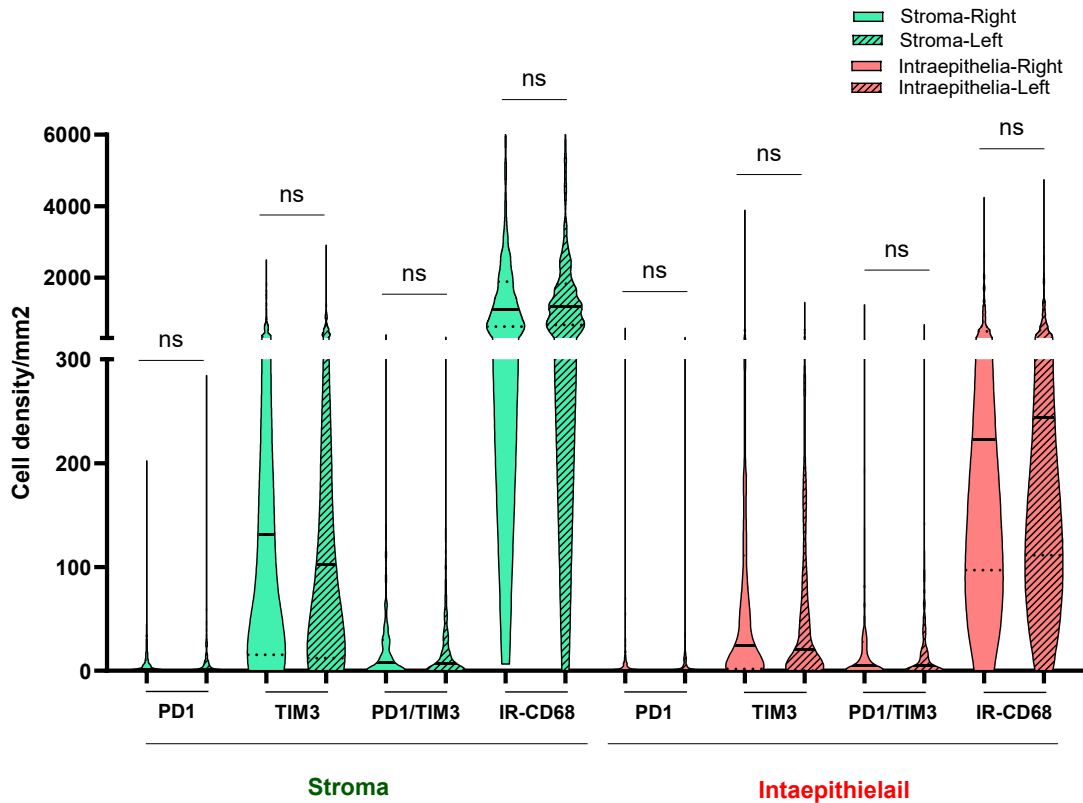


Figure 119. Comparison of macrophage cell densities in stromal and intraepithelial regions of right and left sided CRC showing there is no difference in macrophage density between right and left CRC.

Violin plots showing the distribution of Macrophage cells densities (cells/mm²) in Right sided CRC (plain graphs) and left sided CRC (hatched graphs) within stroma (green) and intraepithelial regions (Red). The horizontal black lines within the violins represent the median. Comparisons between groups within each region were made using Mann-Whitney U Test. Significance levels are indicated as follows: * $p < 0.05$, ** $p < 0.01$, *** $p < 0.001$. Within the stroma, the following comparisons were made: PD1 Right vs. left, $p < 0.97$ (ns); TIM3.Right vs. Left $p < 0.53$ (ns); PD1/TIM3.Right vs. Left, $p < 0.8$ (ns); IR.CD68.Right vs. Left, $p < 0.8$ (ns). Within the intraepithelial compartment, the following comparisons were made: PD1 Right vs. left, $p < 0.3$ (ns); TIM3.Right vs. Left $p < 0.4$ (ns); PD1/TIM3.Right vs. Left, $p < 0.7$ (ns); IR.CD68.Right vs. Left, $p < 0.3$ (ns).

3.5.8.3 Prognostic impact of T cells and macrophage in different sides

In patients with the right-sided CRC, all analysis showed significant better survival in both compartments with the exception of stromal CD3.ex.cell (Figure 108). However, in left sided CRC, only total intraepithelial CD3 significantly correlated with survival.

In patients with left-sided CRC, no significant associations between patient survival and any of the CD3+ cell subsets was seen. The exception was total CD3 in intraepithelial compartments which its higher cell density was statistically significant better survival compared to right side. Similar to right-sided CRC, low stromal density of TIM3+ macrophage related to better outcome ($p < 0.02$), **Figure 110-112**.

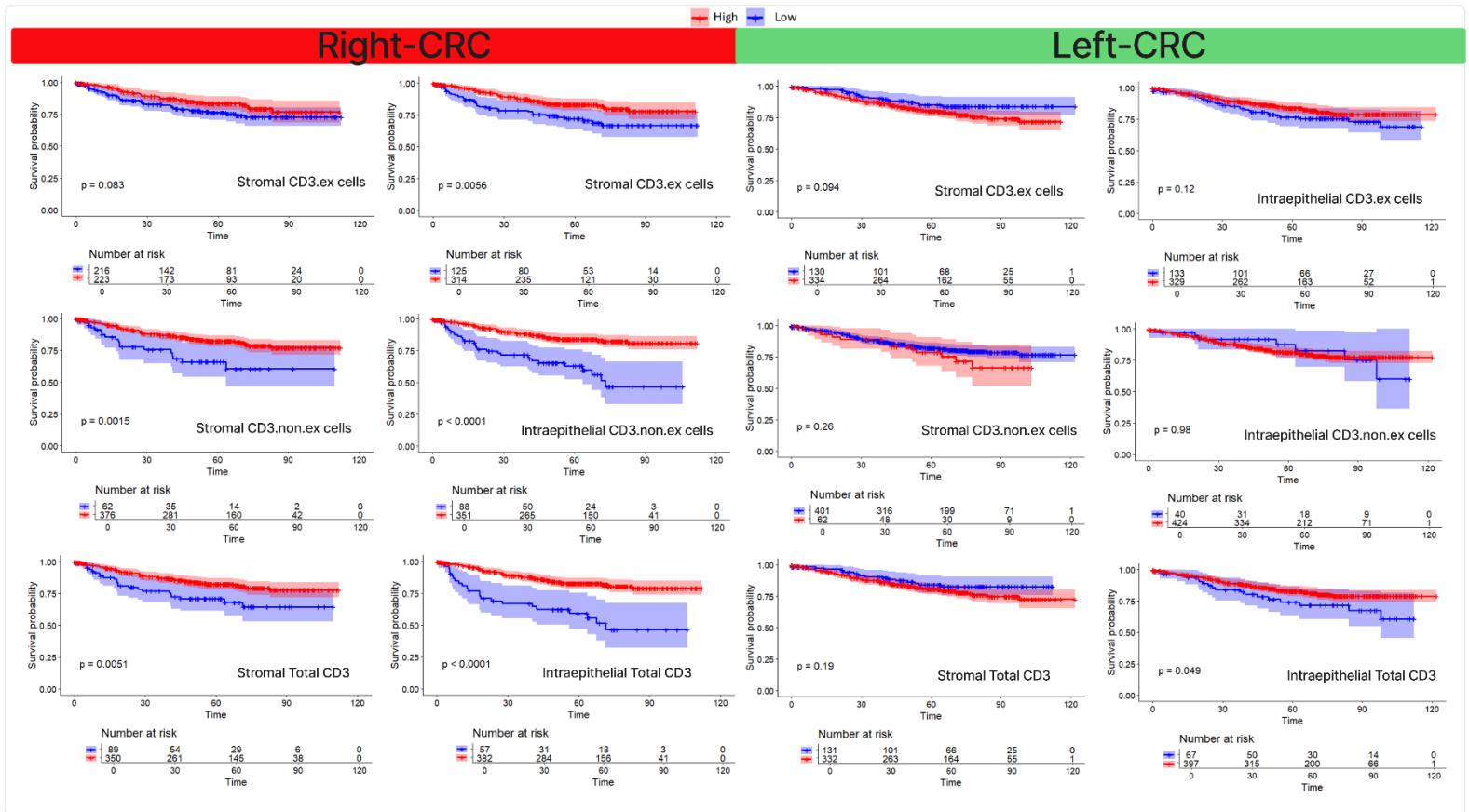


Figure 120. Kaplan-Meier survival curves for overall survival stratified by CD3+ cell density in stromal and intraepithelial compartments of patients with right and left-sided colorectal CRC showing right-CRC provides more prognostic information compared to left-CRC.

Patients were stratified into "High" (red) and "Low" (blue) groups based on the density of CD3+ cells, either with or without expression of exhaustion markers. CD3.non.ex was defined as CD3+ cells not expressing LAG3, PD1, or TIM3 and CD3.ex was defined as CD3+ cells expressing at least one of these markers. P-values were calculated using the log-rank test.

Right-CRC

Left-CRC

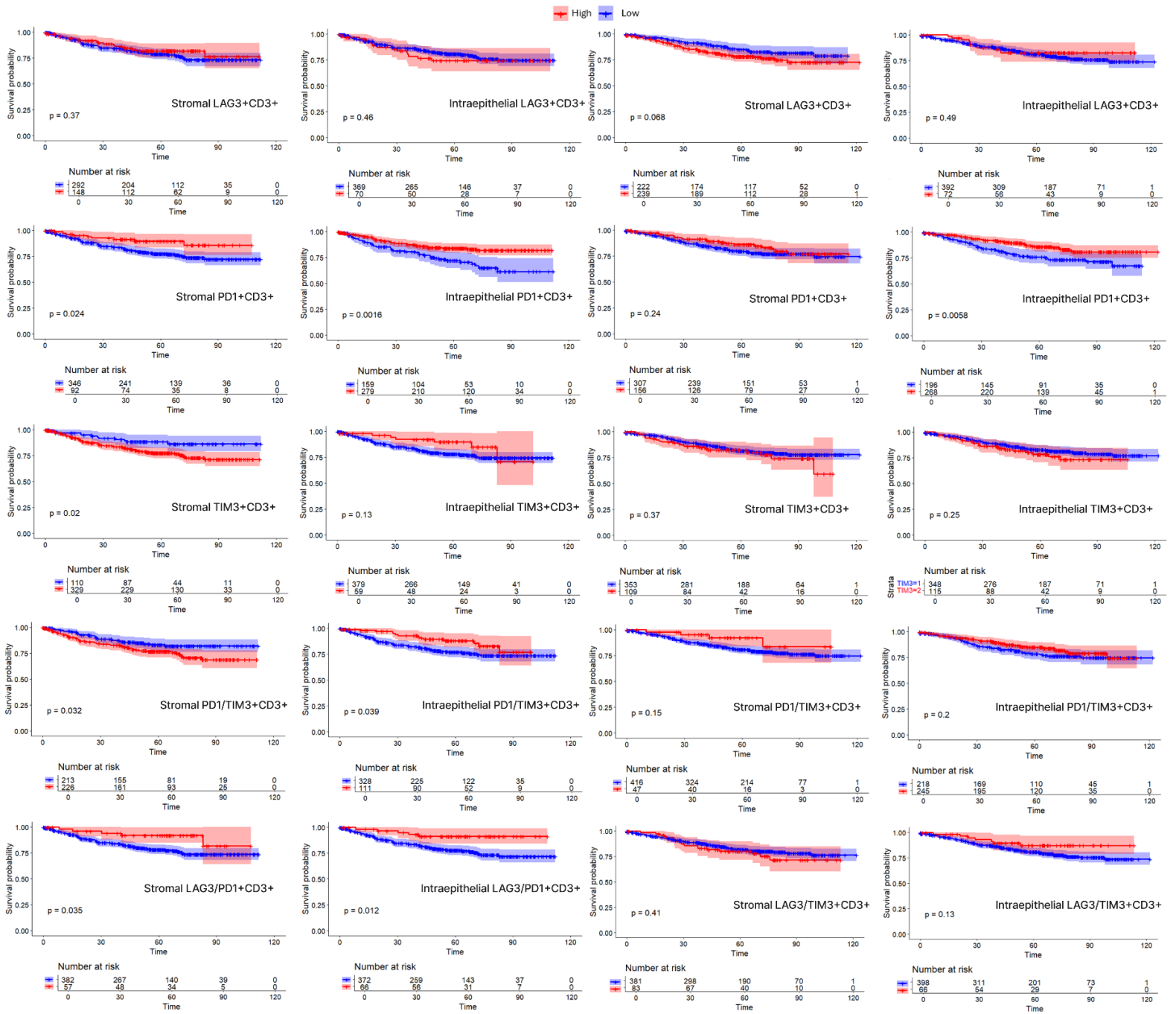


Figure 121. Kaplan-Meier survival curves for overall survival stratified by CD3.ex sub population density in stromal and intraepithelial compartments of patients with Right and Left -sided CRC showing right-CRC provides more prognostic information compared to left-CRC.

Patients were stratified into "High" (red) and "Low" (blue) groups based on the density of CD3+ cells, either with or without expression of exhaustion markers. Optimal cut-off points for dichotomization were determined using X-tile

software. P-values were calculated using the log-rank test. The number of patients at risk at each time point (in months) is shown below each plot. Shaded areas represent 95% confidence intervals.

Right-CRC

Left-CRC

High Low

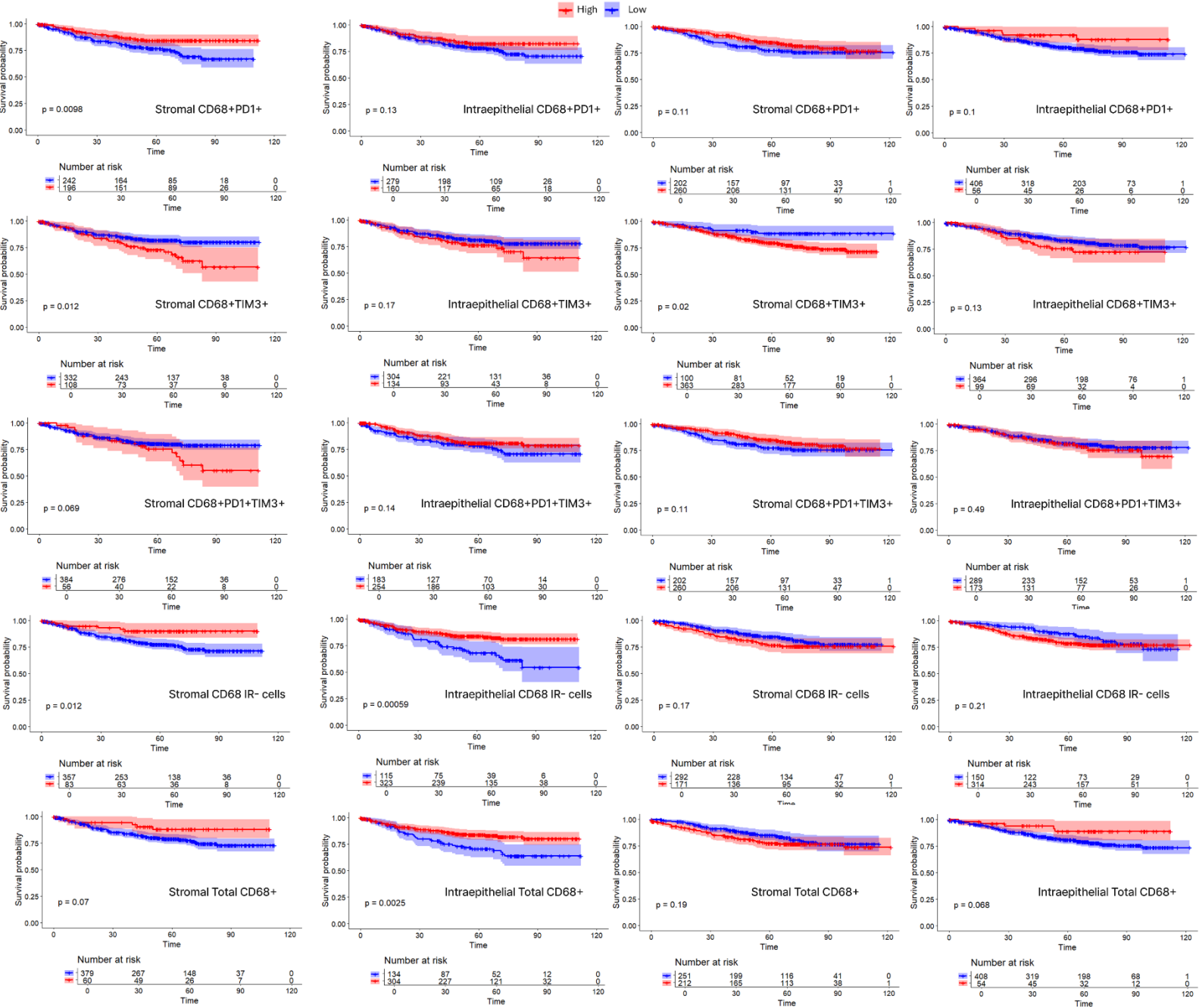


Figure 122. Kaplan-Meier survival curves for overall survival stratified by CD68+ cell density in stromal and intraepithelial compartments of patients with Right and Left-sided CRC showing right-CRC provides more prognostic information compared to left-CRC.

Patients were stratified into "High" (red) and "Low" (blue) groups based on the density of CD68+ cells, either with or without expression of Immune checkpoint inhibitors. Optimal cut-off points for dichotomization were determined using X-tile software. CD68.IR- was defined as CD68+ cells not expressing LAG3, PD1, or TIM3. P-values were calculated using the log-rank test. The number of patients at risk at each time point (in months) is shown below each plot. Shaded areas represent 95% confidence intervals.

To summarize, while the overall cell density does not generally differ between right and left-CRC, there is a significant prognostic difference, with right-sided CRC predominantly providing prognostic information.

3.5.9 MMR status and immune infiltration

Microsatellite Instability (MMR) status is a critical biomarker in colorectal cancer, strongly influencing tumour biology and often associated with distinct immune responses and differential outcomes to therapies. Given its established role in shaping the tumour microenvironment, we investigated how T cell densities might vary across different MMR statuses.

3.5.9.1 T cell density and MMR status

Mann-Whitney U test showed a significant higher cell density of CD3.ex, CD3.non.ex, and total CD3 in intraepithelial compartment of MSI-CRC compared to MSS-CRC. However, in stromal compartment, only CD3.ex cell density in MSI-CRC was statistically higher over MSS-CRC, **Figure 123**.

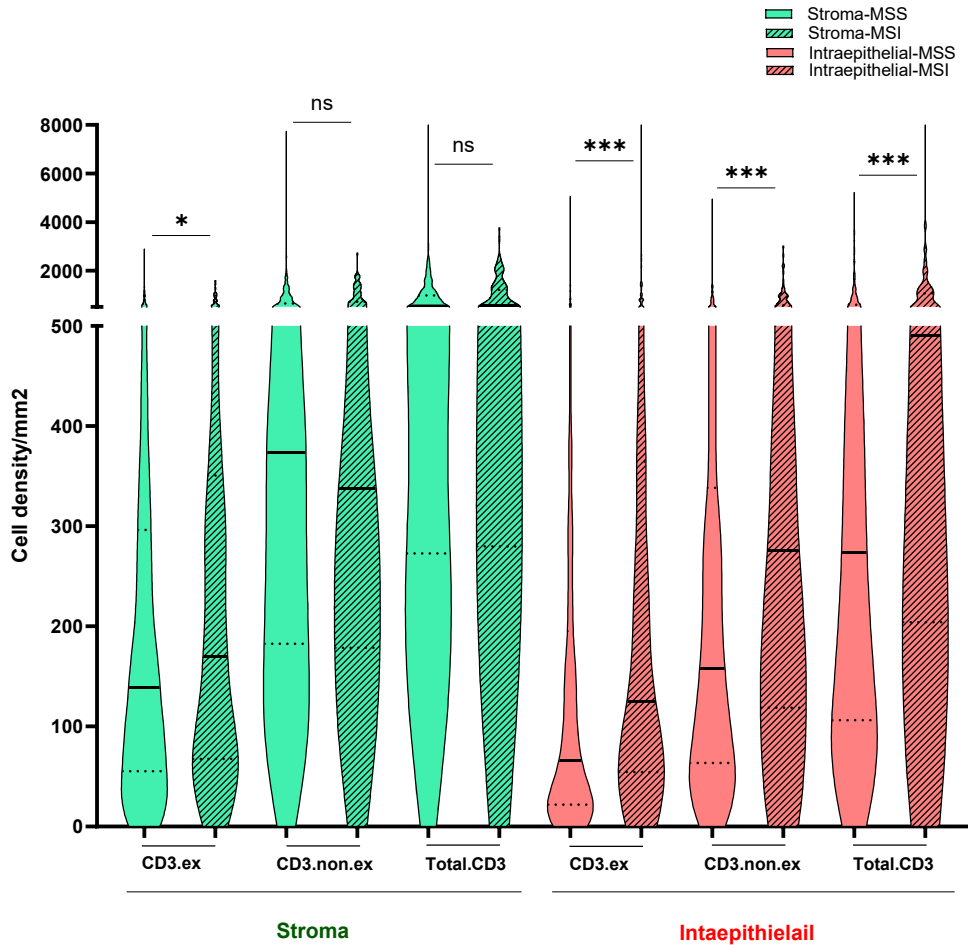


Figure 123. Comparison of CD3 cell densities in stromal and intraepithelial regions of MSS/MSI CRC showing MSI-CRC has significant higher CD3 density compared to MSS-CRC .

Violin plots showing the distribution of CD3 cells densities (cells/mm²) in MSS-CRC (plain graphs) and MSI-CRC (hatched graphs) within stroma (green) and intraepithelial regions (Red). The horizontal black lines within the violins represent the median. Comparisons between groups within each region were made using Mann-Whitney U Test. Significance levels are indicated as follows: *p < 0.05, **p < 0.01, ***p < 0.001. Within the stroma, the following comparisons were made: CD3.ex MSS vs. MSI, p < 0.03 (*); CD3.non.ex.MSS vs. MSI p < 0.6 (ns); Total.CD3.MSS vs. MSI, p < 0.3 (ns). Within the intraepithelial compartment, the following comparisons were made: CD3.ex MSS vs. MSI, p < 0.001 (***); CD3.non.ex.MSS vs. MSI p < 0.001 (***); Total.CD3.MSS vs. MSI, p < 0.001 (***).

3.5.9.2 Macrophage density and MMR status

The cell density of desired phenotypes was shown in Figure 91. Data distribution was non-normal and as they are different unrelated patients, Mann Whitney U test was used to compare cell density between left and right-sided CRC. A significant higher density of intraepithelial IR- macrophage in MSI-CRC compared to MSS-CRC was seen (P< 0.05)

(Figure 124). Stromal IR- macrophage density in MSI-CRC was also higher compared to MSS-CRC, but it was not significant.

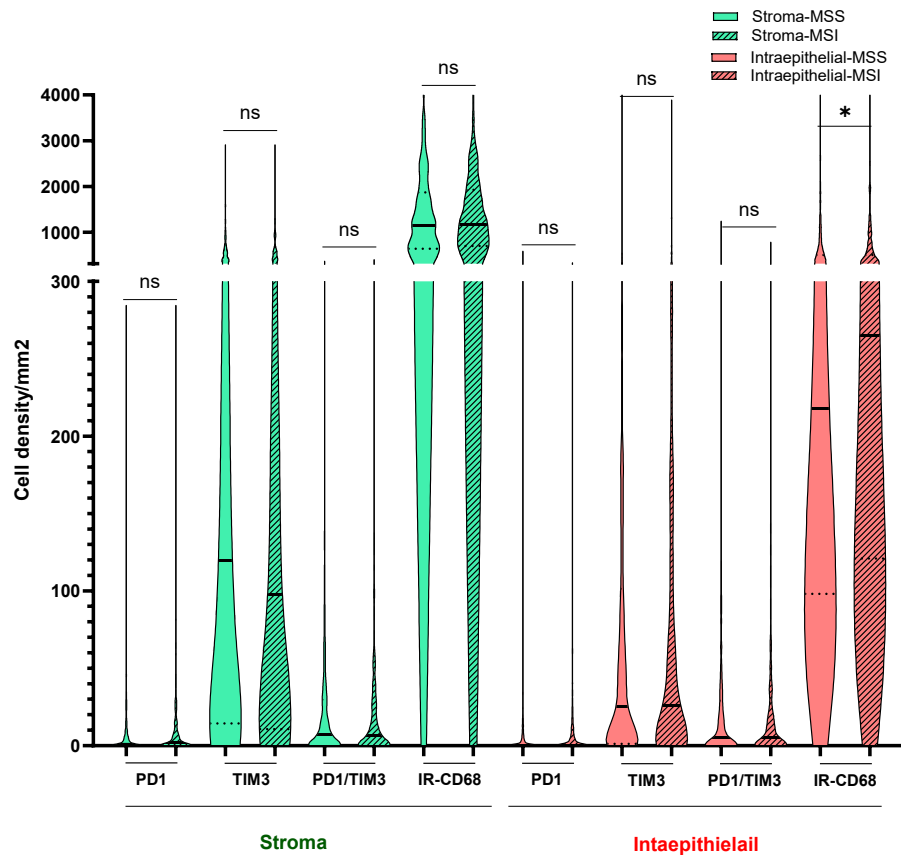


Figure 124. Comparison of macrophage densities in stromal and intraepithelial regions of MSS/MSI CRC showing there is almost no difference in the density of macrophages between MSS and MSI-CRC.

Violin plots showing the distribution of Macrophage cells densities (cells/mm²) in MSS-CRC (plain graphs) and MSI-CRC (hatched graphs) within stroma (green) and intraepithelial regions (Red). The horizontal black lines within the violins represent the median. Comparisons between groups within each region were made using Mann-Whitney U Test. Significance levels are indicated as follows: *p < 0.05, **p < 0.01, ***p < 0.001. Within the stroma, the following comparisons were made: PD1 MSS vs. MSI, p < 0.09 (ns); TIM3.MSS vs. MSI p < 0.2 (ns); PD1/TIM3.MSS vs. MSI, p < 0.2 (ns); IR.CD68.MSS vs. MSI, p < 0.3 (ns). Within the intraepithelial compartment, the following comparisons were made: PD1 MSS vs. MSI, p < 0.1 (ns); TIM3.MSS vs. MSI p < 0.8 (ns); PD1/TIM3.MSS vs. MSI, p < 0.8 (ns); IR.CD68.MSS vs. MSI, p < 0.05 (*).

3.5.9.3 Prognostic value of T cells and macrophages with MMR status

In patients with **MSI and MSS status**, high intraepithelial density of T cells, regardless of the exhaustion marker status, associated with survival (**Figure 125**). However, total stromal T cells in MSS correlated with poor survival.

PD1+ T cells in both compartments of MSS, and only in the stromal compartment of MSI correlated with survival. Stromal TIM3+CD3 cells and TIM3+PD1+ CD3 cells in the MSS correlated with poor survival. Finally intraepithelial LAG3+PD1+ CD3 in the MSS had a good prognosis. (Figure 126).

Macrophage density did not have prognostic value in MSI. However, in MSS, intraepithelial infiltration of PD1+CD68 correlated with improved survival, while both stromal and intraepithelial TIM3+CD68 cells and stromal TIM3+PD1+ CD68 correlated with poor survival. In addition, intraepithelial IR- macrophages and total intraepithelial macrophages in the MSS-CRC showed improved survival, Figure 127.

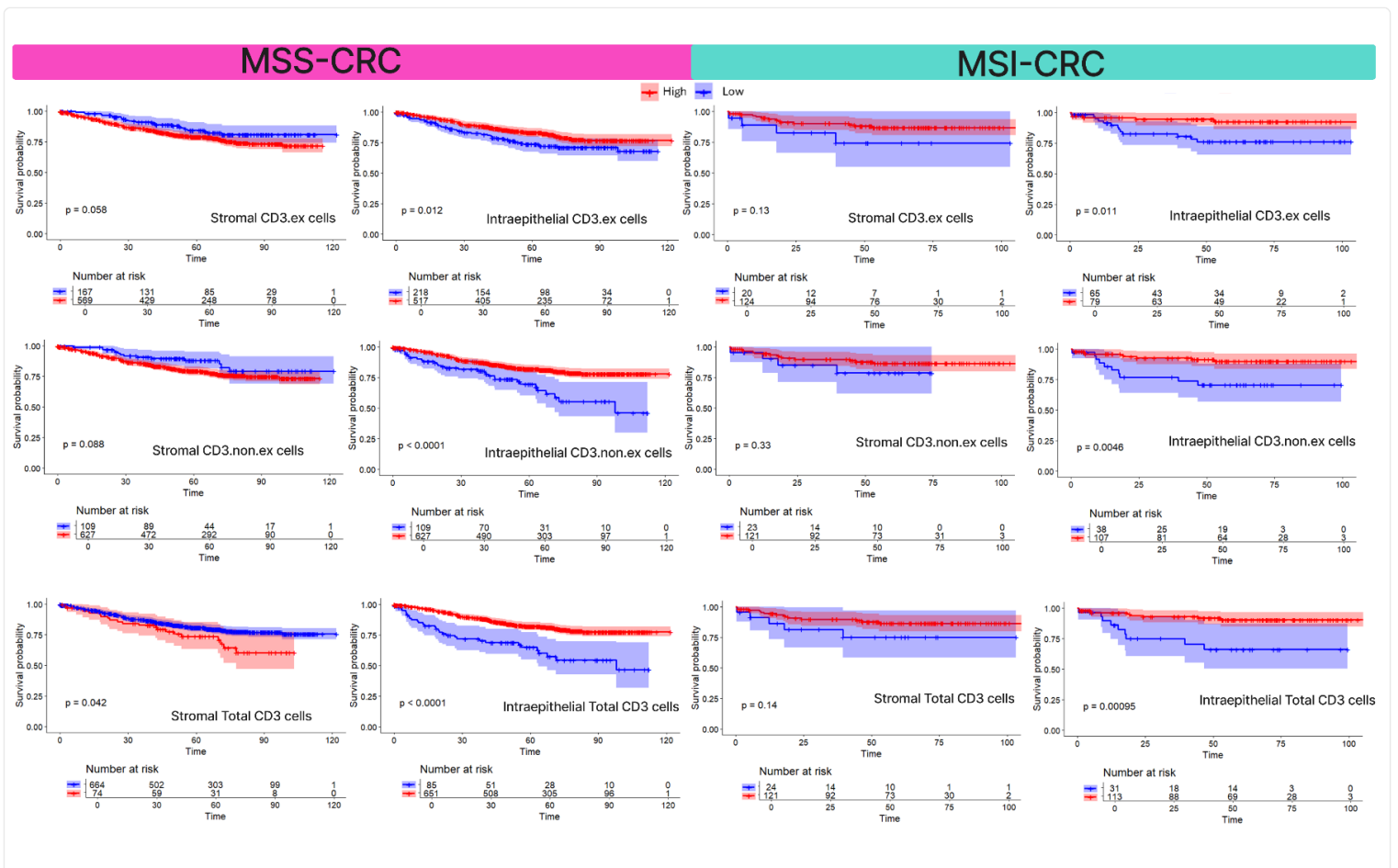


Figure 125. Kaplan-Meier survival curves for overall survival stratified by CD3+ cell density in stromal and intraepithelial compartments of patients with MSS and MSI CRC showing exhausted CD3 cells in MSS -CRC but not MSI-CRC correlated with reduced survival.

Patients were stratified into "High" (red) and "Low" (blue) groups based on the density of CD3+ cells, either with or without expression of Immune checkpoint inhibitors. Optimal cut-off points for dichotomization were determined using

X-tile software. CD3.ex was defined as CD3+ cells expressing LAG3, PD1, or TIM3. P-values were calculated using the log-rank test. The number of patients at risk at each time point (in months) is shown below each plot. Shaded areas represent 95% confidence intervals.

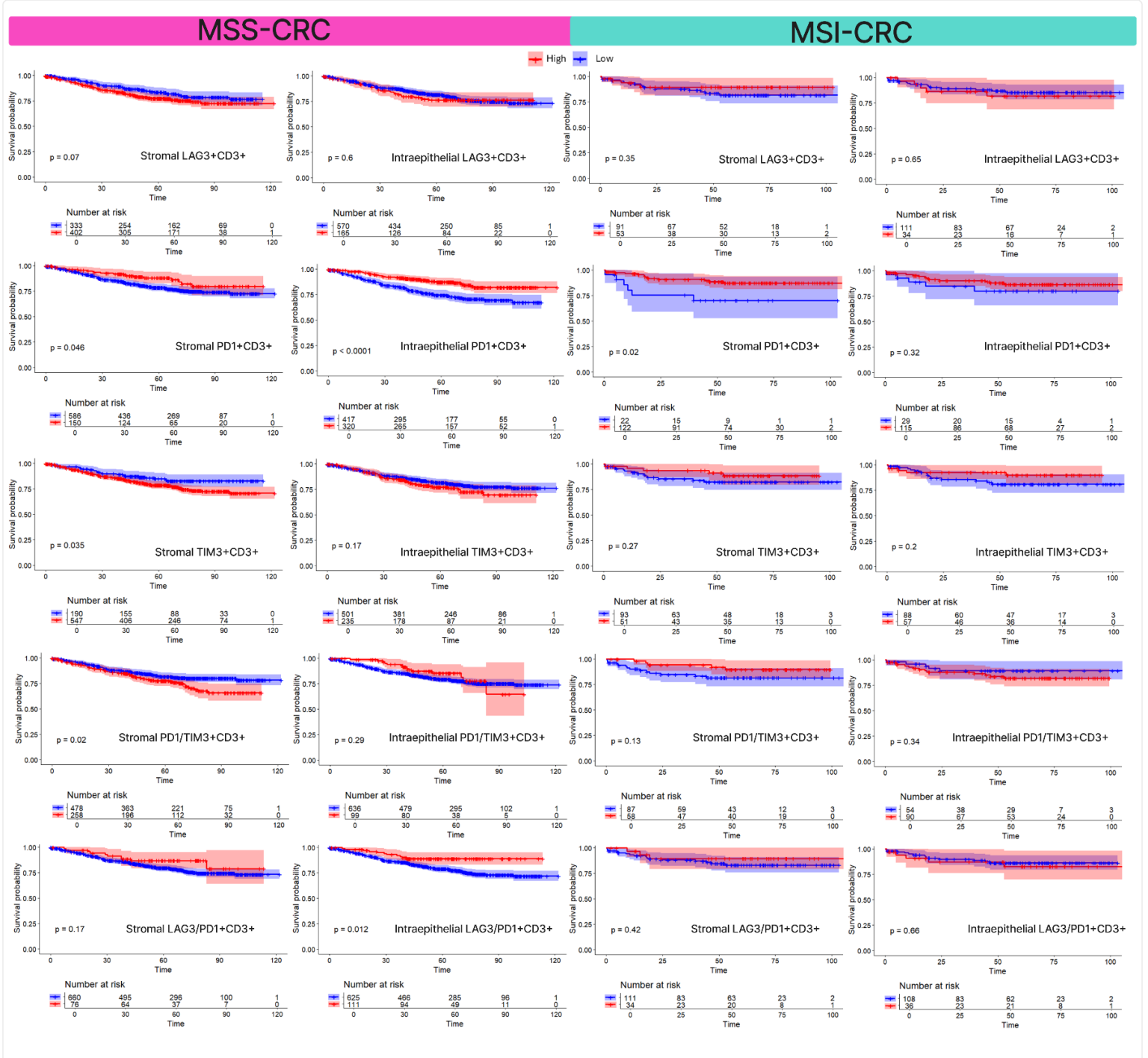


Figure 126. Kaplan-Meier survival curves for overall survival stratified by CD3+ subpopulation cell density in stromal and intraepithelial compartments of patients with MSS and MSI CRC showing Tim3+ T cells in MSS-CRC, but not in MSI-CRC correlated with reduced survival.

Patients were stratified into "High" (red) and "Low" (blue) groups based on the density of CD3+ cells, either with or without expression of Immune checkpoint inhibitors. CD3.ex was defined as CD3+ cells expressing LAG3, PD1, or TIM3. P-values were calculated using the log-rank test.

MSS-CRC

MSI-CRC

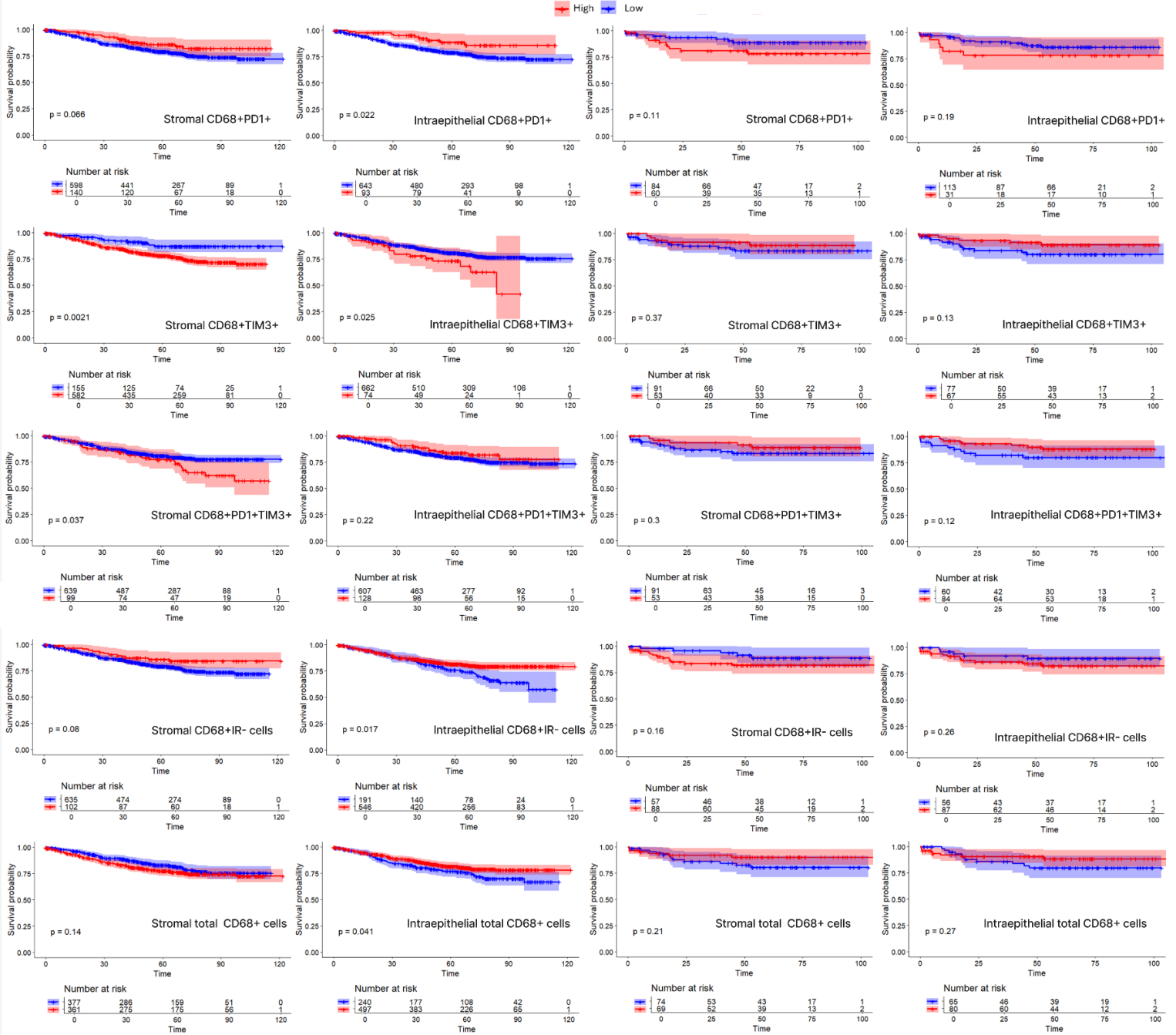


Figure 127. Kaplan-Meier survival curves for overall survival stratified by CD68+ cell density in stromal and intraepithelial compartments of patients with MSS and MSI-CRC showing MSS-CRC provide more prognostic impact compared to MSI-CRC.

Patients were stratified into "High" (red) and "Low" (blue) groups based on the density of CD68+ cells, either with or without expression of Immune checkpoint inhibitors. P-values were calculated using the log-rank test. The number of patients at risk at each time point (in months) is shown below each plot.

As a brief overview, as anticipated, MSI-CRC exhibits a higher density of immune cells and both MSS and MSI-CRC provides prognostic information.

Chapter5: Discussion

The role of ICI in the treatment of CRC has expanded considerably in recent years. Many studies and clinical trials have evaluated their efficacy as monotherapy and in combination regimen, particularly in the context of personalized therapies. However, in contrast to some other cancers, ICIs have demonstrated limited efficacy for CRC [192]. This is largely attributed to the heterogeneous TME, which varies markedly in terms of anatomy, genetics, epigenetics, immune and non-immune cell infiltration, and cancer stage [193]. This study focuses on characterizing the heterogeneity of the CRC TME with respect to immune regulator (IR) cell density, including LAG3, PD1, and TIM3. It aims to comprehensively analyze the density patterns of aforementioned IRs and their subsequent survival impact in relation to various clinical and pathological factors, including TNM stage, MMR status, tumour sidedness, and the location of immune cells within the TME to provide a more detailed description of the density of the IR and their correlation with different factors. For better understanding of the complexity of the current project, we plot the information of univariable survival analysis on a table for both CD3 and CD68 positive cells, **Figure 128**, **Figure 129**. Furthermore, the significant difference in the densities represented in **Figure 130**.

			LAG3	PD1	TIM3	LAG3 PD1	TIM3 PD1	ex	non. ex	Total CD3
Average of tumour related cores		Stromal		*	*		*		*	
		Intraepithelial		***				**	***	***
Location	Adjacent Normal	Stromal	**					*	*	**
		Intraepithelial						*	*	*
	Invasive margin	Stromal		*				*	****	**
		Intraepithelial		**	*	**	*	***	****	****
	Tumour center	Stromal		*	*		*		*	
		Intraepithelial		**				***	****	****
	Luminal Side	Stromal					*			
		Intraepithelial		**				*	***	*
TNM stage	Low stages (I,II)	Stromal		*			*	*		
		Intraepithelial							***	*
	High stages (III, IV)	Stromal					*	*		
		Intraepithelial		**					*	**
MMR function	MSS	Stromal		*	*		*			*
		Intraepithelial		****		**		*	****	****
	MSI	Stromal		*						
		Intraepithelial						*	**	***
Sideness	Right-CRC	Stromal		*	*	*	*		**	**
		Intraepithelial		**		**	*	**	****	****
	Left-CRC	Stromal								
		Intraepithelial		*						*

Improved survival

No

Reduced survival

Figure 128. Summary of associations between CD3+ subset densities and survival in colorectal cancer, stratified by location, TNM stage, MMR status, sidedness, and compartment.

The table summarizes the results of Kaplan-Meier analyses and log-rank tests. Green cells indicate a statistically significant association ($p < 0.05$) between higher cell density and improved survival. Red cells indicate a statistically significant association ($p < 0.05$) between higher cell density and reduced survival. Grey cells indicate no statistically significant association. Asterisks denote the level of statistical significance: * ($p < 0.05$), ** ($p < 0.01$), *** ($p < 0.001$), **** ($P < 0.0001$). CD3 subsets were defined as follows: PD1+CD3+, TIM3+ CD3+, TIM3+/PD1+CD3+, CD3.ex (sum of CD3 cells with exhaustion markers) CD3.non.ex (CD3+ cells without exhaustion markers, Total CD3+(All exhausted and non-exhausted CD3 cells). Abbreviations: AN (adjacent normal), IM (invasive margin), CT (center of tumour), LS (luminal side), MSS (microsatellite stable), MSI (microsatellite instable), R-CRC (right-sided colorectal cancer), L-CRC (left-sided colorectal cancer).

			PD1	TIM3	TIM3 PD1	IR-	Total CD68
Average of tumour related cores		Stromal		**	*		
		Intraepithelial					
Location	Adjacent Normal	Stromal					**
		Intraepithelial		*			
	Invasive margin	Stromal	**		*		
		Intraepithelial			*	*	**
	Tumour center	Stromal		**			
		Intraepithelial					
	Luminal Side	Stromal			*		
		Intraepithelial					
TNM stage	Low stages (I,II)	Stromal				*	
		Intraepithelial				*	***
	High stages (III, IV)	Stromal		*	*		
		Intraepithelial				*	*
MMR function	MSS	Stromal		**	*		
		Intraepithelial	*	*		*	*
	MSI	Stromal					
		Intraepithelial					
Sidedness	Right-CRC	Stromal	**	*		*	
		Intraepithelial				***	**
	Left-CRC	Stromal		*			
		Intraepithelial					

Improved survival

No

Reduced survival

Figure 129. Summary of associations between macrophage subset densities and survival in colorectal cancer, stratified by location, TNM stage, MMR status, sidedness, and compartment.

The table summarizes the results of Kaplan-Meier analyses and log-rank tests. Green cells indicate a statistically significant association ($p < 0.05$) between higher cell density and improved survival. Red cells indicate a statistically significant association ($p < 0.05$) between higher cell density and reduced survival. Grey cells indicate no statistically significant association. Asterisks denote the level of statistical significance: * ($p < 0.05$), ** ($p < 0.01$), *** ($p < 0.001$), **** ($p < 0.0001$). Macrophage subsets were defined as follows: PD1+CD68+, TIM3+ CD68+, TIM3+/PD1+CD68+, IR- (CD68+ macrophages without IR markers), Total CD68+(All IR+ and IR- macrophages). Abbreviations: AN (adjacent

normal), IM (invasive margin), CT (center of tumour), LS (luminal side), MSS (microsatellite stable), MSI (microsatellite instable), R-CRC (right-sided colorectal cancer), L-CRC (left-sided colorectal cancer).



Figure 130. Significant Differences in Cell Density of CD3+ Cells and Macrophages in Colorectal Cancer.

The figure summarizes significant differences ($p < 0.05$) in cell density within the intraepithelial (T) and stromal (S) compartments of colorectal cancer. The upper pairs illustrate comparisons for CD3+ T cells, while the lower pairs show comparisons for macrophages. Light colors indicate lower significant densities, and deep colors represent higher significant densities. Comparisons are shown between: MSS vs. MSI: Microsatellite Stable versus Microsatellite Instability colorectal cancer, Lower vs. Higher Stages: Stage I/II versus Stage III/IV colorectal cancer, R vs. L: Right-sided versus Left-sided colorectal cancer, AN vs. T: Adjacent Normal tissue versus Tumour-related tissue. IR: Immune Regulator.

We developed a multiplex panel to evaluate the expression of three key immune checkpoints on T cells and macrophage in a cohort of 1,000 CRC patients. The optimized panel showed two distinct patterns for LAG3: a cytoplasmic intracellular dotted form resembling vesicles and a membranous pattern, referring the biogenesis of LAG3. For PD1 and TIM3, we observed both cytoplasmic and membranous patterns in immune cells, whereas CD68 and pan CK primarily exhibited a cytoplasmic pattern, and CD3 displayed a membranous pattern. All Opal dyes had limited background interference, and the signal intensity fell within the acceptable range suggested by Akoya, indicating a reliable assessment without the common multiplex errors associated with cross-talk, carry-over, and bleed-through.

Numerous studies have investigated T cells and macrophage in CRC. However, many of these focus on general aspects of the TME, such as overall infiltration without considering cellular location (stroma vs. epithelium) or functional status (e.g., exhaustion markers). Furthermore, key confounding factors, such as MMR status, TNM stage, tumour sidedness, and section location are not always adequately addressed. In our large cohort study, we comprehensively assessed the density and prognostic impact of distinct T cell and macrophage populations, accounting for tumour location, exhaustion status, MMR status, TNM stage, and tumour sidedness. The current multi-faceted approach allows for a more nuanced understanding of the immune response in CRC and may clarify discrepancies in the data reported in previous literature.

4.1 Intraepithelial CD3 is a strong prognostic factor regarding all variables in CRC tumour microenvironment.

To the best of our knowledge, this study is one of the largest exploring T cell and macrophage distribution and exhaustion in CRC. Spatial analysis revealed 5 main regions in the TME based on the distribution of macrophages, T cells, other cells, and epithelial cells in four different regions of the tumour.

Approximately one percent of T cells in CRC are NKT cells [194]. CD3 is a pan-T cell marker, expressed on all T cell subsets and throughout T cell development. It is an essential component of the T cell receptor (TCR) complex, responsible for transducing activation signals. While infiltration of cytotoxic T cells (CTLs) and T helper 1 (Th1) cells associates with improved survival in many cancers, including CRC, other T cell subsets, such as Th2, Th17, and regulatory T cells (Tregs) commonly associate with unfavorable outcomes [90, 195]. Immunoscore considers both CD3 and CD8 cells to stratify patient

prognosis. However, even with this refined consideration, CD3 cells may express IRs, which theoretically their inhibitory signals transmission have been demonstrated and subsequent exhausted T cells unable to suppress tumour growth [196]. The current project studied two main T cell subsets, namely with and without exhaustion markers.

The first data on classifying CRC patients based on T cell density comes from Jass. et .al study in which patient categorized into four classifications from 0 density to high density [197]. Jakubowska and coworkers showed that 80 percent of CRC patients had T cell infiltration in tumour regions, including invasive margin and center of the tumour. Several studies support Immunoscore showing a higher density of CD3 cells correlates with survival and vice versa [48, 198].

The stromal and intraepithelial compartments exhibit different T cell density. A key difference is that intraepithelial T cells are activated directly via tumour cells presenting tumour antigen. However, stromal T cells are mainly triggered by antigen presenting cells including macrophage [199]. One study showed that a decrease in stromal T cells correlates with angiogenesis, lymph node involvement, and metastasis suggesting this is a crucial part of TME [198]. Our results were consistent with this data and showed higher cell density of stromal T cells compared to intraepithelial ones. Despite these findings, data on the prognostic values of the stromal T cells remains controversial and indeed some studies showed higher stromal T infiltration is an unfavorable prognostic factor for CRC [200-202], others improved survival [203] or no association [198]. Our results showed no survival association with stromal T-cells in the tumour area. However, we found that elevated intraepithelial density-cells predicted survival. This remained significant in both univariable analyses and multivariable Cox regression model adjusting for confounding variables and therefore agrees with Immunoscore. The higher density of exhausted and non-exhausted T cells were found in the stromal compartment compared to intraepithelial, alongside a positive correlation between total and exhausted CD3+ T cell densities in both compartments, suggest that T cell infiltration is associated with a higher proportion of cells expressing exhaustion markers.

Our finding that stromal exhausted T cells associate with poor survival aligns with the established role of exhaustion markers in limiting T cell effector function and promoting tumour progression. That detrimental effect was restricted to the stroma, and not the intraepithelial compartment, suggests that the stromal microenvironment may be more conducive to T cell exhaustion and possibly reflecting higher levels of immunosuppressive factors [204]. Intraepithelial exhausted T cells may retain some degree of anti-tumour activity due to closer proximity to tumour antigens and potentially greater access to co-stimulatory signals.

Previous research has shown that the prognostic significance of various phenotypes of exhausted T cells differs in CRC [205-207]. T cells in this project exhibited the lowest LAG3 expression, with higher levels of PD1 and TIM3, and a notable proportion co-expressing PD1 and TIM3. These phenotypes are consistent with published findings [138]. Increased expression of PD1 associated with improved survival is in agreement with a large meta-analysis [208]. While this association might seem to contradict the known inhibitory function of PD1, it likely reflects a greater overall infiltration of T cells within TME. Furthermore, PD1 expression increases upon T cell activation suggesting that, in this context, the presence of PD1+ cells indicates an ongoing, albeit potentially restrained, anti-tumour immune response [209]. It is important to note that PD1, like LAG3 and TIM3, can be stored in cytoplasmic vesicles that lack functionality. Additionally, mIHC cannot differentiate between active functional membrane PD1 and cytoplasmic PD1[210]. On the other hand, higher stromal TIM3 association with diminished survival, is a consistent finding with previous studies in colorectal cancer.[211]. In contrast, the role of LAG3 in CRC prognosis is more complex. While some studies have linked LAG3 expression on CD3+ cells to decreased survival [212], others have reported an association with improved overall survival [213]. Our study found no significant correlation between LAG3 expression and patient survival.

4.2 CD68 marker in the right sided CRC of all stages can be prognostic factor

A number of parameters affect the phenotype and function of macrophages in the context of heterogenous CRC microenvironment. Macrophage plasticity in response to the environmental stimuli significantly affects their anti or pro-cancer role [214]. M1-like macrophages through phagocytosis and presenting Ag to lymphocytes play an important role in anti -tumour response and correlate with improved survival while the tumour promoting functions of M2-like macrophages links to poor survival [215]. While TAM in CRC were previously thought to exhibit primarily an M2-like phenotype, it is now widely accepted that the complex TME elicits a mixed TAM phenotype [216]. CD68 is involved in phagocytosis of apoptotic cells but expressed on both M1 and M2 macrophages exhibiting markedly different functions. Compatible with this information, overall stromal and intraepithelial macrophage density did not correlate with patient survival in our data. A large cohort study of over 4000 patients also found no association between overall macrophage density and survival in CRC; however, they observed significantly improved survival in patients with higher M1 macrophage infiltration and worse survival with higher M2 macrophage infiltration[217].

Previous literature showed elevated stromal macrophages than intraepithelial, in line with our findings [218]. Nowak et al. found that M1-like macrophages are more prevalent in the stroma, while M2-like macrophages are more abundant in the intraepithelial compartment of tumours. Based on this, we can hypothesize that stromal macrophages, initially associated with better survival, might migrate into the intraepithelial compartment and transition to an M2-like phenotype, thus contributing to a worse prognosis.[217]. A weaker correlation between IR phenotype in the stroma compared to intraepithelial macrophages suggested that M2 macrophages likely express IR in greater amounts than M1 macrophages. Precise evaluating of IR markers on macrophages revealed that TIM3 in macrophages expressed more than PD1, a finding reported in gastric cancer [138] . In our study, PD1 expression on macrophages was frequently accompanied by TIM3 expression. The negative relationship with survival associated with TIM3+ and TIM3+PD1+ macrophages suggests these may exhibit an M2-like phenotype. This interpretation aligns with previous publications indicating that PD-1 expression on macrophages correlate with reduced survival and M2 polarization, characterized by decreased secretion of IL-6 and IL-12 [219, 220]. Furthermore, anti-PD-1 therapy promotes a shift from M2 to M1 behaviour [221]. PD-1 signaling in macrophages is also linked to reduced phagocytic activity [139]. and a recent study also showed that TIM3 expression correlated with M2 polarization [222]. Interestingly, while prior work suggests a negative role for PD-1+ macrophages, our analysis, stratifying macrophages into those expressing PD-1 alone versus those co-expressing PD-1 and TIM-3, revealed that PD-1 expression alone did not significantly correlate with adverse outcomes.

4.3 Impact of the location:

T cells: To investigate the spatial heterogeneity of the immune response in CRC, we analyzed immune cell distribution across four distinct tumour regions. The LS, facing the intestinal lumen, is known to be enriched for gut-associated lymphoid tissue (GALT), a mucosal tissue containing a variety of innate and adaptive immune cells [223]. The IM represents the actively invading tumour front, a region typically characterized by high immune cell infiltration and considered a critical zone of anti-tumour activity [199]. The CT represents the deeper portion of the tumour. Despite the importance of spatial context, data on immune cell densities in the LS and AN regions of CRC are scarce. This study provides a novel comparison of T cells and macrophages densities across all four regions, including the understudied LS and AN.

Previous data mainly focus on tumour related sections and frequently showed that IM has more infiltration compared to CT, which is supported by our data. [224, 225]. The higher

density of T cells observed in the intraepithelial compartment of AN compared to tumour-related cores may be attributed to the proximity of IM and AN that some sections identified as AN may be related to IM. However, more importantly, previous findings from our group on the same sample set using the CD8 marker indicated that the majority of our samples exhibited characteristics of a cold tumour, which is associated with low density of TIL in intraepithelial regions of tumour sections compared to AN [191]. Interestingly the density of stromal CD3.ex in the tumour related cores was significantly higher than AN, and this was not seen for intraepithelial CD3.ex which indicates the critical impact of exhaustion markers in the stromal compartment.

We found a strong correlation between T-cell infiltration in the intraepithelial compartment of IM and improved survival. This finding aligns with Immunoscore, which prognostically-prioritizes the intraepithelial compartment of the CT and IM regions [56]. Increased T cells within the intraepithelial IM, even those expressing exhaustion markers, associated with improved survival. This suggests that such T-cells may retain some functional anti-tumour capacity, proposing a potential window of therapeutic opportunity focusing on the immune cells in IM. In contrast to the IM the reduced survival impact of TIM3 expression in the CT and LS suggests that prolonged antigen exposure and chronic inflammation within the TME might lead to more complete engagement of TIM3's inhibitory pathways, consistent with prior reports [205]. While prior research has also identified LAG3 as a positive prognostic marker at the IM [226], our data additionally suggest that a higher density of dual-positive LAG3+PD1+ T cells in the IM is associated with even better survival outcomes, highlighting the complex interplay of immune checkpoint molecules.

Macrophage: Increased infiltration of stromal macrophages in tumour-related sections compared to AN highlights the importance of chemotaxis to tumour areas [227]. In tumour-related cores, the stromal luminal side had the highest cell density among different regions. The luminal side is often the initial site of tumour formation and likely contains a greater number of GALT-associated macrophages compared to other sections. Previous studies have demonstrated that GALT has a higher concentration of macrophages, which may explain the increased macrophage presence in the luminal side. [228]. Prior research indicated that CD68 alone does not show any differences in macrophage cell densities across various sections. However, when additional macrophage markers were included, marked differences emerged, reflecting that CD68 serves as a pan marker and macrophage subpopulations infiltration are various across these different sections [229]. The higher density of IR+ and IR- macrophages in the stromal tissue of tumour-related sections compared to those in AN not only supports the notion of increased macrophage infiltration into the tumour sections but reinforces our hypothesis that TAMs are more abundant in the tumour sections and express IR at a higher density than in AN tissue. Our

finding aligns with previous studies that also demonstrated a better prognosis linked to macrophage infiltration at the invasive margin [230]. This suggests that the majority of macrophages in the IM and AN exhibit anti-inflammatory response similar to M1 macrophages, correlating with improved survival.

Macrophage at the IM correlated with improved survival, independent of PD1/TIM3 status. Conversely, TIM3+ macrophages in other tumour regions predicted worse survival. These findings are consistent with previous studies demonstrating that a higher infiltration of CD80+ (M1-like) macrophages in the IM correlates with better survival, while a higher infiltration of CD163+ (M2-like) macrophages associates with worse outcomes [231]. Furthermore, increased M2 polarization in the center of the tumour inversely correlates with survival [232]. However, to the best of our knowledge, no studies have specifically investigated the differences in macrophage polarization across different tumour regions in CRC. Our observations suggest that the IM exhibits a greater degree of M1 polarization compared to other tumour-associated areas, but further investigation is required to confirm this.

4.4 Impact of the sidedness:

T cells: We found no difference in total T cell density between right and left CRC. One study showed that there is critical divergence between left and right CRC regarding the type of T cell infiltration, while right-CRC was abundant with CD8 cells, increased T reg were seen in left-CRC. Furthermore, right-sided cases may have increased expression of exhaustion markers [233]. This agreed with our observations that right-CRC had a higher density of CD3.ex cells, but there were no differences in non-exhausted T cells. This likely indicates the heterogeneity of T-cell subsets in the left and right colon. For instance, one study showed a significant higher distribution of CD8 cells in right-CRC and higher NK distribution on the left [234]. Another study showed that T reg from left-CRC has more genes related to immunotherapy and suggested these cells were good candidates for immunotherapy [235].

Previous studies confirmed that T cells in both left and right sided CRC are favorable prognostic indicators [236]. While the prognostic value of immune cell density is well-established in right-sided CRC, the situation in left-sided CRC is less well characterized. Emerging evidence suggests that not all T cell populations, and specifically tissue-resident memory T cells (TRM), are associated with improved prognosis in left-sided CRC [191]. Based on our data intraepithelial T cell density was prognostic on the left, whereas in right-sided CRC, survival associated with total T-cell density (all phenotypes).

The anatomical location of CRC affects the expression of particular exhaustion markers. Some studies have reported overexpression of LAG3 and PD1 in right-sided CRC [237], although other data show no difference in PD1 [238]. These findings underscore the distinct immunological landscapes of right and left sided disease, which likely stem from their differing embryological origins [239]. This developmental divergence is reflected in histological and genomic differences [240, 241], right-CRC exhibit distinct histological features and a higher frequency of MSI, while tumours in the left colon are frequently characterized by CIN [240]. Collectively, these factors contribute to the generally observed stronger association between immune infiltration and favorable prognosis in right-sided disease.

Macrophage: There was no difference in the total density of macrophages between right-sided and left-sided CRC. This may be attributed to the use of CD68, a pan-macrophage marker. Although the data is inconsistent, some studies showed that M2 like macrophages are more abundant in the left side CRC, others have shown a significantly higher density of M1 and M2 macrophages in right-sided CRC [242]. Our data showed that total density of CD68 and IR-macrophages in right-sided CRC is associated with improved survival. This agrees with a recent RNA-Seq study on CRC sidedness, which showed elevated M2 markers in left-CRC [243] and combined with our data suggests more M1 macrophages in right-sided disease.

Investigating the role of specific immune checkpoint molecules on macrophages revealed that TIM3 expression associated with reduced survival irrespective of sidedness. This supports the notion that TIM3 expression on macrophages is a marker of M2 polarization, which is generally associated with a pro-tumour environment and poorer outcomes, irrespective of sidedness. In contrast, the prognostic significance of PD1+macrophages was side-dependent as they only associated with survival in right-sided disease. While previous studies have linked PD1 expression to M2 macrophages, our results suggest that its impact on macrophage polarization and function is less definitive than that of TIM3 and may require co-expression with TIM3 to drive a robustly pro-tumour M2 phenotype. Therefore, the presence of PD1+ macrophages in the right may, in fact, indicate a greater degree of macrophage infiltration with some preserved anti-tumour (M1-like) activity, contributing to a favorable prognosis. Further research is needed to fully elucidate the complex roles of these exhaustion markers on macrophage function and their impact on CRC outcomes.

4.5 Impact of MMR status:

To better understand the TME, we classified patients into MSS (and MSI categories). Previous data showed the higher T cell density in MSI-CRC patients correlated with survival [244]. Consistent with previous studies, our data showed a higher cell density of total intraepithelial T cells and exhausted T cells in MSI patients. MSI-CRC has a higher T cell infiltration because of the possession of a highly mutable genome producing neoantigen and is therefore more immunogenic than MSS [245]. Given the positive correlation between T cells and exhaustion status, this data suggests that prolonged exposure to antigen leads to increased exhaustion in way that even proinflammatory cytokines, like type I interferon (α and β), may function as a double edge sword and induce T cell exhaustion. It therefore may be postulated that exhaustion can be assumed as a critical archenemy of hot tumours like MSI-CRC [246].

Although intraepithelial T cells in both MSI and MSS-CRC correlate with survival, high T cell density in the stromal compartment of MSS-CRC significantly associated with unfavorable survival. The adverse survival outcome of stromal T cells in MSS-CRC may indicate a dominant inhibitory subpopulation in the stroma. Such a phenotype was reported by a study showing a significant higher T-reg density in MSS-CRC [247]. In addition, this data suggests that the distribution of T cells subpopulations within the intra-tumour compartment of MSS is notably different. There is a higher density of favourable T cells in the intraepithelial regions, while the stromal regions of MSS are predominantly enriched with adverse T cells. This observation was further reinforced by evidence that the stromal non-exhausted T cells, while not reaching statistical significance, negatively impacted survival.

Both PD1 and TIM3 exhibited higher densities in MSI-CRC compared to MSS-CRC. While stromal TIM3 and PD1, when considered individually, did not reach statistical significance for this difference, this may be partly due to the substantial co-expression of these markers. Importantly, in the intraepithelial compartment, both PD1 and TIM3 showed significantly higher densities in MSI-CRC. These findings support previous studies [232, 248], although some studies have reported no significant difference in PD1 density between MSI and MSS-CRC [238]. PD1 positive prognostic values in both MSS and MSI-CRC and TIM3, TIM3+PD1+ T cell negative impact on survival in MSS-CRC, but not MSI-CRC is an important finding. Most CRCs are MSS and respond poorly to anti-PD1 monotherapy, unlike MSI-CRC, where PD1 blockade is highly effective and FDA-approved. Our findings suggest that while PD1 alone may indicate T cell exhaustion, co-expression with TIM3 in MSS CRC signifies a more profound T cell exhaustion, leading to a worse prognosis.

Macrophages: Intraepithelial macrophages were more abundant in MSI-CRC, supporting a wealth of previous studies [217, 249]. This is expected, as MSI- CRCs are characterized by a more immunogenic TME due to high mutational burden and neo-antigen load. Surprisingly, macrophage density only in MSS CRC, was associated with improved survival. A similar pattern was reported in a meta-analysis by Li. et al [250]. In contrast, other studies reported a better survival of macrophages in MSI-CRC [217]. This may reflect a relatively greater contribution of M1-like, anti-tumorigenic macrophages in the context of the lower overall immune infiltration typically seen in MSS. In MSI-CRC, the robust T cell response driven by the high neo-antigen load could diminish the relative contribution of total macrophage density to prognosis. Interestingly our data showed that higher density of TIM3 and TIM3+PD1+ macrophages in MSS correlate with reduced survival. These phenotypes are representative of M2 macrophages, which tend to be higher in MSS-CRC. Nevertheless, one previous study showed a higher TIM3 expression and M2 polarization in MSS-CRC with worse survival [222]. Further investigations, including detailed analysis of macrophage polarization markers (e.g. M1 vs M2 markers) are essential to elucidate the complex interplay of macrophage subsets and clinical outcomes in MSS and MSI-CRC.

4.6 Impact of TNM stage:

T cells: The stage of CRC profoundly impacts the TME, reflecting the progressive invasion of the tumour through the layers of the colonic wall. CRC begins with dysplastic polyp growth on the luminal surface and, with progression, invades the mucosa, submucosa, muscularis propria, and potentially the serosa/adventitia. Stage I tumours are limited to mucosa and submucosa. Stage II tumours extend into the muscularis propria without regional lymph node involvement. Stage III is characterized by the spread to regional lymph nodes. Stage IV tumours exhibit distant metastasis, a process often accompanied by increased angiogenesis and invasion of larger blood vessels. After stage II, a higher degree of necrotic tissue is expected due to reduced access to blood supply [251]. Each stage transition is associated with alterations in the TME, including changes in immune cell infiltration, cytokine profiles, and stromal components [252].

The lower T cell density in earlier stages aligns with previous research by Markowski et. al., which found that higher stages of CRC, characterized by lymph node involvement and metastasis, exhibited a reduced density of CD4 and CD8 cells. This may result from chronic exposure to an immunosuppressive TME [225]. Previous literature has shown that the population of T cells differs significantly between the early and advanced stages of CRC. In early stages, the invasive margin is predominantly enriched with CD4 cells,

whereas higher stages are characterized by a greater presence of CD8 cells in the center of the tumour [225, 253].

In both early and advanced CRC, a higher density of intraepithelial T cells is associated with better prognosis with a stronger association in advanced stages as expected. Although this described before [254], others showed elevated density of T cells only in early stages associated with improved survival [255]. The reduced survival link of higher densities of stromal CD3.ex in both early and advanced stages of and improved impact of intraepithelial CD3.ex on survival levels across all stages of CRC suggests that exhausted CD3 cells, primarily found in the stromal compartment, may possess the exhausted function. While intraepithelial T cells expressed exhaustion markers, they demonstrated some degree of functionality. Subsequent analysis revealed no correlation between LAG3 expression and survival in our cohort, contrasting with a previous study that reported improved survival associated with LAG3 expression in lower-stage CRC [213]. Furthermore, while we observed a higher density of PD1+ T cells in lower-stage tumours, this differs from prior data indicating a higher density of PD1+ T cells in advanced stages with lymph node involvement and metastasis [238]. This discrepancy might reflect differences in patient populations, methodologies, or the specific compartments analyzed. However, our finding could also suggest a diminished overall anti-tumour T cell response in advanced stages. Our data showed that higher density of PD1+ in early stages correlated with decreased survival, unlike the improved survival of higher PD1 CD3 density in advanced stages. T cells expressing TIM3 and PD1 inversely associated with survival in both early and late stages. This reconfirms the complexity of the CRC TME and may indicate that although patients in the early stages of CRC, may show the classic functionality of PD1 and have more exhausted T cells, they might have dominant immune suppressive players other than PD1 biologic function which leads to this reduced survival impact in the early stages. Hence, the use of anti-PD1 in early stages should be cautioned. On the other hand, double expression and reduced survival impact in both early and advanced stages, may present potential for dual-blockade therapy to increase the response to the treatment.

Macrophage: Whilst a body of data describes similar cell density of macrophages in different stages of CRC [92], some studies revealed higher TNM stages correlate with higher macrophage infiltration and worse prognosis [256, 257], others conversely reported higher densities of macrophages in early stages [227]. Stratifying the current cohort into different stages according to TNM classification, showed no difference in the density of total macrophages between early and advanced stages of CRC. Inconsistent reports can arise from the different macrophage markers used, leading to various subpopulations

identifications, as well as from unrecognized confounding variables present in the study samples.

Macrophages correlated with better survival in early and late stage CRC. Previous studies on CLEVER-1/Stabilin-11+ macrophages revealed a dual nature, showing that in less advanced CRC, a high density associated with improved survival, while in more advanced stages this was reversed [258]. IR-negative macrophages were associated with improved survival in early stages in both compartments, but only in the intraepithelial compartment in advanced stages. This supports the concept that CD68 identifies a heterogeneous macrophage population that can polarize into functionally distinct subtypes influenced by the specific microenvironment at different stages of CRC progression. The shift to reduced survival during transition to advanced stages may suggest a higher prevalence of M1-like macrophages in less advanced CRC, whereas the later stages may be characterized by a predominance of M2-like macrophages. Previous studies showed that lower stages had more M1 macrophages compared to higher M2 macrophages of advanced CRC stages [231]. Our data revealed a higher density of PD1+ macrophages in early-stage CRC compared to advanced-stage disease. Furthermore, PD-1 expression on macrophages, particularly within the invasive margin of MSS, right-sided CRC, was associated with improved survival. This suggests that PD1+ macrophages may exhibit anti-tumour characteristics of M1-polarized and their numbers decrease with tumour progression. However, the co-expression of PD1 and TIM-3 on macrophages points towards an M2-like, pro-tumour phenotype. Further investigation is required to confirm these proposed macrophage polarization states and their functional consequences.

Expression of IR on epithelial cells: In addition to leukocytes, immune checkpoint molecules can be expressed by epithelial cells. Ample data exists on the expression of TIM3 on carcinoma cells [174-176] and even the oncogene functionality of TIM3 has been demonstrated in epithelial colon cancer cells [143]. PD1 also can be expressed by epithelial tumour cells. Wang.et.al showed PD1 mRNA was expressed in a subpopulation of cell lines, including HT-29, RKO, SW480, and HCT-116 [259]. Through flowcytometry they also showed that 1.66, 4.59, 37.9, and 6.20 percent of HT-29, RKO, SW480, and HCT-116 respectively expressed surface PD1 [259]. Ieranò.et al also showed that PD1 was expressed by HT-29 and HCT-116 and also showed PD1 expression on human epithelial cancer cells (11 out of 48 patients). Furthermore, they revealed that PD1 signaling in the tumour cells functions as a tumour suppressor gene in which using Anti-PD1 in CRC cell lines expressing PD1 promotes tumour growth and decreases the effect of chemotherapy [260]. Treating mice bearing colorectal tumours with anti-PD1 increased ki67 expression and decreased cancer cell apoptosis [260].

We identified PD1 and TIM3 expression in a portion of tumour cells. However, in contrast to leukocytes expression was mostly nuclear. PD1 has five main transcripts generated through alternative splicing, and these may contribute to subcellular localization of translated PD1, particularly in different cell types [261]. Previous confocal microscopy study showed the cytoplasmic expression of PD1 in NK cells which is available for rapid transfer to the cell surface [262]. However, to the best of our knowledge, there is no concrete data regarding the expression pattern of PD1 in epithelial tumour cells, but there are controversial data on nuclear-localized PDL1. Although there is some data claiming nuclear PDL1 is attributed side effects of wrong fixation [263], there are strong recent data showing novel functionality for nuclear PDL1 with immune independent roles involving EGFR pathways promoting angiogenesis, tumorigenesis, and therapy resistance [264]. Our nuclear pattern is unlikely to be a consequence of improper fixation as nuclear staining was only seen in a portion of epithelial cells but not in all positive cells. Furthermore, similar patterns of nuclear PD1 were observed with both chromogenic and fluorescent techniques. These findings could be validated by using different clones of anti-PD1.

As we mainly aimed to train Inform algorithms to identify immune cells with PD1 or TIM3, and it was not possible to train two different patterns at the same time. We will plan to train the same slide set for analyzing epithelial tumour cells expressing checkpoint inhibitors in the future.

While the current findings provide valuable insights into the prognostic significance of T cell and macrophage subpopulation infiltration, the current project highlights the main limitations regarding mIHC technique in assessing the function of a molecule. It emphasizes the need to explore alternative methods for distinguishing between expressed and functional forms of proteins. Specifically, TIM3, LAG3, and PD1 are all expressed in the cytoplasmic vesicles and membranes of cells, but only the membrane-bound form may be biologically functional. In this context, PD1, as a well-known immune regulator, correlates with improved survival in nearly all cases involving T cells within this project. This suggests that highly activated T cells express PD1 and one study suggested PD1 as a marker of T cell activation in both *in vivo* and *in vitro* [265]. Furthermore, this indicates a high level of T cell infiltration and a potentially greater response to anti-PD1 therapy [266]. In contrast, while PD1 is predominantly expressed on T cells, TIM3 shows higher expression in macrophages. This distinction is crucial when considering blocked therapies, as it is important to identify the main target cell type.

Interestingly, the double expression of TIM3 and PD1 on T cells also correlates with decreased survival. These findings highlight the significance of combination therapy to

enhance treatment effectiveness [267]. In contrast to other cancers, the expression of LAG3 in the TME of CRC is relatively low, based on previous studies [268]. In our project, we observed that macrophages do not express LAG3, although a small portion of CD3+ T cells do exhibit LAG3 expression. Notably, the co-expression of LAG3 and PD1 in the invasive margin of MSS, right-sided CRC is associated with improved survival. This further underscores the potential benefits of combination checkpoint molecule therapy to overcome the limitations of single-agent therapies and improve outcomes for CRC patients. Further research is needed to identify optimal combinations and predictive biomarkers for patient selection.

The effectiveness of checkpoint inhibitor therapies in CRC is limited by our incomplete understanding of checkpoint inhibitor expression within the complex CRC tumour microenvironment. Further investigation is crucial to fully elucidate checkpoint molecule expression in epithelial cells, including their density, and the subsequent functional implications. Specifically, there is a need for research to explore and confirm the correlation between checkpoint expression and function in diverse macrophage states. This includes characterizing macrophages in different statuses (quiescent versus active, hypoxia versus normoxia, and M1 versus M2 polarization) to distinguish between distinct situations and subsets. Although there is limited research on exploring macrophage checkpoint molecules expression, inhibition of their expression on macrophages has been suggested as a promising strategy in treating cancers, including CRC [269]. A similar approach is warranted for T cells and other cell populations present in the CRC tumour microenvironment, such as fibroblasts and natural killer cells. Furthermore, additional checkpoint inhibitor expressions, such as CTLA-4 and TIGIT, are compelling candidates for investigation [270]. Studies should explore their function and prognostic impact through large-scale analyses employing sophisticated multiplex devices capable of supporting panels with more than six markers. This technology would enable a more comprehensive investigation of checkpoint molecule expression on different cell types within the CRC tumour microenvironment.

Current therapeutic strategies are increasingly focused on personalized medicine. However, a standardized approach is still lacking. According to the FDA, mismatch repair deficiency status is often used to guide anti-PD-1 therapy [271], irrespective of the PD-1 source cell or the functional status of PD-1. It is important to note that a more refined approach is needed. It would be advantageous to establish a standardized methodology for determining an exhaustion profile for patients [272], which would then inform the initiation of therapy based on more specific criteria beyond simple mismatch repair testing.

The interplay between different cells, mediated by checkpoint molecules, plays a critical role in tumour progression and response to therapy [273]. In the context of therapeutic intervention, it is essential to consider both the cell types expressing checkpoint markers and information regarding spatial relationships within the tumour microenvironment. For instance, as spatial data showed a region enriched in macrophages and T cells in our data, this could suggest the potential interaction between these two cells, and with respect to the specific expression of markers, a bispecific or Trispecific molecule targeting CD3 and CD68, in conjunction with one of the exhaustion markers, may represent a promising therapeutic strategy [274].

In conclusion, while checkpoint inhibitor therapy holds significant promise, substantial gaps remain in our understanding of their biological, prognostic, and therapeutic impact. Our study highlights the importance of considering not only the expression of checkpoint molecules but also their spatial distribution and the complex interplay between different cell types within the CRC TME. Further research in this area is crucial for the development of effective immunotherapeutic strategies and personalized treatment approaches.

Chapter6: Reference

1. Al Zein, M., et al., *Immunotherapy and immunoevasion of colorectal cancer*. Drug Discovery Today, 2023. **28**(9): p. 103669.
2. Organization, W.H. and I.A.f.R.o. Cancer, *Globocan, 2012* (<http://globocan.iarc.fr/Default.aspx>). 2016, Accessed.
3. Baran, B., et al., *Difference between left-sided and right-sided colorectal cancer: a focused review of literature*. Gastroenterology research, 2018. **11**(4): p. 264.
4. de Campos, F.G.C., et al., *El cáncer colorrectal en la poliposis adenomatosa familiar:¿ existen factores clínicos de predicción?* Cirugía Española, 2010. **88**(6): p. 390-397.
5. Lynch, H.T., T. Smyrk, and J.F. Lynch, *Molecular Genetics and Clinical-Pathology Features of Hereditary Nonpolyposis Colorectal Carcinoma (Lynch Syndrome) Historical Journey from Pedigree Anecdote to Molecular Genetic Confirmation*. Oncology, 1998. **55**(2): p. 103-108.
6. Kellokumpu, I. and A. Husa, *Colorectal adenomas: morphologic features and the risk of developing metachronous adenomas and carcinomas in the colorectum*. Scandinavian journal of gastroenterology, 1987. **22**(7): p. 833-841.
7. Luo, Y., et al., *Differences in DNA methylation signatures reveal multiple pathways of progression from adenoma to colorectal cancer*. Gastroenterology, 2014. **147**(2): p. 418-429. e8.
8. Kuipers, E.J., et al., *Colorectal cancer*. Nature reviews. Disease primers, 2015. **1**: p. 15065.
9. Galon, J., et al., *Towards the introduction of the 'Immunoscore' in the classification of malignant tumours*. The Journal of pathology, 2014. **232**(2): p. 199-209.
10. Arvelo, F., F. Sojo, and C. Cotte, *Biology of colorectal cancer*. Ecancermedicalsecience, 2015. **9**.
11. Arrington, A.K., et al., *Prognostic and predictive roles of KRAS mutation in colorectal cancer*. International journal of molecular sciences, 2012. **13**(10): p. 12153-12168.
12. East, J.E., B.P. Saunders, and J.R. Jass, *Sporadic and syndromic hyperplastic polyps and serrated adenomas of the colon: classification, molecular genetics, natural history, and clinical management*. Gastroenterology clinics of North America, 2008. **37**(1): p. 25-46.
13. Glatz, K., et al., *A multinational, internet-based assessment of observer variability in the diagnosis of serrated colorectal polyps*. American journal of clinical pathology, 2007. **127**(6): p. 938-945.
14. Loeb, L.A., *Cancer cells exhibit a mutator phenotype*. Advances in cancer research, 1997. **72**: p. 25-56.
15. Boland, C.R. and A. Goel, *Microsatellite instability in colorectal cancer*. Gastroenterology, 2010. **138**(6): p. 2073-2087. e3.

16. Sinicrope, F.A. and D.J. Sargent, *Molecular pathways: microsatellite instability in colorectal cancer: prognostic, predictive, and therapeutic implications*. *Clinical cancer research*, 2012. **18**(6): p. 1506-1512.
17. Ho, A.S., S. Turcan, and T.A. Chan, *Epigenetic therapy: use of agents targeting deacetylation and methylation in cancer management*. *OncoTargets and therapy*, 2013: p. 223-232.
18. Jass, J.R., *Hyperplastic polyps and colorectal cancer: is there a link?* *Clinical Gastroenterology and Hepatology*, 2004. **2**(1): p. 1-8.
19. Bettington, M., et al., *The serrated pathway to colorectal carcinoma: current concepts and challenges*. *Histopathology*, 2013. **62**(3): p. 367-386.
20. Chittenden, T.W., et al., *Functional classification analysis of somatically mutated genes in human breast and colorectal cancers*. *Genomics*, 2008. **91**(6): p. 508-511.
21. Nagtegaal, I.D., P. Quirke, and H.-J. Schmoll, *Has the new TNM classification for colorectal cancer improved care?* *Nature reviews Clinical oncology*, 2012. **9**(2): p. 119-123.
22. Mlecnik, B., et al., *Tumor immunosurveillance in human cancers*. *Cancer and Metastasis Reviews*, 2011. **30**: p. 5-12.
23. Hanahan, D. and L.M. Coussens, *Accessories to the crime: functions of cells recruited to the tumor microenvironment*. *Cancer cell*, 2012. **21**(3): p. 309-322.
24. Pietras, K. and A. Östman, *Hallmarks of cancer: interactions with the tumor stroma*. *Experimental cell research*, 2010. **316**(8): p. 1324-1331.
25. Catalano, V., et al. *Tumor and its microenvironment: a synergistic interplay*. in *Seminars in cancer biology*. 2013. Elsevier.
26. Valkenburg, K.C., A.E. De Groot, and K.J. Pienta, *Targeting the tumour stroma to improve cancer therapy*. *Nature reviews Clinical oncology*, 2018. **15**(6): p. 366-381.
27. Fenner, J., et al., *Macroscopic stiffness of breast tumors predicts metastasis*. *Scientific reports*, 2014. **4**(1): p. 5512.
28. Chang, R.B. and G.L. Beatty, *The interplay between innate and adaptive immunity in cancer shapes the productivity of cancer immunosurveillance*. *Journal of Leucocyte Biology*, 2020. **108**(1): p. 363-376.
29. Shankaran, V., et al., *IFN γ and lymphocytes prevent primary tumour development and shape tumour immunogenicity*. *Nature*, 2001. **410**(6832): p. 1107-1111.
30. Koebel, C.M., et al., *Adaptive immunity maintains occult cancer in an equilibrium state*. *Nature*, 2007. **450**(7171): p. 903-907.
31. Vesely, M.D., et al., *Natural innate and adaptive immunity to cancer*. *Annual review of immunology*, 2011. **29**(1): p. 235-271.
32. Network, C.G.A., *Comprehensive molecular characterization of human colon and rectal cancer*. *Nature*, 2012. **487**(7407): p. 330.
33. Matsushita, H., et al., *Cancer exome analysis reveals a T-cell-dependent mechanism of cancer immunoediting*. *Nature*, 2012. **482**(7385): p. 400-404.
34. Rosenthal, R., et al., *Neoantigen-directed immune escape in lung cancer evolution*. *Nature*, 2019. **567**(7749): p. 479-485.
35. Angelova, M., et al., *Evolution of metastases in space and time under immune selection*. *Cell*, 2018. **175**(3): p. 751-765. e16.

36. Rooney, M.S., et al., *Molecular and genetic properties of tumors associated with local immune cytolytic activity*. Cell, 2015. **160**(1): p. 48-61.
37. Lawrence, M.S., et al., *Discovery and saturation analysis of cancer genes across 21 tumour types*. Nature, 2014. **505**(7484): p. 495-501.
38. Gangoso, E., et al., *Glioblastomas acquire myeloid-affiliated transcriptional programs via epigenetic immunoediting to elicit immune evasion*. Cell, 2021. **184**(9): p. 2454-2470. e26.
39. Giannakis, M., et al., *Genomic correlates of immune-cell infiltrates in colorectal carcinoma*. Cell reports, 2016. **15**(4): p. 857-865.
40. Schneider, R., et al., *Lynch syndrome: clinical, pathological, and genetic insights*. Langenbeck's archives of surgery, 2012. **397**: p. 513-525.
41. Fleming, M., et al., *Colorectal carcinoma: Pathologic aspects*. Journal of gastrointestinal oncology, 2012. **3**(3): p. 153.
42. Oliveira, G., et al., *Phenotype, specificity and avidity of antitumour CD8+ T cells in melanoma*. Nature, 2021. **596**(7870): p. 119-125.
43. Caushi, J.X., et al., *Transcriptional programs of neoantigen-specific TIL in anti-PD-1-treated lung cancers*. Nature, 2021. **596**(7870): p. 126-132.
44. Maurice, N.J., A.K. Taber, and M. Prlic, *The ugly duckling turned to swan: a change in perception of bystander-activated memory CD8 T cells*. The Journal of Immunology, 2021. **206**(3): p. 455-462.
45. Sznol, M. and L. Chen, *Antagonist antibodies to PD-1 and B7-H1 (PD-L1) in the treatment of advanced human cancer*. Clinical cancer research, 2013. **19**(5): p. 1021-1034.
46. Junttila, M.R. and F.J. De Sauvage, *Influence of tumour micro-environment heterogeneity on therapeutic response*. Nature, 2013. **501**(7467): p. 346-354.
47. Mlecnik, B., et al., *Histopathologic-based prognostic factors of colorectal cancers are associated with the state of the local immune reaction*. Journal of clinical oncology, 2011. **29**(6): p. 610-618.
48. Galon, J., et al., *Type, density, and location of immune cells within human colorectal tumors predict clinical outcome*. Science, 2006. **313**(5795): p. 1960-1964.
49. Galon, J., et al., *Cancer classification using the Immunoscore: a worldwide task force*. Journal of translational medicine, 2012. **10**: p. 1-10.
50. Fox, B.A., et al., *Defining the critical hurdles in cancer immunotherapy*. Journal of translational medicine, 2011. **9**: p. 1-15.
51. Anitei, M.-G., et al., *Prognostic and predictive values of the immunoscore in patients with rectal cancer*. Clinical Cancer Research, 2014. **20**(7): p. 1891-1899.
52. Hiraoka, K., et al., *Concurrent infiltration by CD8+ T cells and CD4+ T cells is a favourable prognostic factor in non-small-cell lung carcinoma*. British journal of cancer, 2006. **94**(2): p. 275-280.
53. Tu, J.-F., et al., *Regulatory T cells, especially ICOS+ FOXP3+ regulatory T cells, are increased in the hepatocellular carcinoma microenvironment and predict reduced survival*. Scientific reports, 2016. **6**(1): p. 1-8.

54. Kumar, V., et al., *The nature of myeloid-derived suppressor cells in the tumor microenvironment*. Trends in immunology, 2016. **37**(3): p. 208-220.
55. Chen, D.S. and I. Mellman, *Elements of cancer immunity and the cancer-immune set point*. Nature, 2017. **541**(7637): p. 321-330.
56. Hendry, S., et al., *Assessing tumor-infiltrating lymphocytes in solid tumors: a practical review for pathologists and proposal for a standardized method from the international immunooncology biomarkers working group: part 1: assessing the host immune response, TILs in invasive breast carcinoma and ductal carcinoma in situ, metastatic tumor deposits and areas for further research*. Advances in anatomic pathology, 2017. **24**(5): p. 235-251.
57. Pagès, F., et al., *In situ cytotoxic and memory T cells predict outcome in patients with early-stage colorectal cancer*. Journal of clinical oncology, 2009. **27**(35): p. 5944-5951.
58. Tumei, P.C., et al., *PD-1 blockade induces responses by inhibiting adaptive immune resistance*. Nature, 2014. **515**(7528): p. 568-571.
59. Bruni, D., H.K. Angell, and J. Galon, *The immune contexture and Immunoscore in cancer prognosis and therapeutic efficacy*. Nature Reviews Cancer, 2020. **20**(11): p. 662-680.
60. Nagarsheth, N., M.S. Wicha, and W. Zou, *Chemokines in the cancer microenvironment and their relevance in cancer immunotherapy*. Nature Reviews Immunology, 2017. **17**(9): p. 559-572.
61. Dangaj, D., et al., *Cooperation between constitutive and inducible chemokines enables T cell engraftment and immune attack in solid tumors*. Cancer cell, 2019. **35**(6): p. 885-900. e10.
62. Spranger, S., et al., *Density of immunogenic antigens does not explain the presence or absence of the T-cell-inflamed tumor microenvironment in melanoma*. Proceedings of the National Academy of Sciences, 2016. **113**(48): p. E7759-E7768.
63. Beatty, G.L., et al., *Exclusion of T cells from pancreatic carcinomas in mice is regulated by Ly6Clow F4/80+ extratumoral macrophages*. Gastroenterology, 2015. **149**(1): p. 201-210.
64. Molon, B., et al., *Chemokine nitration prevents intratumoral infiltration of antigen-specific T cells*. Journal of Experimental Medicine, 2011. **208**(10): p. 1949-1962.
65. Mariathasan, S., et al., *TGFβ attenuates tumour response to PD-L1 blockade by contributing to exclusion of T cells*. Nature, 2018. **554**(7693): p. 544-548.
66. Liu, Y. and X. Cao, *The origin and function of tumor-associated macrophages*. Cellular & molecular immunology, 2015. **12**(1): p. 1-4.
67. Bain, C.C. and A.M. Mowat, *Macrophages in intestinal homeostasis and inflammation*. Immunological reviews, 2014. **260**(1): p. 102-117.
68. Gordon, S., *Alternative activation of macrophages*. Nature reviews immunology, 2003. **3**(1): p. 23-35.
69. Duffield, J.S., *The inflammatory macrophage: a story of Jekyll and Hyde*. Clinical science, 2003. **104**(1): p. 27-38.
70. Mantovani, A., A. Sica, and M. Locati, *Macrophage polarization comes of age*. Immunity, 2005. **23**(4): p. 344-346.

71. Mantovani, A., et al., *Cancer-related inflammation*. nature, 2008. **454**(7203): p. 436-444.
72. Movahedi, K., et al., *Different tumor microenvironments contain functionally distinct subsets of macrophages derived from Ly6C (high) monocytes*. Cancer research, 2010. **70**(14): p. 5728-5739.
73. Wang, H., T. Tian, and J. Zhang, *Tumor-associated macrophages (TAMs) in colorectal cancer (CRC): from mechanism to therapy and prognosis*. International journal of molecular sciences, 2021. **22**(16): p. 8470.
74. Bowman, R.L., et al., *Macrophage ontogeny underlies differences in tumor-specific education in brain malignancies*. Cell reports, 2016. **17**(9): p. 2445-2459.
75. Loyher, P.-L., et al., *Macrophages of distinct origins contribute to tumor development in the lung*. Journal of Experimental Medicine, 2018. **215**(10): p. 2536-2553.
76. Zhu, Y., et al., *Tissue-resident macrophages in pancreatic ductal adenocarcinoma originate from embryonic hematopoiesis and promote tumor progression*. Immunity, 2017. **47**(2): p. 323-338. e6.
77. Bronte, V., et al., *Recommendations for myeloid-derived suppressor cell nomenclature and characterization standards*. Nature communications, 2016. **7**(1): p. 12150.
78. Nguyen, N., et al., *Tumor infiltrating lymphocytes and survival in patients with head and neck squamous cell carcinoma*. Head & neck, 2016. **38**(7): p. 1074-1084.
79. Italiani, P. and D. Boraschi, *From monocytes to M1/M2 macrophages: phenotypical vs. functional differentiation*. Frontiers in immunology, 2014. **5**: p. 514.
80. Chistiakov, D.A., et al., *CD68/macrosialin: not just a histochemical marker*. Laboratory investigation, 2017. **97**(1): p. 4-13.
81. Cui, H., et al., *Molecular characterization, expression, evolutionary selection, and biological activity analysis of CD68 gene from Megalobrama amblycephala*. International Journal of Molecular Sciences, 2022. **23**(21): p. 13133.
82. Novak, M.L. and T.J. Koh, *Macrophage phenotypes during tissue repair*. Journal of Leukocyte Biology, 2013. **93**(6): p. 875-881.
83. Mantovani, A., et al., *Tumour-associated macrophages as treatment targets in oncology*. Nature Reviews Clinical Oncology, 2017. **14**(7): p. 399-416.
84. Sica, A. and A. Mantovani, *Macrophage plasticity and polarization: in vivo veritas*. The Journal of clinical investigation, 2012. **122**(3): p. 787-795.
85. Ngambenjawong, C., H.H. Gustafson, and S.H. Pun, *Progress in tumor-associated macrophage (TAM)-targeted therapeutics*. Advanced drug delivery reviews, 2017. **114**: p. 206-221.
86. Trombetta, A.C., et al., *A circulating cell population showing both M1 and M2 monocyte/macrophage surface markers characterizes systemic sclerosis patients with lung involvement*. Respiratory research, 2018. **19**: p. 1-12.
87. Chanmee, T., et al., *Tumor-associated macrophages as major players in the tumor microenvironment*. Cancers, 2014. **6**(3): p. 1670-1690.
88. Lavin, Y., et al., *Regulation of macrophage development and function in peripheral tissues*. Nature Reviews Immunology, 2015. **15**(12): p. 731-744.

89. Qian, B.-Z. and J.W. Pollard, *Macrophage diversity enhances tumor progression and metastasis*. Cell, 2010. **141**(1): p. 39-51.
90. Fridman, W.H., et al., *The immune contexture in human tumours: impact on clinical outcome*. Nature Reviews Cancer, 2012. **12**(4): p. 298-306.
91. Wang, X., J. Jiang, and C. Wu, *Prognostic significance of tumor-associated macrophage infiltration in gastric cancer: a meta-analysis*. Genet Mol Res, 2016. **15**(4): p. gmr15049040.
92. Pinto, M.L., et al., *The two faces of tumor-associated macrophages and their clinical significance in colorectal cancer*. Frontiers in immunology, 2019. **10**: p. 1875.
93. Lian, G., et al., *Colon cancer cell secretes EGF to promote M2 polarization of TAM through EGFR/PI3K/AKT/mTOR pathway*. Technology in cancer research & treatment, 2019. **18**: p. 1533033819849068.
94. Huang, Y.-J., et al., *Preclinical investigation of ovatodiolide as a potential inhibitor of colon cancer stem cells via downregulating sphere-derived exosomal β -catenin/STAT3/miR-1246 cargoes*. American journal of cancer research, 2020. **10**(8): p. 2337.
95. Coburn, L.A., et al., *Loss of solute carrier family 7 member 2 exacerbates inflammation-associated colon tumorigenesis*. Oncogene, 2019. **38**(7): p. 1067-1079.
96. Zhao, P., et al., *Response gene to complement 32 expression in macrophages augments paracrine stimulation-mediated colon cancer progression*. Cell Death & Disease, 2019. **10**(10): p. 776.
97. Allavena, P., et al., *The chemokine receptor switch paradigm and dendritic cell migration: its significance in tumor tissues*. Immunological reviews, 2000. **177**: p. 141-149.
98. Luput, L., et al., *Tumor-associated macrophages favor C26 murine colon carcinoma cell proliferation in an oxidative stress-dependent manner*. Oncology reports, 2017. **37**(4): p. 2472-2480.
99. Phinney, B.B., et al., *MK2 regulates macrophage chemokine activity and recruitment to promote colon tumor growth*. Frontiers in immunology, 2018. **9**: p. 1857.
100. Lim, S.Y., et al., *Tumor-infiltrating monocytes/macrophages promote tumor invasion and migration by upregulating S100A8 and S100A9 expression in cancer cells*. Oncogene, 2016. **35**(44): p. 5735-5745.
101. Wei, C., et al., *Crosstalk between cancer cells and tumor associated macrophages is required for mesenchymal circulating tumor cell-mediated colorectal cancer metastasis*. Molecular cancer, 2019. **18**: p. 1-23.
102. Mantovani, A., et al., *Macrophage polarization: tumor-associated macrophages as a paradigm for polarized M2 mononuclear phagocytes*. Trends in immunology, 2002. **23**(11): p. 549-555.
103. Bobryshev, Y.V., *Dendritic cells and their role in atherogenesis*. Laboratory investigation, 2010. **90**(7): p. 970-984.
104. Kitamura, T., B.-Z. Qian, and J.W. Pollard, *Immune cell promotion of metastasis*. Nature Reviews Immunology, 2015. **15**(2): p. 73-86.

105. Yang, L. and Y. Zhang, *Tumor-associated macrophages: from basic research to clinical application*. Journal of hematology & oncology, 2017. **10**: p. 1-12.
106. Sun, L., et al., *T cells in health and disease*. Signal transduction and targeted therapy, 2023. **8**(1): p. 235.
107. Mariuzza, R.A., P. Agnihotri, and J. Orban, *The structural basis of T-cell receptor (TCR) activation: An enduring enigma*. Journal of Biological Chemistry, 2020. **295**(4): p. 914-925.
108. Dong, D., et al., *Structural basis of assembly of the human T cell receptor-CD3 complex*. Nature, 2019. **573**(7775): p. 546-552.
109. Reth, M., *Antigen receptor tail clue*. Nature, 1989. **338**: p. 383.
110. Rickert, R.C., *New insights into pre-BCR and BCR signalling with relevance to B cell malignancies*. Nature Reviews Immunology, 2013. **13**(8): p. 578-591.
111. Call, M.E., et al., *The organizing principle in the formation of the T cell receptor-CD3 complex*. Cell, 2002. **111**(7): p. 967-979.
112. Ngoenkam, J., W.W. Schamel, and S. Pongcharoen, *Selected signalling proteins recruited to the T - cell receptor-CD3 complex*. Immunology, 2018. **153**(1): p. 42-50.
113. Tjon, J.M., et al., *Defective synthesis or association of T-cell receptor chains underlies loss of surface T-cell receptor-CD3 expression in enteropathy-associated T-cell lymphoma*. Blood, The Journal of the American Society of Hematology, 2008. **112**(13): p. 5103-5110.
114. Cenerenti, M., et al., *The era of cytotoxic CD4 T cells*. Frontiers in immunology, 2022. **13**: p. 867189.
115. Kaech, S.M. and E.J. Wherry, *Heterogeneity and cell-fate decisions in effector and memory CD8+ T cell differentiation during viral infection*. Immunity, 2007. **27**(3): p. 393-405.
116. Qin, S., et al., *Novel immune checkpoint targets: moving beyond PD-1 and CTLA-4*. Molecular cancer, 2019. **18**: p. 1-14.
117. Schietinger, A., et al., *Tumor-specific T cell dysfunction is a dynamic antigen-driven differentiation program initiated early during tumorigenesis*. Immunity, 2016. **45**(2): p. 389-401.
118. Zajac, A.J., et al., *Viral immune evasion due to persistence of activated T cells without effector function*. The Journal of experimental medicine, 1998. **188**(12): p. 2205-2213.
119. Hadrup, S.R., et al., *Longitudinal studies of clonally expanded CD8 T cells reveal a repertoire shrinkage predicting mortality and an increased number of dysfunctional cytomegalovirus-specific T cells in the very elderly*. The Journal of Immunology, 2006. **176**(4): p. 2645-2653.
120. Cornberg, M., et al., *Clonal exhaustion as a mechanism to protect against severe immunopathology and death from an overwhelming CD8 T cell response*. Frontiers in immunology, 2013. **4**: p. 475.

121. Nishimura, H., et al., *Development of lupus-like autoimmune diseases by disruption of the PD-1 gene encoding an ITIM motif-carrying immunoreceptor*. *Immunity*, 1999. **11**(2): p. 141-151.
122. Wherry, E.J. and R. Ahmed, *Memory CD8 T-cell differentiation during viral infection*. *Journal of virology*, 2004. **78**(11): p. 5535-5545.
123. Rajagopalan, S. and E.O. Long, *Cellular senescence induced by CD158d reprograms natural killer cells to promote vascular remodeling*. *Proceedings of the National Academy of Sciences*, 2012. **109**(50): p. 20596-20601.
124. Heissmeyer, V., et al., *Calcineurin imposes T cell unresponsiveness through targeted proteolysis of signaling proteins*. *Nature immunology*, 2004. **5**(3): p. 255-265.
125. O'Brien, K.L. and D.K. Finlay, *Immunometabolism and natural killer cell responses*. *Nature Reviews Immunology*, 2019. **19**(5): p. 282-290.
126. Bernard, D., et al., *Costimulatory receptors in jawed vertebrates: conserved CD28, odd CTLA4 and multiple BTLAs*. *Developmental & Comparative Immunology*, 2007. **31**(3): p. 255-271.
127. Khan, M., S. Arooj, and H. Wang, *NK cell-based immune checkpoint inhibition*. *Frontiers in immunology*, 2020. **11**: p. 167.
128. Ribas, A. and J.D. Wolchok, *Cancer immunotherapy using checkpoint blockade*. *Science*, 2018. **359**(6382): p. 1350-1355.
129. Diaz, L.A. and D.T. Le, *PD-1 blockade in tumors with mismatch-repair deficiency: To the editor [2]*. *New England Journal of Medicine*, 2015. **373**(20).
130. Gao, J., et al., *Loss of IFN- γ pathway genes in tumor cells as a mechanism of resistance to anti-CTLA-4 therapy*. *Cell*, 2016. **167**(2): p. 397-404. e9.
131. Sade-Feldman, M., et al., *Resistance to checkpoint blockade therapy through inactivation of antigen presentation*. *Nature communications*, 2017. **8**(1): p. 1136.
132. Sivori, S., et al., *Human NK cells: surface receptors, inhibitory checkpoints, and translational applications*. *Cellular & molecular immunology*, 2019. **16**(5): p. 430-441.
133. Anderson, A.C., N. Joller, and V.K. Kuchroo, *Lag-3, Tim-3, and TIGIT: co-inhibitory receptors with specialized functions in immune regulation*. *Immunity*, 2016. **44**(5): p. 989-1004.
134. Graydon, C.G., S. Mohideen, and K.R. Fowke, *LAG3's enigmatic mechanism of action*. *Frontiers in immunology*, 2021. **11**: p. 615317.
135. Keane, C., et al., *LAG3: a novel immune checkpoint expressed by multiple lymphocyte subsets in diffuse large B-cell lymphoma*. *Blood Advances*, 2020. **4**(7): p. 1367-1377.
136. Li, N., et al., *Biochemical analysis of the regulatory T cell protein lymphocyte activation gene-3 (LAG-3; CD223)*. *The Journal of Immunology*, 2004. **173**(11): p. 6806-6812.
137. Workman, C.J. and D.A. Vignali, *The CD4 - related molecule, LAG - 3 (CD223), regulates the expansion of activated T cells*. *European journal of immunology*, 2003. **33**(4): p. 970-979.

138. Park, Y., et al., *Expression of the immune checkpoint receptors PD-1, LAG3, and TIM3 in the immune context of stage II and III gastric cancer by using single and chromogenic multiplex immunohistochemistry*. *Oncoimmunology*, 2021. **10**(1): p. 1954761.
139. Gordon, S.R., et al., *PD-1 expression by tumour-associated macrophages inhibits phagocytosis and tumour immunity*. *Nature*, 2017. **545**(7655): p. 495-499.
140. Ocaña-Guzman, R., L. Torre-Bouscoulet, and I. Sada-Ovalle, *TIM-3 regulates distinct functions in macrophages*. *Frontiers in immunology*, 2016. **7**: p. 229.
141. Shi, A.-P., et al., *Immune checkpoint LAG3 and its ligand FGL1 in cancer*. *Frontiers in immunology*, 2022. **12**: p. 785091.
142. Chen, M., L. Bie, and J. Ying, *Cancer cell-intrinsic PD-1: Its role in Malignant progression and immunotherapy*. *Biomedicine & Pharmacotherapy*, 2023. **167**: p. 115514.
143. Yu, M., et al., *Tim-3 is upregulated in human colorectal carcinoma and associated with tumor progression*. *Molecular medicine reports*, 2017. **15**(2): p. 689-695.
144. Huard, B., et al., *Characterization of the major histocompatibility complex class II binding site on LAG-3 protein*. *Proceedings of the National Academy of Sciences*, 1997. **94**(11): p. 5744-5749.
145. MacLachlan, B.J., et al., *Molecular characterization of HLA class II binding to the LAG - 3 T cell co - inhibitory receptor*. *European Journal of Immunology*, 2021. **51**(2): p. 331-341.
146. Dunic, J., S. Dabelic, and M. Flögel, *Galectin-3: an open-ended story*. *Biochimica et Biophysica Acta (BBA)-General Subjects*, 2006. **1760**(4): p. 616-635.
147. Bae, J., et al., *Targeting LAG3/GAL-3 to overcome immunosuppression and enhance anti-tumor immune responses in multiple myeloma*. *Leukemia*, 2022. **36**(1): p. 138-154.
148. Xu, F., et al., *LSECTin expressed on melanoma cells promotes tumor progression by inhibiting antitumor T-cell responses*. *Cancer research*, 2014. **74**(13): p. 3418-3428.
149. Wang, J., et al., *Fibrinogen-like protein 1 is a major immune inhibitory ligand of LAG-3*. *Cell*, 2019. **176**(1): p. 334-347. e12.
150. Yamamoto, T., et al., *Molecular cloning and initial characterization of a novel fibrinogen-related gene, HFREP-1*. *Biochemical and biophysical research communications*, 1993. **193**(2): p. 681-687.
151. Andrews, L.P., et al., *Resistance to PD1 blockade in the absence of metalloprotease-mediated LAG3 shedding*. *Science immunology*, 2020. **5**(49): p. eabc2728.
152. Li, N., et al., *Metalloproteases regulate T - cell proliferation and effector function via LAG - 3*. *The EMBO journal*, 2007. **26**(2): p. 494-504.
153. Mao, X., et al., *Pathological α -synuclein transmission initiated by binding lymphocyte-activation gene 3*. *Science*, 2016. **353**(6307): p. aah3374.

154. Woo, S.R., et al., *Differential subcellular localization of the regulatory T - cell protein LAG - 3 and the coreceptor CD4*. European journal of immunology, 2010. **40**(6): p. 1768-1777.
155. Vari, F., et al., *Immune evasion via PD-1/PD-L1 on NK cells and monocyte/macrophages is more prominent in Hodgkin lymphoma than DLBCL*. Blood, The Journal of the American Society of Hematology, 2018. **131**(16): p. 1809-1819.
156. Bauché, D., et al., *LAG3+ regulatory T cells restrain interleukin-23-producing CX3CR1+ gut-resident macrophages during group 3 innate lymphoid cell-driven colitis*. Immunity, 2018. **49**(2): p. 342-352. e5.
157. McLane, L.M., M.S. Abdel-Hakeem, and E.J. Wherry, *CD8 T cell exhaustion during chronic viral infection and cancer*. Annual review of immunology, 2019. **37**(1): p. 457-495.
158. Chen, B.J., et al., *The immune checkpoint molecules PD-1, PD-L1, TIM-3 and LAG-3 in diffuse large B-cell lymphoma*. Oncotarget, 2019. **10**(21): p. 2030.
159. Gao, X., et al., *TIM-3 expression characterizes regulatory T cells in tumor tissues and is associated with lung cancer progression*. PloS one, 2012. **7**(2): p. e30676.
160. Ndhlovu, L.C., et al., *Tim-3 marks human natural killer cell maturation and suppresses cell-mediated cytotoxicity*. Blood, The Journal of the American Society of Hematology, 2012. **119**(16): p. 3734-3743.
161. Phong, B.L., et al., *Tim-3 enhances FcεRI-proximal signaling to modulate mast cell activation*. Journal of Experimental Medicine, 2015. **212**(13): p. 2289-2304.
162. Rangachari, M., et al., *Bat3 promotes T cell responses and autoimmunity by repressing Tim-3-mediated cell death and exhaustion*. Nature medicine, 2012. **18**(9): p. 1394-1400.
163. Wolf, Y., A.C. Anderson, and V.K. Kuchroo, *TIM3 comes of age as an inhibitory receptor*. Nature Reviews Immunology, 2020. **20**(3): p. 173-185.
164. Möller-Hackbarth, K., et al., *A disintegrin and metalloprotease (ADAM) 10 and ADAM17 are major sheddases of T cell immunoglobulin and mucin domain 3 (Tim-3)*. Journal of Biological Chemistry, 2013. **288**(48): p. 34529-34544.
165. Hansen, J.A., et al., *A novel soluble form of Tim-3 associated with severe graft-versus-host disease*. Biology of Blood and Marrow Transplantation, 2013. **19**(9): p. 1323-1330.
166. Ge, W., et al., *Tim-3 as a diagnostic and prognostic biomarker of osteosarcoma*. Tumor Biology, 2017. **39**(7): p. 1010428317715643.
167. Clayton, K.L., et al., *Soluble T cell immunoglobulin mucin domain 3 is shed from CD8+ T cells by the sheddase ADAM10, is increased in plasma during untreated HIV infection, and correlates with HIV disease progression*. Journal of virology, 2015. **89**(7): p. 3723-3736.
168. Yang, X., et al., *T cell Ig mucin-3 promotes homeostasis of sepsis by negatively regulating the TLR response*. The Journal of Immunology, 2013. **190**(5): p. 2068-2079.

169. Jiang, X., et al., *Tim-3 promotes intestinal homeostasis in DSS colitis by inhibiting M1 polarization of macrophages*. Clinical immunology, 2015. **160**(2): p. 328-335.
170. Kashio, Y., et al., *Galectin-9 induces apoptosis through the calcium-calpain-caspase-1 pathway*. The Journal of Immunology, 2003. **170**(7): p. 3631-3636.
171. Zhang, Y., et al., *Tim-3 negatively regulates IL-12 expression by monocytes in HCV infection*. PLoS one, 2011. **6**(5): p. e19664.
172. Ma, C.J., et al., *Cis association of galectin-9 with Tim-3 differentially regulates IL-12/IL-23 expressions in monocytes via TLR signaling*. PLoS One, 2013. **8**(8): p. e72488.
173. Yan, W., et al., *Tim-3 fosters HCC development by enhancing TGF- β -mediated alternative activation of macrophages*. Gut, 2015. **64**(10): p. 1593-1604.
174. Piao, Y.-R., et al., *Prognostic value of T cell immunoglobulin mucin-3 in prostate cancer*. Asian Pac J Cancer Prev, 2013. **14**(6): p. 3897-901.
175. Zheng, H., et al., *Distinct role of Tim-3 in systemic lupus erythematosus and clear cell renal cell carcinoma*. International journal of clinical and experimental medicine, 2015. **8**(5): p. 7029.
176. Wiener, Z., et al., *TIM-3 is expressed in melanoma cells and is upregulated in TGF-beta stimulated mast cells*. Journal of Investigative Dermatology, 2007. **127**(4): p. 906-914.
177. Chamoto, K., M. Al-Habsi, and T. Honjo, *Role of PD-1 in immunity and diseases*. Emerging concepts targeting immune checkpoints in cancer and autoimmunity, 2017: p. 75-97.
178. Okazaki, T. and T. Honjo, *PD-1 and PD-1 ligands: from discovery to clinical application*. International immunology, 2007. **19**(7): p. 813-824.
179. Kinter, A.L., et al., *The common γ -chain cytokines IL-2, IL-7, IL-15, and IL-21 induce the expression of programmed death-1 and its ligands*. The Journal of Immunology, 2008. **181**(10): p. 6738-6746.
180. Hsu, J.-M., et al., *STT3-dependent PD-L1 accumulation on cancer stem cells promotes immune evasion*. Nature communications, 2018. **9**(1): p. 1908.
181. Bousiotis, V.A., *Molecular and biochemical aspects of the PD-1 checkpoint pathway*. New England Journal of Medicine, 2016. **375**(18): p. 1767-1778.
182. Meng, X., et al., *FBXO38 mediates PD-1 ubiquitination and regulates anti-tumour immunity of T cells*. Nature, 2018. **564**(7734): p. 130-135.
183. Wang, Y., et al., *Dynamics of TIGIT and PD-1 expression on NK cells during the course of normal pregnancy*. Immunology Letters, 2021. **230**: p. 42-48.
184. Ishida, Y., *PD-1: its discovery, involvement in cancer immunotherapy, and beyond*. Cells, 2020. **9**(6): p. 1376.
185. Zippelius, A., et al., *Effector function of human tumor-specific CD8 T cells in melanoma lesions: a state of local functional tolerance*. Cancer research, 2004. **64**(8): p. 2865-2873.
186. Catakovic, K., et al., *T cell exhaustion: from pathophysiological basics to tumor immunotherapy*. Cell Communication and Signaling, 2017. **15**: p. 1-16.

187. Iwai, Y., et al., *Involvement of PD-L1 on tumor cells in the escape from host immune system and tumor immunotherapy by PD-L1 blockade*. Proceedings of the National Academy of Sciences, 2002. **99**(19): p. 12293-12297.
188. Hartley, G.P., et al., *Programmed cell death ligand 1 (PD-L1) signaling regulates macrophage proliferation and activation*. Cancer immunology research, 2018. **6**(10): p. 1260-1273.
189. Malhotra, J., S.K. Jabbour, and J. Aisner, *Current state of immunotherapy for non-small cell lung cancer*. Translational lung cancer research, 2017. **6**(2): p. 196.
190. Galluzzi, L., et al., *Immunological effects of conventional chemotherapy and targeted anticancer agents*. Cancer cell, 2015. **28**(6): p. 690-714.
191. Talhouni, S., et al., *Activated tissue resident memory T-cells (CD8+ CD103+ CD39+) uniquely predict survival in left sided "immune-hot" colorectal cancers*. Frontiers in immunology, 2023. **14**: p. 1057292.
192. Kim, T.K., R.S. Herbst, and L. Chen, *Defining and understanding adaptive resistance in cancer immunotherapy*. Trends in immunology, 2018. **39**(8): p. 624-631.
193. Lee, G., et al., *Is right-sided colon cancer different to left-sided colorectal cancer?—a systematic review*. European Journal of Surgical Oncology (EJSO), 2015. **41**(3): p. 300-308.
194. Väyrynen, J.P., et al., *Spatial organization and prognostic significance of NK and NKT-like cells via multimarker analysis of the colorectal cancer microenvironment*. Cancer immunology research, 2022. **10**(2): p. 215-227.
195. Salama, P., et al., *Tumor-infiltrating FOXP3+ T regulatory cells show strong prognostic significance in colorectal cancer*. Journal of clinical oncology, 2009. **27**(2): p. 186-192.
196. Pang, N., et al., *The level of Tim-3+ CD8+ T cells can serve as a potential marker for evaluating the severity of acute graft-versus-host disease after haplo-PBSCT*. Brazilian Journal of Medical and Biological Research, 2023. **56**: p. e12997.
197. Jass, J., et al., *Assessment of invasive growth pattern and lymphocytic infiltration in colorectal cancer*. Histopathology, 1996. **28**(6): p. 543-548.
198. Jakubowska, K., et al., *Stromal and intraepithelial tumor-infiltrating lymphocytes in colorectal carcinoma*. Oncology letters, 2017. **14**(6): p. 6421-6432.
199. Seitz, S., et al., *Reconstitution of paired T cell receptor α - and β -chains from microdissected single cells of human inflammatory tissues*. Proceedings of the National Academy of Sciences, 2006. **103**(32): p. 12057-12062.
200. van Pelt, G.W., et al., *Scoring the tumor-stroma ratio in colon cancer: procedure and recommendations*. Virchows Archiv, 2018. **473**: p. 405-412.
201. Huijbers, A., et al., *The proportion of tumor-stroma as a strong prognosticator for stage II and III colon cancer patients: validation in the VICTOR trial*. Annals of oncology, 2013. **24**(1): p. 179-185.
202. Eriksen, A.C., et al., *The prognostic value of tumour stroma ratio and tumour budding in stage II colon cancer. A nationwide population-based study*. International journal of colorectal disease, 2018. **33**: p. 1115-1124.

203. Kasurinen, J., et al., *Tumor-associated CD3-and CD8-positive immune cells in colorectal cancer: The additional prognostic value of CD8+to-CD3+ ratio remains debatable*. *Tumor Biology*, 2022. **44**(1): p. 37-52.
204. Mao, Y., et al., *Stromal cells in tumor microenvironment and breast cancer*. *Cancer and Metastasis Reviews*, 2013. **32**: p. 303-315.
205. Mokhtari, Z., et al., *Tim3 and PD-1 as a therapeutic and prognostic targets in colorectal cancer: Relationship with sidedness, clinicopathological parameters, and survival*. *Frontiers in oncology*, 2023. **13**: p. 1069696.
206. Lee, L.H., et al., *Patterns and prognostic relevance of PD-1 and PD-L1 expression in colorectal carcinoma*. *Modern Pathology*, 2016. **29**(11): p. 1433-1442.
207. Al-Mterin, M.A., K. Murshed, and E. Elkord, *PD-1 expression, among other immune checkpoints, on tumor-infiltrating NK and NKT cells is associated with longer disease-free survival in treatment-naïve CRC patients*. *Cancer Immunology, Immunotherapy*, 2023. **72**(6): p. 1933-1939.
208. Zhang, Y., et al., *Prognostic significance of programmed cell death 1 (PD-1) or PD-1 ligand 1 (PD-L1) Expression in epithelial-originated cancer: a meta-analysis*. *Medicine*, 2015. **94**(6): p. e515.
209. Liu, R., H.-F. Li, and S. Li, *PD-1-mediated inhibition of T cell activation: Mechanisms and strategies for cancer combination immunotherapy*. *Cell insight*, 2024. **3**(2): p. 100146.
210. Saylor, J., et al., *Spatial mapping of myeloid cells and macrophages by multiplexed tissue staining*. *Frontiers in immunology*, 2018. **9**: p. 2925.
211. Xu, B., et al., *Circulating and tumor-infiltrating Tim-3 in patients with colorectal cancer*. *Oncotarget*, 2015. **6**(24): p. 20592.
212. Huang, Y., et al., *114P The prognostic role of LAG-3 expression in metastatic colorectal cancer*. *Annals of Oncology*, 2023. **34**: p. S1514-S1515.
213. Rhyner Agocs, G., et al., *LAG-3 expression predicts outcome in stage II colon cancer*. *Journal of personalized medicine*, 2021. **11**(8): p. 749.
214. Murray, P.J., *Macrophage polarization*. *Annual review of physiology*, 2017. **79**(1): p. 541-566.
215. Yang, M., et al., *Diverse functions of macrophages in different tumor microenvironments*. *Cancer research*, 2018. **78**(19): p. 5492-5503.
216. Guerriero, J.L., *Macrophages: the road less traveled, changing anticancer therapy*. *Trends in molecular medicine*, 2018. **24**(5): p. 472-489.
217. Väyrynen, J.P., et al., *The prognostic role of macrophage polarization in the colorectal cancer microenvironment*. *Cancer immunology research*, 2021. **9**(1): p. 8-19.
218. Kim, Y., et al., *The distribution of intratumoral macrophages correlates with molecular phenotypes and impacts prognosis in colorectal carcinoma*. *Histopathology*, 2018. **73**(4): p. 663-671.
219. Tsukamoto, H., et al., *Combined blockade of IL6 and PD-1/PD-L1 signaling abrogates mutual regulation of their immunosuppressive effects in the tumor microenvironment*. *Cancer research*, 2018. **78**(17): p. 5011-5022.

220. Ma, C.J., et al., *PD - 1 negatively regulates interleukin - 12 expression by limiting STAT - 1 phosphorylation in monocytes/macrophages during chronic hepatitis C virus infection*. Immunology, 2011. **132**(3): p. 421-431.
221. Dhupkar, P., et al., *Anti - PD - 1 therapy redirects macrophages from an M2 to an M1 phenotype inducing regression of OS lung metastases*. Cancer medicine, 2018. **7**(6): p. 2654-2664.
222. Katagata, M., et al., *TIM-3 expression and M2 polarization of macrophages in the TGF β -activated tumor microenvironment in colorectal cancer*. Cancers, 2023. **15**(20): p. 4943.
223. Pelaseyed, T., et al., *The mucus and mucins of the goblet cells and enterocytes provide the first defense line of the gastrointestinal tract and interact with the immune system*. Immunological reviews, 2014. **260**(1): p. 8-20.
224. Chan, L.F., et al., *Tissue-infiltrating lymphocytes as a predictive factor for recurrence in patients with curatively resected colon cancer: a propensity score matching analysis*. Oncology, 2020. **98**(10): p. 680-688.
225. Markowski, A.R., et al., *Simultaneous analysis of tumor-infiltrating immune cells density, tumor budding status, and presence of lymphoid follicles in CRC tissue*. Scientific reports, 2022. **12**(1): p. 21732.
226. Tavana, S., et al., *Clinicopathological significance and prognostic role of LAG3+ tumor-infiltrating lymphocytes in colorectal cancer; relationship with sidedness*. Cancer Cell International, 2023. **23**(1): p. 23.
227. Sickert, D., et al., *Characterization of macrophage subpopulations in colon cancer using tissue microarrays*. Histopathology, 2005. **46**(5): p. 515-521.
228. Koscsó, B., et al., *Gut-resident CX3CR1^{hi} macrophages induce tertiary lymphoid structures and IgA response in situ*. Science immunology, 2020. **5**(46): p. eaax0062.
229. Huang, Y.-K., et al., *Macrophage spatial heterogeneity in gastric cancer defined by multiplex immunohistochemistry*. Nature communications, 2019. **10**(1): p. 3928.
230. Forssell, J., et al., *High macrophage infiltration along the tumor front correlates with improved survival in colon cancer*. Clinical cancer research, 2007. **13**(5): p. 1472-1479.
231. Pinto, M., et al., *The two faces of tumor-associated macrophages and their clinical significance in colorectal cancer*. Front Immunol. 2019; **10**: 1875. 1875, Epub 2019/09/05. <https://doi.org/10.3389/fimmu.2019.01875> PMID: 31481956.
232. Elomaa, H., et al., *Spatially resolved multimarker evaluation of CD274 (PD-L1)/PDCD1 (PD-1) immune checkpoint expression and macrophage polarisation in colorectal cancer*. British Journal of Cancer, 2023. **128**(11): p. 2104-2115.
233. Lu, J., et al., *Single-Cell Analysis Reveals Immune Profile of T Cell Exhaustion-Associated Microenvironment in Colorectal Cancer*. Medp Oncol, 2024. **3**(2).
234. Zhang, L., et al., *Immune landscape of colorectal cancer tumor microenvironment from different primary tumor location*. Frontiers in immunology, 2018. **9**: p. 1578.
235. Guo, W., et al., *Resolving the difference between left-sided and right-sided colorectal cancer by single-cell sequencing*. JCI insight, 2022. **7**(1): p. e152616.

236. Berntsson, J., et al., *The clinical impact of tumour - infiltrating lymphocytes in colorectal cancer differs by anatomical subsite: A cohort study*. International journal of cancer, 2017. **141**(8): p. 1654-1666.
237. Niu, M., et al., *Comprehensive analysis of the differences between left-and right-side colorectal cancer and respective prognostic prediction*. BMC gastroenterology, 2022. **22**(1): p. 482.
238. Wang, S., et al., *Expressions of CXCR3 and PD-1 on T cells and their clinical relevance in colorectal cancer*. International Immunopharmacology, 2024. **132**: p. 111988.
239. Mik, M., et al., *Right-and left-sided colon cancer—clinical and pathological differences of the disease entity in one organ*. Archives of Medical Science, 2017. **13**(1): p. 157-162.
240. Glebov, O.K., et al., *Distinguishing right from left colon by the pattern of gene expression*. Cancer Epidemiology Biomarkers & Prevention, 2003. **12**(8): p. 755-762.
241. Marzouk, O. and J. Schofield, *Review of histopathological and molecular prognostic features in colorectal cancer*. Cancers, 2011. **3**(2): p. 2767-2810.
242. Hu, Y., et al., *Differential expression and prognostic correlation of immune related factors between right and left side colorectal cancer*. Frontiers in Oncology, 2022. **12**: p. 845765.
243. Guo, W., et al., *Resolving the difference between left-sided and right-sided colorectal cancer by single-cell sequencing*. JCI insight, 2022. **7**(1).
244. Sinicrope, F.A., et al., *Prognostic impact of deficient DNA mismatch repair in patients with stage III colon cancer from a randomized trial of FOLFOX-based adjuvant chemotherapy*. Journal of clinical oncology, 2013. **31**(29): p. 3664-3672.
245. Lu, C., et al., *DNA sensing in mismatch repair-deficient tumor cells is essential for anti-tumor immunity*. Cancer cell, 2021. **39**(1): p. 96-108. e6.
246. Ma, X., et al., *Targeting TCF19 sensitizes MSI endometrial cancer to anti-PD-1 therapy by alleviating CD8+ T cell exhaustion via TRIM14-IFN- β axis*. Cell reports, 2023. **42**(8).
247. Le Gouvello, S., et al., *High prevalence of Foxp3 and IL17 in MMR-proficient colorectal carcinomas*. Gut, 2008. **57**(6): p. 772-779.
248. Llosa, N.J., et al., *The vigorous immune microenvironment of microsatellite instable colon cancer is balanced by multiple counter-inhibitory checkpoints*. Cancer discovery, 2015. **5**(1): p. 43-51.
249. Mlecnik, B., et al., *Integrative analyses of colorectal cancer show immunoscore is a stronger predictor of patient survival than microsatellite instability*. Immunity, 2016. **44**(3): p. 698-711.
250. Li, J., et al., *Tumor-associated macrophage infiltration and prognosis in colorectal cancer: systematic review and meta-analysis*. International Journal of Colorectal Disease, 2020. **35**: p. 1203-1210.
251. Kastinen, M., et al., *Immunological and prognostic significance of tumour necrosis in colorectal cancer*. British Journal of Cancer, 2023. **128**(12): p. 2218-2226.

252. McDermott, A.J. and G.B. Huffnagle, *The microbiome and regulation of mucosal immunity*. Immunology, 2014. **142**(1): p. 24-31.
253. Guo, G., et al., *Immune cell concentrations among the primary tumor microenvironment in colorectal cancer patients predicted by clinicopathologic characteristics and blood indexes*. Journal for ImmunoTherapy of Cancer, 2019. **7**: p. 1-13.
254. Lalos, A., et al., *Prognostic significance of CD8+ T-cells density in stage III colorectal cancer depends on SDF-1 expression*. Scientific reports, 2021. **11**(1): p. 775.
255. Millen, R., et al., *CD8+ tumor - infiltrating lymphocytes within the primary tumor of patients with synchronous de novo metastatic colorectal carcinoma do not track with survival*. Clinical & translational immunology, 2020. **9**(7): p. e1155.
256. Kang, J.C., et al., *Intratumoral macrophage counts correlate with tumor progression in colorectal cancer*. Journal of surgical oncology, 2010. **102**(3): p. 242-248.
257. Bailey, C., et al., *Chemokine expression is associated with the accumulation of tumour associated macrophages (TAMs) and progression in human colorectal cancer*. Clinical & experimental metastasis, 2007. **24**: p. 121-130.
258. Ålgars, A., et al., *Type and location of tumor - infiltrating macrophages and lymphatic vessels predict survival of colorectal cancer patients*. International journal of cancer, 2012. **131**(4): p. 864-873.
259. Wang, X., et al., *Tumor cell-intrinsic PD-1 receptor is a tumor suppressor and mediates resistance to PD-1 blockade therapy*. Proceedings of the National Academy of Sciences, 2020. **117**(12): p. 6640-6650.
260. Ieranò, C., et al., *In PD-1+ human colon cancer cells NIVOLUMAB promotes survival and could protect tumor cells from conventional therapies*. Journal for immunotherapy of cancer, 2022. **10**(3).
261. Niu, M., et al., *Biological characteristics and clinical significance of soluble PD-1/PD-L1 and exosomal PD-L1 in cancer*. Frontiers in Immunology, 2022. **13**: p. 827921.
262. Mariotti, F.R., et al., *PD-1 in human NK cells: evidence of cytoplasmic mRNA and protein expression*. Oncoimmunology, 2019. **8**(3): p. 1557030.
263. Jöhrens, K. and J. Rüschoff, *The challenge to the pathologist of PD-L1 expression in tumor cells of non-small-cell lung cancer—An overview*. Current Oncology, 2021. **28**(6): p. 5227-5239.
264. Yu, J., et al., *Nuclear PD-L1 promotes EGR1-mediated angiogenesis and accelerates tumorigenesis*. Cell Discovery, 2023. **9**(1): p. 33.
265. Jubel, J.M., et al., *The role of PD-1 in acute and chronic infection*. Frontiers in immunology, 2020. **11**: p. 487.
266. Vareki, S.M., C. Garrigós, and I. Duran, *Biomarkers of response to PD-1/PD-L1 inhibition*. Critical reviews in oncology/hematology, 2017. **116**: p. 116-124.
267. Zhang, Y., et al., *Efficacy and safety of PD-1/PD-L1 checkpoint inhibitors versus anti-PD-1/PD-L1 combined with other therapies for tumors: A systematic review*. Cancers, 2023. **15**(3): p. 682.

268. Kitsou, M., G.D. Ayiomamitis, and A. Zaravinos, *High expression of immune checkpoints is associated with the TIL load, mutation rate and patient survival in colorectal cancer*. International journal of oncology, 2020. **57**(1): p. 237-248.
269. Brom, V.C., et al., *The role of immune checkpoint molecules on macrophages in cancer, infection, and autoimmune pathologies*. Frontiers in Immunology, 2022. **13**: p. 837645.
270. Shao, Q., et al., *TIGIT induces (CD3+) T cell dysfunction in colorectal cancer by inhibiting glucose metabolism*. Frontiers in Immunology, 2021. **12**: p. 688961.
271. Chen, X., et al., *Anti-PD-1/PD-L1 therapy for colorectal cancer: Clinical implications and future considerations*. Translational Oncology, 2024. **40**: p. 101851.
272. Zhang, C., et al., *Prioritizing exhausted T cell marker genes highlights immune subtypes in pan-cancer*. Iscience, 2023. **26**(4).
273. Norton, S.E., et al., *Immune cell interplay in colorectal cancer prognosis*. World journal of gastrointestinal oncology, 2015. **7**(10): p. 221.
274. Tapia-Galisteo, A., L. Álvarez-Vallina, and L. Sanz, *Bi-and trispecific immune cell engagers for immunotherapy of hematological malignancies*. Journal of Hematology & Oncology, 2023. **16**(1): p. 83.